Exploring Type Ia Supernova Systematics:

the Host Galaxy Bias and Intrinsic Variability

by

Jared Hand

B.S. Physics, Boise State University, 2017,

M.S. Physics, University of Pittsburgh, 2019

Submitted to the Graduate Faculty of

the Dietrich School of Arts and Sciences in partial fulfillment

of the requirements for the degree of

Doctor of Philosophy

University of Pittsburgh

2023

UNIVERSITY OF PITTSBURGH

DIETRICH SCHOOL OF ARTS AND SCIENCES

This dissertation was presented

by

Jared Hand

It was defended on

July 26, 2023

and approved by

Michael Wood-Vasey, Department of Physics and Astronomy

Rachel Bezanson, Department of Physics and Astronomy

Joe Boudreau, Department of Physics and Astronomy

John Hillier, Department of Physics and Astronomy

Rachel Mandelbaum, Department of Physics, Carnegie Mellon University

Exploring Type Ia Supernova Systematics:
the Host Galaxy Bias and Intrinsic Variability

Jared Hand, PhD

University of Pittsburgh, 2023

Type Ia supernovae are bright transient events with similar peak brightness. Once calibrated and standardized, type Ia supernova samples become powerful cosmological probes, especially for measuring dark energy and the universe's accelerating expansion. Rising tensions between independent measurements in an era of precision cosmology underscores the importance of accounting for systematic errors in analyses. This is particularly true for type Ia supernova cosmology, where observations are fit to empirical models in place of elusive theoretical alternatives. Additional concerning systematics include those arising from redshift dependence of the underlying supernova population.

This dissertation explores two topics in type Ia supernova systematics. The established type Ia supernova host galaxy bias, where intrinsically brighter type Ia supernovae prefer less massive, younger hosts, alongside its potential dependence on observation methods and fitting techniques, is studied in chapter two. Various host galaxy stellar mass and specific star formation rates samples are estimated from photometry or spectroscopy using different galaxy property fitting software, from which different estimates of the host bias are calculated and then compared. No evidence is found that the choice in method or technique influences the host bias, let alone being the source of it.

The dissertation's third chapter introduces a new physics-agnostic empirical model which provides more detailed exploration of phase-independent flux variation than that afforded by ubiquitous comparable models, such as SALT2. It is demonstrated that there is sufficient signal-to-noise in available data sets to constrain models beyond the commonly used two parameter empirical model. The results also indicate that intrinsic flux variation can be misidentified as dust-like, highlighting the difficulty estimated dust properties of type Ia supernovae. For the second project, more work is needed to better separate dust-like flux variation from intrinsic variability, and to analyze the model's standardization performance

for cosmology applications.

Both topics studied advance our understanding of supernova cosmology systematics while stressing nuance in exploring sources of and solutions to these errors.

Table of Contents

List of Tables

List of Figures

Preface

There are hundreds of people I could individually thank for helping me reach this point. Each of you know who you are. That said, I want to thank those who were instrumental for getting me where I am today.

First and foremost, I thank my parents, Loraine and John Hand, who dedicated their lives to support me and my siblings. They provided us a safe, steady home and opportunities for higher education that evade too many people in our communities. Even when I gave up on myself, neither one of them ever gave up on me. Both supported me unconditionally as I struggled with obsessive compulsive disorder from a young age — support that had I not received, then I'd surely not be writing this preface right now. They instilled a deep compassion for others and a determined work ethic, all while providing a safe and humble environment to grow and thrive in.

Each of my five siblings, Christine Sansotta, Myles Sansotta, Rorie Ellison, Andrew Hand, and Leaha Hand, have all contributed their support to me in their unique ways. Similarly, I want to thank my many aunts, uncles, and cousins, notably Ryan Hand and Thomas McNevin, who have all stuck with me through good and ill. Never once have my siblings or cousins given time or consideration to my self doubts. They all have believed in me unconditionally, even when I didn't believe in myself.

I honestly do not think I would have finished this program without my fiancé Lorena Mezini's unwavering support and unconditional love, especially during a particularly difficult period between 2019 and 2021. She is the most caring and understanding person I have ever met, and I am beyond fortunate to be with her. Lorena is my role model and confidant, and I look forward to spending my life becoming a better person with her next to me.

I thank my childhood friends Jeff Bull Jr., Christopher Brackett, Justin Ranum, and Artemis Johnson, amongst others, back in Boise, Idaho. They all have always voiced their support and excitement since telling them I was moving to Pittsburgh. These enduring friendships were key to my transition to living in Pittsburgh and eventual success in my first year of graduate school. We have remained close despite distance's stress, and I look forward

to remaining close as I start life's next journey.

I thank my 2017 University of Pittsburgh Physics Ph.D. cohort. That first year was incredibly challenging and this group's camaraderie was foundational to my eventual completion of the program and becoming established in Pittsburgh. I remain eternally grateful for these friendships and shared memories.

I extend special gratitude to Dr. Alex Kim and Prof. Michael Wood-Vasey. I very nearly left the program due to overwhelming mental health issues in 2020. Their unwavering support and patience during my extended recovery were instrumental to me eventually completing my Ph.D. Their selfless devotion to my eventual success will forever be remembered, and I hope to emulate them well if I am ever in their position in the future. The Physics and Astronomy Department also has my thanks for their similar enduring support during that period.

Last but not least, I want to thank my dog Phelan. He taught me patience, responsibility, and mindfulness in a way that no human could. That dog has been there from the very beginning of my physics journey, through all of life's trials within, and through some of the most destructive battles against my obsessive compulsive disorder. I cannot imagine making it through the last ten years without him.

This dissertation is dedicated to those whose mental health struggles have painfully colored their experiences working towards fulfilling their dreams, and to those whose dreams were cut short because of life's inequitable and unwavering constraints. It is also dedicated to those who believe, or are told by others, that they are not good enough to achieve their goals. You are good enough — you always have been and you always will be.

1.0 Introduction

1.1 Cosmology and Dark Energy

Cosmology is the study of the universe and its evolution. Although every society has developed and celebrated unique and varied explanations of the universe since well before the written word, it is only relatively recent that a rigorous scientific framework was harnessed to quantify answers to some timeless questions: how old is the universe, where did it come from, and how will it end?

The first half of the twentieth century saw two important scientific developments leading to the genesis of modern cosmology. The first was empirical, beginning with definitive observational evidence of the universe's expansion, as measured by Edwin Hubble in 1929 and initially proposed by Georges Lemaître in 1927 [76, 103]. Observed recessional velocities of galaxies is independent of viewing angle (more succinctly, it is isotropic), with recessional velocity following a linear relation with respect to measured distance. This relationship is the Hubble-Lemaître law (commonly referred to as Hubble's Law):

$$v = H_0 d \tag{1}$$

where H_0 is the Hubble constant, a cosmological parameter quantifying the present expansion rate of the universe usually given in units of km s^{-1} Mpc^{-1}.

The Hubble constant, being independent of viewing angle, alongside the Copernican principle, gives rise to two cosmological principles: that at sufficiently large distance scales, the universe is effectively isotropic and homogeneous. These properties, alongside an additional constraint of path connectedness, are encapsulated within an expanding spacetime geometry called the Friedmann–Lemaître–Robertson–Walker (FLRW) metric [57]. A spacetime interval for the FLRW metric is

$$-d\tau^2 = -c^2 dt^2 + a(t)^2 \left[dr^2 + S_k(r)^2 d\Omega \right] \tag{2}$$

where $d\Omega = d\theta^2 + sin^2\theta d\phi^2$ and $S_k(r)$ is a function of r and Gaussian curvature k:

$$S_k(r) = \begin{cases} \sqrt{k}^{-1} \sin(r\sqrt{k}) & \text{if } k > 0 \\ r & \text{if } k = 0 \\ \sqrt{|k|}^{-1} \sinh(r\sqrt{k}) & \text{if } k < 0. \end{cases} \tag{3}$$

Cosmic Microwave Background observations, alongside baryon acoustic oscillations measurements from large scale structure surveys, place exceptionally strong constraints on the universe's spatial curvature, finding $k = 0$ at 0.2% precision [127]. For simplicity, only flat FLRW geometries are considered in further detail (i.e. $k = 0$ and $S_k(r) = r$). $a(t)$ is the scale factor, which relates the physical distance between objects given the coordinate distance on an FLWR manifold at time t. This is readily clear when considering a constant t ($dt = 0$), which reduces Equation 2 to an isotropic and homogeneous spatial geometry.

The second key development was Albert Einstein's general theory of relativity in 1915, which relates the curvature of spacetime to the mass-energy distribution within, providing a necessary framework to formally describe the time evolution of the universe's underlying geometry [50]. Specifically, general relativity affords a model of $a(t)$'s time evolution as functions of the universe's constituent energy and mass densities such as bayronic matter, dark matter, photons, neutrinos, etc. Applying the Einstein field equations to the FLRW metric produce the Friedmann equations [57], which equate the time evolution of $a(t)$ to pressure p and density ρ, alongside an integration constant Λ, referred to here as the cosmological constant:

$$\begin{aligned} \left(\frac{\dot{a}}{a}\right)^2 &= H^2 \\ &= \frac{8\pi G\rho}{3} + \frac{\Lambda c^2}{3} \end{aligned} \tag{4}$$

and an acceleration equation

$$\frac{\ddot{a}}{a} = -\frac{4\pi G}{3}\left(\rho + \frac{3p}{c^2}\right) + \frac{\Lambda c^2}{3}. \tag{5}$$

$H(t)$ is the Hubble parameter and is a measure of the universe's expansion rate at time t. Here, the Hubble constant H_0 is interpreted as the Hubble parameter measured at present.

Both parts of the right side of equation 5 are worth interpreting. The linear combination of pressure and density leads to a decrease in the scale factor's acceleration, which is what one would expect from gravity: mass and energy should slow expansion due to the attractive nature of gravity. This is in stark contrast to cosmological constant, which instead allows for an effective negative pressure and providing a possible energy density that can not only maintain expansion, but even accelerate it. The cosmological constant is an example dark energy model, models of energy densities that exerts negative pressure. In this case, a cosmological constant results in dark energy density that is constant with respect to time. Other models for dark energy have been proposed but will not be considered here — see Weinberg et al. 2013 for more about alternative dark energy models or modifications to general relativity to similarly account for an accelerating universe [167].

Equation 4 is commonly rewritten in terms of density parameters Ω_i, where each density component ρ_i is divided by a critical density $\rho_c = 8\pi G/3H^2$. Accounting for each density component's dependence on $a(t)$, Equation 4 can be rewritten as

$$H^2 = H_0^2[\Omega_M a^{-3} + \Omega_\Lambda] \tag{6}$$

where indices M and Λ correspond to the density parameters for matter and the cosmological constant as measured at present, respectively. Relativistic species, such as photons and neutrinos, have negligible contributions to this expression during the epochs probed by SN Ia observations and are omitted.

Equation 6's empirical utility is limited by its explicit use of $a(t)$, a quantity not directly measurable. Fortunately, the relationship between cosmological redshift (z, the redshift due to the expansion of the universe) and $a(t)$ affords an easy substitution. Defining the present scale factor $a_0 = 1$, this relationship is $a(z) = 1/(1+z)$, with z is defined as $(\lambda_{\text{observed}} - \lambda_{\text{emitted}})/\lambda_{\text{emitted}}$. Therefore, the line of sight coordinate distance $d_c^{mod}(z)$ between an Earth-based observer and an object with measured redshift z can be solved by integrating a null geodesic line element from Equation 6 after an appropriate transformation from a to z:

$$d_c^{mod}(z) = \frac{c}{H_0}\int_0^z \frac{dz}{[\Omega_M(1+z)^3 + \Omega_\Lambda]^{1/2}}. \tag{7}$$

The time elapsed between photon emission and observation can also be directly inferred from its observed redshift via an integration similar to Equation 7. Similarly, the current age of the universe can be calculated from said equation, with best estimates currently being around 13.7 billion years [127, 1]. As such, there are explicit one-to-one relationships between photon travel time, photon travel distance, observed redshift, and the scale factor.

1.2 Constraining Cosmologies From Observations

The explicit dependence of coordinate distance on key cosmological parameters (namely, H_0 and energy densities Ω_M and Ω_Λ) means observations from Earth can directly constrain an FLRW-derived cosmological model. One such approach is to compared predicted physical distances derived from $d_c^{mod}(z)$ from the observed flux of an object with known luminosity and redshift z. See Hogg 1999 for a pedagogical summary of this formalism, including generalizations of the following derivations for $k \neq 0$ cosmologies [72].

The observed luminosity distance d_L is

$$F = \frac{L}{4\pi d_L^2} \tag{8}$$

where L is the absolute luminosity (the luminosity that would be measured by an observed at 10 pc) and F is the observed flux. For a $k = 0$ cosmology, the predicted luminosity $d_L^{mod}(z)$ at redshift z is

$$d_L^{mod}(z) = (1+z)d_c^{mod}(z). \tag{9}$$

In the limit as $z \to 0$, $d_L^{mod}(z) \approx cz/H_0$, meaning Hubble's law is recovered in this low redshift limit since $v/c \approx z$ in this regime. Note that at low redshifts it is effectively impossible to constrain energy densities Ω_M and Ω_Λ — see Figure 1. Assuming sufficiently large redshifts (i.e. $z > 0.2$), comparisons between the observed luminosity distance d_L and the predicted luminosity distance $d_L^{mod}(z)$ can directly constrain cosmological models. With a sufficiently bright class of objects with known or derivable absolute luminosity, we should be able to estimate cosmological parameters.

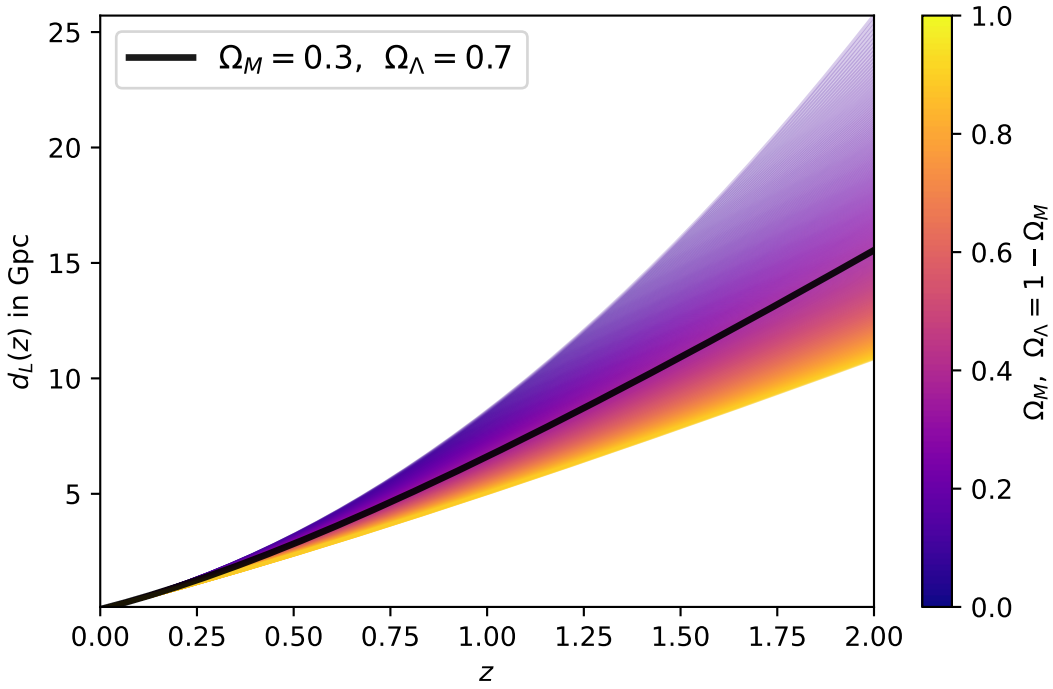

Figure 1: This plot compares luminosity distance predicted from differing flat cosmologies $k = 0$ for a fixed $H_0 = 70$ km s^{-1} Mpc^{-1}, with $0 \leq \Omega_M \leq 1$. Labeled is the current best estimates: $\Omega_M = 0.3$ and $\Omega_\Lambda = 0.7$. At low redshifts ($z < 0.2$) it is very difficult to differentiate between different cosmologies — that SNe Ia are visible out to $z \approx 2$ makes clear their utility for observational cosmology.

The luminosity distance $d_L^{mod}(z)$ is almost always presented as a distance modulus, or the apparent magnitude for an observer at 10 pc. For an object with known intrinsic brightness here indexed by i, the predicted and observed distance moduli are respectively defined as:

$$\mu^{mod}(z_i) = 5\log_{10}\left[\frac{d_L^{mod}(z_i)}{10}\right] \tag{10}$$

$$\mu_i = m_i - M = 5\log_{10}(d_{L,i}) - 5 \tag{11}$$

m is the observed apparent magnitude and M is the object's absolute magnitude (or apparent magnitude at 10 pc). Astrophysical phenomena with known or estimable M that are sufficiently similar for all population members are called standard candles. Such astronomical objects may vary with time (they might be transient or variable events). We care most about these objects' peak brightness.

Obviously, standard candles have immediate utility in constraining cosmologies. For distance measurements made with these objects, a quantity of interest is the Hubble residual, which is the difference between observed and predicted distance moduli:

$$\Delta\mu_i = \mu_i - \mu^{mod}(z_i). \tag{12}$$

With a sample of observed standard candles, cosmological parameters can therefore be inferred by minimizing Hubble residual scatter.

A class of astrophysical objects must satisfy additional important properties before being used as a standard candle. First, their underlying population properties should be relatively constant with redshift, or any redshift-depend change in properties must be well understood. As a simple example, consider a hypothetical standard candle that becomes intrinsically brighter as the universe expands, and that this is not accounted for. The result will be cosmological parameter estimates will be systematically biased by erroneously inferring shorter distances due to the redshift dependence of the underlying object's population properties.

Standard candles also need to be sufficiently bright. Bright objects are more likely to be observed and are visible at greater distances. Sufficiently bright means that the objects exist within the Hubble flow, or at a sufficient distance that cosmic expansion dominates the observed redshift. This corresponds to an observed redshift of $z > 0.03$, or a recessional velocity

of at least ≈ 9000 km s^{-1}. Peculiar redshifts, or redshift arising from local gravitational interaction, can easily dominate the observed redshift for $z < 0.03$. For $H_0 = 70$ km s^{-1} Mpc^{-1}, this redshift corresponds to a distance of 128 Mpc. Comparing predicted $d_L z$ to measured d_L without first correcting for peculiar motion will increase Hubble residual scatter — peculiar velocity can be both positive and negative relative to an Earth-based observer. For redshifts $z < 0.03$, peculiar velocity dominates the observed motion. Naturally, having a standard candles bright enough to be readily observed beyond $z = 0.03$ is advantageous since it reduces the impact of peculiar motion. See Davis et al. 2011 for a summary peculiar velocity error treatment for standard candles in cosmology [46].

Constraining cosmological parameters from data is ultimately an exercise in regression, so in general the more data we have, the more precise our estimates. This is particularly true since observational error and intrinsic brightness dispersion decrease the statistical weight of individual standard candle observations. Naturally, for a fixed intrinsic luminosity, a more frequent standard candle is preferred over a less frequent one, since this affords more frequent observed events. Here again, brighter standard candles probing higher redshifts further improve regression by extending data set's 'lever arm'. Observations of standard candles with discernible peak luminosity dispersion will necessarily be biased towards brighter objects at higher redshifts due to observational limitations here on Earth: in other words, we will preferentially observe brighter objects when at the limit of our detector's sensitivity. This is called the Malmquist Bias and must be corrected for to prevent any subsequent systematic error [105].

There is no clear cut requirement over how 'standard' a standard candle must be. In principle, a more frequent hypothetical standard candle with a larger observed sample (say, $N \sim 10^3$) that has an intrinsic brightness dispersion of ~ 1 mag may be preferable to another hypothetical type with an dispersion closer to ~ 0.1 mag, but with only has a dozen such observed objects. Ignoring systematic errors, statistical constraining power goes $\sigma/\sqrt{N}$ for some intrinsic dispersion σ and sample size N. Obviously, the larger the population size and the tighter the population's luminosity dispersion, the more constraining power the standard candle has. Systematic errors complicate this otherwise straightforward calculation.

1.3 Distance Indicators: Type Ia Supernovae

Supernovae are the cataclysmic end of certain stars or stellar remnants. A star's evolution is largely determined by its starting mass: for those with $M < 8M_\odot$ (where $M_\odot$ is one solar mass), the terminal phase is a degenerate stellar core called a white dwarf, while for $M > 8M_\odot$ the result is a core-collapse supernovae. White dwarf stars, under certain conditions, also lead to a supernovae.

Supernovae are intensely energetic events being capable of outshining their entire host galaxy for weeks after exploding. This brightness is key to their utility: we can observe these transient events at immense distances, distances sufficient to constrain fundamental cosmological parameters. These derived luminosity distances from line-of-sight observations provide exceptional constraining power on Ω_Λ by directly probing how the universe has expanded.

For historic reasons, supernovae are classified by spectral line features, or the lack thereof: type I supernovae, which lack hydrogen lines, and type II supernovae, which feature hydrogen lines [114]. All Type II supernovae are core collapse supernovae. If a type I supernova features distinct silicon features, then it is labeled a type Ia supernova — these supernovae are thermonuclear explosions of white dwarf progenitors [51]. Other type I supernova subclasses lacking silicon exist and instead result from stellar core collapse. For brevity throughout, type Ia supernova will be shortened to SN Ia (SNe Ia for plural).

Much of the following discussion summarizing SNe Ia research is from the Maoz et al. 2014 review [111]. SNe Ia are believed to result from the thermonuclear combustion of white dwarfs due to binary system interactions [73]. This is fundamentally different than other supernovae types, which instead result from the core collapse of massive stars incapable of further exothermic fusion. Unique among supernovae are that SNe Ia occur in both young *and* old stellar populations — indeed, SNe Ia are among the most numerous of all supernova types. They also exhibit a remarkable homogeneity in their spectral evolution and peak brightness. This peak brightness is particularly high, even compared to most other supernovae, averaging at about 10^{43} erg s^{-1} near maximum brightness. About 85% of the explosion energy is deposited between rest frame U and I band wavelengths (between 3600

and 8000 Å), which makes SNe Ia easily observable from ground-based observatories.

Binary systems that include carbon/oxygen white dwarf stars are excellent candidate SN Ia progenitor systems. The degenerate equation of state governing a white dwarf means the electron-degenerate gas has an effectively unchanging volume or pressure with response to temperature change. This means that if a runaway nuclear reaction starts on an otherwise stable white dwarf — a reaction which is strongly dependent upon temperature — the result will be the rapid and efficient nuclear combustion of almost the entire white dwarf. This provides sufficient energetics to account for the observed $\sim 10^4$ km s^{-1} feature broadening in spectra, an artifact of an expanding cloud of radioactive debris and ash left over from the explosion. It also explains the apparent lack of hydrogen and helium in SN Ia spectra, which are present in nearly all other stellar systems. A massive production of radioactive material then heats the expanding ejecta born from the explosion, resulting in an increase in observed brightness until it peaks approximately two or three weeks after explosion[1]. ^{56}Ni, with a half-life of 9 days, decays into ^{56}Co, which has a half-life of 114 days, which finally decays into stable ^{56}Fe [7]; this decay channel naturally explains the characteristic 'dog leg' in SN Ia light curves about one week post B-band maximum. White dwarf stars have a theoretical maximum Chandrasekhar mass $M_{\text{limit}} = 1.44 M_{\odot}$, which if exceeded could lead to a cataclysmic thermonuclear event. Such a limit purports a natural explanation for why SNe Ia have similar peak brightness. These transients remain readily visible for many months, with the expanding, opaque ejecta cloud being energized by the aforementioned radioactive decay.

This relatively large time window for observation, their observability in wavelengths transparent to Earth's atmosphere, relatively consistent peak brightness, and sufficiently high frequency seem to make SNe Ia a prime choice to measure cosmic distances. With an accurate model capturing an SN Ia's spectral evolution, observations could be fit to photometric/spectroscopic time series (also called light curves) from which derive peak luminosity can be inferred. With this peak luminosity information, we could then constrain cosmological parameters from using a suitably large number of observed events.

This ideal portrayal is incomplete. As summarized in Maoz et al. and further in

[1]This exact time of peak brightness is wavelength dependent.

Soker 2019 [156], theoretical modeling for SNe Ia is incomplete. For example, how a white dwarf star is destabilized leading to a runaway thermonuclear explosion is not understood. There are two proposed progenitor scenarios, or channels, that attempt to explain this destabilization. Single degenerate models propose a binary star system where a degenerate star accretes material from a non-degenerate companion until the the Chandrasekhar mass is exceeded, which, under certain conditions, then results in an SN Ia [169]. Double degenerate models instead propose accretion of matter from within an inspiraling white dwarf binary system, with one binary dwarf eventually exceeding the Chandrasekhar limit, or both merging with catastrophic consequences [78]. Apart from many outstanding theoretical uncertainties in both proposed scenario, neither are able to actually replicate observed SN Ia spectral evolution. Similarly, proposed detonation or deflagration models ostensibly sourced by the aforementioned progenitor channels fail to produce chemical abundances within an expanding ejecta that match observations [170]. This all has been complicated further by observational evidence supporting notable variation in SN Ia ejecta mass as derived from bolometric luminosity light curves, demonstrating that there are significant rates of non-Chandrasekhar mass progenitors in nature [148].

From the perspective of observational astronomers, SNe Ia do not form a homogeneous population. Despite their similar peak brightness, there are discernible degrees of variation in color, light curve duration (also called stretch or width), and spectral feature properties such as equivalent width line velocity. That there appears to be spectral SN Ia subtypes calls into question the supposed physical homogeneity of SN Ia [166, 21, 17] and at present, no theoretical model can account for these variations or subtypes, let alone average population behavior. Intrinsic SN Ia peak brightness dispersion is $\sim$ 1 mag in rest-frame B-band brightness, the wavelength range where they are the brightest [22, 152]. Such dispersion makes it difficult to constrain cosmologies without a very large sample size, a size not afforded by past and current observational resources. Some mechanisms, such as variable progenitor metallicity influencing ^{56}Ni production [170], or temperature dependence driving Fe line blanketing [85], provide some meaningful insight into the underlying physics of SNe Ia, but a complete, cohesive theoretical framework remains elusive.

During the early 1990s, a growing pool of evidence for SN Ia variety and subtypes nearly

derailed SNe Ia's usage in observational cosmologies as standard candles. Fortunately, in exploring this diversity, significant empirical relationships between SN Ia brightness and other observables were identified [22]. Importantly, these relationships identified correlations between peak brightness with other observables. Because these other observables were measured or inferred independently of peak brightness measurements, these relationships could be exploited to correct for intrinsic brightness dispersion in a process called standardization.

1.3.1 Type Ia Supernova Standardization and Dark Energy

It was the seminal Branch letter in 1993 that confirmed without doubt that peak luminosity correlated both with light curve duration (width or stretch) and with B-band peak $B-V$ color [22]. These relations will be referred to throughout this dissertation as the width-luminosity relationship (WLR) and color-luminosity relationship (CLR), respectively. SN Ia samples standardized via the WLR and CLR then provided convincing evidence of a universe undergoing accelerating expansion at the end of the millennia and establishing SNe Ia's exceptional utility as distance measures for modern observational cosmology [123, 131].

The first two decades of the twenty-first century have seen SN Ia cosmology [16, 25], baryon acoustic oscillations inferred from large scale structure surveys [9], spatial correlations from weak lensing [77, 109], galaxy cluster abundance constraints [13], and CMB observations [74, 127] all establish ΛCDM[2] as the leading cosmological model of the universe, with dark energy in the form of the cosmological constant currently dominating the universe's energy budget [16, 127, 1].

SNe Ia observations are first fit to a model quantifying light curve properties such as peak brightness, stretch, and color at maximum before the sample is standardized. As mentioned, empirical models, such as the popular SALT2[3] model, are used in place of theoretical models [65]. A standardization model is then selected — here the ubiquitous linear Tripp standardization model [161]. The Tripp model for SALT2 (with per-SN parameters x_1 and

[2]CDM refers to cold dark matter, a nonrelativistic dark matter model that weakly interacts with baryonic matter [121] Current observations favor CDM for its ability to explain hierarchical structure formation in the universe.

[3]SALT2 x_1 and c capture stretch and $(B-V)_{\max} - \langle (B-V)_{\max} \rangle$ variation in the SN Ia population, respectively. It has been used in every major SN Ia cosmology analysis since 2014 and is, at the time of writing, the *de facto* standard in the field.

c) defines the standardized SN Ia distance modulus $\mu^*_{s,i}$ as an augmented Equation 11 with two additional global nuisance variables α and β:

$$\mu^*_{s,i} = m_i - M_s + \alpha x_{1,i} - \beta c_i \tag{13}$$

where M_s is a now free parameter, interpreted as the standardized absolute magnitude. Specifically, M_s would the peak absolute brightness of an SNe Ia's after its light curve shape has been appropriately corrected for by parameters x_1 and c, respectively. The effectiveness of the Tripp standardization procedure with the SALT2 model is profound, decreasing SN Ia intrinsic dispersion from ≈ 1 mag to ≤ 0.15 mag in recent analyses [16, 152, 1].

With the standardization model a χ^2 objective function can then be defined over a sample of N SNe Ia indexed by i:

$$\chi^2_{SN} = \sum_i^N \frac{[m_i - M_s + \alpha x_{1,i} - \beta c_i - \mu(z_i|H_0, \Omega_M, \Omega_\Lambda)]^2}{\sigma_i^2 + \sigma_{int}^2} \tag{14}$$

.

For brevity, Equation 14 assumes each SNe Ia to be independent, ignoring the covariance arising from population brightness dispersion, instrument calibration, and light curve fitting, amongst others. See Betoule et al. 2014 for a summary of covariance matrix estimation and handling for multi-survey SN Ia cosmology analyses [16]. Optimizing χ^2_{SN} with respect to global parameters then provides a best-fit cosmology estimate alongside nuisance variables M_s, α, and β, which directly inform sample standardization. See Kim 2011 for a detailed summary of this process and comparison of different techniques to optimize χ^2_{SN}, including a discussion about estimating the intrinsic dispersion parameter σ^2_{int} frequently fit for in SN Ia cosmological studies [96].

1.3.2 Distance Ladders

H_0 cannot be directly constrained with standardized SN Ia samples due to a degeneracy between M_s and H_0. This is made apparent by inserting Equation 13 into the Hubble residual definition Equation 12:

$$\Delta\mu^{mod}(z_i) = m_i - M_s + \alpha x_{1,i} - \beta c_i + \log\left(\frac{H_0}{c}\right) - \log(1+z_i) - \log\left(\int_0^{z_i} \frac{dz}{[\Omega_M(1+z)^3 + \Omega_\Lambda]^{1/2}}\right).$$

M_s and H_0 are both global offset parameters — any attempt to minimize $\Delta\mu(z)$ dispersion will lead to degenerate M_s and H_0 solutions. In other words, standardized SNe Ia alone provide only relative distance measurements — they cannot provide a distance scale zero point[4].

Fortunately, other standard candles with absolute magnitudes not inferred via standardization can break the M_s-H_0 degeneracy, assuming these other standard candles occur in SN Ia host galaxies. Cepheids, variable stars whose peak luminosity is directly related to their luminosity periodicity, are readily observed in nearby galaxies, including numerous SN Ia hosts. By constraining H_0 locally, Cepheid observations calibrate SN Ia distance moduli onto an absolute distance scale, effectively breaking the $M_s - H_0$ degeneracy. A recent example of this technique is the SH0ES project by Riess et al. 2019 [133]. Pinning relative SN Ia distance measurements with absolute Cepheid observations is an example of a distance ladder.

Cepheids are not the only distance indicators used to build up the SN Ia distance ladder. A relatively recent alternative is the tip of the red giant branch (TGRB) method to estimate as absolute distances, as demonstrated by Freedman et al. 2019 in conjunction with the Carnegie Supernova Project [56]. Calibration of standardized SN Ia distance moduli with local standard candles are examples of cosmic distance ladders in action[5] — see Figure 2 examples ladder workflows.

[4] You can constrain Ω_M and Ω_Λ with only SNe Ia, despite the M_s-H_0 degeneracy.
[5] You can also anchor SN Ia distances using the CMB.

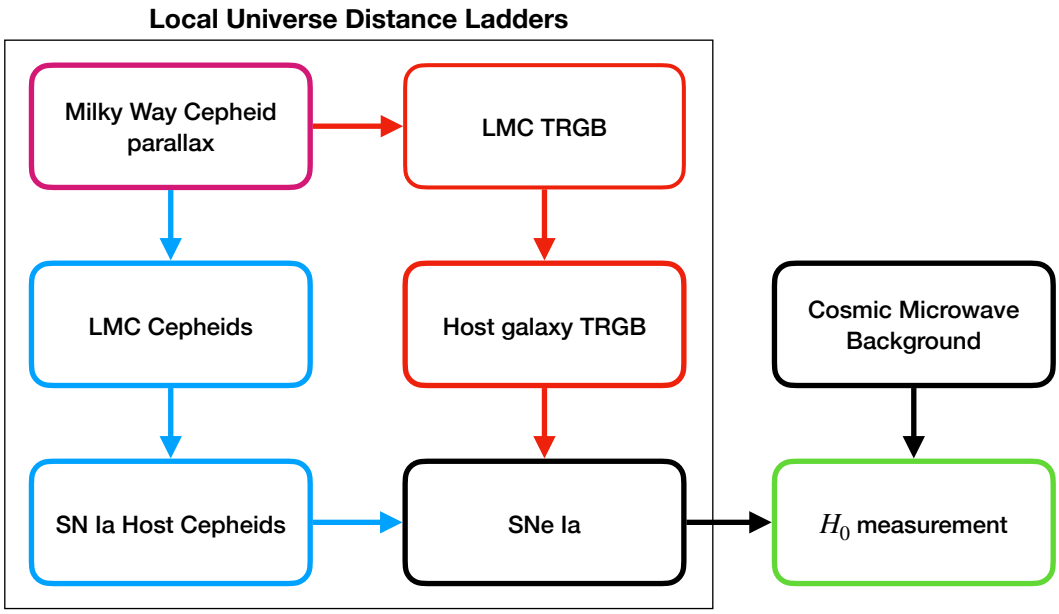

Figure 2: A workflow summarizing various local universe distance ladders used to calibrate absolute distance scales for type Ia supernova cosmology.

1.4 Present Tensions and Systematic Errors

To first order, the larger the SN Ia sample, the more constraining power one has on cosmological parameters as estimated with Equation 14. Naturally, appreciable resources have been allocated to observing more SNe Ia along an increasingly wide redshift range via sequences of ever-improving SN Ia surveys. Dark energy was discovered at the turn of the millennia using two data sets of 42 and 34 SNe Ia, respectively, with a maximum redshift of $z = 0.83$ — the recent Pantheon+ joint survey analysis by Brout et al. 2022 sports over 1550 spectroscopically-confirmed SNe Ia out to redshift $z = 2.26$ [25]. This dramatic increase in statistics will soon be dwarfed by the upcoming Legacy Survey of Space and time (LSST) through the Vera C. Rubin Observatory, which is expected to observe $\sim 10^7$ over its ten year program starting in 2024 [79]. Such a massive sample size provides impressive constraining power on dark energy measurements and have ushered in an era of precision SN Ia cosmology. It has also highlighted the growing concern of systematic errors, known or unknown, that could bias such precise cosmological parameter estimates.

Such improvements are not isolated to SN Ia cosmology. Similarly impressive strides in baryon acoustic oscillations and CMB measurements have placed increasingly tight constraints on energy densities Ω_M and Ω_Λ, and H_0 independent of SN Ia cosmology. Unfortunately, these increasingly confident measurements have come into tension with those found for the local universe using SNe Ia, particularly when anchored with Cepheids [55]. Here, local observations mean, in a cosmological sense luminosity distances tracing cosmological history out to about $z \approx 2$, corresponding to when the universe was dark energy or matter dominated. In contrast, CMB observations, which corresponds to a redshift of $z \approx 1100$, an era when the universe's evolution was instead dominated by radiation. Figure 3 compares different H_0 measurements and makes obvious the divergence between Cepheid and CMB measurements (Planck provides the most recent CMB H_0 measurement). More recently, researchers from the H0LiCOW project have exploited strongly lensed quasars to locally constrain H_0 via lens-induced time delays [171]. Such a measurement is a measurement independent of those made from SNe Ia and CMB cosmology analyses.

This so called 'Hubble tension' has brought parameter estimation methodologies under

unprecedented scrutiny as opposing teams scour their own and other's techniques. A major concern is this tension arises not from some exciting new physics, but instead arises from improperly handled or unaccounted for systematic errors. As discussed, SN Ia cosmology requires a hierarchy of steps to yield parameter constraints. Each of these steps can introduce multiple systematic errors into one's analysis, some of which are known and others that are not. Although all empirical research is prone to systematic error and subsequent bias, SN Ia cosmology's distance ladder calibration, empirical modeling, and standardization procedures puts these analyses at particular risk. That we lack a theoretical underpinning of SN Ia progenitor and explosion physics only complicates this matter further. Indeed, understanding the source of and properly accounting for these systematics has been of primary focus for SN Ia cosmologists well before the Hubble tension developed.

Here, we separate sources of SN Ia systematic errors into two broad categories[6]: distance ladder calibration systematics which primarily affect H_0 measurements, and SN Ia modeling or standardization systematics which directly impact Ω_M and Ω_Λ, amongst other energy density parameters. Historically, researchers also had to account for systematic errors arising from calibrating different SN Ia survey samples which requires challenging photometric zero-point calibrations and covariance propagation[16, 152, 25]. These joint analyses were necessary not only to decrease statistical error, but to increase the joint sample's redshift range. Current and future surveys such as the Dark Energy Survey and LSST have partly or will largely alleviate this source of systematic error, so these will not be considered further.

Two of the competing SNe Ia distance ladder schemes are an excellent case study of distance ladder calibration influencing H_0 estimates due to systematics. SH0ES is the leading Cepheid calibration program and finds $H_0 = 73.2 \pm 1.3$ km s^{-1} Mpc^{-1}, while Carnegie Supernova Project's tip of the red giant branch (TRGB) calibration finds $H_0 = 69.6 \pm 1.9$ km s^{-1} Mpc^{-1} [133, 56]. Cepheid-based measurements contrast with Planck's most recent $H_0 = 67.5 \pm 0.5$ km s^{-1} Mpc^{-1} at a 5σ significance level. Both teams have subsequently reanalyzed the other's data sets and scrutinized each calibration methodology, trying to explain the discrepancy between Cepheids and TRGB calibration as improper handling of systematics.

[6]Excluded here are systematics arising from of instrument calibration and peculiar velocities, the latter of which is notoriously challenging for low redshift SNe Ia. For a review on SN Ia peculiar velocities, see Davis et al. 2011 [46].

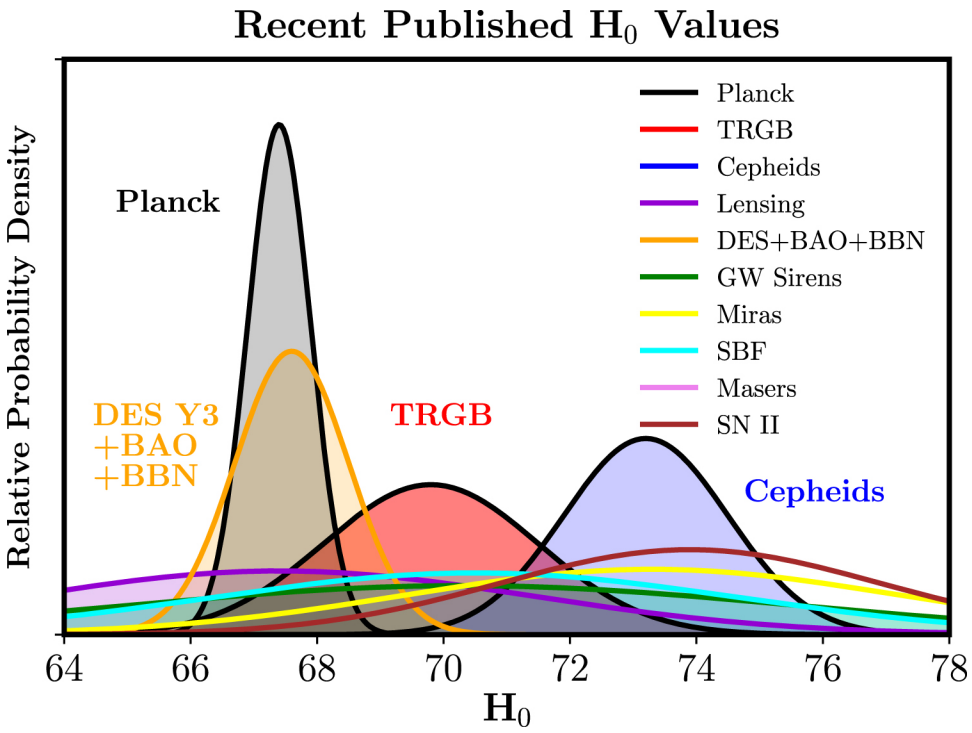

Figure 3: A comparison of recent H_0 measurements for various methods taken from Freedman 2021 [55]. Here, TRGB and cepheids are local H_0 determinations constrained using SNe Ia. Planck provides the most recent CMB measurements. At present, SNe Ia with cepheids and CMB measurements have a 3σ discrepancy, which could be the result of new physics that diverges local and CMB cosmological parameter estimates, or faults in respective analyses. Such faults could include observational bias and improper handling or consideration of systematic errors.

Such a development is in an excellent example of systematic error treatment being placed under extreme scrutiny by researchers — see Valentino et al. 2021 for a summary of this Hubble tension, including additional comparisons with other H_0 measurements [48].

The second category concerns itself with the underlying SN Ia population's properties and how they could potentially bias cosmological analyses. Such systematics bias relative distance measurements between SNe Ia. Of chief concern is population drift with redshift, something that would quickly undermine a standard candle's utility for cosmology. There is circumstantial evidence for such drift in the SN Ia population, such as progenitor metallicity[54] and host galaxy properties both correlating with peak brightness; see Section 2.2 for a review of this host bias. Galaxy demographics and average metallicity rates are functions of redshift, which means the underlying SN Ia population could change with redshift. There is also evidence than current standardization procedures do not capture all SN Ia population flux variation that correlates with peak brightness, either because of incomplete modeling [147, 20] or limited standardization formalism [144]. Accounting for incomplete standardization also requires improved understanding of SN Ia foreground dust extinction, which likely relates further to the measured dependence of standardized Hubble residuals on host galaxy properties [26].

1.5 Dissertation Summary

The focuses of this work are two topics in SN Ia systematics research that impact relative distance measurements, although the first topic may be important in understanding distance ladder calibration systematics as well. The first explores the dependence of observational method and fitting technique on host bias measurements, paying particular attention to host mass and specific star formation rate. The second project introduces a new empirical SN Ia model that extends phase-independent flux variation templates beyond past models to explore both intrinsic and dust-like variability in greater detail allowed in past analyses. Neither directly pertain to cosmological measurements, but instead explore SN Ia population properties, properties which are of fundamental importance for precision cosmology,

especially for next generation surveys.

1.5.1 Chapter 2: The Host Bias

Measuring the host bias requires observing host galaxies either before or after SN Ia. How these host galaxies are observed, and how physical properties are derived from said observations, could influence the measured host bias and its implication Chapter 2 summarizes research comparing SN Ia host galaxy property estimates from various observational methods and fitting techniques and see if SN Ia bias measurements change with methodology or technique. Clarifying this potential source of systematics is an important step to understanding the host bias and its origins by identifying or removing an obvious source candidate. This chapter also discusses best practices for galaxy property estimations and some limits of respective observational methods.

1.5.2 Chapter 3: Dust Attenuation and Intrinsic Variation

Dust extinction is a constant component of observational astronomy or cosmology, Dust preferentially affects lower wavelengths, resulting in severely diminished SN Ia flux in the rest frame B-band. Because there is no theoretical model for SN Ia spectral evolution, it is difficult to ascertain a dust extinction zero point for SNe Ia. This further results in a degeneracy between intrinsic variability and dust extinction for a given SN Ia. Chapter 3 introduces a new empirical SN Ia model that attempts to better separate or constrain intrinsic variability from dust-like behavior. Constraining intrinsic and extrinsic modes of variation better illuminates the underlying SN Ia population's nuanced properties, paving the way to an improved standardization scheme via superior empirical modeling.

2.0 The Dependence of the Type Ia Supernova Host Bias on Observation or Fitting Technique

This chapter was published in the Astrophysical Journal in January 2022 and was authored by Jared Hand, Shu Liu, Lluís Galbany, Daniel Perrefort, Michael Wood-Vasey, and Chris Burns [68].

More luminous Type Ia supernovae (SNe Ia) prefer less massive hosts and regions of higher star formation. This correlation is inverted during width-color-luminosity light curve standardization resulting in step-like biases (here called the host step bias) of distance measurements with respect to host properties. Using the PISCO supernova host sample and SDSS, GALEX, and 2MASS photometry, we compare host stellar mass and specific star formation rate (sSFR) from different observation methods, including local vs. global, and fitting techniques to measure their impact on the host step biases. Mass step measurements for all our mass samples are consistent within a 1σ significance from -0.03±0.02 mag to -0.04±0.02 mag. Including or excluding UV information had no effect on measured mass step size or location. Specific SFR (sSFR) step sizes are more significant than mass step measurements and varied from 0.05 ± 0.03 mag (Hα) and 0.06 ± 0.02 mag (UV) for a 51 host sample. The sSFR step location is influenced by mass sample used to normalize star formation and by sSFR tracer choice. The step size is reduced to 0.04±0.03 mag when using all available 73 hosts with Hα measurements. This 73 PISCO host subsample overall lacked a clear step signal, but here we are searching for whether different choices of mass or sSFR estimation can create a step signal. We find no evidence that different observation or fitting techniques choice can create a distance measurement step in either mass or sSFR.

2.1 Introduction

Brighter (dimmer) SNe Ia prefer less (more) massive and star-forming (quiescent) host galaxies — this trend is reversed post-standardization. The most commonly used host property to quantify this bias is stellar mass (see Section 2.2 for details), with recent SN Ia analyses incorporating a luminosity correction term for host mass during standardization [40, 16, 152]. This effect is typically quantified against Hubble residuals $\mu_{\rm SN} - \mu_{\rm mod}(z_{\rm SN})$, or the difference between the standardized brightness and that predicted by the best-fit cosmology. The ubiquitous host bias measured post-standardization is the mass step, but similar step-like trends between specific star formation rate (sSFR) and Hubble residuals for both global and local 1 kpc apertures have been observed [45, 137]. As dust, age, and metallicity correlate with mass and sSFR, similar trends have been observed for they properties; all trends are more pronounced when compared to stretch (see 2.2 for more details). The existence of these biases in historical data sets is not ubiquitous, though. Variation in trends between SFR and SN Ia properties based on SFR calibration was observed in D'Andrea et al. 2011 [45], and no mass step was found in the initial analysis of DES SNe Ia [24]; subsequent DES analyses have measured a mass step [155, 89]. This prompts the question: does the measured host-property bias depend on the chosen observation method and fitting technique used to estimate host galaxy properties?

Any attempt to explain the relationship between SNe Ia and their host galaxy's properties should begin with quantifying whether the significance of observed trends vary between choice of observation method and fitting technique. The host bias extends from the local 1 kpc environment to the entirety to a global aperture; integral field spectroscopy (IFS) samples such as PISCO [59], in providing resolved spectral information of a galaxy, are an ideal tool to measure the host bias. Pragmatism has necessitated the use of photometry to constrain host properties in nearly all cosmology analyses. We considered the following questions:

1. Does observational technique have a significant effect on measured global and local host bias?
2. Does the fitting technique used to estimate host properties effect the measured host bias?

We here built a set of of host galaxy samples and then inferred galaxy properties using different observational and fitting techniques. We compared stellar mass and SFR estimates from the PISCO sample. Using the PISCO SN Ia subsample, we then compared different stellar mass and sSFR estimate samples to SN Ia properties, looking primarily for differences in the resulting host-SN Ia property trends between mass/sSFR estimate samples. Finally, the larger observed size and strength of the sSFR host bias relationship relative to the stellar mass host bias is both presented and discussed.

In Section 2.2 we summarize SN Ia host studies up to the present followed by a summary of the considered data set in Section 2.3. Section 2.4 provides an overview of our methodology, including summaries of fitting techniques used. Our results are provided and discussed in Section 2.5, and concluding remarks presented in Section 2.6.

2.2 Background

The inferred presence of an observed correlation between the properties of SNe Ia and their host's properties is common in the literature. Parameters of light curve width variation (such as x_1 in SALT2 [65]) see lower x_1 values prefer more massive hosts, older stellar populations, and environments of larger SFR [158, 88, 64, 40, 16, 152]. Both Sullivan et al. 2010 and Gupta et al. 2011 saw a relationship between the SALT2 color parameter c and host mass and host age, respectively, albeit at a lower significance than x_1 [158, 64]; Scolnic et al 2018 found no significant color trend [152]. Recently, Pruzhinskaya et al. 2020 found a statistically significant dependence of SALT2 x_1 on host galaxy morphology, with lower x_1 SNe Ia preferring elliptical and lenticular galaxies [130].

The observed correlation between SNe Ia and host properties are not explicitly included nor accounted for with a canonical Tripp standardization model, resulting in an apparent over-correction of the host bias post-standardization. For example, both the SN Legacy Survey [158] and SDSS SN Survey [145] found a 'mass step', where SNe Ia with brighter Hubble residuals were on average hosted by more massive galaxies [88, 99, 64]. In comparing residuals in the fitted distance modulus of SNe Ia with respect to cosmological prediction

to their host masses, both SDSS and SNLS samples observed a sudden step-like change in Hubble residual vs mass near $10^{10}M_{\odot}$. [40], [16], and [152] also observed this mass step at $10^{10}M_{\odot}$ in their combined SN Ia sample analyses. Initial analysis by [24] of Dark Energy Survey (DES) SN Ia found no evidence for a mass step post-standardization, although more thorough methodology for an updated SN Ia sample did indeed recover a mass step [155, 89]. Using SNIFS spectrophotometry from SNFactory, Rigault et al. 2013 & 2018 [138, 137] found that Hubble residuals are strongly dependent upon SFR and sSFR, respectively, the latter having observed a 5σ relationship between Hubble residual and sSFR and confirming the tentative findings of [45]. Recently, Jones et al. 2018 compared $u - g$ color of SN Ia 1.5 kpc local environment apertures against randomly selected 1.5 kpc apertures within the host, finding that the SN Ia environment correlates with SN Ia distance slightly more than random apertures, and found a local stellar mass step after the global mass step had been corrected for [83]. Hayden et al. 2013 used both mass and metallicity to reduce Hubble residual scatter [70]. Roman et al. 2018 used $U - V$ as a proxy for stellar age and found an age mass step of similar magnitude and significance as the fiducial mass step, and found a 7σ relationships between local $U - V$ measurement and distance [140]. Rose et al. 2019, using principal component analysis, found a strong relationship between a linear combination of host galaxy properties and Hubble residuals [141]. Brout et al. 2020 presented a model that explain the mass step post-light curve standardization via SALT2 resulting from improper treatment of host dust, which was further expanded in Popovic et al. 2021 [26, 129]. In contrast, Uddin et al. 2020 found a clear dependence on Hubble residuals calculated from light curves fit with SNooPy with host mass calculated for visible and NIR light curves that was inconsistent with the model presented by Brout and Popovic [162]. Both Gonzalez-gaitan et al. 2020 and Ponder et al. 2020 found tentative evidence for a host mass step for SNooPy-fit NIR light curves for SN Ia [62, 128].

The use of simple stellar population (SSP) templates and stellar population synthesis (SPS) libraries has been a central part any endeavor to estimate a galaxy properties; these properties include stellar mass [44], stellar age, star formation rate [91, 92], and gas-phase/stellar metallicity [160, 61, 95]. Likewise, complex systematic uncertainties in modeling and from observational limitations propagate into uncertainties in derived property

estimates. Past SN Ia cosmology analyses have generally treated SSP/SPS libraries and fitting software as black boxes when estimating host properties, and frequently relied on few data points from photometry spanning a narrow wavelength range. Redshift, stellar mass, stellar age, dust extinction, metallicity, and star formation rate are often degenerate with each other and large systematic covariances complicate fitting methods [86, 23, 160, 61]. Such degeneracies, together with systematic uncertainties, result in dramatic uncertainties for some best fit parameters (see section 3 introduction for more information).

Although optical multi-wavelength photometry of host galaxies has been the primary tool used to estimate host mass and SFR [158, 88, 37, 16, 152, 24], optical wavelength spectra [45, 82], UV or IR photometry in addition to optical spectra or photometry [64, 6], and IFS [138, 137, 59] have been used. Childress et al. 2013 and Gupta et al. 2011 [37, 64] both found stellar mass estimates using optical, IR, and UV photometry change little from mass estimates using optical photometry only, consistent with the results of Bell & deJong 2001[14]. [45] used sSFR estimates from SDSS II spectra and two different mass estimates: one from SPS model best fits using SDSS II spectra and one from [64]. Hayden 2013[70] directly compared three different mass estimates for a set of SDSS host galaxies using metallicity estimates from the Fundamental Metallicity Relation [110] to further reduce Hubble residual scatter.

2.3 Data

We consider 319 galaxies observed as part of the PMAS/PPak Integral-field Supernova Hosts Compilation from the PISCO project[59]. These observations were complemented by optical *ugriz* photometry from the Sloan Digital Sky Survey (SDSS), near-infrared (NIR) JHK_S photometry from the Two Micron All Sky Survey (2MASS), and ultraviolet (UV) NUV+ and FUV photometry from the Galaxy Evolution Explorer (GALEX). Figure 4 shows the redshift distribution of the sample, which spans a range of $0.00013 < z < 0.0875$. These 319 galaxies host 375 SNe, of which 198 are SNe Ia.

PanSTARRS DR1 [36] was considered to expand coverage, but added complexity with overlapping visible wavelength photometry and our constraint to northern hemisphere tar-

gets resulted in it being disregarded in favor of SDSS. Follow up analyses will likely make use of PanSTARRs DR2, especially if our observation footprint extends into the southern hemisphere.

2.3.1 PISCO Supernova Sample

PISCO is a compilation of SN host galaxies observed with integral field unit (IFU) spectroscopy using the same instrument PMAS/PPak [143, 90] mounted to the 3.5 m Calar Alto telescope. PISCO was built from an initial sample of SN host galaxies obtained by the CALIFA survey [146, 60, 58] and extended with new observations of SN hots based on different science goals. See the PISCO paper for more details [59].

The PISCO SN Ia subsample had 198 objects. When calculating distance moduli all 14 peculiar SNe Ia were ignored (e.g. SN 1991bg and 1991T-like objects), while 83 normal SNe Ia lacked available optical photometry, with many only having NIR light curves. SN 2014J was excluded due to its extremely low redshift and host galaxy M82's mass estimation difficulties. We used the SALT2 output fits for 30 unpublished SNe Ia from Carnegie Supernova Project II (CSPII, Suntzeff et al., in prep), bringing the sample to 101. During SALT2 fitting we removed SN 2006lf, which had an very high Milky Way color excess of $E(B-V) = 0.821$, giving a final total of 100 SNe Ia used. SDSS coverage reduced this count to 76, while mutual SDSS and GALEX coverage further reduced the number to 66 (Section 2.5.2). Four SN Ia hosts lacked Hα flux measurements and 11 host galaxies had unavailable GALEX FUV or NUV flux measurements. These too were all excluded, bringing the total SN Ia count to 51 for sSFR analysis (Section 2.5.4). See Tables 1 and 2 for a summary of sample reductions.

2.3.2 PISCO Host Galaxy Global Parameters

Stellar mass estimates and integrated Hα flux measurements of all PISCO galaxies were taken from [59] with mass estimates made using STARLIGHT [39]. Mass estimates were calculated using a SSP library built using [27] (BC03) with a [35] initial mass function (IMF). PISCO used a more complex set of basis templates, instead of just BC03 used here (see , Section 3.2.1 of PISCO 2018 for more details [59]) — otherwise, the methodology we used

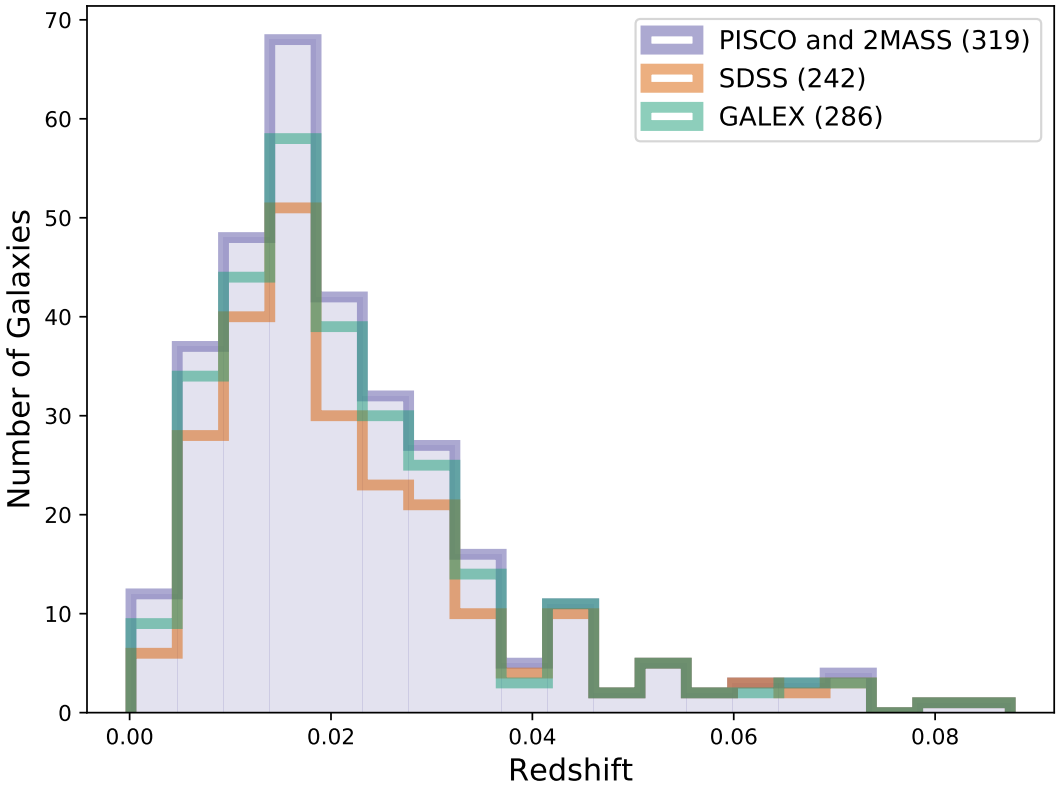

Figure 4: Distribution of redshifts for galaxies considered by this paper. This includes a total of 319 galaxies selected from the PISCO sample with supplementary observations from 2MASS, SDSS DR12, and GALEX. All considered targets were observed by PISCO and detected in 2MASS.

Table 1: Summary of SNe Ia sample size reductions. Details on specific SN Ia removal is provided in Section 2.3.1 Each row defines a subgroup of the row described above.

SN Ia Subsample Condition	SN Ia Count
Total PISCO SNe Ia	198
Normal SNe Ia	184
Available visible photometry + CSPII	101
Excluding specific SNe Ia	100
Available STARLIGHT mass estimates	97

to estimate masses with STARLIGHT was identical.

2.3.3 SDSS DR12 Optical Photometry

The Sloan Digital Sky Survey (SDSS) is a multi-year, multi-program survey performed at the Apache Point Observatory (APO) using the SDSS 2.5 m telescope [173, 63]. We used observations from SDSS Data Release 12 [3] to provide imagining data for host galaxies in the *ugriz* filters [49]. Mutual coverage between SDSS and PISCO is available for 239 of the 319 galaxies (74.9%).

All SDSS fields were selected using the nearest neighbor search functions built into the DR12 CASJOBS database[1] and downloaded from the Science Archive Server (SAS)[2].

2.3.4 2MASS IR Photometry

The Two Micron All Sky Survey (2MASS) was a three-year program run at the Whipple Observatory and Cerro Tololo Inter-American Observatory [154]. 2MASS observed 99.998% of the sky with three near infrared (NIR) passbands JHK_s, resulting in all PISCO galaxies having corresponding 2MASS images. Optimal operations result in a 2.5–3.4" PSF with a

[1] `http://skyserver.sdss.org/CasJobs/SchemaBrowser.aspx`
[2] `https://dr12.sdss.org/`

Table 2: Summary of mass and sSFR step analyses subsample sizes starting with 97 available STARLIGHT mass estimates.

SN Ia Subsample	SN Ia Count
SDSS coverage	76
SDSS+GALEX coverage	66
Available Hα measurements	73
Available Hα and SDSS+GALEX coverage	51

Pixel size of 2.0". Images were obtained using the Infrared Science Archive (IRSA).[3]

2.3.5 GALEX Photometry

The Galaxy Evolution Explorer (GALEX) is a space-based observatory with a 1.2 degree diameter circular field of view that observed through two ultra-violet (UV) bands, FUV (135–175 nm) and NUV (175–280 nm) [113]. A total of 287 PISCO galaxies reside within GALEX's footprint for a mutual coverage of 90.0%, although only 203 were also within SDSS coverage. Images were downloaded from the four primary GALEX surveys using STSci MAST services [4], with precedent placed on exposure time when choosing fields. Where possible we used "Deep Imaging Survey" fields (DIS: 30,000 s exposure), followed by "Medium Imaging Survey" fields (MIS: 1500 s exposure), and finally the "All-sky Imaging Survey" fields (AIS: 100×10 s exposures [113]. If available, Nearby Galaxy Survey (NGS) fields were used instead of AIS fields. Guest investigator fields were also used when necessary. 2.2% of PISCO galaxies had DIS coverage, 5.1% had NGS coverage, 14.4% had MIS coverage, and 80.9% had AIS coverage or were observed as part of the guest investigator program.

[3] `https://irsa.ipac.caltech.edu/frontpage/`
[4] `https://mast.stsci.edu/portal/Mashup/Clients/Mast/Portal.html`

2.4 Methodology

We performed our global photometry and combined that with corresponding PISCO IFS to estimate host galaxy properties. For details on PISCO data reduction we refer the reader to [59]. As one brief note, the PISCO IFS apertures were hexagonal, while the apertures on the imaging data we analyzed here are elliptical.

2.4.1 Photometric Image Preparation

Foreground objects in images from each data set were removed by masking. The position and appropriate aperture size of foreground objects in SDSS images were determined using Source Extractor on r-band images [15]. All identified objects were visually reviewed and assigned a proportion factor ($\alpha_{\rm SDSS}$) which corrected the Kron radius calculated by Source Extractor (r_k):

$$r_k^{\rm cor} = \alpha_{\rm SDSS}\ r_k.$$

This factor was used to decrease the area of measured foreground objects so to not compromise the shape of the host galaxy. Pixel values within the scaled aperture were masked and replaced using an interpolation to account for lost photons in the masked region.

For SDSS, we replaced all foreground objects within a circular region of the host less than $A \times r_k^{\rm cor}$ using a two-dimensional linear interpolation. With GALEX and 2MASS, we instead masked foreground objects due to lower field signal-to-noise leading to unrealistic interpolation results. All foreground objects outside this radius but within a radius of $2.8(A \times r_k^{\rm cor})$ were simply masked and unused. For 2MASS and GALEX we masked all foreground objects within a radius of $2.8(A \times r_k^{\rm cor})$. SDSS images were provided background-subtracted with FITS header information for background reconstruction. Background images were provided with GALEX field downloads and were used directly in background subtraction. Zero pixels in both image and provided background fields were masked for GALEX NUV and FUV data sets. As both fields were masked, this did not increase our background estimation.

2.4.2 Galaxy Parameter Estimation

To explore how the host galaxy bias varies with fitting technique, we required host property estimates from multiple techniques. To this end, we used three fitting programs to estimate host properties two for photometry and one for IFS. These fitting techniques make use of simple stellar population (SSPs) libraries, or use stellar population synthesis (SPS) libraries built by convolving a set of SSPs with a star formation history (SFH) parameterization and a recipe to handle dust extinctions to produce a library of composite stellar populations (CSPs) [165, 42]. It is important to explicitly note that simple stellar population (SSP) or stellar population synthesis (SPS) libraries contain numerous sources of systematic uncertainties and that even with high-quality observations, systematic model uncertainties endemic to SPS libraries are larger than what is expected from observational errors alone [43].

2.4.2.1 ZPEG

ZPEG estimates galaxy redshifts by fitting photometry against a library of CSPs constructed from the theoretical spectral library PEGASE.2. This resulting template fit provides additional information such as stellar mass, star formation rate, etc. The best-fit template is determined using maximum likelihood analysis with a χ^2 function for the difference between synthetic photometry computed from templates and observed photometry. Specifically, χ^2 values are calculated for each point along a four-dimensional grid of parameters ($E(B-V)$, t_*, redshift, and template), with the best-fit model being the minimal χ^2 value on the grid

$$\chi^2_Z = \sum_i^N \frac{\left[F_{\lambda,i} - \alpha F_{\lambda,\mathrm{mod}}\big(t_*, E(B-V), z\big)\right]^2}{\sigma_i^2} \tag{15}$$

where N is the number of filters, F_{mod} is the model flux density from given template of age t_* and color excess $E(B-V)$, σ_i^2 is the measured observation variance for data point i, and α is a scaling parameter to match normalized template SEDs to the observed flux. Uncertainty in the best-fit model is determined by calculating the reduced χ^2 (χ^2_r) value of the best-fit model and finding the corresponding model parameters whose model χ^2 (χ^2_{err})

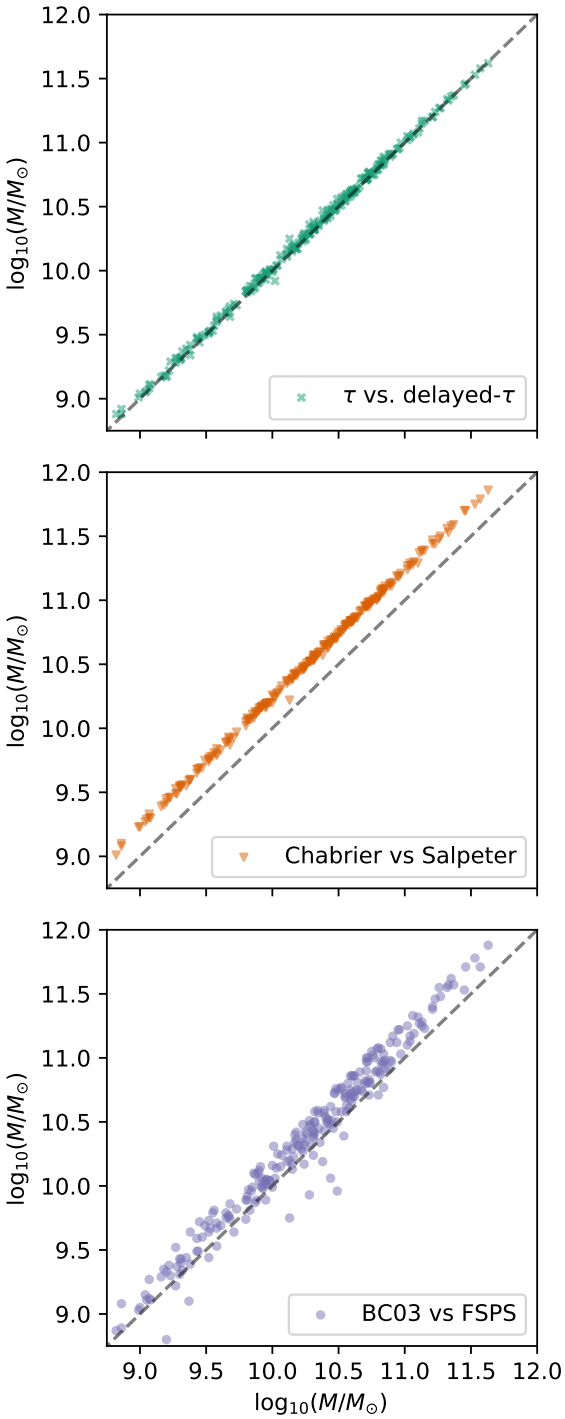

Figure 5: Systematic variation in estimated mass (left column) from variation in SFH (top), IMF (middle), and SPS library (bottom). Along the x-axes are the base template sets with a delayed-τ SFH (top), a Chabrier IMF (middle), and a BC03 library (bottom). Along the y-axes are (top) an exponential decay τ model, (middle) a Salpeter IMF, (bottom) FSPS.

satisfy $\chi^2_{\rm err} \leq \chi^2_r + 1$. Spectroscopic redshifts can be provided for each object to simplify fitting.

With ZPEG, we used the PEGASE.2 library, a Salpeter IMF, included nebular emissions, and averaged SFR over 500 million years starting at present. We used the default 200-ages Salpeter library of 15 galaxy templates provided with ZPEG, excluding the starburst template due to its extremely nonphysical description of galaxy evolution. A foreground dust screen with color excess $E(B-V)$ with values ranging from 0 to 0.4 mags in intervals of 0.2 mags was added for each template when fitting. There is a setting "AGE_CONSTR_Z0" for ZPEG that when turned off can result in dramatic underestimation of mass, especially if the starburst template is included. We kept the default setting of "T" to keep it enabled.

2.4.2.2 FAST++

FAST++ is a C++ implementation of FAST with added functionality [98, 150, 151]. Given photometry or spectra, FAST++ determines a best-fit SED from a provided SPS library on a five-dimensional grid, with each grid point corresponding to a CSP SED with age t_*, SFH time scale τ, V band extinction A_V, and stellar metallicity Z_* at some redshift z. Note that the CSP is constructed using the selected SFH parameterization and dust extinction model. The redshift parameter can be fixed by providing a spectroscopic redshift value as input for fitting. At each point on the grid a χ^2 value is calculated:

$$\chi^2_F = \sum_i^N \frac{\left[F_{\lambda,i} - F_{\lambda,\rm mod}(t_*, \tau, A_V, Z_*, z)\right]^2}{\sigma_i^2} \tag{16}$$

where N is the number of combined photometric and spectroscopic data points and σ_i^2 is the observation variance for data point i. Confidence intervals for parameters and derived quantities (such as stellar mass and SFR) are determined using Monte Carlo sampling of the grid around the lowest χ^2.

SFR was averaged over the last 500 million years as done with ZPEG. Unless otherwise stated, we used a Calzetti dust law with a uniform and constant foreground dust screen with the BC03 SPS library calculated using a delayed exponential (delayed-τ) SFH and a Chabrier IMF [32, 35].

Using FAST++ we compared the systematic effects of changing different SPS library components (Figure 5). Mass estimates exhibited the expected systematic offset from a change in IMF (Chabrier vs. Salpeter) and were unchanged for different SFH models (exponential or τ vs. delayed-τ). The global shift from changing to a Salpeter IMF was 0.24 dex. Leaving IMF and SFH fixed, when then compared mass estimates for the SPS libraries from BC03 to the newer FSPS [43]. The particular FSPS library used was the default provided by FAST/FAST++ as described in Aird et al. 2017, Appendix A [2]. FSPS estimated systematically higher mass at 0.12 dex with a standard deviation of 0.12 dex — a higher scatter than that due to changing IMF or SFH but well within the average error in mass estimates and the expected 0.3 dex template uncertainty.

2.4.2.3 Fitting IFS with STARLIGHT

STARLIGHT fits observations to linear combinations of SSPs attenuated by a given dust law in a process called spectral inversion fitting [39]. This differs from FAST++ and ZPEG which instead fit observations to a library of composite stellar populations, themselves built from SSPs using some star formation history and dust law.

STARLIGHT fits spectra by masking emission lines. A Fitzpatrick dust model with $R_V = 3.1$ was used for dust correction [52]. The best-fit SED is determined by minimizing the resulting χ^2 value against the model SED M_λ using an implementation of the Metropolis algorithm [39], with:

$$M_\lambda = M_{\lambda,0} 10^{-0.4(A_\lambda - A_{\lambda,0})} \left[\sum_i^{N_*} x_i F_{\lambda,i} \right] \odot \mathcal{N}(v_*, \sigma_{v_*}) \tag{17}$$

where x_i and $F_{\lambda,i}$ are the fractional contribution and synthetic flux density of ith SSP SED, respectively, $\odot$ is the convolution operator, and the normal distribution $\mathcal{N}$ models velocity dispersion due to stellar motion v_*. $M_{\lambda,0}$ is the normalized synthetic flux density. The population vector elements x_i serve as weights for each $F_{\lambda,i}$, from which one can infer SFH, metallicity, and other properties as a weighted sum of the properties of each contributing $F_{\lambda,i}$. To improve consistency with FAST++'s BC03 and the Chabrier IMF template library described above, the PISCO mass estimates used here were recalculated using a SPS library constructed from the BC03 library and Chabrier IMF as well.

2.4.3 Hubble Residuals

Hubble residuals are the difference between the measured distance modulus and that predicted by the assumed cosmology at a given redshift $z_{\rm CMB}$: $\mu - \mu_{\rm mod}(z_{\rm CMB}; H_0, \Omega_\Lambda)$. To better facilitate comparison with existing literature, Hubble residuals were estimated in a similar fashion to the Joint Light-Curve Analysis, or JLA using the light curve fitter SALT2 [16].

70 of 100 used PISCO SNe Ia had light curves fit with the SNCOSMO implementation of SALT2 using the JLA fiducial light curve template [65, 12]. In particular, we fit for the scaling parameter (x_0), the effective stretch parameter (x_1), and the color parameter (c). Milky Way dust extinction was taken into account during fitting using [149] dust maps with a Cardelli dust law [33]. If a light curve was observed by more than one survey, then each set of observations were fit separately. The light curve fits were then visually inspected and the better fit was used.

The 30 remaining SNe Ia were observed as part of the unpublished CSPII (Suntzeff et al, in prep). Preliminary SALT2 parameters were provided by CSPII for this analysis, as many low-mass PISCO SN Ia hosts consisted primarily of CSPII hosts.

To standardize fitted SN Ia luminosity, cosmological parameters were held fixed assuming a flat ΛCDM cosmology with $H_0 = 70$ and $\Omega_\Lambda = 0.7$ using astropy's cosmology suite [8]. The distance modulus per SN is calculated assuming a linear relationship between both SALT2 color parameter c and SALT2 stretch parameter x_1 versus absolute B-band magnitude M_B with slopes α and β, respectively [161]:

$$\mu_B = m_B + \alpha x_1 - \beta c - M_B. \tag{18}$$

Here, α and β are nuisance variables calculated using a maximum likelihood analysis akin to the JLA's treatment:

$$\chi^2_H = \sum_i^{N_{\rm SN}} \frac{\left(\mu_{B,i} - \mu_{\rm mod}(z_{{\rm CMB},i}; H_0, \Omega_\Lambda)\right)^2}{\sigma_i^2 + \sigma_{\rm int}^2}. \tag{19}$$

We ignored covariance between SNe for simplicity and fixed intrinsic dispersion to $\sigma^2_{\rm int} = 0.1$ to be consistent with the recent Pantheon analysis [152]. We did not decompose intrinsic

scatter into components incorporating dependencies on α and β [112]. Given this project's focus on studying the host bias before and after standardization, no attempt was made to incorporate host properties into equation 19. Magnitude uncertainty due to peculiar velocity was estimated using an empty-universe approximation with a peculiar velocity of $\sigma_v = 300$ km s^{-1} for each SN [46]:

$$\sigma_\mu = \frac{\sigma_v}{c}\frac{5}{\ln(10)}\left[\frac{1+z_{\rm CMB}}{z_{\rm CMB}(1+\frac{z_{\rm CMB}}{2})}\right]. \tag{20}$$

2.4.4 Linear Regression and `Stan`

When comparing SFR estimates we used a Bayesian linear regression mixture model LinMix developed and described by [87] [5]. This model takes into account uncertainties in both dependent and independent variables by modeling the true values of said variables as latent parameters described by a Gaussian mixture model. Otherwise, Ordinary Least Squares (OLS) linear regression implemented with SciPy[6] was used where noted [164].

We used Stan[7] to sample the posterior of a model between Hubble residuals and host property in place of a step function. The built-in `Stanc`Hamiltonian Monte Carlo sampler approximates the Jacobian of model parameters, and since a step function features an undefined derivative at the step location, we instead used a shifted and scaled hyperbolic tangent (tanh) model:

$$[\mu - \mu_{\rm mod}(z)](x) = \Delta\mu \tanh\frac{x - x_s}{\alpha} + \Delta\mu_0 \tag{21}$$

where x is the host property of interest (mass or sSFR). $\Delta\mu$ and x_s parameterized the step size and step location, respectively with $x_s(M_\odot) \doteq M_s$ and $x_s(sSFR) \doteq sSFR_s$ for the mass and sSFR step location parameters. Parameter $\Delta\mu_0$ accounted for any systematic y-axis offset. Parameter α determined the transition scale and was fixed to $\alpha = 0.01$ to enforce a step-like trend, akin to the logistics model for Pantheon [152]. Appendix B details priors used and their respective motivations.

[5] `https://github.com/jmeyers314/linmix`
[6] `https://www.scipy.org/`
[7] `https://mc-stan.org/`

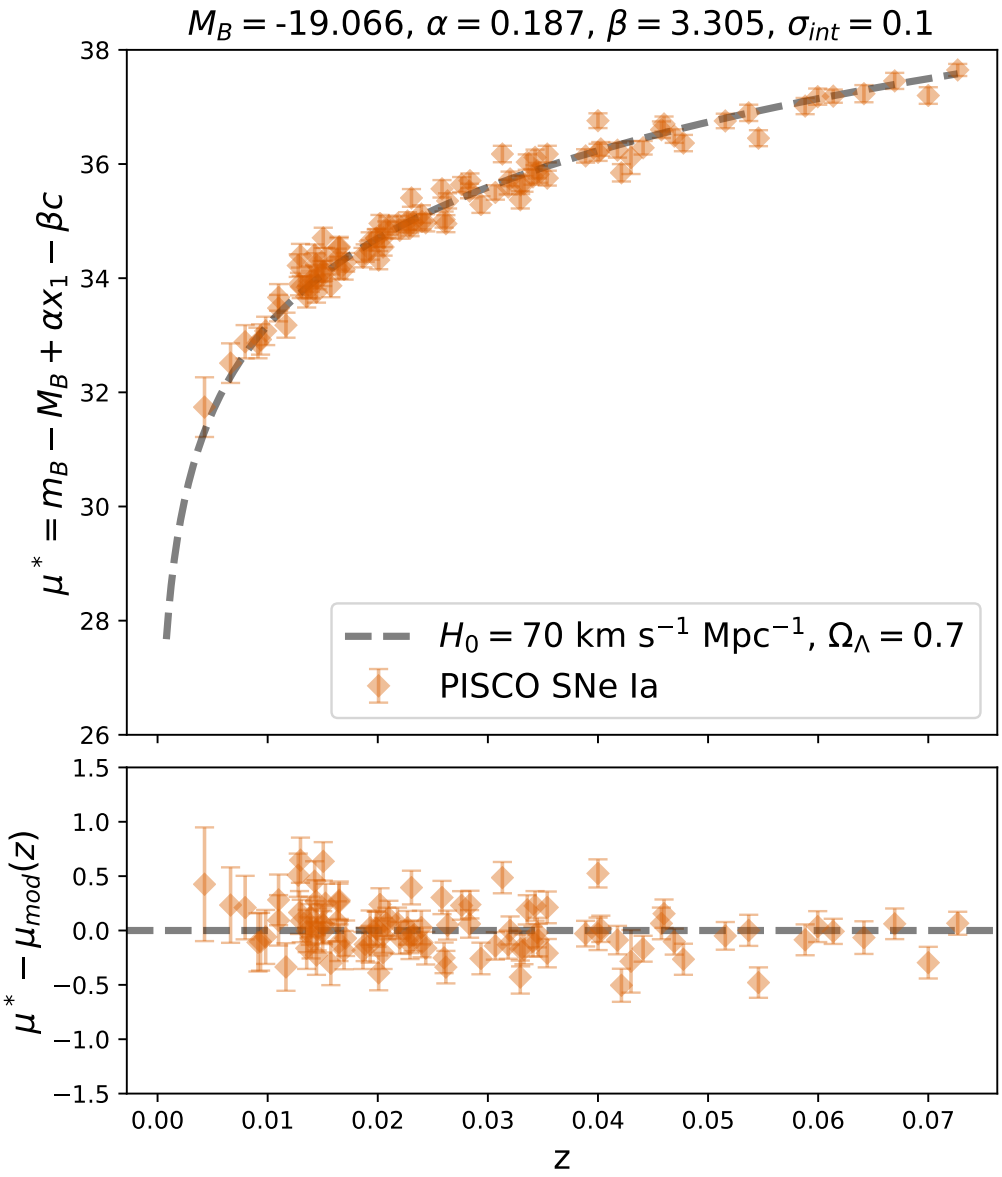

Figure 6: (top) Hubble diagram comparing SALT2-standardized PISCO SN Ia distance moduli to a predicted flat ΛCDM cosmology with H_0 = 70 km s^{-1} Mpc^{-1} and Ω_Λ = 0.7 given as the dashed line. Nuisance parameters M_B, α, and β, and the fixed intrinsic SN Ia scatter $\sigma_{\rm int}$ are given at the top of the top plot. (bottom) Hubble residuals $\mu - \mu_{\rm mod}(z)$ against redshift, with a dashed line at $\mu - \mu_{\rm mod}(z) = 0$ for reference.

2.5 Results and Analysis

The mass step is the most common characterization of the host-correlated bias in SN Ia distance standardization [40, 16, 152]. But given that all host properties are is correlated with other host properties, it is not surprising that both SFR and sSFR step-like biases have also been detected [45, 138, 136, 137]. In this work we use our available Hα flux and UV photometry alongside optical spectra and photometry to estimated various mass and sSFR samples to determine if any chosen observation method or fitting technique leads to a significant change in the measured host bias.

The analysis is presented with each subsection having both a summary of results followed by a discussion to make our analysis more digestible for the reader.

2.5.1 Mass Estimate Comparisons

Figure 7 compares fit mass estimates from FAST++ and ZPEG using SDSS and SDSS+GALEX photometry. There was a median offset of -0.43 dex (for SDSS only) and -0.54 dex (for SDSS+GALEX), largely consistent with that expected from differences between the Chabrier and Salpeter IMFs ($\sim$0.2 dex) and the stellar libraries BC03 and PEGASE.2 ($\sim$0.1 dex) [116]. The increase in median offset after including GALEX was likely driven by discrepancies between handling of young, massive stars in the respective libraries.

We compared mass estimates from FAST++ and ZPEG using SDSS optical *ugriz* to STARLIGHT mass estimates using PISCO optical spectra. Only 308 of 319 PISCO hosts had BC03+Chabrier IMF STARLIGHT mass estimates. Of those 308 PISCO targets, very low redshift hosts Andromeda, M82, and NGC 6946 had failed mass estimates. Low redshift NGC 2276 was observed as three targets, each with failed mass estimates and were excluded. This reduced the usable STARLIGHT mass sample to 302 galaxies with STARLIGHT mass estimates. Our requirement for mutual SDSS coverage reduced our working sample to 237 hosts. In comparing mass estimates, we measured an average offset of 0.03 dex between the FAST++ and STARLIGHT mass samples with a standard deviation of 0.33 dex (Figure 8). This small offset stemmed from the FAST++ SPS library and the SSP basis used by

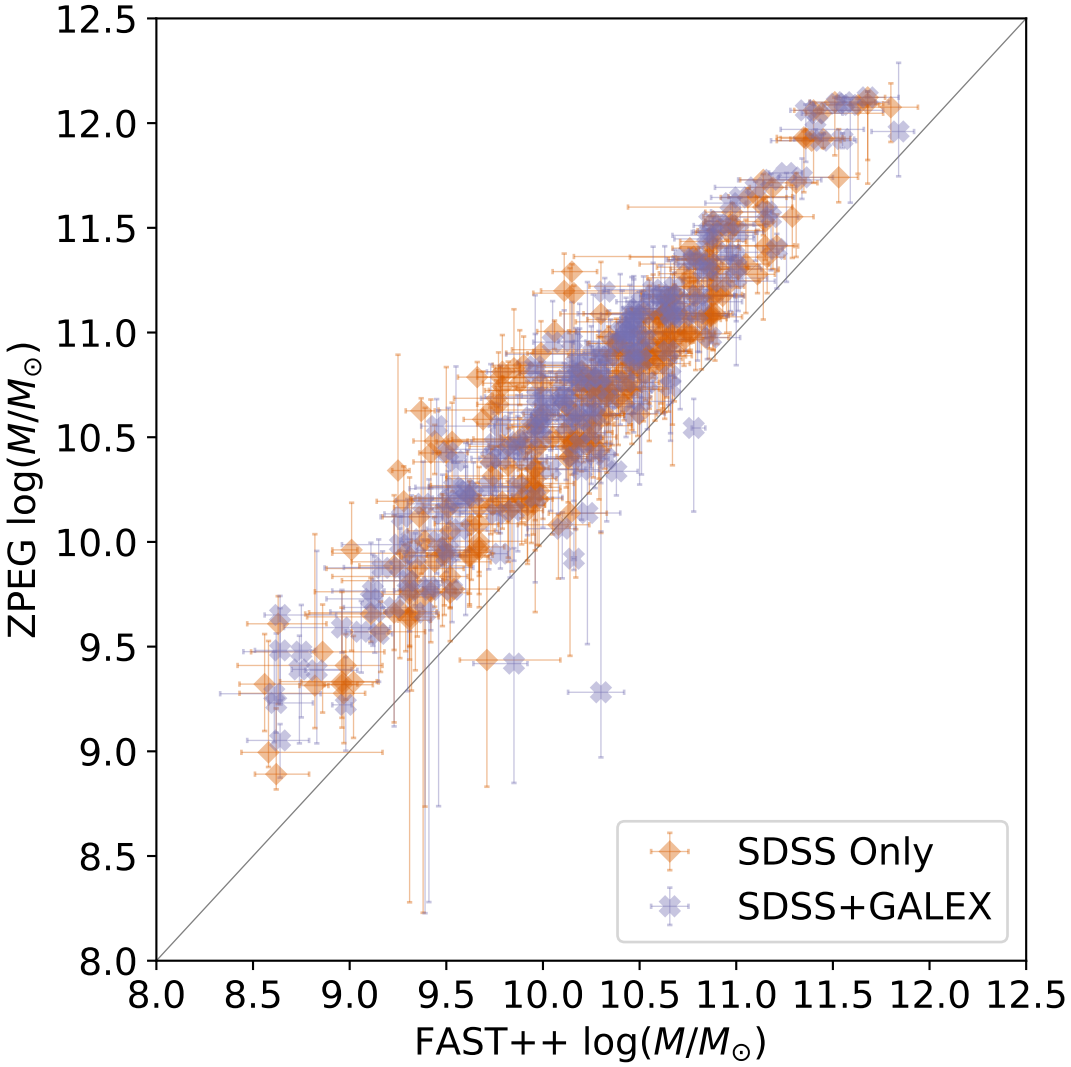

Figure 7: A comparison of stellar mass estimates between ZPEG and FAST++ for SDSS-only and SDSS+GALEX photometry. Error bars are taken directly from the respective fitting technique. A diagonal one-to-one grey line is included for reference.

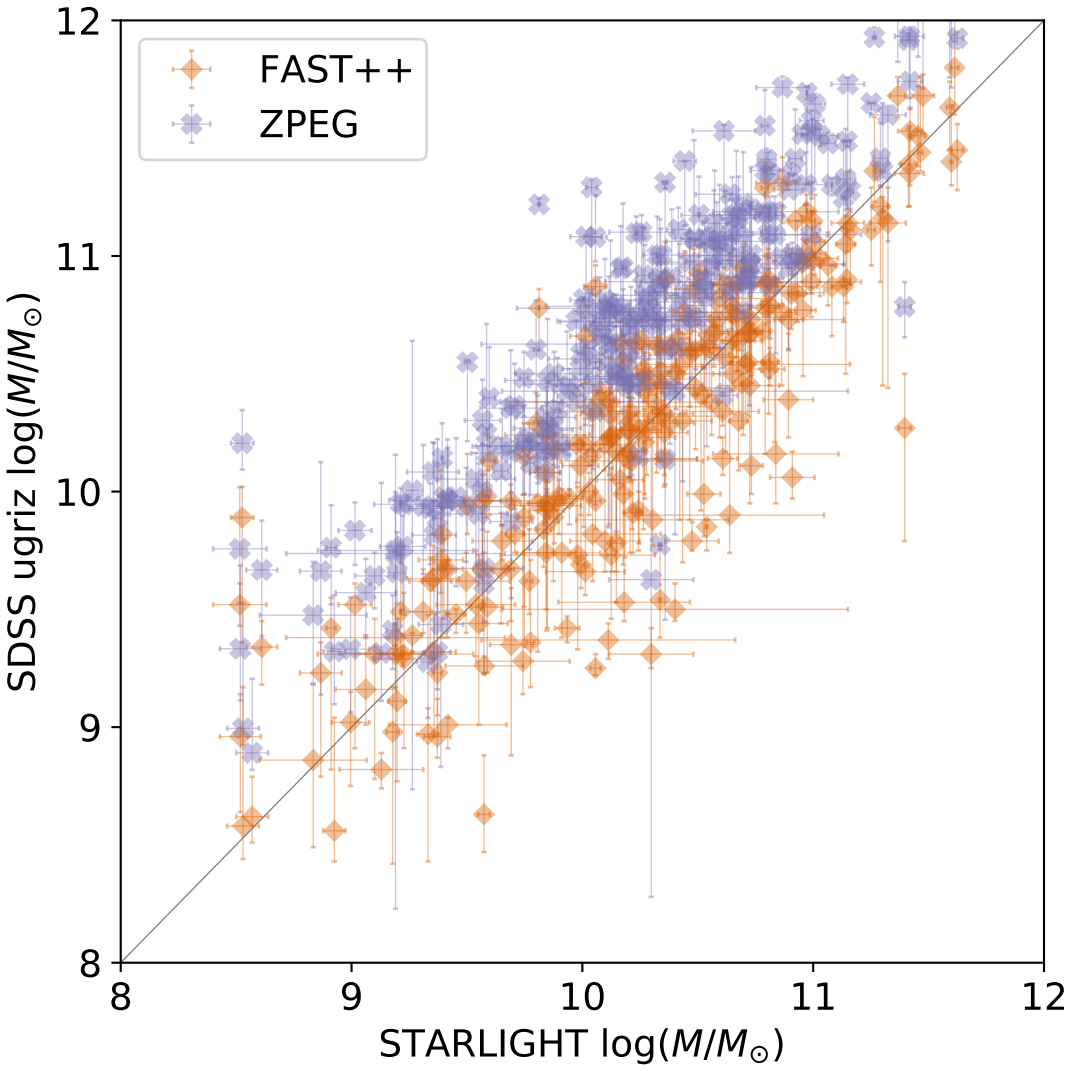

Figure 8: A comparison of mass estimate techniques. We found an offset of 0.47 dex between ZPEG and STARLIGHT mass estimates. Standard deviation between mass estimate differences were 0.28 dex for ZPEG (with the 16 erroneous estimates excluded) and 0.33 dex for FAST++.

STARLIGHT both being constructed with a BC03 library and a Chabrier IMF. A global median offset of 0.47 dex towards larger ZPEG mass estimates was caused by use of a Salpeter IMF and the PEGASE.2 spectral library for ZPEG [116]. Mass offset standard deviation between the ZPEG and STARLIGHT mass samples was 0.28 dex, slightly less than that measured for FAST++ mass values.

Mass estimates from optical photometry and IFS were mostly consistent with predicted global offsets. ZPEG mass estimates made with only SDSS photometry had systemically $\sim$0.15 dex higher values than their STARLIGHT or FAST++ counterparts — this could be from the choice in library or dust model of ZPEG being biased towards older red stellar populations without UV constraints. Random variation was consistent with SPS library uncertainties of $\sim$0.3 dex, with some further scatter arising from different aperture size and shape between PISCO IFS and our in-house photometry.

2.5.1.1 Effects of Incorporating UV Information

With FAST++ we compared mass estimates with and without GALEX NUV and FUV photometry. This required GALEX coverage and limited our sample to 211 galaxies from 237. Adding UV information helped better constrain FAST++'s A_V dust parameter, with average A_V uncertainty decreasing by a factor of 2 from 0.6 mag to 0.3 mag. There was an appreciable anti-correlation between the change in fit A_V and the change in fit mass (Pearson's r score of -0.74). Figure 9 shows three clear outliers where mass increased by more than 0.6 dex once UV information was included: UGC 02134 and UGC 09165, both inclined spiral galaxies with clear UV signals, and 2MASXJ02305208, the smallest of a triple elliptical cluster. Note that both SN Ia hosts UGC 09165 and 2MASXJ02305208 had mass estimates shift from above to below the canonical mass step location $\log_{10}(M/M_{\odot}) = 10$, but that these SNe Ia lacked optical light curves and were not used in our mass step analysis (Section 2.5.2).

UV flux comes from active or recent star formation. A quiescent galaxy incorrectly described with a star forming model SED using only optical photometry can be correctly identified as elliptical once UV information is included, as was the case for 2MASXJ02305208.

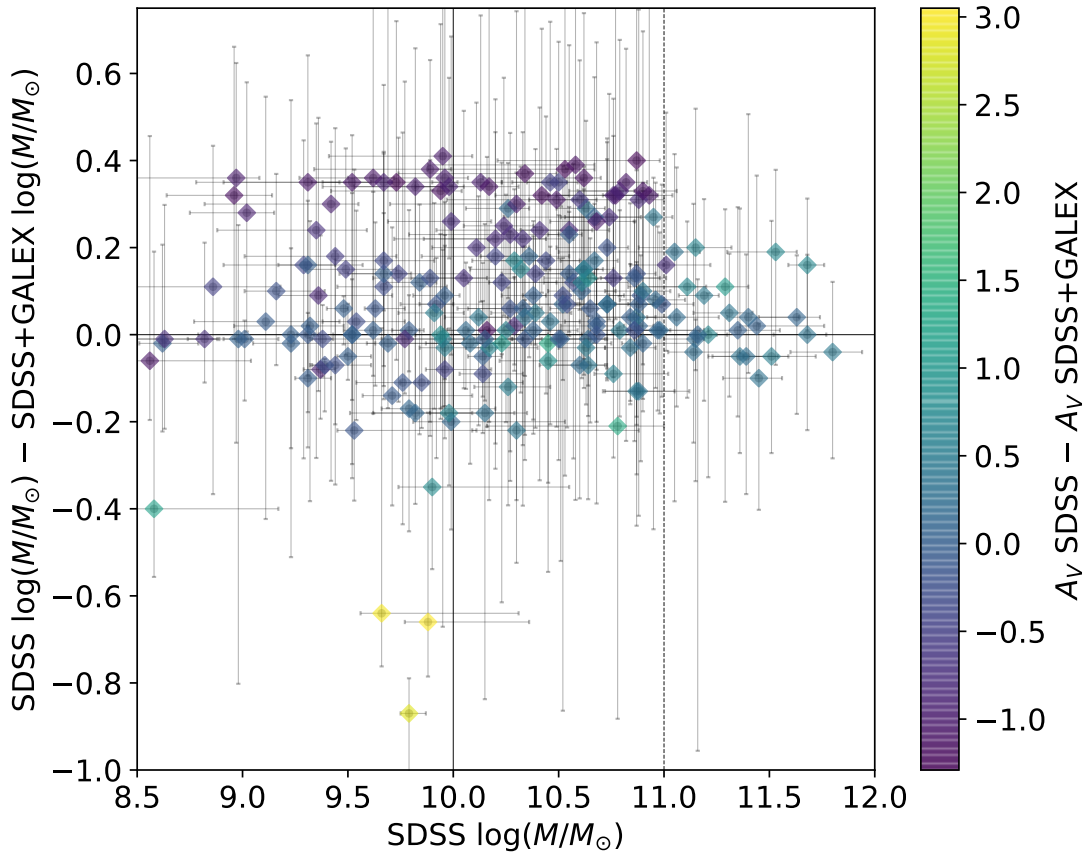

Figure 9: Absolute change in BC03 FAST++ stellar mass estimates after including GALEX photometry for 211 hosts. Three outliers exhibit mass increases of > 0.6 dex, which would shift them over the fiducial mass step location marked with the vertical solid line. However we don't have light curves for the corresponding SNe Ia and thus these hosts aren't actually used in the host galaxy bias analysis present here. No mass shift magnitude greater than 0.2 dex was observed for massive hosts with $\log_{10}(M/M_\odot) > 11$, marked with the vertical dotted line. Note the correlation between differences in the best-fit A_V and mass — an example of the mass-age-dust degeneracy.

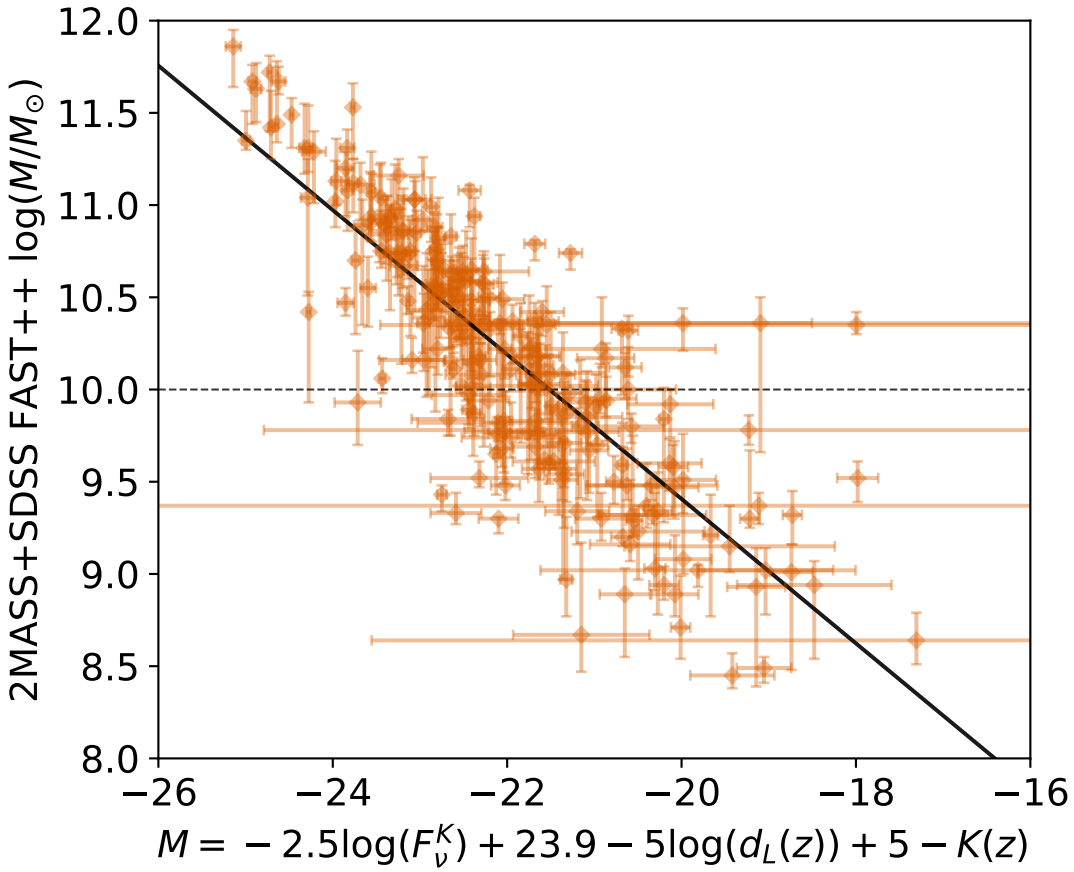

Figure 10: A comparison between K–band absolute magnitude and FAST++ mass estimates determined using 2MASS+SDSS photometry for our PISCO sample. The dashed black line references $\log_{10}(M/M_{\odot}) = 10$, the approximate location of the canonical mass step. The standard deviation of residual in mass estimates for galaxies above the dotted line is 0.35 dex compared to 0.46 dex for those below. The solid black line is the linear OLS fit.

For UGC 02134 and UGC 09165, UV information provided further information about dust-obscured star formation, resulting in a lower stellar mass estimate after UV addition. Apart from these these outliers, remaining shifts in mass were within the 0.4 dex, with 52 estimates shifting with absolute value greater than 0.2 dex. All but five of theses 52 hosts with absolute value shifted from higher to lower mass with UV information included. This information helped break the color degeneracy for these 47 objects, with redness instead attributed to dust-obscured young stars with lower mass-to-light ratios as opposed to older red dwarf stars with high mass-to-light ratios, reducing mass estimates.

Nonetheless, aside from identifying galaxies that are forming no stars, mass estimation is largely insensitive to dust effects [42]. This means that including UV information does not significant change mass estimates the vast majority of our sample (1.4% of our 211 hosts for this subsample). No hosts with SDSS mass $\log_{10}(M/M_{\odot}) > 11$ changed by more than 0.2 dex after including UV information. Overall, we do recommend including UV information when estimating mass given its ability to partially break the color degeneracy by distinguishing old stellar populations from dust-obscured young stars, but it does not significant change mass estimates for the sample.

2.5.1.2 Mass from NIR

We also experimented with including 2MASS NIR information with SDSS photometry, finding mass estimate averages effectively unchanged. Fit mass estimate uncertainty decreased for hosts with $\log_{10}(M/M_{\odot}) > 10$, though.

We considered the linear relationship between 2MASS K-band magnitudes and FAST++ mass estimates using 2MASS and SDSS photometry, akin to the methodology used in the JLA [16] (Figure 10). Two trends were present: (1) a linear relationship between absolute magnitude and mass estimate, with brighter absolute magnitudes being correlated with larger masses; and (2) an increase in the typical magnitude uncertainty for dimmer objects. The standard deviation of mass estimate residual was 0.35 dex below $\log_{10}(M/M_{\odot}) = 10$ and 0.46 dex above. Neither relationship was surprising, but we explicitly mention these as the resulting trend is visibly and logically heteroscedastic — dimmer objects will have

larger observational errors, thus biasing lower-mass galaxies towards greater mass estimate uncertainties. This should have no influence upon a step function model for a host bias correction, as the ordering of mass estimates would be effectively unchanged given the K-mag trend with mass is clearly linear: a change in slope would have no impact upon said step model.

2.5.2 Host Mass Bias Comparison

Hubble residuals for 76 SNe Ia were compared against three mass estimates samples: FAST++ using SDSS, ZPEG using SDSS, and STARLIGHT using PISCO IFS. These SN Ia hosts had both SDSS coverage and available STARLIGHT mass estimates. The decision to use only visible wavelength SDSS photometry for FAST++ mass estimates here were to maximize our usable sample and because PISCO SED only covers visible wavelengths. Linear OLS regressors fit for all three mass samples found slope values consistent with a zero slope. Using our tanh step model implemented with Stan, we found $M_s = 9.78 \pm 0.37$ and $\Delta\mu = -0.04 \pm 0.02$ mag for the FAST++ mass sample. For the STARLIGHT mass sample we found $M_s = 9.91 \pm 0.56$ and $\Delta\mu = -0.03 \pm 0.02$ mag. With all available 97 STARLIGHT mass estimates the fit step size and location were more consistent with the 76 FAST++ mass sample at $M_s = 9.83 \pm 0.33$ and $\Delta\mu = -0.04 \pm 0.02$ mag. ZPEG fit parameters for the 76-host sample saw a less than 1σ-significant shift of 0.23 dex to $M_s = 10.06 \pm 0.53$ with a slightly reduced step size of $\Delta\mu = -0.03 \pm 0.02$ mag. This shift toward a higher mass step location relative to the FAST++ mass sample was consistent with an expected $\sim$0.3 dex bias towards higher mass due to ZPEG's using the PEGASE.2 library and a Saltpeter IMF (Section 2.5.1). Also, the ZPEG and STARLIGHT step locations coincided with center of our mass step location bounds, $[9, 11]$, albeit with ZPEG's step location being 0.15 dex higher than STARLIGHT's. These parameter uncertainties were higher than their FAST++ counterpart by 0.16 dex and 0.19 dex for ZPEG and STARLIGHT, respectively, and were sufficient to span the allowed step location parameter space. See Table 3 for a summary of tanh model results for our used mass subsamples.

We found no evidence that using optical spectra versus optical photometry created any

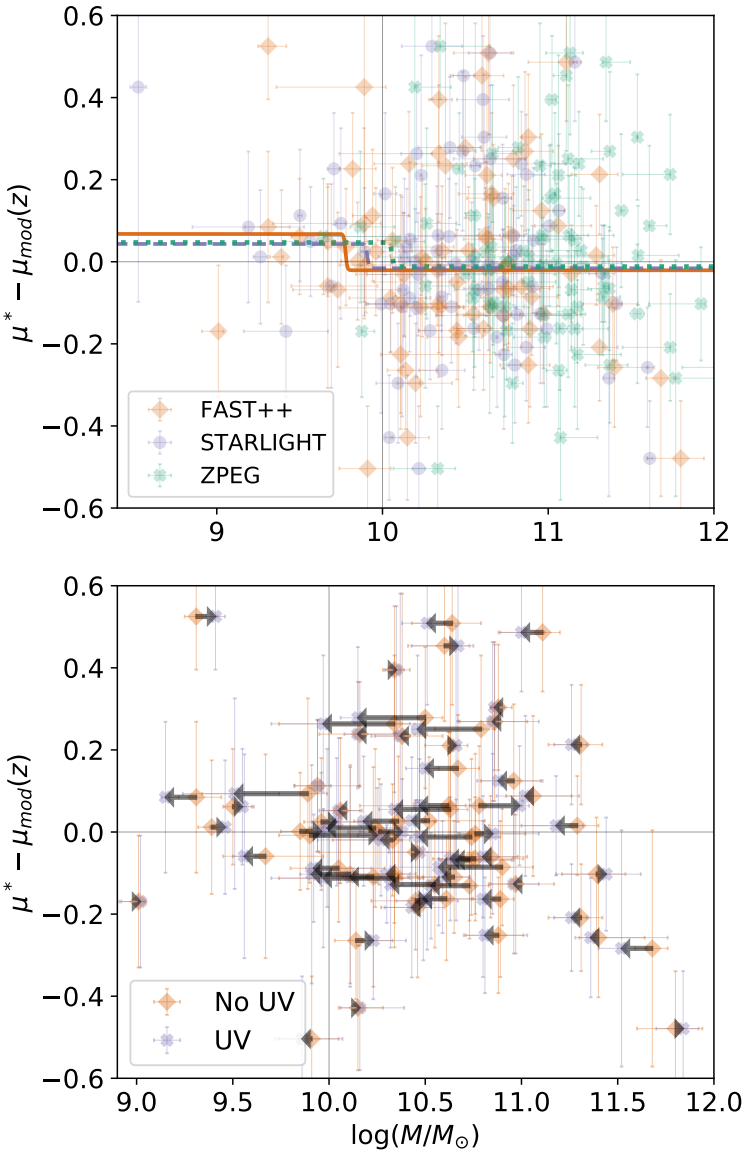

Figure 11: Comparison of 76 PISCO Hubble residuals to three sets of stellar mass estimates. SDSS *ugriz* photometry was used to calculate FAST++ and ZPEG mass estimates. The bias towards high-mass SN Ia hosts in the PISCO sample is apparent. Tanh function fit results are given as a solid orange line for FAST++, a dashed green line for ZPEG, and a dotted purple line for STARLIGHT. The bottom panel is a comparison of 66 mass estimates from FAST++ excluding (orange diamonds) and including (purple x's) GALEX photometry from the base SDSS *ugriz*. Despite noted shifts from high to low mass, both samples measured the same step function size, despite 10 fewer data points.

Table 3: Tanh model parameter results for the various mass samples used in this analysis.

Mass Sample	M_s	$\Delta\mu$	$\Delta\mu_0$
76 FAST++	9.78 ± 0.37	-0.04 ± 0.02	0.02 ± 0.02
66 FAST++	9.73 ± 0.39	-0.04 ± 0.03	0.02 ± 0.02
66 FAST++ & UV	9.76 ± 0.35	-0.05 ± 0.03	0.02 ± 0.02
76 ZPEG	10.06 ± 0.53	-0.03 ± 0.02	0.02 ± 0.02
76 STARLIGHT	9.91 ± 0.56	-0.03 ± 0.02	0.01 ± 0.02
97 STARLIGHT	9.83 ± 0.33	-0.04 ± 0.02	0.02 ± 0.02

biased mass step. All step size variation between the 76-host mass samples were within 1σ of each other. Despite these two mass samples having different observation method and fitting technique, using all 97 STARLIGHT mass estimates produced fits results clearly consistent with the 76-host FAST++ mass sample fit parameters. We interpreted the increased step location uncertainty and reduced step size of the 76-host STARLIGHT sample fit as an artifact of our reduced sample size. The ZPEG mass step location was predicted to be greater than that fit for STARLIGHT and FAST++ mass samples (Section 2.5.1), but its reduced step size relative to FAST++ results and a less constrained step location could have affected the best-fit ZPEG step location. A similar weakness in mass step signal for the 76-host ZPEG and STARLIGHT samples relative to the FAST++ sample was partly due to the lower scatter between ZPEG and STARLIGHT mass estimates as presented in Section 2.5.1. Again, our reduced statistics were likely to blame for weak signal detection.

2.5.2.1 Effects of Incorporating UV Information

The 66 SN Ia hosts with both SDSS and GALEX coverage had mass estimates compared both with and without UV photometry. As seen in Figure 9, below $\log_{10}(M/M_\odot) < 11$ there was a preferred shift to lower mass for a substantial portion of the PISCO sample once UV information was included. This trend carried over for these 66 hosts, with arrows in the

bottom plot of Figure 11 predominately pointing towards lower mass. In particular, eight mass estimates changed by $2\sigma = 0.28$ dex, with seven of the eight shifting to a lower mass once UV information was included. For the 66 mass estimates fit with GALEX information we found $M_s = 9.73 \pm 0.39$ and $\Delta\mu = -0.04 \pm 0.03$ mag; mass estimates made only SDSS only fit for parameter values $M_s = 9.76 \pm 0.35$ and $\Delta\mu = -0.05 \pm 0.3$ mag. T hese were both relatively consistent and consistent with the previously discussed 76-host SDSS sample results.

None of the three PISCO hosts with mass changes greater than 0.6 dex were used in our mass step analysis, thus preventing an extreme shift in mass over the mass step location. We observed an asymmetry in mass change direction after including UV information for many of our SN Ia, but these mass changes were relatively small at ~ 0.4 dex and did not translate to notable qualitative change in the step model parameter values or uncertainties. Adding UV information caused an insignificant 0.33-σ change in mass step from -0.04 mag to -0.05 mag. Although we cannot rule out the possibility of occasional SN Ia host galaxies being misidentified when UV information is excluded, the majority of hosts had largely stable mass estimates with or without UV information (98.5% in our 211 sample). Regardless, we recommend mass estimates be made with UV information included where possible to prevent potentially large mass estimate errors.

2.5.3 SFR Comparison

Hα SFR estimates were calculated using a linear relationship provided by Calzetti et al. 2013 [31]. For consistency, a similar linear relationship for UV luminosity was also used to estimate UV SFR values. Using a single parameter star formation history for both ZPEG and FAST++ resulted in poorly constrained template SFR values. As such, we excluded template SFR samples from the remainder of our analysis.

Hα and UV SFR values were estimated using relationships from Leitherer et al. 1999 recalibrated for a Chabrier IMF [102]. Hα SFRs were calibrated for a stellar mass range of 0.1–100 $M_\odot$ and star forming timescale $\tau \geq 6$ Myr. Type-B recombination was assumed

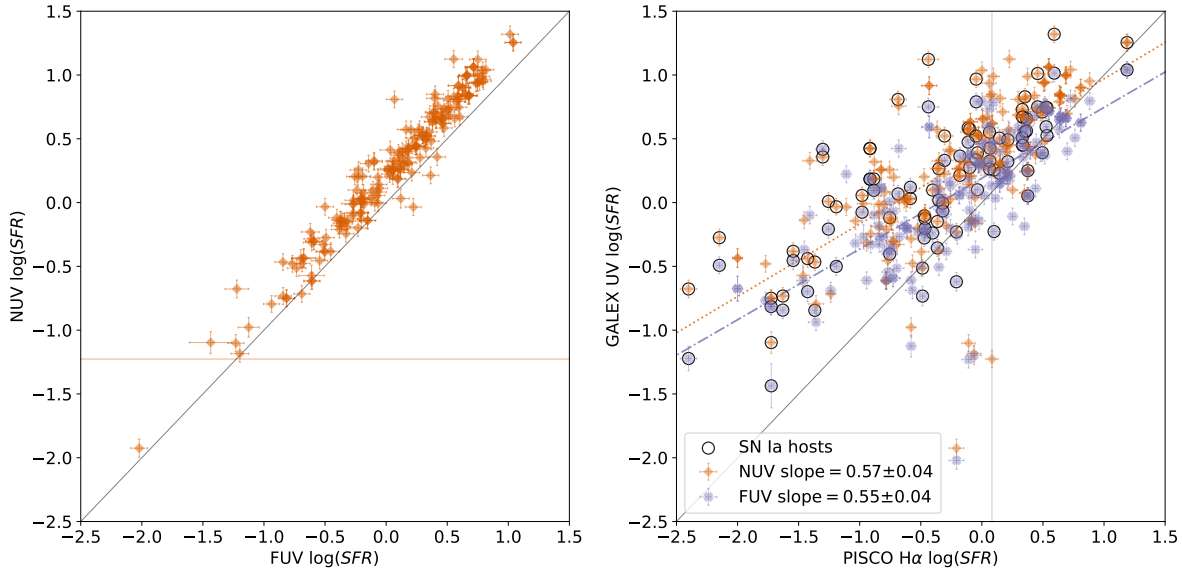

Figure 12: A comparison of global aperture SFR estimates using various techniques. The left-hand plot compares FUV and NUV SFR estimates, which show very clear agreement with each other. The right-hand plot compares FUV and NUV SFR estimates to Hα SFR estimates. The orange dotted line corresponds to NUV LinMix mean fit, while the purple dot-dashed line corresponds to FUV LinMix mean fit. Note that UV-calibrated SFR estimates include two sources of error: one from UV flux uncertainty and another 15% fractional error from calibration uncertainty. Open circles correspond to the PISCO SN Ia subsample.

with $T_e = 10^4$K and $n_e = 100$ cm^{-1}:

$$\mathrm{SFR}(\mathrm{H}\alpha) = (0.88)\ 5.5 \times 10^{-42} L(\mathrm{H}\alpha) \tag{22}$$

where the factor of 0.88 accounts for our use of a Chabrier IMF instead of a Salpeter IMF and $L(\mathrm{H}\alpha)$ is the luminosity calculated from the observed flux and luminosity distance. PISCO corrected Hα flux for nebular host attenuation using measured versus theoretical Hα/Hβ ratios [59].

We used a UV SFR calibration valid for stellar mass range of 0.1-100 M$_\odot$ and star forming timescale $\tau = 10$ Myr:

$$\mathrm{SFR}(\mathrm{UV}_i) = (0.88)\ 4.3 \times 10^{-47} \lambda_i L(\mathrm{UV}_i) \tag{23}$$

where i indexes the NUV and FUV effective wavelengths. For both equations, L has units ergs s^{-1}. STARLIGHT A_V values were used to dust-correct UV flux via a Fitzpatrick dust extinction law with $R_V = 3.1$, consistent with STARLIGHT's dust treatment described in Subsection 2.4.2.3 [52]. Note that UV-calibrated SFR estimates carried a further 15% fractional error added in quadrature with luminosity uncertainty [31].

Four SN Ia hosts lacked Hα flux measurements, excluding these from further analysis. We also note that SN Ib SN2003i's host IC2481 had erroneously large FUV flux uncertainty, as seen in both plots of Figure 12.

The left-hand plot from Figure 12 demonstrated expected consistency between our NUV and FUV SFR estimates. There was a global median offset of 0.22 dex towards higher NUV SFR estimates, an artifact in the chosen SFR calibration's explicit linear dependence on wavelength that is partly accounted for by the mentioned 15% fractional error added to our estimates. Indeed, the offset remained unchanged when UV SFR estimates uncorrected for attenuation were instead used.

In the right-hand plot of Figure 12, we compared UV-calibrated SFR estimates to Hα-calibrated SFR estimates from PISCO spectra. To account for uncertainties along both axes we used LinMix to regress these UV samples against our Hα sample. Said regressions both had fit slopes less than one; OLS linear regression results were nearly identical to the mean LinMix model parameters. When UV photometry was uncorrected for dust, UV-Hα SFR

regression slopes were shallower at a 2.5σ significance. An physical source of the observed scatter resulted from UV flux tracing SFR timescales of 10-100 Myr; nebular emissions such as Hα trace a near-instantaneous (< 10 Myr) SFR timescale [91]. We attempted to alleviate this by using a UV SFR relationship recalibrated for a shorter star formation timescale (≈ 10 Myr), but such recalibration translates to only a global offset in $\log_{10}(SFR)$ estimates. Readily apparent in Figure 13 is said star formation timescale reducing the fit slope in SFR sample comparison, with UV SFR values being consistently larger than Hα SFR estimates in the range $\log_{10}\mathrm{SFR}(\mathrm{H}\alpha) < -1$. This was consistent with Hα and UV flux both capturing very early star formation, but only UV flux capturing B-type stellar flux contribution after ionizing O-type stars have died out. Difference in our elliptical UV photometry apertures and PISCO's hexagonal apertures contributed to the observed scatter as well.

2.5.4 sSFR Bias Comparison

In the top plot of Figure 14 we took 51 Hubble residuals of SNe Ia with PISCO Hα and GALEX FUV+NUV photometry coverage to three sSFR samples: FUV and NUV SFRs normalized by FAST++ mass estimates, and Hα SFR normalized by STARLIGHT mass estimates. FAST++ mass estimates were calculated with GALEX and SDSS photometry. Linear OLS fits gave consistent slopes relative to each sSFR sample and were each statistically consistent with a zero slope. With our Stan-implemented tanh model we found all three 51 host sSFR samples fit for slightly larger (and positive) step sizes than our mass step results with Hα giving $\Delta\mu = 0.05 \pm 0.02$, NUV giving $\Delta\mu = 0.06 \pm 0.02$, and FUV giving $\Delta\mu = 0.06 \pm 0.02$. NUV and FUV step locations were $\mathrm{sSFR}_s = -10.14 \pm 0.42$ and $\mathrm{sSFR}_s = -10.28 \pm 0.52$, respectively. The fit Hα step location was at a 0.5 dex lower sSFR with $\mathrm{sSFR}_s = -10.96 \pm 0.41$. Normalizing H$\alpha$ sSFR values with FAST++ mass estimates gave a step location closer to its UV sSFR counterparts with $\mathrm{sSFR}_s = -10.48 \pm 0.52$ and $\Delta\mu = 0.06 \pm 0.03$ mag. Using instead all available 73 SN Ia hosts with global Hα flux to fit Hα sSFR values against Hubble residuals saw the step size inexplicably drop a 1σ-significant shift by 0.03 mag to only $\Delta\mu = 0.02 \pm 0.02$, with the step location parameter fitting for $\mathrm{sSFR}_s = -10.83 \pm 0.73$. This step location was effectively unconstrained within the bounds

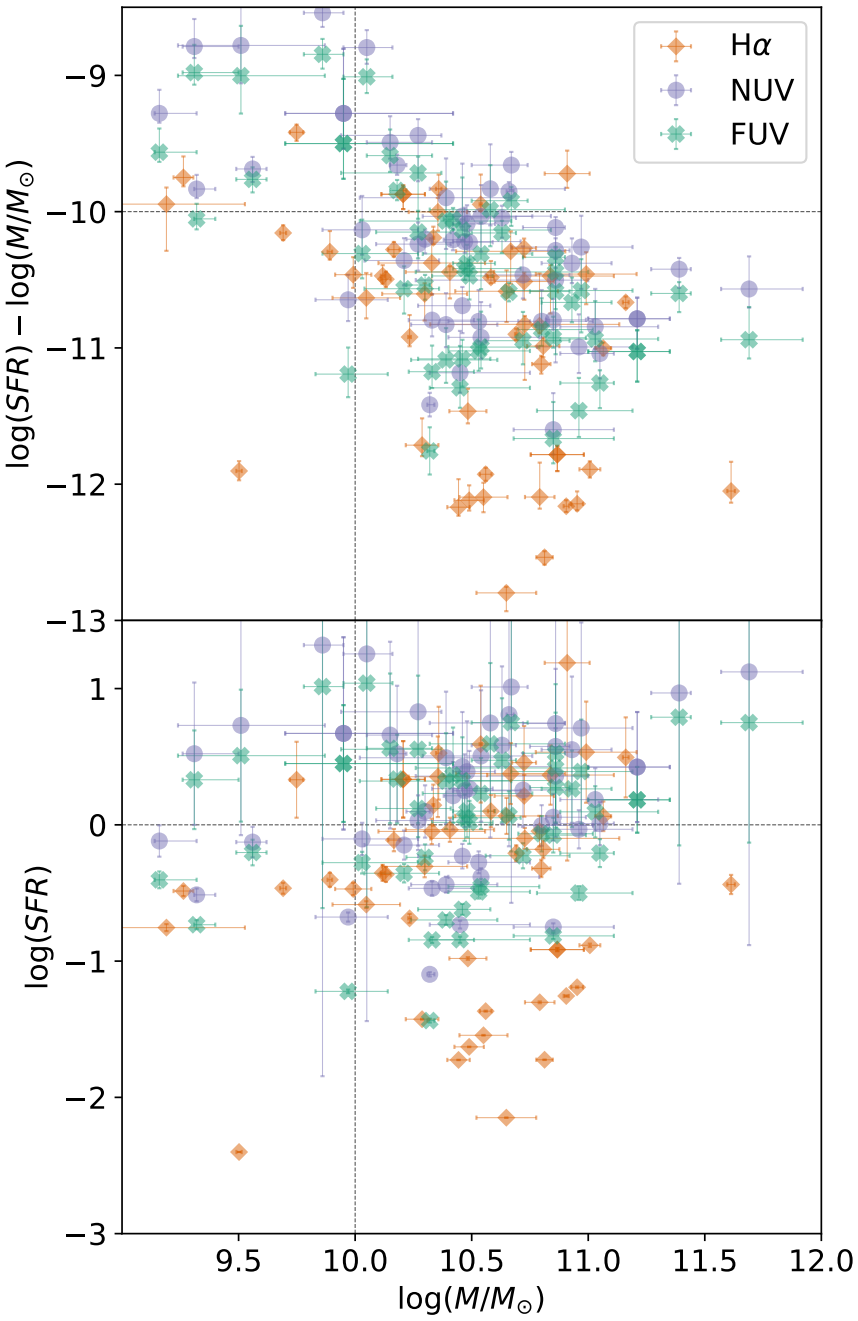

Figure 13: The top plot compares sSFR to stellar mass for all three flux-calibrated SFR samples for global aperture for our 51 host SN Ia subsample. The bottom plot similarly compares SFR to stellar mass. The lack of UV sSFR values below -12 dex is apparent. Dashed lines are for reference.

Table 4: Tanh model parameter results for the various sSFR samples used in this analysis.

sSFR Sample	$sSFR_s$	$\Delta\mu$	$\Delta\mu_0$
51 Hα	-10.96 ± 0.48	0.05 ± 0.03	0.03 ± 0.02
73 Hα	-10.83 ± 0.73	0.02 ± 0.03	0.02 ± 0.02
51 Hα & FAST++	-10.42 ± 0.41	0.06 ± 0.03	0.03 ± 0.02
51 FUV	-10.28 ± 0.52	0.06 ± 0.02	0.04 ± 0.02
51 NUV	-10.14 ± 0.42	0.06 ± 0.02	0.04 ± 0.03

enforced on the sampler. See Table 4 for a summary of all sSFR tanh model results.

In Figure 15 we compared SALT2 parameters x_1 and c to the same three sSFR samples, marking with vertical lines the best-fit sSFR step location for each of the three samples. Obvious in this plot were the lowest Hα sSFR estimates being less than the lowest UV sSFR estimates by an order of magnitude. To see if the SN Ia host bias was dependent on SFR tracer, we calculated the rank correlations coefficient Spearman's ρ of the three sSFR samples against SALT2 x_1. A relative comparison of these ρ values demonstrated uniformity with modest rank correlation with $\rho = 0.61$ for Hα, $\rho = 0.66$ for NUV, and $\rho = 0.62$ for FUV sSFR samples, providing tempered support for star formation epoch (10 Myr versus 100 Myr) being an insignificant factor in our host bias measurement. Interestingly, when repeated with UV SFR estimates uncorrected for dust, both NUV and FUV Spearman's ρ values decreased to $\rho = 0.55$ and $\rho = 0.54$, highlighting the important of dust corrections when measuring the SN Ia host bias.

Hα sSFR step size parameters had uncertainties within 2σ significance of a zero step fit, but FUV and NUV sSFR step size parameters fit with a 3σ significance from a zero step. Despite a modest sample size of 51 hosts, this 3σ significance was the the best of any step models we fit in our analysis. The combination of SFR and stellar mass provided a stronger and larger step signal than mass alone, consistent past results [142, 137]. The mass sample chosen to normalize Hα SFR values influenced sSFR step location, with Hα SFR normalized by FAST++ mass values having a step location closer to UV sSFR estimates by

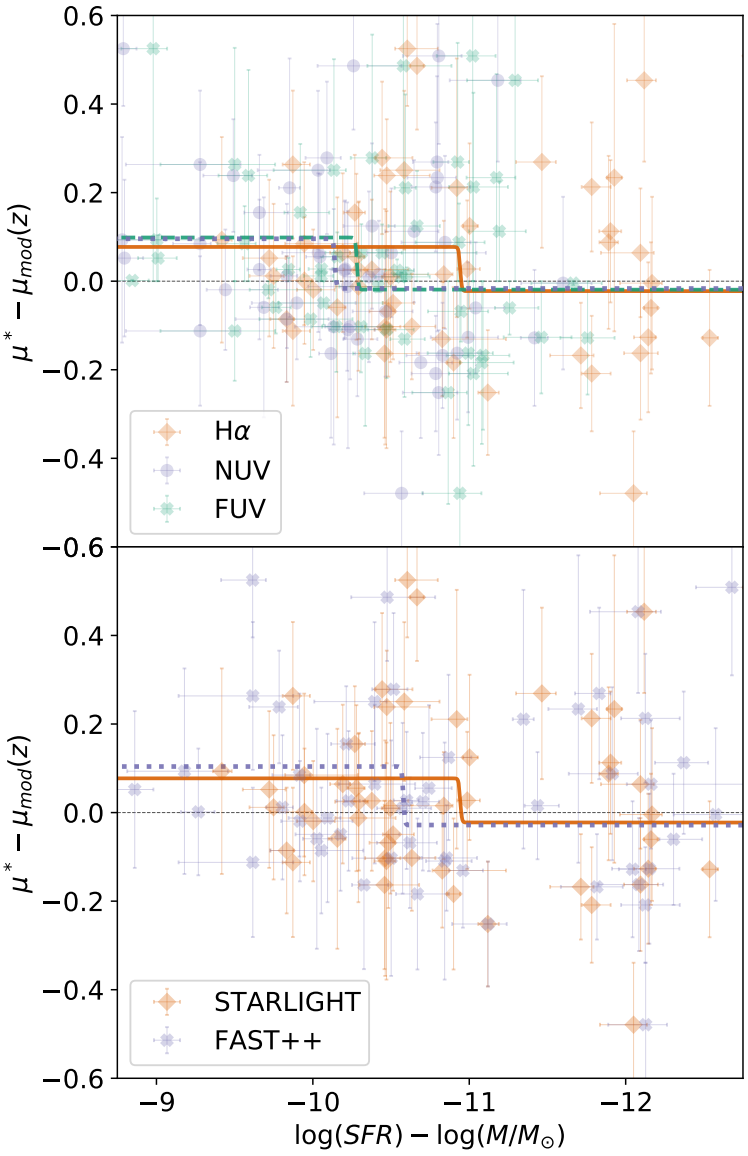

Figure 14: The top plot is a comparison of differing sSFR estimates to Hubble residuals for 51 SNe Ia. The bottom plot is a comparison the Hα sSFR estimates using STARLIGHT or FAST++ mass estimates (consistent and inconsistent apertures, respectively). sSFR tanh model fits are given in the top plot for Hα (solid orange), NUV (dotted purple), and FUV (dashed green). The bottom plot compares Hα sSFR normalized using STARLIGHT (orange diamonds) and FAST++ (purple x's) masses. The solid orange line is the best fit tanh model for sSFR values from STARLIGHT mass estimates, the dotted purple line is the tanh model result instead using FAST++ mass values.

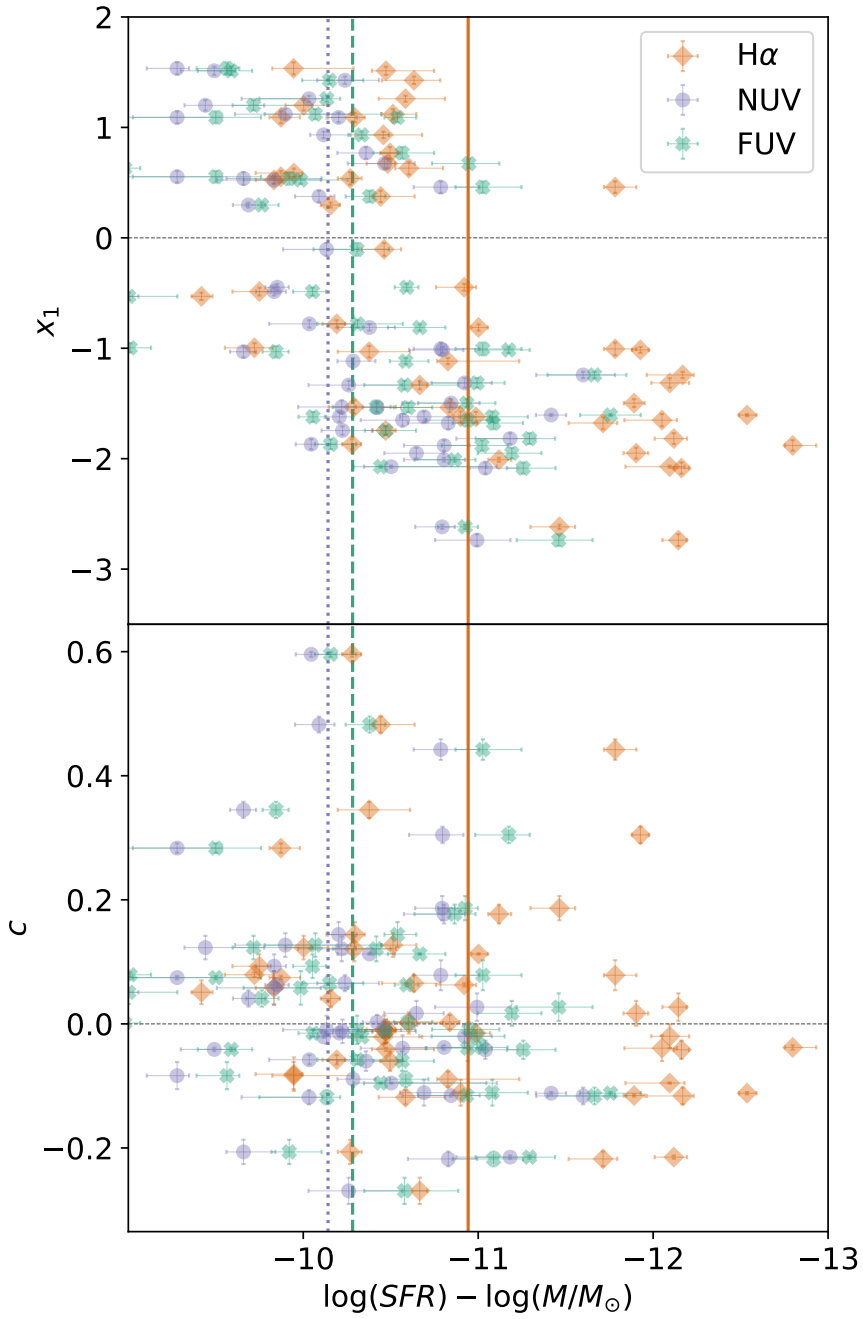

Figure 15: A comparison of global sSFR estimates to SALT2 parameters x_1 (top) and c (bottom) for 51 SNe Ia. Best-fit Hubble residual step locations are given by the vertical lines: Hα corresponds to solid orange, NUV corresponds to dotted purple, and FUV corresponds to dashed green. FUV and NUV step locations overlap. The discrepancy in lower sSFR values between Hα and UV sSFR values is clear in both plots.

0.05 dex. This observed sSFR step location shift was an order of magnitude larger than the corresponding 0.05 dex median mass offset between these 51 FAST++ and STARLIGHT mass values. The lower minimum Hα SFR (as seen in Figures 13 and 15) explained the remaining difference between the the Hα and UV sSFR step locations. The observed step location change for NUV and FUV sSFR samples was a consequence of an explicit wavelength dependence in our SFR UV calibration. There was only a slight increase in step size from Hα to UV sSFR samples. This less than 1σ change was statistically insignificant and provided no evidence that tracing differing star formation timescales influenced sSFR step size. Using all available 73 Hα sSFR values normalized by STARLIGHT did result in weak step size detection well within 1σ of a zero step. When fitting for the mass step using only these 73 PISCO hosts, we found an unconstrained mass step location, evidence that this particular PISCO host subset simply had a weak to nonexistent mass step signal.

We found no evidence that observation method nor fitting technique influenced sSFR step size. Lending support to this conclusion, the host bias strength inferred from Spearman's ρ rank correlations between x_1 and sSFR samples were very similar. The sSFR step location was partly influenced by SFR tracer choice. Different SFR tracers measure different star formation ages Hα-based SFR tracks young O-type stars, while UV-based SFR includes a wider range massive stars.

2.6 Conclusion

This project sought to determine whether different observation methods or fitting techniques create or change the observed SN Ia host bias in the SN Ia standardized magnitudes. When we examined subsets with more complete complementary photometry, the reduced statistics resulted in all mass step sizes being at or within a 2σ significance with respect to a zero step, ranging from -0.03$\pm$0.02 mag to -0.04$\pm$0.02 mag. Mass step size values for our three optical wavelength mass samples (FAST++ and ZPEG with SDSS, STARLIGHT with PISCO) were all relatively consistent, being within a 1σ significance of each other (Table 3). The mass step location, but not size, varied under different IMF and stellar spectra choice.

Including GALEX UV when fitting for photometric mass estimates with FAST++ led to an insignificant 0.33σ change in mass step size and no discernible change in corresponding step location. Not including UV information could ostensibly influence mass step measurement, but that was not the case for our used PISCO subsample. Given that this could matter, including available UV information during SPS fitting is the best practice.

The dust-corrected sSFR samples were fit against Hubble residuals for a 51-host subsample with both UV and SDSS coverage alongside available Hα flux measurements (Table 4). Physically different star formation timescales traced by Hα and UV flux sourced a Hα sSFR step location $\sim$0.7 dex lower than UV sSFR step locations. Step size parameter values for these sSFR samples were all within 1σ of each other. The sSFR steps from both FUV or NUV sSFR samples were the most statistically significant of all our step model runs at 3σ, with a step size of 0.06 ± 0.02 mag. Alternatively, using all available 73 PISCO SN Ia hosts with Hα flux produced the smallest step size of any model fit, being more than a factor of two less than the corresponding 51 host sample Hα step size parameter value and within a 1σ significance of a zero step. With the 51 PISCO sample across all three sSFR samples the sSFR step sizes were clearly consistent for all observation methods and fitting techniques. Thus, we concluded that the methodology or technique choice had no significant effect on sSFR step size measurements. Indeed, for this project only a particular change in sample size led to a discernible change in sSFR step parameter value for our particular data set.

We undertook this study expecting to find that these differences would matter for the current state of SN Ia cosmology. We found that they did not in the presently available sample, but we nevertheless urge continued attention by the SN cosmology community to advances in our understanding of galaxy properties. Given the complex nature of the SN Ia host bias problem, it is paramount that galaxy community resources be researched and utilized to reach a resolution in the future and to be mindful of coming developments in both SED fitting and SPS research.

2.7 Acknowledgements

This work was supported in part by the US Department of Energy Office of Science under DE-SC0007914. The authors thank the referee for their time, patience, and valued input in reviewing this paper in its submissions. The authors thank the Carnegie Supernova Project II for generously sharing the SALT-2 fits for unpublished SNe Ia whose hosts were part of the PISCO sample. The authors would also like to thank Dr. Alex Kim for both the introduction to and guidance using `Stan`. L.G. acknowledges financial support from the Spanish Ministerio de Ciencia e Innovación (MCIN), the Agencia Estatal de Investigación (AEI) 10.13039/501100011033, and by the European Social Fund (ESF) "Investing in your future" under the 2019 Ramón y Cajal program RYC2019-027683-I and the PID2020-115253GA-I00 HOSTFLOWS project.

Based on observations collected at the Centro Astronómico Hispano-Alemán (CAHA) at Calar Alto, operated jointly by Junta de Andalucía and Consejo Superior de Investigaciones Científicas (IAA-CSIC). Funding for SDSS-III has been provided by the Alfred P. Sloan Foundation, the Participating Institutions, the National Science Foundation, and the U.S. Department of Energy Office of Science. The SDSS-III web site is http://www.sdss3.org/.

SDSS-III is managed by the Astrophysical Research Consortium for the Participating Institutions of the SDSS-III Collaboration including the University of Arizona, the Brazilian Participation Group, Brookhaven National Laboratory, Carnegie Mellon University, University of Florida, the French Participation Group, the German Participation Group, Harvard University, the Instituto de Astrofisica de Canarias, the Michigan State/Notre Dame/JINA Participation Group, Johns Hopkins University, Lawrence Berkeley National Laboratory, Max Planck Institute for Astrophysics, Max Planck Institute for Extraterrestrial Physics, New Mexico State University, New York University, Ohio State University, Pennsylvania State University, University of Portsmouth, Princeton University, the Spanish Participation Group, University of Tokyo, University of Utah, Vanderbilt University, University of Virginia, University of Washington, and Yale University.

This publication makes use of data products from the Two Micron All Sky Survey, which is a joint project of the University of Massachusetts and the Infrared Processing and Analysis

Center/California Institute of Technology, funded by the National Aeronautics and Space Administration and the National Science Foundation.

Both pandas and NumPy were constantly utilized throughout this project [69, 119].

3.0 An Agnostic Approach To Building Empirical Type Ia Supernova Light Curves: Evidence for Intrinsic Color Variation using Nearby Supernova Factory Data

This chapter is the product of a DoE Office of Science SCGSR 2019 Award[1] alongside DoE advisor Dr. Alex Kim of the Lawrence Berkeley National Laboratory. At the time of writing it is in internal review with the Nearby Supernova Factory[2] [5]. It will be submitted to the Astrophysical Journal Summer 2023.

We present a new empirical type Ia supernova (SN Ia) model with three chromatic flux variation templates: one phase-dependent and two phase-independent. No underlying dust extinction model or patterns of intrinsic variability are assumed. Implemented with `Stan` and trained using spectrally-binned Nearby Supernova Factory spectrophotometry, we examine this model's two-dimensional, phase-independent flux variation space using two motivated basis representations. In both, the first phase-independent template captures variation that appears dust-like, while the second captures a combination of effectively intrinsic variability and second order dust-like effects. Previous empirical SN Ia models either assume an effective dust extinction recipe in their architecture, or only allow for a single mode of phase-independent variation. The presented results demonstrate such an approach may be insufficient, because it could 'leak' noticeable intrinsic variation into phase-independent templates. Per-SN dust properties are then estimated with additional forward modeling, where we find that including intrinsic-color-dominated SNe Ia in effective R_V estimation biases one's results low, albeit by an amount too small to explain chronically low average R_V estimates from most past SN Ia sample analyses. An effective $R_V = 2.55$ is recovered for dust-dominated SNe Ia. For intrinsic-dominated SNe Ia we find $R_V = 2.25$, and for the whole sample we find $R_V = 2.47$. Future work will increase our model's wavelength bin count and incorporate a third phase-independent template to better separate intrinsic variation from dust-like variability.

[1] `https://science.osti.gov/wdts/scgsr`
[2] `https://snfactory.lbl.gov/`

3.1 Introduction

There are two errors that limit SNe Ia's capacity to constrain cosmological parameters: the number of observed SNe Ia (statistical uncertainty) errors resulting from observation bias, modeling error, and calibration (systematics). Recent SN Ia cosmology analyses have significantly reduced statistical uncertainty by utilizing over 10^3 spectroscopically confirmed SNe Ia [16, 152]. LSST, via the Vera Rubin Observatory, will further increase our usable SN Ia sample by at least an order of magnitude over ten years after its commissioning [79]. Although internal photometric calibration will remain an important systematic to account for, LSST will alleviate tedious inter-survey photometric calibration systematics performed in many past analyses while still providing impressive statistics. As a result, LSST will increase the relative importance of systematics arising from SN Ia light curve modeling and standardization for constraining cosmological parameters.

3.1.1 Photometric Variation and Empirical Models

All SNe Ia peak in brightness at the rest-frame B-band wavelength and exhibit a single local maximum blueward of 5000 Å. As mentioned, light curve width correlates with B-band maximum brightness so that longer duration SNe Ia are systematically brighter [124]. We refer to this as the width-luminosity relation (WLR). Similarly, bluer SN Ia light curves are systematically brighter at B-band maximum, which we similarly refer to as the color-luminosity relation (CLR) [132].

One can interpret SN Ia empirical models as transforming high-dimensional sets of observations to a lower-dimensional set of parametric latent templates that inscribe dominant modes of SN Ia variability. Many models directly obtain light curves and modes of light curve variability (namely, the WLR and CLR) directly from photometry [135, 80, 29]. These light curve fitters or distance estimators require K-corrections of observed photometry to model rest-frame pass-bands, complicating error propagation alongside other issues [97, 117, 108]. More importantly, they only capture aforementioned photometric variational modes, being insensitive to substantially more complex SN Ia variability revealed with spectroscopy.

SN Ia spectral variability is either intrinsic to SN Ia populations or is extrinsic, instead arising from processes external to the explosion, such as dust extinction or an SN Ia's interaction with its circumstellar environments [117, 80]. Furthermore, photometric relationships emerge from spectral variation, with the temperature dependence of Fe line blanketing at least partly driving the WLR and explaining its wavelength dependence being such an example [85]. Variation in progenitor mass also contributes to the WLR, as lower-mass SN Ia progenitors are systematically dimmer and have faster-declining light curves compared to their more massive counterparts [148]. Certain spectral features directly correlate with photometric SN Ia properties, such as the F(6420 Å)/F(4430 Å) line ratio correlating with maximum B-band brightness [11], and the ratio of Si II $\lambda\lambda$5972 and 6355 Å (or Si II $\lambda\lambda$5972 and 3858 Å) correlating with light curve width [118].

Many SN Ia subtypes have been categorized by their spectral variation [21, 17]. Grouping SNe Ia based on Si II variability during a Tripp standardization procedure has been shown to reduce SN Ia dispersion post-standardization more than use of only color and stretch alone [166, 53]. Furthermore, spectral information can improve effective total-to-selective extinction R_V estimation, with Chotard 2011 using spectral features to recover an effective R_V value consistent the Milky Way average $R_V = 3.1$ [38]. Given this plethora of spectral variety within SNe Ia, and this variety's potential to further improve standardization, commonly used and recent SN Ia models make heavy use of spectroscopic observations in training.

Most recent SN Ia models reduce the dimensionality of SN Ia observations by constructing combinations of underlying spectral or color variation templates, with one template capturing the average, or fiducial, spectral evolution of SNe Ia. This approach removes any need for K-corrections and related uncertainty propagation [108]. The ubiquitous SALT model family (and its cousin SiFTO) are the canonical example of the spectral template technique [65, 41, 16, 126]. This family of linear SN Ia models capture variation beyond a mean spectral surface with a first-order flux variation template and a phase-independent color template (with per-SN contribution parameters x_1 and c, respectively). SALT2's success over prior models saw its widespread adoption and continuous improvement, with the most recent version SALT3 extending its wavelength coverage to the near-infrared (NIR) [93].

More statistically rigorous linear spectral template models have also been developed, such as BayeSN with its potent hierarchical Bayesian framework [107, 108, 159].

A plethora of sophisticated models have recently been developed using SNfactory's spectrophotometric time series [5]. [147] and their SNEMO model extracts up to 15 linear principal functional components from a set of SN Ia spectral surfaces trained using Gaussian processes to maximally explain SN Ia variation. Alternatively, Leget et al. in their SUGAR model treats SN Ia variation as a linear combination of spectral index templates, extending the initial work of Chotard 2011 into a fully generative model [101]. SNEMO and SUGAR, along with all the models mentioned so far, utilize linear dimensionality reduction techniques.

Boone et al. 2011 apply the Isomap method with their Twins Embedding model to train a nonlinear parameterization of intrinsic SN Ia variation at maximum brightness [20] , while Stein et al. 2022 introduce a nonlinear probabilistic autoencoder (PAE) that captures intrinsic variation across both wavelength and phase [157]. Both find that a nonlinear approach requires only three intrinsic model components to describe SN Ia spectral variation where more traditional linear principal component analysis model would require seven components or more [147]. These two models also demonstrate noticeable improvements over SALT2 in standardized SN Ia dispersion from ≈ 0.12 mags to ≤ 0.09 mags. Improvements through nonlinear technique application are not limited to light curve models: Rubin et al. 2015 introduce the hierarchical Bayesian framework UNITY that allows for nonlinear standardization, leading again to improved SN Ia dispersion post-standardization relative to the linear Tripp approach [144].

3.1.2 The R_V Question

Phase-independent SN Ia variation is an amalgamation of extrinsic and (possibly) intrinsic components [117, 80, 125]. Assumptions are usually made to decouple these two variational modes, be it by assuming a functional dependence of intrinsic phase-independent variation on SN Ia light curve shape [125, 28], fitting for or assuming an effective dust extinction curve with some effective R_V [80, 94, 29, 108], or combining all phase-independent

variational modes into a single effective 'color' template [65, 93].

The steepness with respect to wavelength of SN Ia extinction curves that describe extrinsic variation, commonly quantified with R_V, is a source of ongoing debate — all mentioned approaches (or combinations thereof) recover suspiciously steep extinction curves (or low R_V). For example, Kessler et al. 2009 find a best-fit $R_V \approx 2$ trying to minimize Hubble residual scatter with MCLS2k2 or when fitting an effective dust curve to SALT2's phase-independent color model [94]. Similarly, Phillips et al. 2013 and Burns et al. 2014 recover low R_V values when assuming dependence of intrinsic phase-independent variation on light curve proxies (i.e. $\Delta m_{15}(B)$ or SNooPY's S_{BV}) [125, 28].

Alternatively, hierarchical Bayesian spectral template models such as BayeSN recover $R_V \approx 2.9$ [107, 108], more consistent with the Milky Way Average [33], while single-epoch spectroscopic methods have recovered higher R_V values as well [38, 75] Nevertheless, it remains unanswered if low R_V values are an artifact of incomplete modeling, or if SN Ia do actually do 'prefer' steeper extinction curves. If SN Ia are indeed better described with steeper extinction curves, then it is unclear whether this steepness arises from peculiar host galaxy dust properties, or from improper 'leaking' of intrinsic variation into an empirical model's extracted extinction curve(s).

Improper derivation of SN Ia R_V is a proposed source for the now ubiquitous mass step bias. This bias sees brighter standardized SN Ia occur more frequently in more massive hosts [88, 158, 128, 162]; similar step biases for star formation rate and stellar population age also exist [45, 138, 137, 140, 141]; Brout et al. 2019 finds that if one models the underlying per-SN R_V population with a relatively wide Gaussian distribution centered at $R_V \approx 2$, then the mass step bias is largely nullified [24]. Alternatively, with BayeSN Thorp et al. 2021 finds that lower and higher mass hosts feature different effective R_V values at a $\approx 1\sigma$ significance, with both host mass subsamples obtaining systematically higher R_V values than that found by Brout et al. 2019 [159]. Overall, clarifying per-SN R_V population properties is an important step to understanding the mass step's size and origin.

3.1.3 Shortcomings in Phase-Independent Modeling

All past models either assume a dust extinction model for explicit phase-independent templates (MCLS2k2, SNooPY, SNEMO, SUGAR, BayeSN, and current nonlinear models) or include a single phase-independent template which does not differentiate between intrinsic and extrinsic variation (the SALT family). Excluding the maximum brightness model Twins Embedding, each of these models characterize phase-independent variability with only a single model component. Physical considerations alone demonstrate this to be an insufficient treatment. As summarized in Weingartner 2001, one would expect at least two extrinsic variation parameters per SN Ia: one gauging dust column density or optical depth (i.e. A_V) and the other probing second order characteristics such as dust grain properties (i.e. R_V) [168]. Furthermore, it is plausible that empirical SN Ia models could extract intrinsic variation into a phase-independent template set. In this era of precision cosmology, modeling and standardization systematics remain stubborn obstacles to maximizing current and future SN Ia survey utility. Better understanding underlying extracted modes of phase-independent variation could answer outstanding questions about the SN Ia population (i.e. the low SN Ia R_V debate or the source of the bias associated with host properties), and improve both SN Ia modeling and standardization.

We present a new SN Ia empirical model to explore deeper the phase-independent variability of SNe Ia. This model features three chromatic flux variation templates: one phase-dependent and two phase-independent. These two phase-dependent components provide the flexibility to account for multi-parameter dust models while also absorbing an intrinsic time-averaged flux variation beyond that accounted for by the phase-dependent component. All templates are physics-agnostic, as no assumptions are made about expected spectral features or dust treatment. This new model is trained on SNfactory's rest-frame spectrophotometric time series.

Our model bears some similarities with BayeSN. Both models are linear models implemented with `Stan`. How phase-independent variability is accounted for varies in approach, though. BayeSN implements a single-component dust extinction recipe within a hierarchical model framework, from which they recover an effective R_V that is largely consistent with the

Milky Way average. This dust extinction recipe only considers a global R_V for their training sample. In contrast, our model has two phase-independent templates, providing it two model degrees of freedom for which no physical assumptions are made. Unlike BayeSN, our model does not directly incorporate redshift information, nor model spectral surface residuals.

In Section 3.2 we introduce the training set and its quality cuts. We describe our model and fitting technique in Section 3.3, with global model template and refit per-SN parameter results being presented in Section 3.4. Section 3.5 explores per-SN dust property estimates after additional forward modeling with an assumed underlying absolute extinction population model. Finally, we provide concluding remarks in Section 3.6.

3.2 Data

Between 2004 and 2014 SNfactory observed spectrophotometric time series of nearly 300 SNe Ia with the SuperNova Integral Field Spectrograph [5] (SNIFS, Lantz [100]). SNIFS is continuously mounted at the University of Hawaii 2.2 m telescope, using dual-channel, moderate resolution ($R \sim 600 - 1300$) spectrographs to simultaneously observe transient events from 3200 to 5200 Å and 5100 to 10000 Å, respectively. This unique and homogeneous SN Ia data set is calibrated with CALSPEC and Hamuy standard stars [18, 67, 66]. The photometric calibration method is summarized in Buton et al. 2013, with Pereira et al. 2013 further describing non-photometric-night calibration [122, 30]. Host-galaxy subtraction methodology is presented in Bongard et al. 2011 [19]. Each SNe Ia has also been fit using SALT2.4 [16].

For our SN Ia training sample we generate synthetic SN-frame photometry using n_λ log-distributed top-hat filters from published rest-frame SNfactory spectra [4]. These rest-frame observed spectra are in units of 10^{10}erg s^{-1} cm^{-2} and have been de-redshifted to a reference redshift $z = 0.05$. Cosmological time dilation is also accounted for by the aforementioned rest-frame transformations. This work does not attempt to fit absolute magnitudes or fit for cosmological parameters, so per-SN redshifts are not used. Due to high flux variance at wavelength boundaries, and because most objects have a higher redshift than $z = 0.05$, the

per-spectra reference frame wavelength range is truncated to between 3350 Å and 8030 Å.

The spectral resolution of this top-hat filter synthetic photometry is flexible — for this work, we use a modest $n_\lambda = 10$ filter count. These $n_\lambda = 10$ bins are spaced at constant spectral resolution R, providing a wavelength bin size of ≈ 400 Å resolution for bluer bands and ≈ 500 Å for redder bands. SNfactory data consists of flux densities along a uniform grid of wavelengths. Because of this uniform spacing, we simply sum flux densities along the wavelength range defining our top-hat filters and then multiply said sum by the filter's wavelength range to calculate top-hat synthetic photometry:

$$F_{\text{bin}} = [\lambda_{\text{max}} - \lambda_{\text{min}}] \sum_{i=i_{\text{min}}}^{\text{max}} f_{\lambda_i}. \tag{24}$$

Similarly, each corresponding variance spectrum is summed in quadrature to calculate synthetic photometry uncertainties.

For every observation, for the binned synthetic photometry a signal-to-noise ratio (SNR) of at least SNR > 5 is required. It is also required that each SN Ia to have at least eight separate days of observations. Where a single SN Ia has multiple spectra for a given night, the weighted average of these flux values is used as a single effective observation. Given the difficulty in constraining date of maximum in SN Ia empirical models, we demand that there exist at least one observation two days before SALT2 maximum phase. Furthermore, no SNe Ia with an observation gap greater than four days within a four-day range before and after SALT2 maximum are used. SN Ia light curves do not have significant structure less than four days, so gaps of this size or smaller have no discernible impact on results. For consistency, the chosen maximum gap size of four days is the same as our fixed Gaussian process mean predictor length scale hyperparameter later described in Section 3.3. These cuts leave 80 SNe Ia in the training sample.

The distribution of SN Ia color parameters for any model is asymmetric due to the positive-definite nature of dust extinction [153, 107, 26]. SN Ia stretch parameters such as SALT2's stretch proxy x_1 are also best modeled with asymmetric distributions [153]. We are interested in the Gaussian core of these distributions and partly 'symmetrize' the data set by clipping extended tails of our SALT2 c and x_1 samples. Specifically, a 2σ clipping is done on each SALT2 c and x_1 parameter samples in the direction each parameter's longer

tail (Figure 16). The c clipping prevent heavily reddened SNe Ia from dominating recovered dust-like behavior and obscuring dust properties of the average SN Ia in training set — this c cut removes particularly reddened SNe Ia with peak apparent $B-V>0.18$. The clipping is motivated by our interest in the core of the SN distribution that is used for cosmology, but comes at the expense of removing rarer objects that potentially provide more information on modeling SN colors. A total of 73 SNe Ia remain after SALT2-parameter σ clippings, consisting of 1155 individual spectra. The redshift range for this subsample is $0.01<z<0.08$ along a range of host galaxy masses ($8<\log_{10}(M)<12$).

Relative to Aldering et al. 2020 [4], and similar in spirit to Boone et al. 2021 [20], we remove spectra having poor extractions caused by very low SNR. This step removes seven spectra, leaving 1148 to train the model.

3.3 Model

Global template parameters and per-SN parameters are differentiated by upper-case and lower-case characters, respectively. This model discretizes phase and wavelength space, using $n_p=16$ phase nodes ranging from $-16\leq t_{p,i}\leq 44$ in four-day intervals; as mentioned in Section 3.2, $n_\lambda=10$ with bins of constant R. Each phase-dependent template is an $n_p\times n_\lambda$ matrix of parameter nodes, while each phase-independent template is a length-n_λ vector.

The model prediction of the time-dependent SED evolution of an individual SN Ia is based on a temporal interpolation over a set of wavelength-dependent light curves at fixed phases $F_{\lambda,\text{eff}}$ that are specific to that supernova. The interpolation is controlled by a kernel K, which operates on $F_{\lambda,\text{eff}}$ as shown in Eq. 25. This equation is the same used to predict the mean in a Gaussian process, so we refer to this interpolation scheme as the Gaussian Process Mean Predictor (GPMP):

$$f_\lambda(t)=\mathbf{K}(t-t_0,\mathbf{t}_p)\mathbf{K}^{-1}(\mathbf{t}_p,\mathbf{t}_p)\mathbf{F}_{\lambda,\text{eff}}. \tag{25}$$

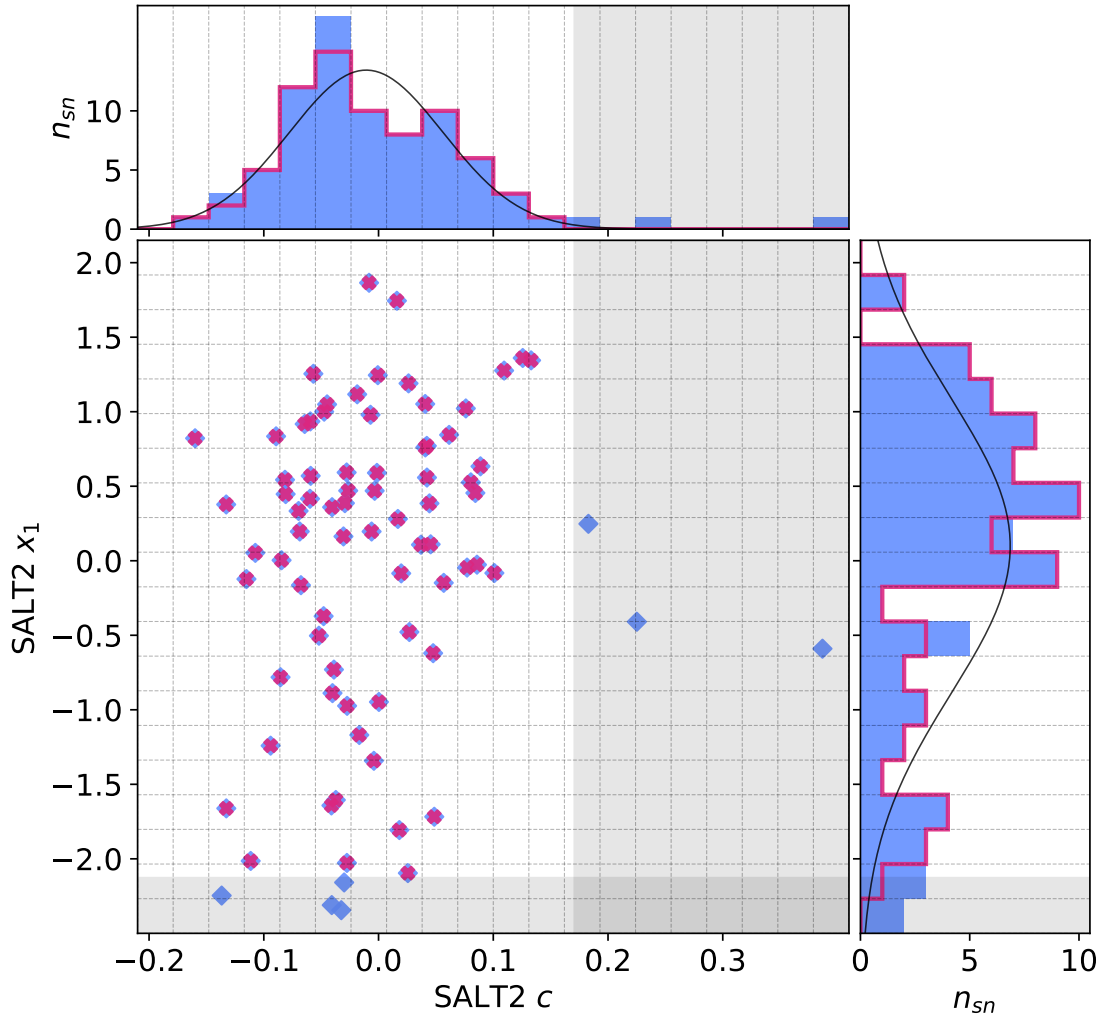

Figure 16: SALT2 c and x_1 cuts to better capture a Gaussian 'core' for training. The shaded regions correspond to 2σ clippings along the longer tail of each respective c and x_1 distribution.

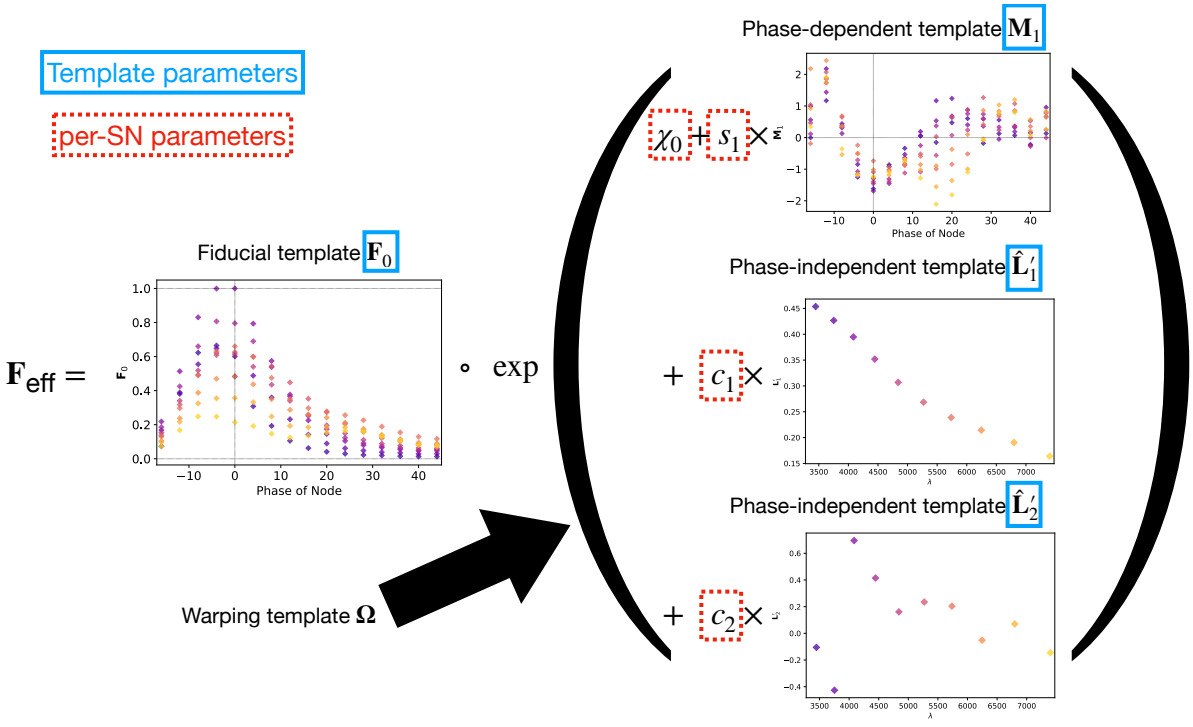

Figure 17: A schematic of our model's flux nodes. Each SN Ia has an effective flux node matrix $\mathbf{F}_{\text{eff}}$ that is an element-wise product of the sample's fiducial flux template $\mathbf{F}_0$ and a warping matrix $\mathbf{\Omega}$. This warping matrix includes the phase-dependent chromatic flux variation template $\mathbf{M}_1$, two phase-independent chromatic flux variation templates $\mathbf{L}_1{}'$ and $\mathbf{L}_2{}'$ (which make up the two dimension phase-independent chromatic variation model), and per-SN parameters χ_0 (achromatic offset), s_1 (phase-dependent chromatic flux variation contribution), and c_1 and c_2 (phase-independent chromatic flux template contributions). Presented here are the $\mathbf{L}_1{}'$ and $\mathbf{L}_2{}'$ basis representation of the phase-independent templates (see Section 3.3.3 for more information). Per-band nodes are presented in this plot having the same figure color.

These GPMP kernel matrices $\mathbf{K}$ specifically are calculated with a stationary $p = 2$ Matérn covariance function $C_{5/2}$ to ensure interpolated curves are twice-differentiable:

$$K_{ij} = C_{5/2}(|t_{p,i} - t_{p,j}|; \rho, \sigma^2). \tag{26}$$

$\mathbf{F}_{\lambda,\text{eff}}$ is the light curve at wavelength λ on a grid of phase nodes; all $n_\lambda = 10$ light curves form the flux node matrix $\mathbf{F}_{\text{eff}}$. $t_{p,i} \in \mathbf{t}_p$ is a vector indexing the model's n_p phase nodes and the per-SN parameter t_0 aligns said SN Ia's observations with the model's phase grid. Intuitively, the first kernel matrix $\mathbf{K}$ in Eq. 25 maps each observation to our phase node space after said observation phase t_i is translated by t_0, while the second accounts for $\mathbf{F}_{\lambda,\text{eff}}$ flux node covariance at grid phases $t_{p,i}$ and $t_{p,j}$. GPMPs provide a natural framework to translate observed phase t_i by the per-SN t_0 parameter to the model grid's phase zero-point.

Note that t_0 is not the fit date of maximum brightness—instead, $t - t_0$ aligns observation phase with the model's phase grid $\mathbf{t}_p$. As we train the model using rest-frame transformed spectrophotometry, each t_0 is fit in its SN Ia's reference $z = 0.05$ frame. The kernel length scale hyperparameter ρ is fixed to match the phase node interval resolution of 4 days, although the model is insensitive to any reasonable choice in ρ (for example, $\rho \approx 1$ week). Furthermore, by fixing $\rho = 4$, the matrix $\mathbf{K}$ is calculated and inverted only once during sampling. The uncertainty hyperparameter σ^2 is set to unity since it cancels out in Eq. 25.

The $\mathbf{F}_{\text{eff}}$ of each SN is decomposed via element-wise multiplication (also called the Hadamard operation $\circ$) from a fiducial flux template matrix $\mathbf{F}_0$ and a warping matrix $\mathbf{\Omega}$:

$$\mathbf{F}_{\text{eff}} = \mathbf{F}_0 \circ \mathbf{\Omega}. \tag{27}$$

$\mathbf{F}_0$ encodes the training sample's mean flux evolution via a set of fiducial light curves, while $\mathbf{\Omega}$ encodes deviations from these fiducial light curves for a given SN Ia. Specifically, each column $\mathbf{\Omega}_\lambda$ of matrix $\mathbf{\Omega}$, for a given λ node, is defined as:

$$\log(\mathbf{\Omega}_\lambda) = -2.5(\chi_0 + s_1\mathbf{M}_{\lambda,1} + c_1 L_{\lambda,1} + c_2 L_{\lambda,2}). \tag{28}$$

$\mathbf{M}_{\lambda,1}$ is the λ-node column of the phase-dependent chromatic flux variation template matrix $\mathbf{M}_1$. $\mathbf{M}_1$ therefore encodes training sample light curve variation. $L_{\lambda,1}$ and $L_{\lambda,2}$ are the λ-node elements of the two phase-independent chromatic flux variation template vectors $\mathbf{L}_1$ and $\mathbf{L}_2$,

respectively (these appear as scalars in Equation 28 because of their phase independence). Each explicit per-SN parameter is contained within the warping template: the achromatic offset parameter χ_0, the phase-dependent chromatic flux variation parameter s_1, and the two phase-independent chromatic flux variation parameters c_1 and c_2. Both intrinsic brightness variability and peculiar velocity effects are accounted for by the χ_0 parameters.

Figure 17 illustrates this model's architecture, specifically displaying the transformed phase-independent template basis $\mathbf{L}_1{}'$ and $\mathbf{L}_2{}'$ vectors later discussed in Section 3.3.3. Figure 18 is a directed acyclic graph of our model. Its conditional probability structure only connects observations to the model flux — deterministic connections (transformations and definitions) are presented with dashed arrows. Global template parameters are located in the top blue box and per-SN parameters in the bottom red box.

3.3.1 Template Constraints and Per-SN parameter Models

The third λ band, $t_{p,i} = 0$ phase node of $\mathbf{F}_0$ is fixed to one — it is referred to here as fixed band 3 and corresponds to the wavelength node at 4084 Å, the top-hat filter band closest to a standard B-band. This constraint prevents any scaling degeneracy between $\mathbf{F}_0$ and the model's χ_0 parameters while also setting the specific phase node that the t_0 parameter aligns observations to. Physical consideration further requires all $\mathbf{F}_0$ flux node parameters be bound to greater than or equal zero, so we enforce nonnegative values for all flux values.

All chromatic flux variation templates $\mathbf{L}_1$, $\mathbf{L}_2$, $\mathbf{M}_1$ have scaling degeneracies with their respective per-SN parameters c_1, c_2, and s_1. For example, the transformations $s_1 \to s_1/\alpha$ and $\mathbf{M}_1 \to \alpha\mathbf{M}_1$ leave the model unchanged; identical degeneracies exist for c_1-$\mathbf{L}_1$ and c_2-$\mathbf{L}_2$. Each scaling degeneracy is removed by requiring these three templates be normalized. This is a straightforward procedure for $\mathbf{L}_1$ and $\mathbf{L}_2$, where each are instantiated in `Stan` as unit vectors, but a more involved process is used to normalize template matrix $\mathbf{M}_1$. We first define a unit vector of length $n_p \times n_\lambda$ that is then transformed into $\mathbf{M}_1$ by 'chopping' said unit vector into n_λ column vectors (each of length n_p) that forms the column space of a now normalized $\mathbf{M}_1$[3]. No further constraints or bounds are placed on template parameters.

[3]The unit vector constraints for $\mathbf{L}_1$, $\mathbf{L}_2$, and $\mathbf{M}_1$ are what prevent these templates from being described as color variation templates. If instead we constrained these templates at a reference wavelength node to be

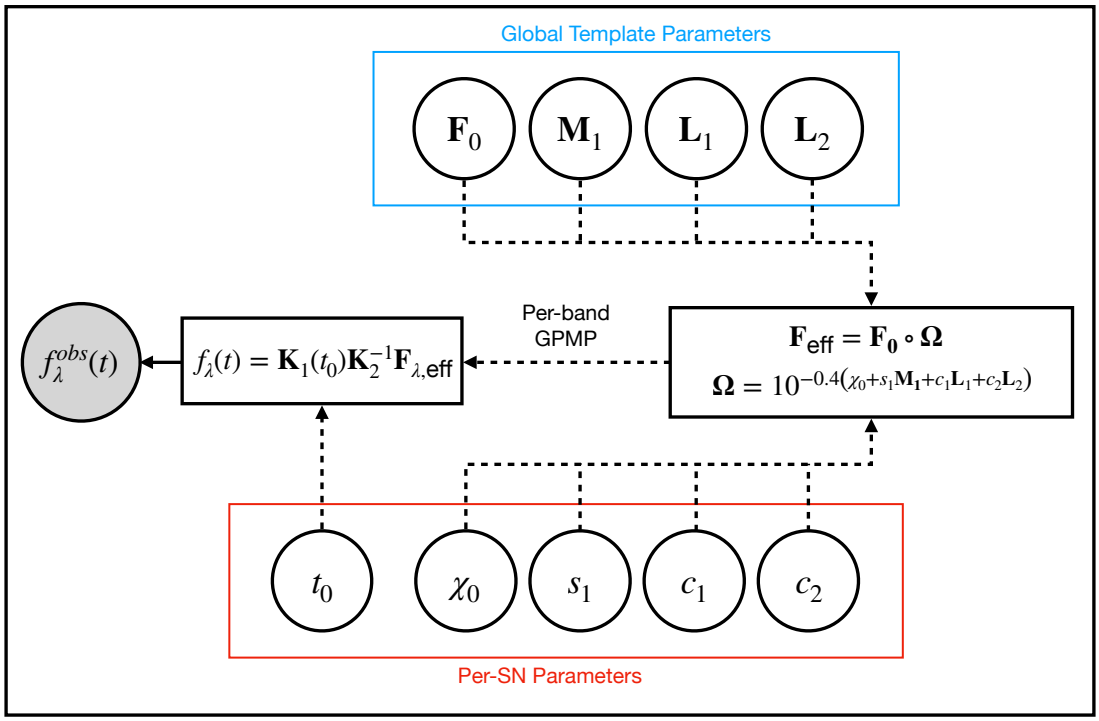

Figure 18: A directed acyclic graph representation of our model. Per-SN model parameters are located in the bottom red box; global template parameters are in the top blue box. The dashed arrows are deterministic relations (transformations and definitions). The only explicit conditional probability in the model's architecture relates observations $f_\lambda^{obs}(t)$ to modeled flux $f_\lambda(t)$. We perform Gaussian process mean predictor (GPMP) interpolation per-band in mapping effective template nodes $\mathbf{F}_{\text{eff}}$ nodes to a predicted flux $f_\lambda(t)$.

Zero-mean constraints are placed on per-SN parameter sets c_1, c_2, and s_1. A reference SN Ia could be selected to serve as the c_1, c_2, and s_1 zero points, but we opt instead to require these per-SN parameter sets to always have a mean of zero. These constraints are enforced structurally by instantiating these parameter sets as centered vectors (Appendix C).

3.3.2 Fitting the Model

The SNfactory data set comes with variance spectra estimated from photon statistics and detector noise. To these we add in quadrature a 3% relative flux error for each observation. For each SN Ia, a further error equal to 2% of said SN Ia's maximum observed flux is also added in quadrature. The first source of error preferentially increases high-flux observational error, while the second largely affects low-flux observations, particularly those 20 or more days after peak brightness. SNfactory spectral variance are chronically underestimated — this injected error is sufficient to allow Stan's instantiated samplers to explore the posterior. All added uncertainty is diagonal: no covariance is injected into our data before training.

To prevent overfitting, the data's measurement errors are sampled from a Cauchy distribution. This distribution's extended symmetric tails places less statistical weight on outliers than a normal distribution otherwise would. For each flux observation $f_\lambda^{obs}(t)$ with its corresponding measurement uncertainty $\sigma_{f_\lambda(t)}$, our likelihood function takes the form:

$$f_\lambda^{obs}(t) \sim \text{Cauchy}\big[f_\lambda(t), \sigma_{f_\lambda(t)}\big]. \tag{29}$$

Each observation is assumed independent.

The model is implemented and trained using the statistics programming language `Stan` [34]. Built into `Stan` is a No U-Turns (NUTS) Hamiltonian Monte Carlo sampler well suited for sampling our model's high-dimensional posterior. No explicit priors are placed on templates or per-SN parameter sets, instead leaving them with default implicit flat priors along any aforementioned bounds (Section 3.3.1).

`Stan` is informed with initial conditions estimated by first running simpler versions of the model. We do this only to improve sampling efficiency — it is not necessary for our model's

fixed to zero, then these templates would have units color, per the usual astronomical definition.

convergence. This process is done iteratively, starting with the simplest model that only obtains t_0, $\mathbf{F}_0$, and χ_0 parameters (a mean light curve model). The results of this simplest model then become the initial conditions for a more complex model that includes $\mathbf{L}_1$ and c_1 parameters. Other components (specifically, $\mathbf{L}_2$ and c_2, and then $\mathbf{M}_1$ and s_1) are then added and trained using prior model iteration's fit as initial conditions until all the described model's components are incorporated. Note that we use SALT2's $t_{\max}$ as initial conditions for t_0 parameters when training the simplest of these models.

With `Stan`'s default NUTS we pull 4000 samples for each of type 16 instantiated samplers: 2000 warm-up followed by 2000 samples iterations per-chain. `Stan` is run on the University of Pittsburgh's Computational Resource Center[4]. Convergence metrics were calculated after post-processing using techniques provided in [163]. After training and post-processing, each SN Ia is refit with template parameters fixed ($\mathbf{F}_0$, $\mathbf{M}_1$, $\mathbf{L}_1$, and $\mathbf{L}_2$) to determine final values for per-SN Ia χ_0, s_1, c_1, and c_2, permitting a direct comparison of these per-SN parameters against other empirical SN Ia models.

There is no selected standard $\Delta M_B = 0$ SN Ia identified in the training sample, leaving a nontrivial linear degeneracy between achromatic offset parameters χ_0 and phase-independent parameters c_1 and c_2. For physical reasons, c_1 and c_2 should not correlate with intrinsic magnitude, which ideally should only be captured by χ_0.

Linear transformations from Leget 2020 are used to remove correlations between both the c_1 and χ_0 parameters, and the c_2 and χ_0 parameters, as summarized in Appendix D [101]. Implementing this directly in the `Stan` model leaves results unchanged but does reduce sampling efficiency, so this step is performed after sampling.

3.3.3 Interpreting the Phase-independent Templates

Each sampler from `Stan` explores a plane spanned by the template vectors $\mathbf{L}_1$ and $\mathbf{L}_2$[5]. Even after decorrelating χ_0 from c_1 and c_2, the output basis $\{\mathbf{L}_1, \mathbf{L}_2\}$ is not unique, a

[4] `https://crc.pitt.edu/`

[5] In general, a plane is an affine space, not a vector space. All planes described in this paper do pass through the embedding vector space's origin, which ensures they are proper 2D vector subspaces. Because of this, all planes discussed either intersect or are parallel. For brevity, in this paper we refer to any 2D subspaces as planes.

consequence of this model's physics-agnostic architecture. This is because for any nonsingular linear transformation the output basis vectors (i.e. $a\,\mathbf{L}_1 + b\,\mathbf{L}_2$ and $c\,\mathbf{L}_1 + d\,\mathbf{L}_2$ for $a, b, c, d \in \mathcal{R}$ and $ab - cd \neq 0$) necessarily span the aforementioned plane. To quantify this plane's convergence (as opposed to only its basis vectors), for each posterior sample we calculate a bivector $\mathcal{L} = \mathbf{L}_1 \wedge \mathbf{L}_2$ that, by definition, spans the plane of interest. Importantly, the bivector representation $\mathcal{L}$ is no longer ambiguous.

A bivector is a geometric object representing an oriented plane element constructed from the wedge product (see Figure 19 for an illustration). Intuitively, a bivector corresponds to a plane like a vector corresponds to a line, and the wedge product is the dual to a cross product in three dimensions. Unlike the cross product, the wedge product generalizes to any finite-dimensional vector space greater than two, meaning bivectors are well-defined in this model's 10-dimensional wavelength node space. Now any SN Ia'a phase-independent chromatic flux variation curve $\mathbf{c} = \mathbf{c}_1\,\mathbf{L}_1 + \mathbf{c}_2\,\mathbf{L}_2$ can be interpreted as residing in the plane spanned by $\mathcal{L}$, regardless of the selected $\mathbf{L}_1, \mathbf{L}_2$ basis.

Each component of the bivector $\mathcal{L}$ is calculated as follows:

$$\mathcal{L}_{ij} = \frac{L_{1,i}L_{2,j} - L_{1,j}L_{2,i}}{\sqrt{\sum_{k=1}^{n_\lambda}\sum_{m>k}^{n_\lambda}\left(L_{1,k}L_{2,m} - L_{1,m}L_{2,k}\right)}}, \tag{30}$$

where $\hat{L}_{1,i}$ is the ith wavelength component of template $\mathbf{L}_1$ and $\hat{L}_{2,i}$ is the ith wavelength component of template $\mathbf{L}_2$. Importantly, this representation is independent of $\mathbf{L}_1, \mathbf{L}_2$ choice. Note that $\mathcal{L}$ is normalized so as to represent a unit plane element. With these transformed parameters $\mathcal{L}_{ij}$, the model can unambiguously be tested for convergence and the best-fit templates be determined.

3.3.4 Bases for the Phase-Independent Chromatic Variation Model

We now seek a pair of vectors, $\mathbf{L}_1$ and $\mathbf{L}_2$ that span $\mathcal{L}$ and readily provide insight into the physical origin of the model's two-dimensional phase-independent chromatic flux model. Two such bases are considered.

The first basis, called the maximum variance ratio (MVR) basis, is derived directly from the corresponding c_1–c_2 distribution. New and uncorrelated parameter sets c_1^{mvr} and c_2^{mvr}

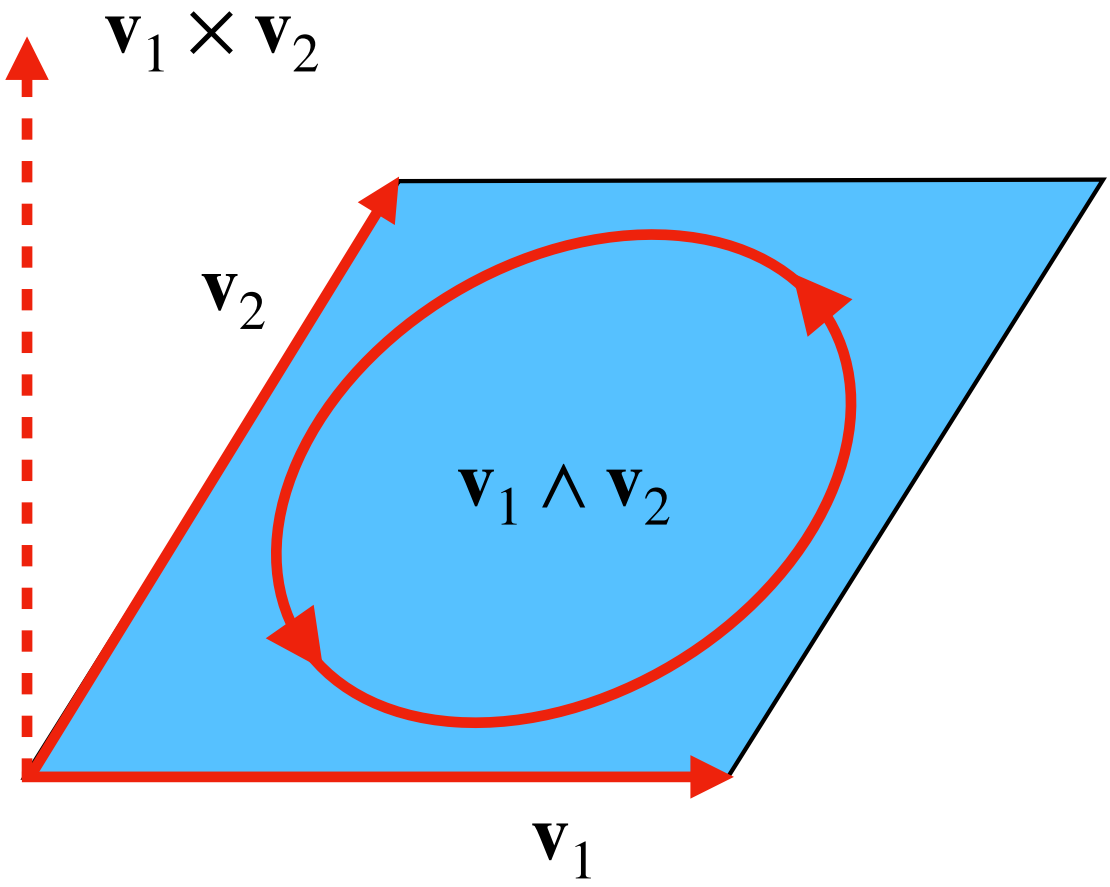

Figure 19: This is an illustration of a bivector (the blue parallelogram) $\mathbf{v}_1 \wedge \mathbf{v}_2$ constructed by the vectors $\mathbf{v}_1$ and $\mathbf{v}_2$ (the red vectors) in three dimensions. A three-dimensional space allows for the corresponding cross product to be included for reference (the red dashed vector). Bivectors, like vectors, are oriented objects, with the bivector $\mathbf{v}_1 \wedge \mathbf{v}_2$ having a counter-clockwise orientation determined by component vector ordering (here represented with an oriented red loop). Reversing the product order reverses a bivector's 'circulation' or orientation: $\mathbf{v}_2 \wedge \mathbf{v}_1 = -\mathbf{v}_1 \wedge \mathbf{v}_2$. Note that the cross product does not generalize to all finite-dimensional vector spaces, while the wedge product $\wedge$ does.

with their relative variance maximized are found via a linear transformation. The result is a basis for $\mathcal{L}$ where ${\mathbf{L}_1}^{\text{mvr}}$ accounts for the most chromatic flux diversity by a single template in $\mathcal{L}$, while ${\mathbf{L}_2}^{\text{mvr}}$ captures any remaining variation. This basis amounts to the assumption that two independent physical effects affect chromatic flux variation (e.g. amount of dust, intrinsic SN Ia diversity) while designating as much of the variance as possible to one source (e.g. dust). This assumption provides some useful insights even if it does not totally satisfy our physical expectations, as it does not consider additional possible effects (e.g. kind of dust), nor that supernovae and their progenitor environments likely correlate with said effects. This basis's solution is found by numeric minimization; it is not orthogonal.

The MVR basis is determined as follows. A basis centered at the origin can be described by the angle between unit vectors and their orientation. Starting with an orthogonalized output basis from `Stan` $\mathbf{L} = [{\mathbf{L}_1}^{\text{orth}}, {\mathbf{L}_2}^{\text{orth}}]$ for $\mathcal{L}$ and a per-SN coefficient matrix $\mathbf{c}$ (here arranged as an $n_{\text{sn}} \times 2$ matrix), adding an extra angle θ between the basis is achieved with the transformation

$$\begin{aligned} \tilde{\mathbf{L}} &= M\mathbf{L} \\ &= \begin{pmatrix} 1 & 0 \\ \sin\theta & \cos\theta \end{pmatrix} \mathbf{L}. \end{aligned} \tag{31}$$

In this $\tilde{\mathbf{L}}$ basis, the per-SN coefficients $\mathbf{c}' = \mathbf{c}M^{-1}$ have an orientation given by V^T from the singular value decomposition (SVD) of $\mathbf{c}' = U\Sigma V^T$. Taking $V^T M$ and normalizing its rows to be unit vectors gives the properly oriented basis given θ. Note that these primed components here are unrelated to those introduced below.

For this basis, the ellipticity of its corresponding c distribution is again found using SVD, given by $\log\Sigma_{11} - \log\Sigma_{22}$. An optimizer is used to determine the θ that maximizes the ellipticity.

We also desire a basis that readily separates rapidly changing chromatic flux variation (i.e. that akin to absorption/emission features) from continuum-like chromatic flux variation (i.e. dust-like behavior). This continuum-like variation is assumed to be dust-like, given dust extinction's ubiquitous contribution to SN Ia color/chromatic flux variation. For the second basis, the vector ${\mathbf{L}_1}'$ simultaneously resides within the planes spanned by both $\mathcal{L}$

and the Cardelli-Clayton-Mathis (CCM89) dust model Cardelli1989, defining the first basis component. This intersection ensures it captures smooth, CCM89-like chromatic variability. The other basis vector $\mathbf{L}_2{}'$ is chosen to be perpendicular to $\mathbf{L}_1{}'$, while still residing in the $\mathcal{L}$ plane; this basis is orthogonal by construction. Note that $\mathbf{L}_2{}'$ will not necessarily be perpendicular to the plane spanned by CCM89, but is still guaranteed to provide the least continuum-like variability w.r.t. wavelength (and therefore, the most spectral-feature-like behavior) allowed by $\mathcal{L}$. This basis provides a useful representation not because it recovers a mathematically valid dust extinction curve, but instead because it clearly separates rapidly changing chromatic flux variation from continuum-like variability. It is important to remember that intrinsic variability could still affect the direction of the first basis vector $\mathbf{L}_1{}'$, which means this basis does not guarantee a physical decomposition into exclusive dust and intrinsic components. As such, any dust-like properties inferred from $\mathbf{L}_1$ in isolation are physically ambiguous. Forward modeling introduced in Section 3.5 explores per-SN and effective dust-like properties.

The CCM89-derived basis is calculated as follows. Since CCM89 has two basis curves $a(\lambda)$ and $b(\lambda)$ (one for each parameter A_V and A_V/R_V, respectively), one can construct a CCM89 unit bivector $\mathcal{L}_{\rm ccm}$ from discretized curves $a(\lambda) \rightarrow \mathbf{a}$ and $b(\lambda) \rightarrow \mathbf{b}$ using an appropriately modified version of Equation 30: $\hat{L}_{1,i} \rightarrow a_i$ and $\hat{L}_{2,i} \rightarrow b_i$. The two planes spanned by $\mathcal{L}$ and $\mathcal{L}_{\rm ccm}$ then intersect within the n_λ-dimensional wavelength vector space along a line. It is the vector which spans this intersecting line that defines the new $\mathbf{L}_1{}'$ template:

$$\mathbf{L}_1{}' = \text{Intersection}[\mathcal{L}, \mathcal{L}_{\rm ccm}]. \tag{32}$$

We are free to choose a new $\mathbf{L}_2$ as long as it resides within the subspace represented by $\mathcal{L}$. To minimize this $\mathbf{L}_2$ template's dust-like properties, $\mathbf{L}_2{}'$ is defined as a $\theta = \pi/2$ radian rotation of $\mathbf{L}_1{}'$ within the plane spanned by $\mathcal{L}$ via a rotation operator $\mathbf{R}_{\mathcal{L}}(\theta/2)$:

$$\mathbf{L}_2{}' = \mathbf{R}_{\mathcal{L}}(\pi/4)\, \mathbf{L}_1{}'\, \mathbf{R}_{\mathcal{L}}^{-1}(\pi/4). \tag{33}$$

This rotation maximizes the component of $\mathbf{L}_2{}'$ that is perpendicular to the plane spanned by $\mathcal{L}_{\rm ccm}$. The new $\{\mathbf{L}_1{}', \mathbf{L}_2{}'\}$ also transforms the c_1 and c_2 parameters sets, here labeled $c_1 \rightarrow c_1'$ and $c_2 \rightarrow c_2'$.

Figure 20 provides a three-dimensional view of the geometric intuition involved in finding the CCM89-derived basis. All calculations discussed here are implemented using geometric algebra, which provides a novel approach to study oriented subspaces. Geometric algebra implementations for calculating intersections, projections, and rotation operations are summarized in Appendix F. Although we exploit geometric algebra's elegance and interpretability to perform all said operations, each operation could be done using more classical linear algebra techniques if desired.

3.3.5 Handling Similar Solutions

In training, the samplers converge to groups of very similar solutions. We find that simultaneously obtaining global template and per-SN parameters leaves the resulting samplers sensitive to the three least representative SNe Ia in the training sample (based on residuals). These groups are associated with slightly different solutions for these three SNe Ia, as seen by eye and quantitatively through their χ_0 solutions. Consider the following analogy: think of a dog with its body being the model's global templates and its tail's position corresponding to per-SN parameters. The dog's body reacts to a small change in the tail's location, but only subtly. It is this 'wagging' of per-SN solutions that is causing a very subtle change in template parameters, preventing complete convergence.

The worst performing SN Ia PTF11mkx consistently sees a 1σ difference between χ_0 values between different chain groups — considering that this χ_0 parameter fit uncertainty is only $\approx 1\%$, this tail wagging is very subtle. Indeed, when refitting per-SN parameters with a one of the group solutions as a fixed global template (Section 3.4.4), all chains converge to the same solutions for the three SNe Ia. Similarly, if two different group solutions are separately held constant and refit individually, the two resulting per-SN parameter sets are indistinguishable. Because each group's solution are consistently very similar, we opt to use the weighted average of all solutions for the best-fit template. This decision to use an average of all groups, as opposed to using a specific solution, has no impact on the remaining analysis.

Note that refitting with fixed t_0 parameters does not prevent this subtle grouping, nor

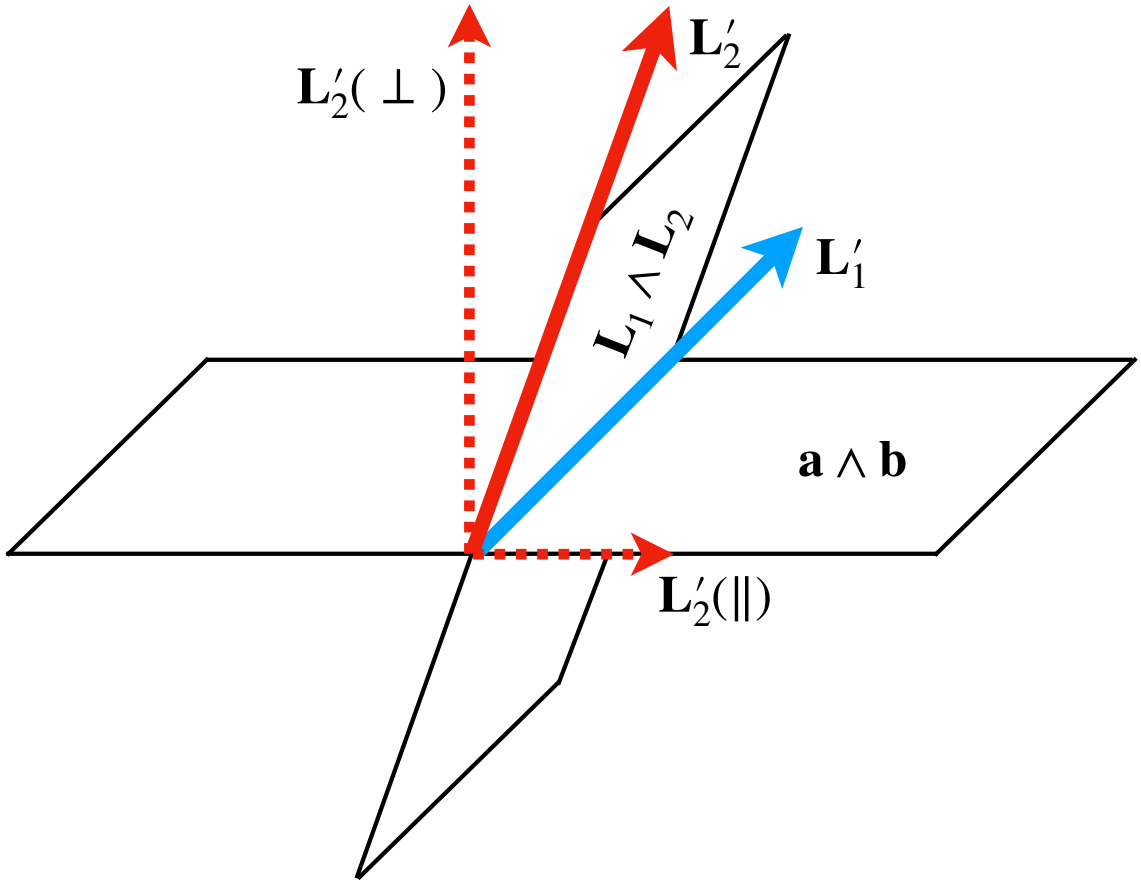

Figure 20: A three-dimensional representation the CCM89-basis's geometric intuition. The blue solid vector is the transformed $\mathbf{L}_1{}'$ template spanning the intersection of two planes, one spanned by the model bivector $\mathcal{L} = \mathbf{L}_1 \wedge \mathbf{L}_2$ and the other spanned by the CCM89 bivector $\mathcal{L}_{\text{ccm}} = \mathbf{a} \wedge \mathbf{b}$. The red solid vector is a $\pi/2$ rotation in the plane spanned by $\mathcal{L}$ that defines the transformed $\mathbf{L}_2{}'$ template. The decomposition $\mathbf{L}_2{}' = \mathbf{L}_2{}'(\parallel) + \mathbf{L}_2{}'(\perp)$ with respect to the CCM89 plane spanned by $\mathcal{L}_{\text{ccm}}$ is given with the red dashed arrows.

does cutting these three SNe Ia from the training set. If these three aforementioned troublesome SNe Ia are removed, the next few SNe Ia that are the least representative of this newly trimmed sample start 'wagging'. This instability may be a feature of our model. In particular, the flat prior we use for the c_1 and c_2 distributions may bias the results for the least representative SNe Ia of a given training sample. Considering that global template parameters again were effectively unchanged with their removal, we retain those three SNe Ia for the remainder of the analysis.

3.4 Best-fit Model Results

Our model, as implemented with `Stan`, consists of global template parameters and per-SN parameters. We define the best fit solution to be the mode of a 365-dimensional template parameter space[6], with each per-SN parameter marginalized before estimating from HMC sampling the posterior's maximum. This mode is estimated using a mean shift clustering algorithm implemented in the scikit-learn package using the default flat kernel [120]. To estimate a consistent best-fit solution, bivector components $\mathbf{L} = \mathbf{L}_1 \wedge \mathbf{L}_2$ (Equation 30) are used instead of $\mathbf{L}_1$ and $\mathbf{L}_2$ components directly. This process is analogous to maximum *a posteriori* estimation of the HMC-sampled posterior, but allows first for the aforementioned post-processing. Marginal posterior dispersion for each parameter are presented as 68%-th percentile error bars. Residuals of the best-fit model, alongside binned averages, are presented in Figure 21.

Two of the 16 HMC samplers were rejected after fitting because 1) their resulting mean t_0 parameter values were notably different from SALT2's maximum phase values, 2) the resulting fit light curves exhibit nonphysical inflection points, and 3) these two samplers have notably inconsistent $\ln p$ values relative to the 14 retained samplers. The 14 remaining samplers converge to three very similar group solutions of which the weighted average is taken; see Section 3.3.5 for more details.

[6] 159 from $\mathbf{F}_0$, 159 from $\mathbf{M}_1$, 9 from $\mathbf{L}_1$ and 9 from $\mathbf{L}_2$, specifically.

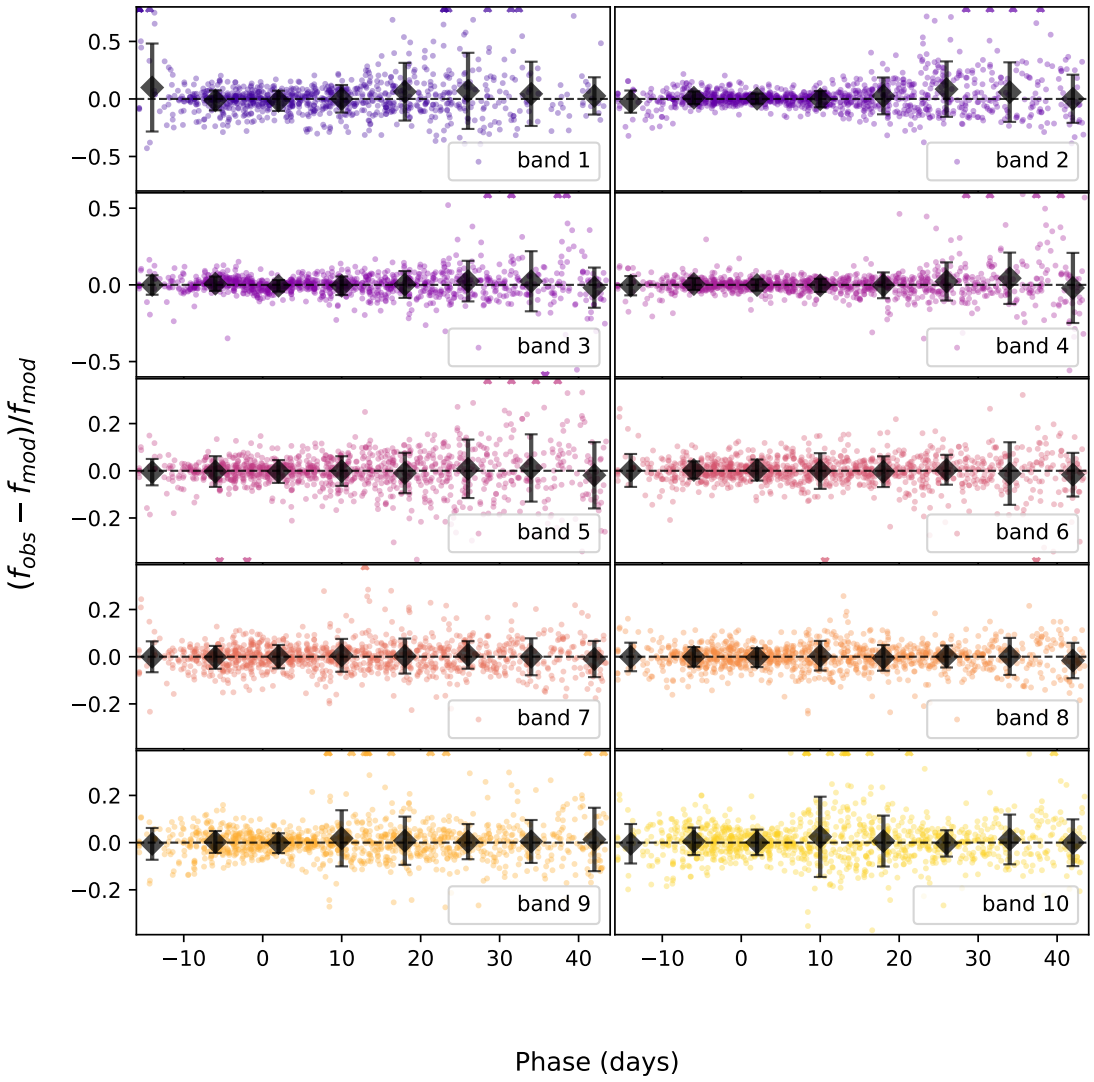

Figure 21: Best-fit model residuals with respect to observations presented for each of our ten bands. Eight day binned averages for each band are presented as black diamonds, with error bars being binned standard deviations.

3.4.1 Phase-independent Chromatic Flux Variation Templates

Ostensibly, if $\mathcal{L}$ were to only capture CCM89 dust-like behavior, then the planes spanned by $\mathcal{L}$ and $\mathcal{L}_{\rm ccm}$ would be effectively parallel and any intersection poorly constrained. This turns out to not be the case, with the best-fit solution recovering a planar separation angle of about 80°.

3.4.1.1 Maximum Variance Ratio Basis

Figure 22 presents the MVR basis as described in Section 3.3.4. Qualitatively, $\mathbf{L}_1{}^{\rm mvr}$ appears nominally more dust-like than its counterpart $\mathbf{L}_2{}^{\rm mvr}$. Figure 22 includes the best fit CCM89 curve $R_V^{\rm mvr} = 2.18$ for reference, showcasing that its most extreme divergence from CCM89 is blueward of 5000 Å. $\mathbf{L}_2{}^{\rm mvr}$, on the other hand, captures variation that is not readily describable as dust-like: normal dust extinction should be absorptive across the optical wavelength range whereas the sign flip in $\mathbf{L}_2{}^{\rm mvr}$ produces simultaneous brightening/dimming on either side of 4000 Å. Although the degree of variation increases as wavelength decreases, there is a distinct flip in behavior around 4000 Å. Such behavior is inconsistent with dust extinction.

The conditions for the target parameter set distributions is to assign maximum variance to one component while keeping the second component uncorrelated. These conditions yield a basis consistent with the expectation that dust-like variation is the primary contributor to SN Ia phase-independent chromatic flux variation while intrinsic SN Ia diversity uncorrelated with dust accounts for additional variability.

3.4.1.2 CCM89-derived Basis

The template $\mathbf{L}_1{}'$ is presented in the top plot of Figure 23. As summarized in Section 3.3.4, the intersection of the plane spanned by $\mathcal{L}$ with the plane spanned by $\mathcal{L}_{\rm ccm}$ defines the first phase-independent chromatic flux template $\mathbf{L}_1{}'$. This $\mathbf{L}_1{}'$ template, as expected, captures continuum-like variation akin to dust extinction.

From $\mathbf{L}_1{}'$ we find an intersection total-to-selective extinction ratio of $R_V^{\rm int} = 2.4$. As men-

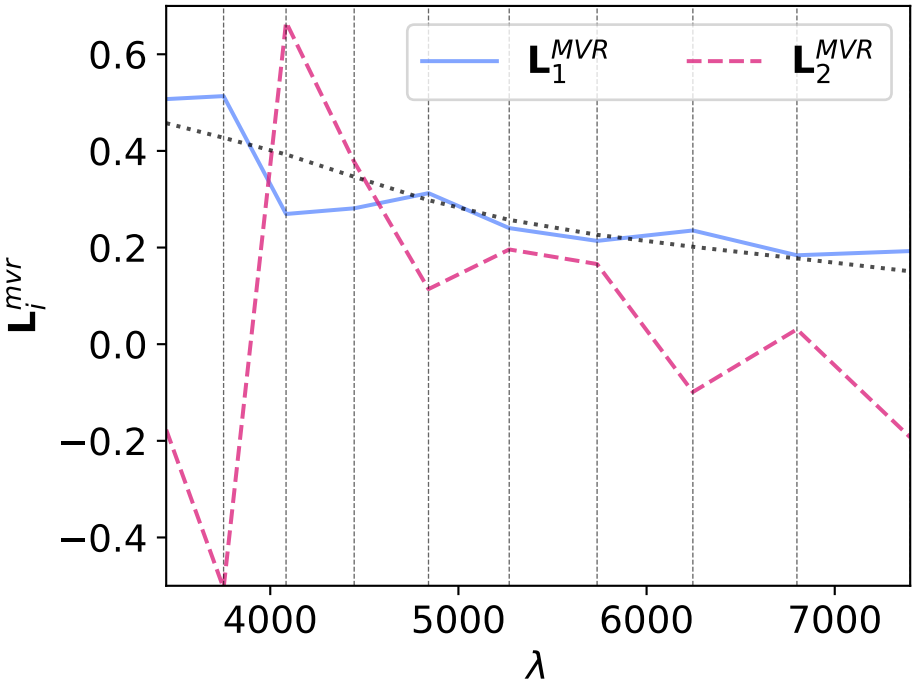

Figure 22: The blue solid line corresponds to the first MVR component $\mathbf{L}_1{}^{\mathrm{mvr}}$, which appears nominally more consistent with dust-like variation than its counterpart $\mathbf{L}_2{}^{\mathrm{mvr}}$, given as the magenta dashed. $\mathbf{L}_1{}^{\mathrm{mvr}}$ has a best-fit $R_V^{\mathrm{mvr}} = 2.18$ given as the gray dotted line, with most of its divergence from a CCM89 curve occurring blueward of 5000 Å. $\mathbf{L}_2{}^{\mathrm{mvr}}$ captures variation not readily describable as dust-like.

tioned in 3.3.4, this R_V is not physically interpretable. Later in Section 3.5, after additional forward modeling we extract per-SN dust properties with an assumed underlying A_V model.

Also presented in the top plot of Figure 23 is template $\mathbf{L}_2{}'$. Unlike $\mathbf{L}_1{}'$, $\mathbf{L}_2{}'$ captures the more rapidly changing flux variability allowable by $\mathcal{L}$. Specifically, $\mathbf{L}_2$ is capturing wavelength variation at scales smaller than that expected by continuum dust variability, at least within the optical regime. Indeed, its features nominally align with spectral feature. Also note the similarity between $\mathbf{L}_2{}'$ and $\mathbf{L}_2{}^{\text{mvr}}$ despite their vastly different constructions.

$\mathbf{L}_2{}'$ is not perpendicular to the CCM89 plane because the plane spanned by $\mathcal{L}$ is itself not perpendicular. As such, $\mathbf{L}_2{}'$ also captures a dust-like component alongside its dominating spectral-like component. The bottom panel presents this template's decomposition into parallel and perpendicular components defined with respect to CCM89's plane for reference. As such, this parallel component $\mathbf{L}_2{}'(\|)$ is used in conjunction with $\mathbf{L}_1{}'$ later in Section 3.5 when we estimate per-SN dust properties with additional forward modeling.

3.4.1.3 Intrinsic Variation

Both of the best-fit template representations $\mathbf{L}_2{}'$ and $\mathbf{L}_2{}^{\text{mvr}}$ capture pronounced phase-independent chromatic flux variation blueward of 4500 Å that is inconsistent with dust (see Figure 24). Indeed, no extrinsic phenomena readily describe this behavior. Variation blueward of 4500 Å includes the prominent Ca II H&K feature and its Si III counterpart, Si II λ4130, C II λ4267, Fe II λ4404, and Mg II λ4481. With our choice of splitting the spectral range into $n_\lambda = 10$ synthetic filters, the model cannot completely distinguish between said features, although at least one node for both $\mathbf{L}_2{}'$ and $\mathbf{L}_2{}^{\text{mvr}}$ and their corresponding variation seemingly align with Ca II H&K. A hint of chromatic flux variability ostensibly aligns with SNe Ia's signature Si II λ6347 feature and the O III NIR triplet are visible in Figure 23, but in practice do not affect any resulting model flux predictions (again, see Figure 24).

We use the same dataset used for the SNEMO model [147]. Comparing both $\mathbf{L}_2{}'$ and $\mathbf{L}_2{}^{\text{mvr}}$ to SNEMO2 and SNEMO7 eigenvectors (with two and seven components, respectively) yields indecisive insight, though. Figure 6 shows SNEMO eigenvectors describing similar $\mathbf{L}_2{}'$ or $\mathbf{L}_2{}^{\text{mvr}}$ behavior at maximum, but all of these eigenvectors are clearly phase

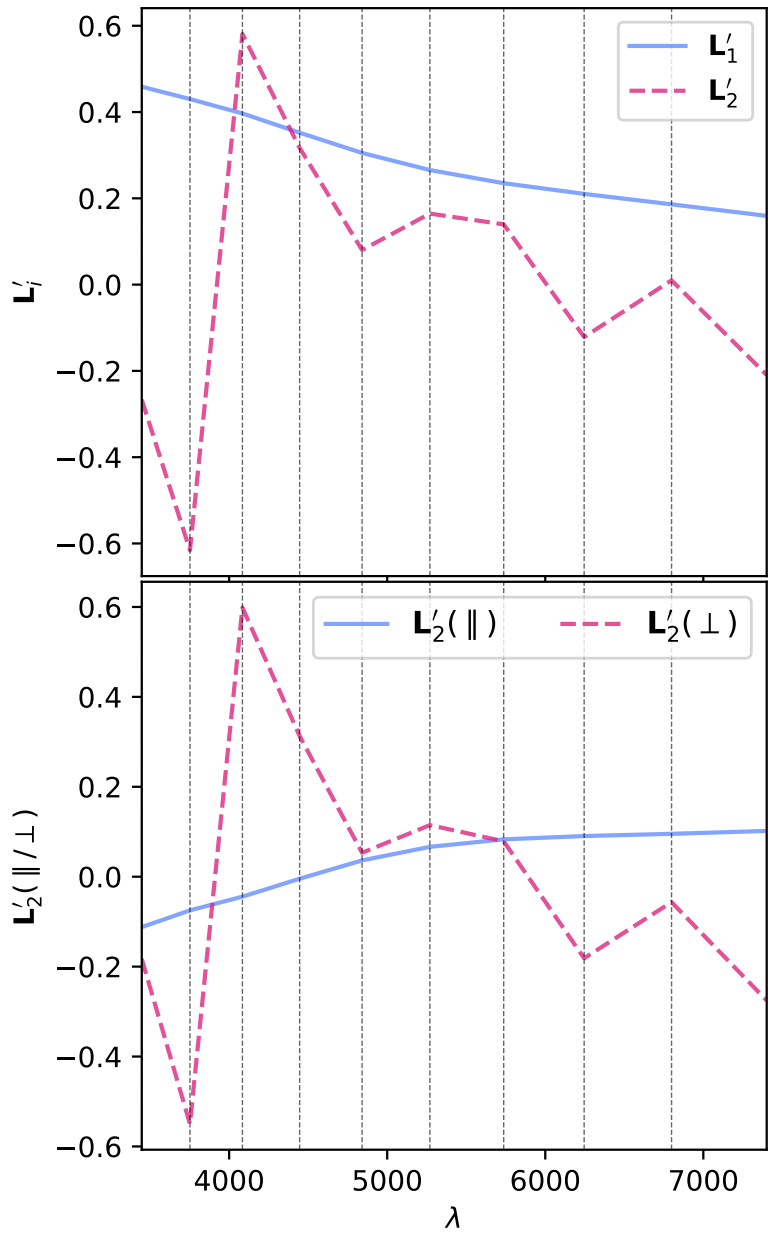

Figure 23: The top plot presents phase-independent chromatic flux variation templates $\mathbf{L}_1{}'$ and $\mathbf{L}_2{}'$. $\mathbf{L}_1{}'$ has a recovered total-to-selective extinction of $R_V^{\rm int} = 2.4$. The bottom plot presents a decomposition of $\mathbf{L}_2{}'$ into its parallel and perpendicular components with respect to the CCM89 plane. $\mathbf{L}_2{}'$ clearly captures some dust-like variability, despite being dominated by intrinsic modes. Although the low-resolution wavelength binning prevents quantification of spectral features, the most impressive $\mathbf{L}_2{}'$ variability appears in the Ca II H&K regime.

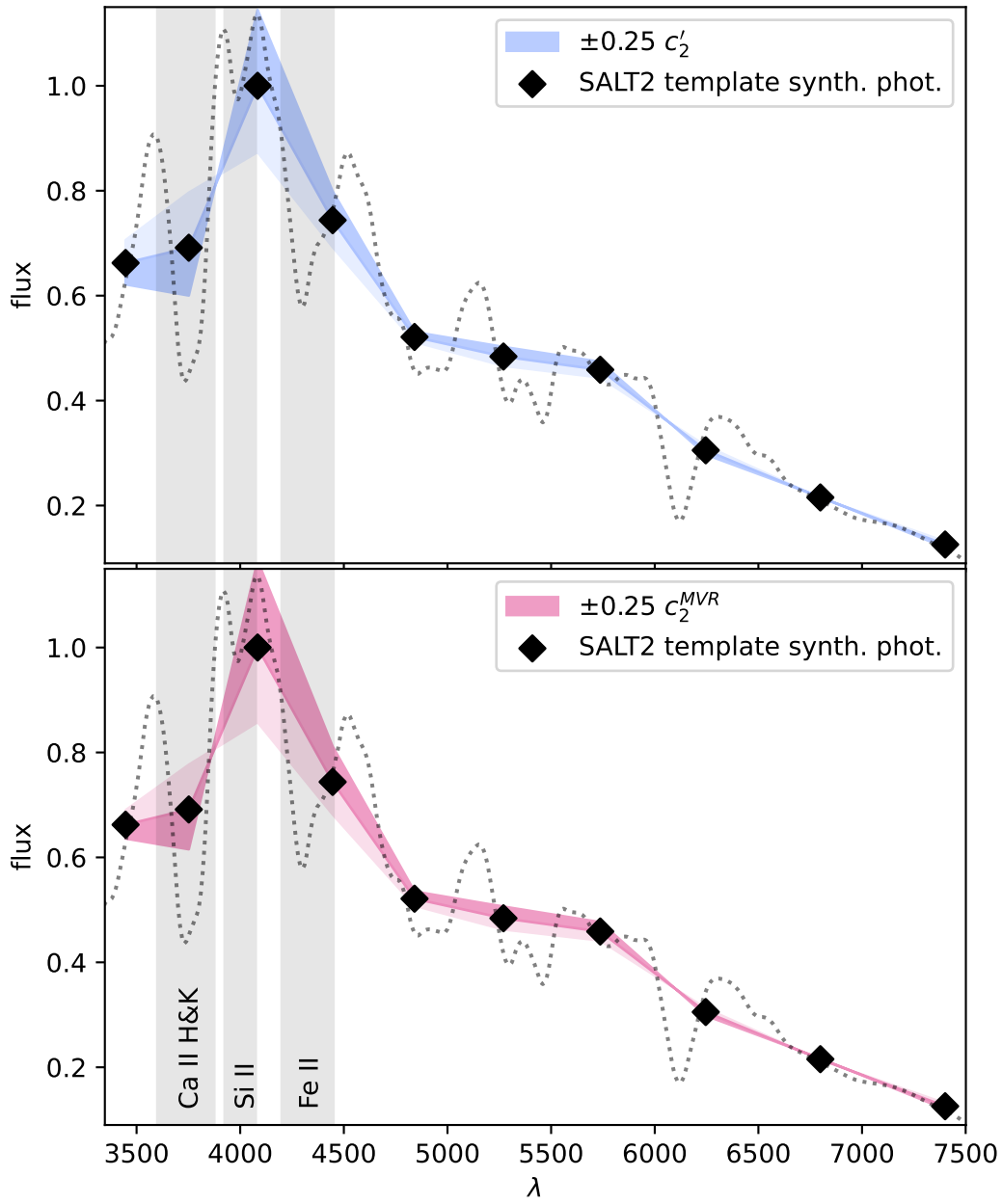

Figure 24: This figure demonstrates a ±0.2 mag c_2 variation (blue for CCM89-basis c_2', maroon for $c_2^{\rm MVR}$) of $\mathbf{L}_2{}'$ overlaid on SALT2's mean template $t = 0$ phase spectrum (dashed black line). The spectrum is binned via synthetic photometry with top hat filters, presented as black diamonds. Flux units are normalized by synthetic photometry wavelength 4048 Å value to unity and example spectral features blueward of 4500 Å are presented for reference.

dependent — no eigenvector's evolution seems approximately phase independent. Figures 9 through 12 present some unexplained variation for SNEMO2 blueward of 4500 Å that is nominally phase-independent up to six days post-maximum; this all but disappears with SNEMO7. That SNEMO2, itself similar to SALT2, sees unexplained phase-independent variability around maximum that aligns with $\mathbf{L}_2{}'$ and $\mathbf{L}_2{}^{\mathrm{mvr}}$ features seems indicative of our model's performance, but such a claim taken alone is likely an excessive interpretation.

SNfactory data is also used for the Twins Embedding nonlinear model [20]. More interesting insight is gained in their comparing their findings with our template representations $\mathbf{L}_2{}'$ and $\mathbf{L}_2{}^{\mathrm{mvr}}$, since Twins Embedding is currently a phase-independent, maximum-phase model. Blueward of 4500 Å, spectral variation recovered by Twins Embedding loosely aligns with the both $\mathbf{L}_2{}'$ and $\mathbf{L}_2{}^{\mathrm{mvr}}$ templates (see there Figures 4, 6, and 10 for reference). Recovering this consistent variation in our phase-independent template, albeit at lower wavelength bin resolution, lends credibility that $\mathcal{L}$ as a whole is capturing intrinsic variation.

Past analyses by Branch 1993 and Riess et al. 1998 find Ca II H&K features are relatively stable in the week before and weeks after peak B-band brightness, with this effective phase-independence being sufficiently stable to exploit for the latter's 'snapshot' methodology from which they constrain luminosity distances [22, 134] . Both $\mathcal{L}$ basis representations do capture intrinsic, phase-independent variation around Ca II H&K, but this alone is not profound evidence of fundamental Ca II H&K time independence in the SN Ia population. SN Ia Ca II H&K features, as with all spectral features, demonstrably evolve with time. In its current form, this model cannot distinguish between phase-averaged spectral variation or truly phase-independent intrinsic variation. Indeed, a goal of this project is to demonstrate that intrinsic chromatic flux variation can 'leak' into phase-independent components, something that is occurring in these results.

3.4.2 Fiducial Template

Figure 25 presents GPMP interpolations of each band's best-fit $\mathbf{F}_{\lambda,0}$'s nodes as solid curves. Fixed band 3's template is the third solid curve presented in the top plot of Figure 25. The ubiquitous NIR bump is recovered for redder bands (bottom plot of Figure 25), with this

second maximum occurring ≈ 25 days after our fixed-band peak brightness as expected [81]. Apart from the reddest template curve centered at 7401 Å, peak-brightness phase per-band occurs earlier for bluer bands and later for redder band, again consistent with established trends [81]. As would be expected by its I-band overlap, the reddest template curve exhibits somewhat more complex behavior than other curves, such as an inflection point between its two local maxima (bottom plot, Figure 25).

Note that each fiducial template light curve's peak brightness phase does not align with our $t_{p,i} = 0$ flux node, meaning t_0 should not be interpreted as the fixed band 3's peak brightness phase. This is ultimately inconsequential, requiring only that each light curve's peak brightness phase be calculated deterministically after fitting, and has no effect on this analysis or its conclusions.

3.4.3 Phase-dependent Chromatic flux Variation Template

As shown in Figure 25, the best-fit phase-dependent variation template $\mathbf{M}_1$ exhibits stretch-like behavior across all bands. The shaded regions in these plots show phase-dependent light curve variation from$-0.09 < s_1 < 0.09$ mag, which approximately captures the dispersion of the fit s_1 parameter set (the set's standard deviation is 0.09 mag). The lighter shaded regions correspond to positive s_1 values, while the darker correspond to negative values. As s_1 increases (decreases), $\mathbf{F}_{\text{eff}}$ node values increases (decreases) with respect to $\mathbf{F}_0$'s node values, resulting in each GPMP interpolation curve global maximum decreasing (increasing). This change in $\mathbf{F}_{\text{eff}}$ node scaling is offset for by a change in χ_0, correlating χ_0 and s_1 parameter sets (see Section 3.4.4).

The sign of $\mathbf{M}_1$ template's contribution is a function of phase: for each curve there are two phases where $\mathbf{M}_1$ template's contribution reverses in sign. For positive (negative) s_1, the result is a narrowing (broadening) of the effective flux curve. The phase and degree of this broadening varies between bands in a manner consistent with theory, being more extreme for bluer wavelengths [85]. Furthermore, Figure 26 plots our model's $\Delta m_3(15)$ as a function of s_1, demonstrating our $\mathbf{M}_1$ template indeed recovers stretch-like behavior for this model's B-band analog fixed band 3.

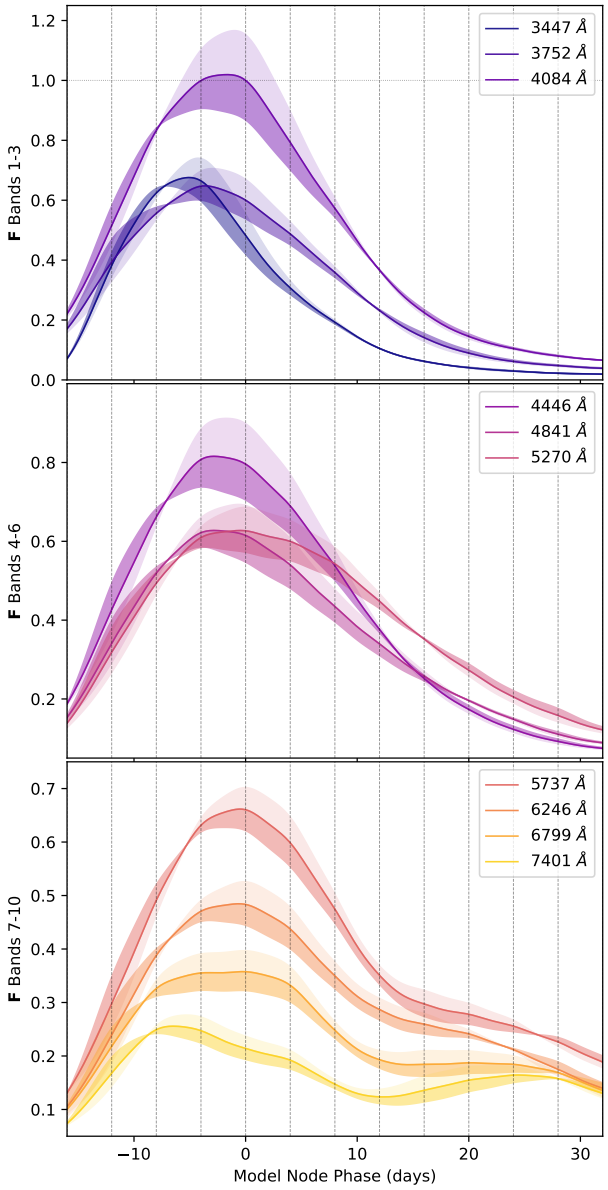

Figure 25: A visualization of ± 0.09 mag variation in s_1 on the model's fiducial flux template $\mathbf{F}_0$, as warped by the phase-dependent chromatic flux template $\mathbf{M}_1$. Positive s_1 contribution is given by light shaded regions, while negative s_1 contribution is given by the dark shaded regions. Solid lines are the GPMP interpolated light curve for that band's fiducial template nodes. The top two plots illustrate recovered stretch-like behavior by the template $\mathbf{M}_1$, with broadening to narrowing of effective light curves as s_1 increases in value. The bottom plot captures stretch-like behavior further convolved with NIR bump variational modes (bump location and size).

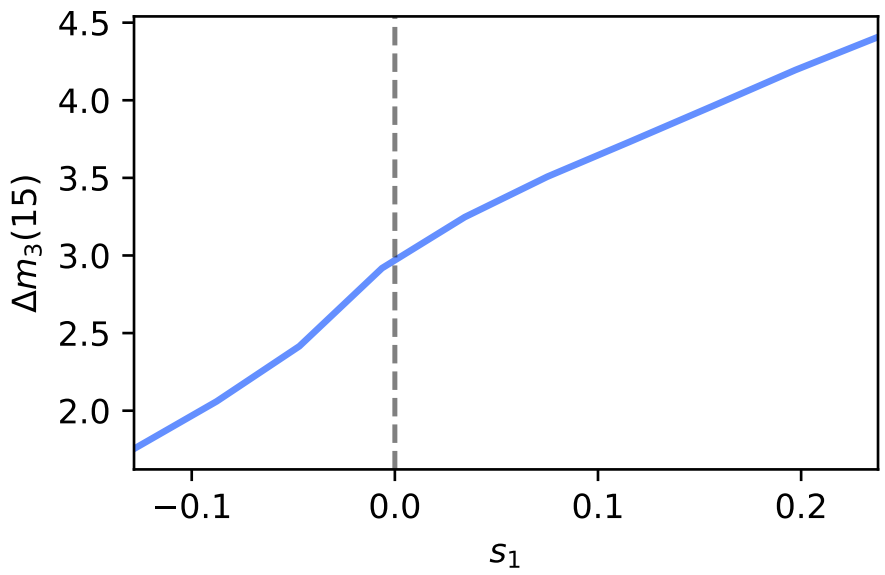

Figure 26: The model's $\Delta m_3(15)$ (the $\Delta m_B(15)$ analog for the fixed band 3) as a function of s_1 calculated for the fixed band 3 along the training sample's obtained s_1 value range.

For redder bands, stretch-like behavior is convolved with NIR bump variation (bottom plot of Figure 25). A 3D mesh plot Figure 27 best illustrates these two modes of NIR variation: bump depth and bump location. As expected, these variation modes also correlate with stretch [29, 47], with stretch appearing as the valley-like feature in Figure 27.

For fixed band 3, the phase of maximum brightness relative to our zero-phase node is a function of s_1. This movement in maximum brightness location, made clear in Figure 25, ranges from +1 day for our most negative $s_1 = -0.15$ mag SN Ia to −3 days for our most positive $s_1 = 0.22$ mag. Again, this has no effect on our analysis, requiring only an *a posteriori* calculation at phase of maximum brightness if desired.

3.4.4 Per-Supernova Results

Each SN Ia is refit with template parameters fixed to the previously discussed best-fit solution. Scatter plots comparing parameter sets include Spearman rank correlation coefficient

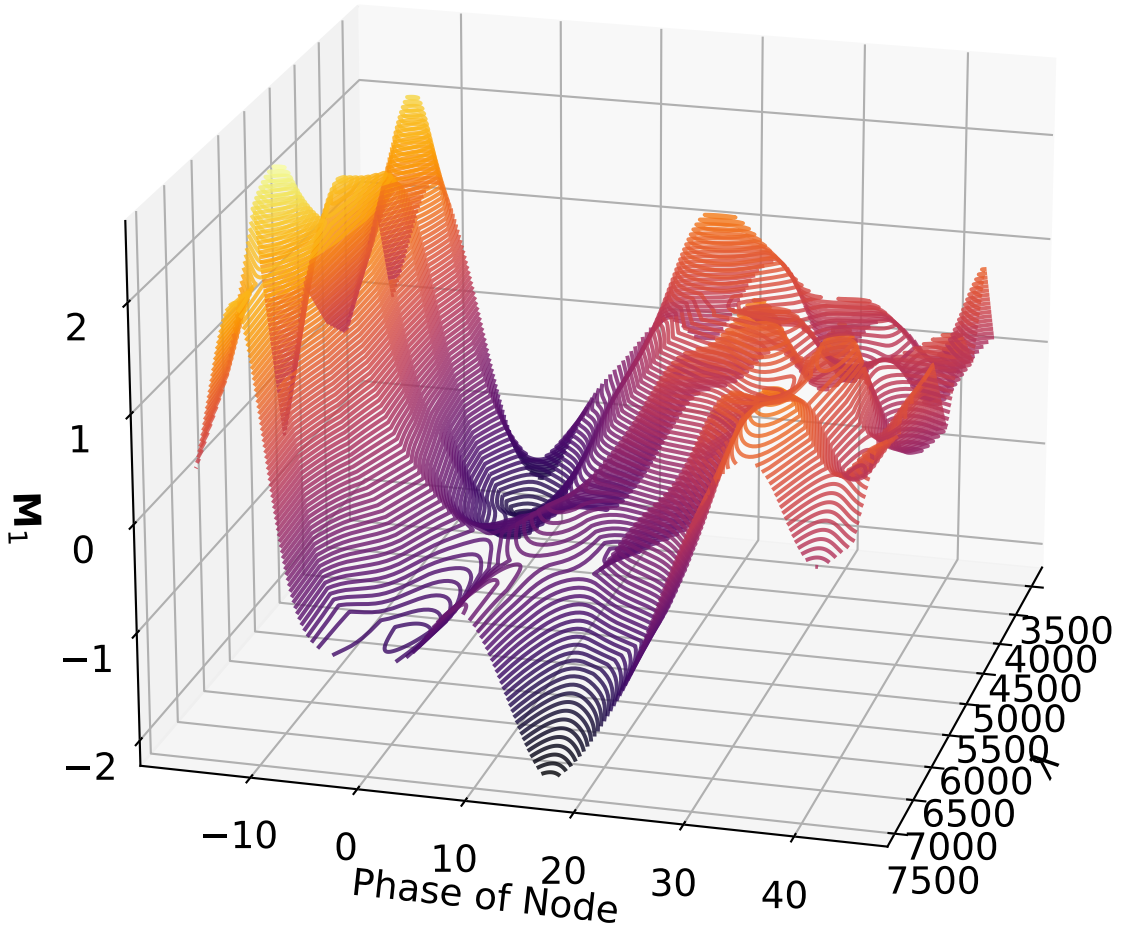

Figure 27: A contoured three-dimensional view of our phase-dependent variation template but with reversed wavelength angle to highlight the NIR bump variation. The valley-like structure corresponds to stretch-like behavior extracted by our $\mathbf{M}_1$ template.

(SCC) calculations alongside corresponding p-values. For color, only the CCM89-derived basis parameter sets c_1' and c_2' are presented. Although both the MVR and CCM89-derived bases yield quite similar results, the latter is more readily interpreted, since it provides for its first component a mathematically valid CCM89 curve and a convenient decomposition of its second.

In Figure 28, per-SN parameter sets for c_1', c_2', and s_1 are compared with corresponding χ_0 values. The measured SCC value of 0.59 between the training sample's s_1 and χ_0 parameter sets results from a varying s_1 changing the resulting $\mathbf{F}_{\text{eff}}$ scaling, requiring a compensating change in χ_0 to offset (see Section 3.4.3). By construction, c_1' and c_2' sets are decorrelated with χ_0 (see Section 3.3.3). Higher rank correlations are recovered for c_1' vs s_1 and c_1' vs c_2' compared to c_2' vs s_1, as seen in the scatter plots of Figure 29.

We also quantify the fractional variance of the c_1' and c_2' bivariate distribution not explained by CCM89-like behavior. Each SN Ia phase-independent chromatic flux variation vector $\mathbf{c} = c_1' \mathbf{L}_1' + c_2' \mathbf{L}_2'$ is first normalized. The perpendicular component with respect to the CCM89 plane spanned by $\mathcal{L}^{\text{ccm}}$ of each normalized $\mathbf{c}$ is then calculated via a projection operation (see Appendix F.2). This resulting distribution has a median value of 0.13 with 68^{th} percentiles $[0.05, 0.4]$ and provides a measure of our sample's fractional variance attributable to captured phase-independent chromatic variability which is not dust-like. Unsurprisingly, dust-like variation, which explains the remaining $\approx 87\%$ variance, dominates captured phase-independent variability. Even if this dust-like variation was the exclusive result of actual dust attenuation (no 'leaking' of intrinsic variability into dust-like behavior), the remaining $\approx 13\%$ variance, which instead arises from intrinsic variability in the sample, is not negligible. $\mathcal{L}$, with $\mathbf{L}_2'$ in particular, is capturing a discernible addition of SN Ia variation over past two-component models (i.e. SALT2).

3.4.4.1 Comparison to SALT2

This new SN Ia model and SALT2 are trained using optical wavelength observations, with neither making assumptions about dust attenuation, making it an obvious comparator. One technical difference is our model's accounting for phase-dependent variability with a

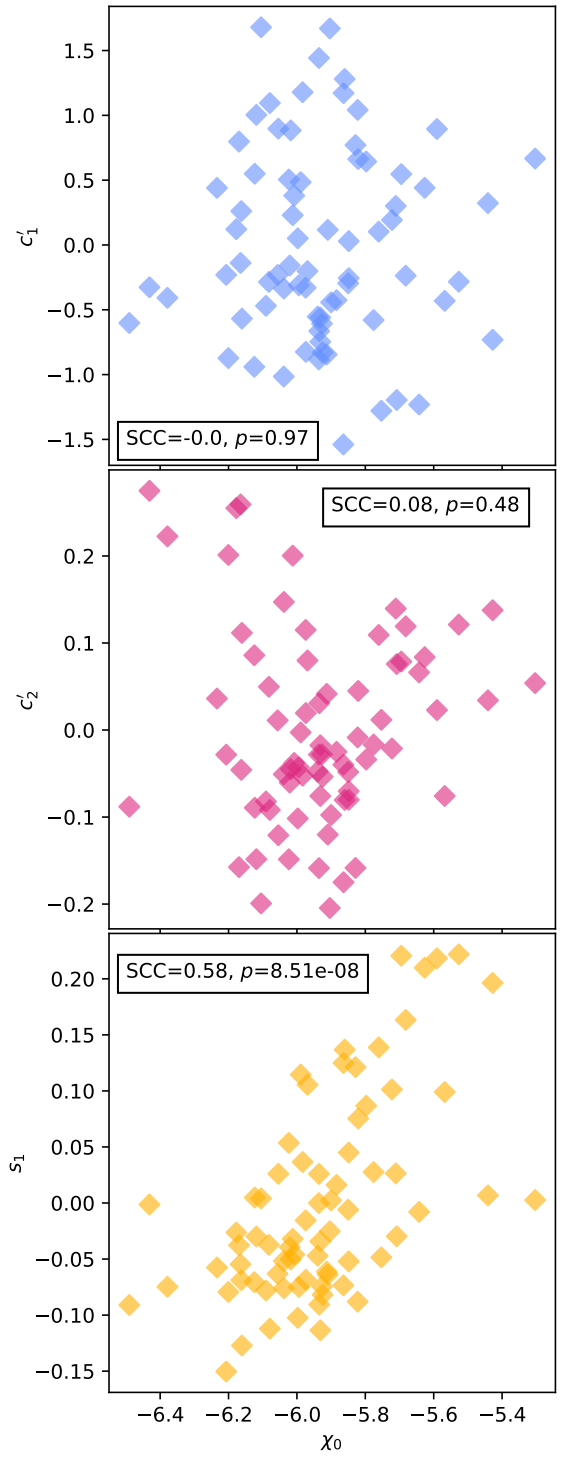

Figure 28: Comparison of fit c_1' (top), c_2' (middle), and s_1 (bottom) samples against our χ_0 samples. The correlation between χ_0 and s_1 arises from s_1's changing of $\mathbf{F}_{\text{eff}}$'s scale, which is then compensated for by a change in χ_0. There are no correlations between either c_1' and χ_0 or c_2' and χ_0 by construction.

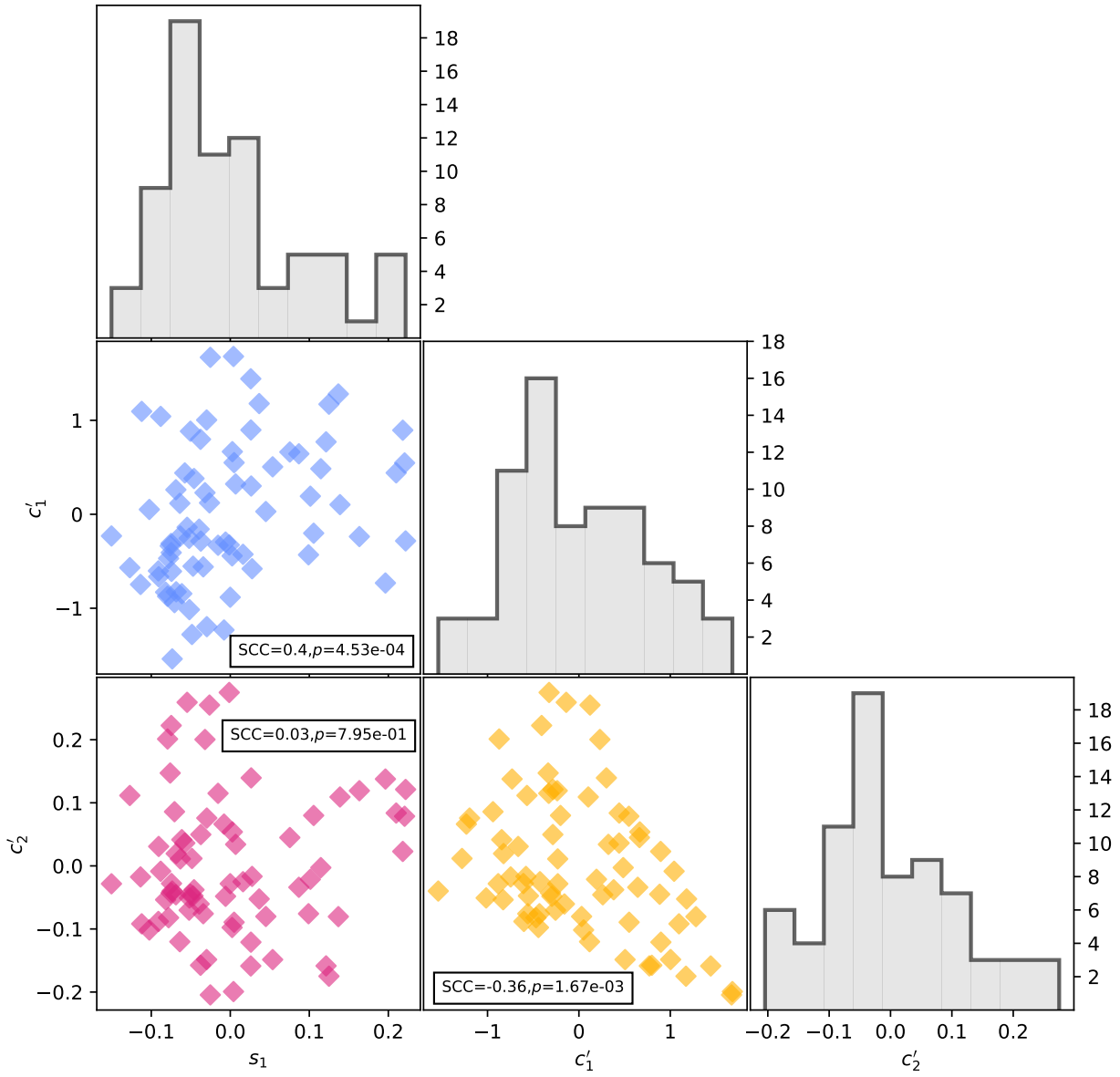

Figure 29: Corner plot for per-SN parameters s_1, c_1', c_2'. We measure only marginal rank correlations between both c_1' vs. s_1 and c_1' vs c_2'.

multiplicative variation template as opposed to SALT2's flux variation linear component, which is obviously additive in flux space. Nonetheless, s_1 and x_1 should correlate. This is the case as seen in Figure 30, with a rank correlation of -0.89 between x_1 and s_1. As presented in Section 3.4.3, this model's $\mathbf{M}_1$ templates obtains stretch-like behavior, just as SALT2's first-order variation template $M_1(t, \lambda)$ does.

The phase-independent chromatic flux variation template basis $\{\mathbf{L}_1{}', \mathbf{L}_1{}'\}$ is selected without consideration of SALT2's $CL(\lambda)$ phase-independent chromatic variation model. As such, any correlations between c_1' or c_2' and SALT2 c are nontrivial — as seen in the top plot of Figure 31, only SALT2 c and c_1' are correlated with a rank correlation of 0.78. Considering $\mathbf{L}_1{}'$ is the maximal CCM89 dust-like vector allowed, that SALT2 c and c_1' are strongly correlated is an artifact of SALT2's $CL(\lambda)$ template predominately capturing dust-like variation. Indeed, the latest SALT3 recovers a $CL(\lambda)$ curve that is consistent with SALT2 and similarly aligns with CCM89 between 4000 Å and 7000 Å [93]. As seen in Figure 13 of Kenworthy et al. 2021, both of SALT2 and SALT3 $CL(\lambda)$ templates begin to diverge from CCM89 near where $\mathbf{L}_2{}'$ starts to exhibit most of its variability [93].

The bottom plot of Figure 31 demonstrates that c_2' and SALT2 c parameter sets are uncorrelated. As one would hope, the presented model's two-component phase-independent chromatic variation model captures SN Ia variation beyond that of SALT2. For reference, we provide best fit linear relationships between SALT2 x_1 and s_1, and between SALT2 c and c_1':

$$c_1'(c) = 8.74(\pm 0.88)c + 0.094(\pm 0.056) \tag{34}$$

$$s_1(x_1) = -0.089(\pm 0.004)x_1 + 0.0089(\pm 0.0035). \tag{35}$$

3.5 Measuring Total-to-selective Extinction

That $\mathbf{L}_1$ and the component of $\mathbf{L}_2{}'$ parallel to the CCM89 plane means there is information in the $\{c_1', c_2'\}$ parameter set to potentially constrain per-SN dust properties if we

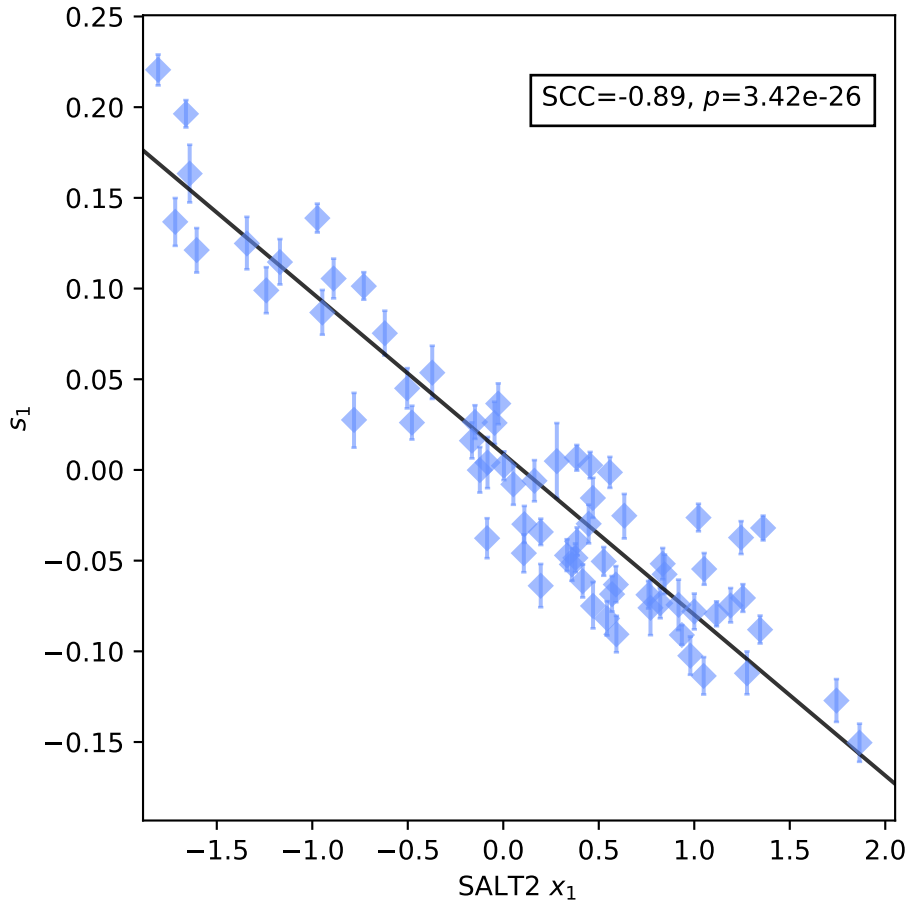

Figure 30: Per-SN comparison of our stretch parameter s_1 versus SALT2's stretch proxy x_1. A linear best fit is provided with a solid black line. Error bars correspond to 68^{th} percentiles.

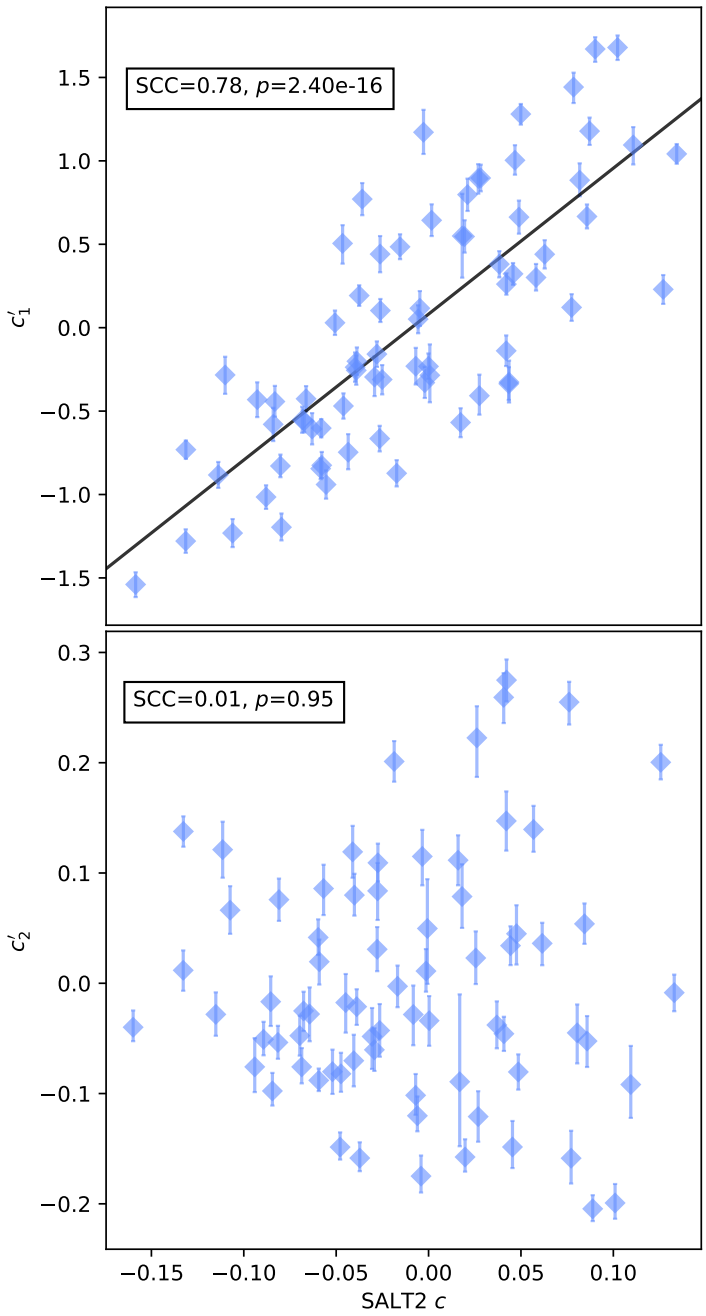

Figure 31: A per-SN comparison of our per-SN chromatic flux variation parameters c_1' (top) and c_2' (bottom) against SALT2's c parameter. We measure a clear rank anticorrelation between c_1' and SALT2 c, but measure no correlation between c_2' and SALT2 c. We interpret this as template $\mathbf{L}_2{}'$ capturing chromatic flux variation not modeled by SALT2. A linear best fit between c_1' and SALT2 c is provided by a solid black line. Error bars correspond to 68-th percentiles.

provide an appropriate A_V model. This section describes the methodology for, results of, and limitations related to estimating these dust-like parameters from our base model.

Before this forward modeling, the parameter set $\{c_1', c_2'\}$ is first transformed to a new parameter set $\{c_a, c_b\}$, where components c_a and c_b are defined with respect to the CCM89 basis vectors **a** and **b**. This is done by projecting each SN Ia chromatic flux variation vector $\mathbf{c} = c_1\,\mathbf{L}_1 + c_2\,\mathbf{L}_2$ onto said CCM89 basis vector, a process described in Appendix E.

An $A_V = 0$ SN Ia spectrum from the training sample is not known *a priori*, no is a candidate $A_V \approx 0$ used as a reference to define an A_V zero point for the SN Ia sample. Indeed, it is partly for this reason that zero-mean constraints are enforced for parameter sets c_1 and c_2, constraints that are necessarily retained in the transformed c_a and c_b parameter sets. Is it also for this reason that $c_a = A_V$ or $c_b = A_V/R_V$ cannot be directly equated — A_V and R_V can only be distinguished by making assumptions about their underlying populations.

3.5.1 Forward Modeling

A hierarchical Bayesian total-to-selective attenuation (TSE) model is used to estimate pertinent per-SN dust parameters from the transformed c_a and c_b samples. Figure 32 presents a directed acyclic graph of this model. As mentioned before, intrinsic SN Ia variation may project onto the CCM89 plane, so instead of fitting for per-SN A_V and R_V values directly, A_V and R_V proxies α_V and ρ_V are respectively fit for instead. Later we attempt to identify valid $A_V \approx \alpha_V$ and $R_V \approx \rho_V$ subsamples from forward modeling results.

It is not known *a priori* if intrinsic variation has been erroneously allocated as CCM89 dust-like behavior, so we account for this by modeling α_V as a combination of extrinsic and intrinsic subpopulations. The extrinsic population, corresponding to dust-dominated SNe Ia[7], is assumed drawn from an exponential distribution with rate λ, while the remaining intrinsic population is drawn from a Gaussian distribution centered at $\mu = 0$ with a scale σ. The full α_V population is a convolution of these exponential and Gaussian distributions, or

[7]Technically, this should read dust-like-dominated SNe Ia, since we cannot say with certainty that this subpopulation's constituents are truly dominated by dust-sourced variation.

an exponentially-modified Gaussian (ExMod) distribution:

$$f(\alpha_V|\mu=0,\sigma,\lambda) \sim \frac{\lambda}{2} e^{\left[\frac{\lambda}{2}(\lambda\sigma^2-2\alpha_V)\right]} \mathrm{erfc}\Big(\frac{\lambda\sigma^2-\alpha_V}{\sqrt{2}\sigma}\Big), \tag{36}$$

where $\mathrm{erfc}(u) = 1-\mathrm{erf}(u)$ is the complimentary error function. This distribution is similarly used by Jha et al. 2007, albeit in their case to model maximum $B-V$ instead of A_V [80]. $\mu = 0$ normalizes the α_V ExMod population so that if $\sigma \to 0$ (no intrinsic 'leaking' into the full α_V population), then the α_V population model will reduce to an exponential distribution.

An informative Gaussian hyperprior is placed on λ centered at $\mu_\lambda = 5$, here taken from Thorp et al.2021 [159], with a narrow dispersion of 0.1. A loose Gaussian hyperprior centered at zero with dispersion of 0.5 is used for σ, serving only to inform this parameter's scale. Both λ and σ are bounded to be greater than zero.

The ρ_V population is modeled with a loose Cauchy distribution that allows for negative ρ_V values. This prior serves only to prevent erratic sampling of ρ_V for $\alpha_V \approx 0$ SNe Ia.

Latent parameters sets c_a^* and c_b^* are introduced for the c_a and c_b sets, respectively, where they are related to the α_V and ρ_V sets via the following transformations:

$$c_a^* = \alpha_V - \bar{\alpha}_V \tag{37}$$

$$c_b^* = \beta_V - \bar{\beta}_V \tag{38}$$

$$\beta_V \equiv \alpha_V/\rho_V. \tag{39}$$

$\bar{\alpha}_V$ and $\bar{\beta}_V$ respectively are location parameters for this each transformation 37 and 38. Due to the positive-definite value of dust attenuation, we require parameters $\bar{\alpha}_V$ and $\bar{\beta}_V$ to both be strictly positive. Each c_a (c_b) observation is then drawn from a normal distribution centered at c_a^* (c_b^*) with a covariance matrix C:

$$[c_a, c_b] \sim \mathrm{N}\big([c_a^*, c_b^*], C\big) \tag{40}$$

This covariance matrix is estimated from the sample covariance for all c_a and c_b samples[8].

[8]The constraints $\langle c_1\rangle = \langle c_2\rangle = 0$ reduce the C's rank by two, so including all 73 training sample SNe Ia leads to a singular covariance matrix. Removing any single SN Ia remedies this problem by extracting one each of the c_a and c_b chains. Our TSE model is robust to removed SN Ia choice; we remove SN2011hr to satisfy $\mathrm{Min}(|c_b - 0.05|)$, which implies $\alpha_V \approx \beta_V \approx 0$.

`Stan` is again used to sample an implemented TSE model's posterior, using four samplers performing 2000 samplings each, 1000 of which serve for burn-in. Satisfactory convergence is obtained for all parameters based on $\hat{R}$ scores. Table 3.5.1 summarizes these TSE model priors and parameter bounds.

3.5.2 Results

TSE model components and marginal posterior estimates are provided in the far-left column of Table 3.5.1. The resulting α_V distribution, given in Figure 33, highlights the consequence of removing heavily-reddened SNe Ia from our training sample (Section 3.2). Although their removal prevents overfitting of phase-independent flux variation templates presented in Section 3.4, it diminishes the training sample's capacity to constrain the TSE model's exponential tail of the α_V population distribution. The strong hyperprior on the exponential rate hyperparameter dominates the resulting α_V distribution's positive tail.

The resulting ρ_V sample is notably more complicated than its α_V counterpart. Because of the pole at $\rho_V = 0$, we ignore SNe Ia with unconstrained rho_V values where $\mathrm{SNR}(\rho_V) = \langle\rho_V\rangle/\mathrm{STD}(\rho_V) > 3$. This signal-to-noise cutoff cutoff is not arbitrary there is pronounced clusterings of $\mathrm{SNR}(\rho_V)$ above $\mathrm{SNR}(\rho_V) = 5$ and where $\mathrm{SNR}(\rho_V) \ll 1$. Physically interpretable R_V values approximately range only from $2 \leq R_V \leq 5$, giving a range $\Delta R_V \approx 3$ for the minimum and maximum valid R_V values [28]. Considering the massive uncertainties for most SNe Ia ρ_V values near α_V, we ignore them as unconstrained through the TSE model.

Remaining SNe Ia with constrained ρ_V are split into a nominally extrinsic subsample where $\alpha_V > 0$, and a nominally intrinsic subsample where $\alpha_V < 0$. Ideally, such a definition would mean dusty objects indeed satisfy $A_V = \alpha_V$ as $alpha \rightarrow \mathrm{inf}$. Results summarized in Section 3.4.1 highlight how intrinsic SN Ia chromatic flux variation could 'leak' into extracted dust-like properties, even for aforementioned extrinsic subsample where $\alpha_V > 0$. At best for the extrinsic subsample, $\alpha_V \approx A_V$.

We recover the following mean (median) values for the ρ_V parameter subset: $\rho_V = 2.55$ (2.50) for extrinsic, $\rho_V = 2.25$ (2.31) for intrinsic, and $\rho_V = 2.47$ (2.46) for the full

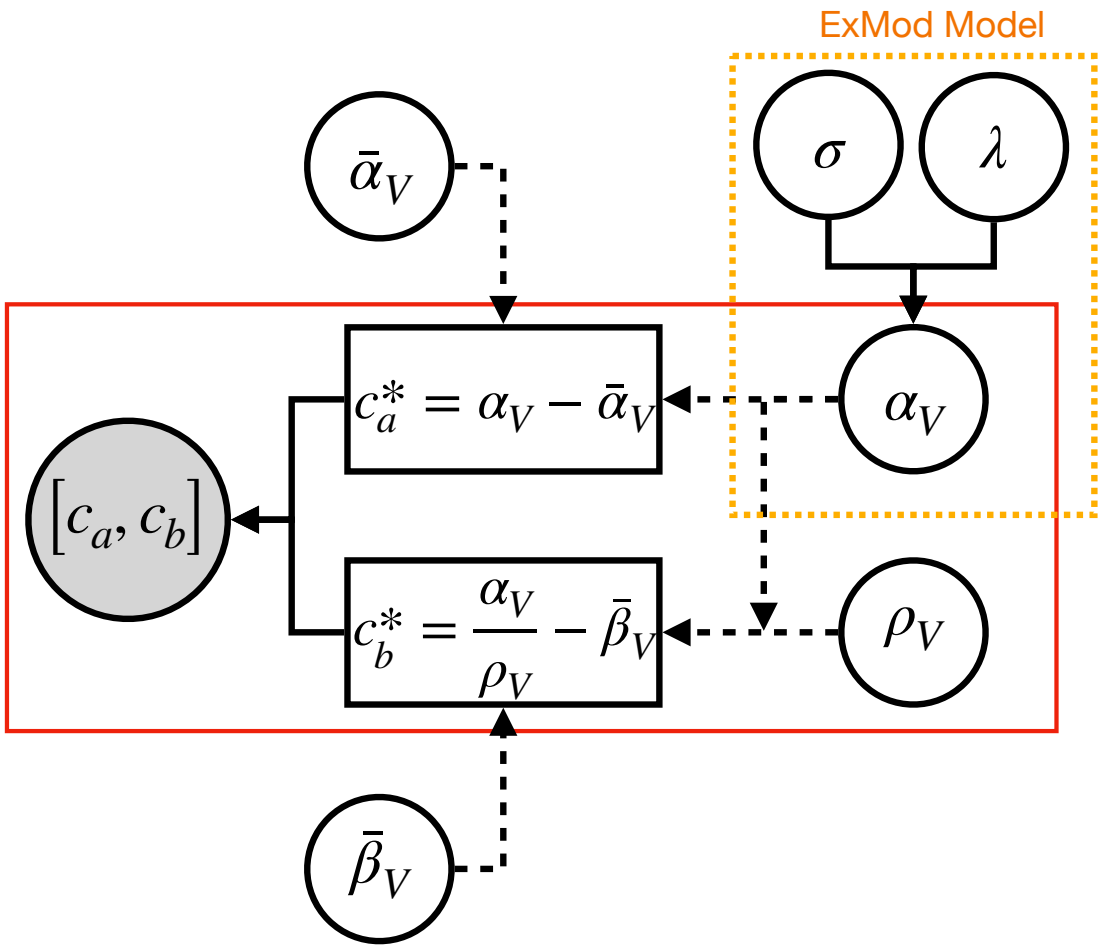

Figure 32: A directed acyclic graph of the total-to-selective attenuation (SE) model. Solid arrows are conditional probabilities; dashed arrows are deterministic relations (transformations or definitions). The red square corresponds to per-SN parameters and data. The dashed orange box contains the α_V population's exponentially modified Gaussian (ExMod) distribution's parameters and hyperparameters. The α_V sample's truncation towards larger α_V is an artifact of cutting heavily reddened SNe Ia from the training sample.

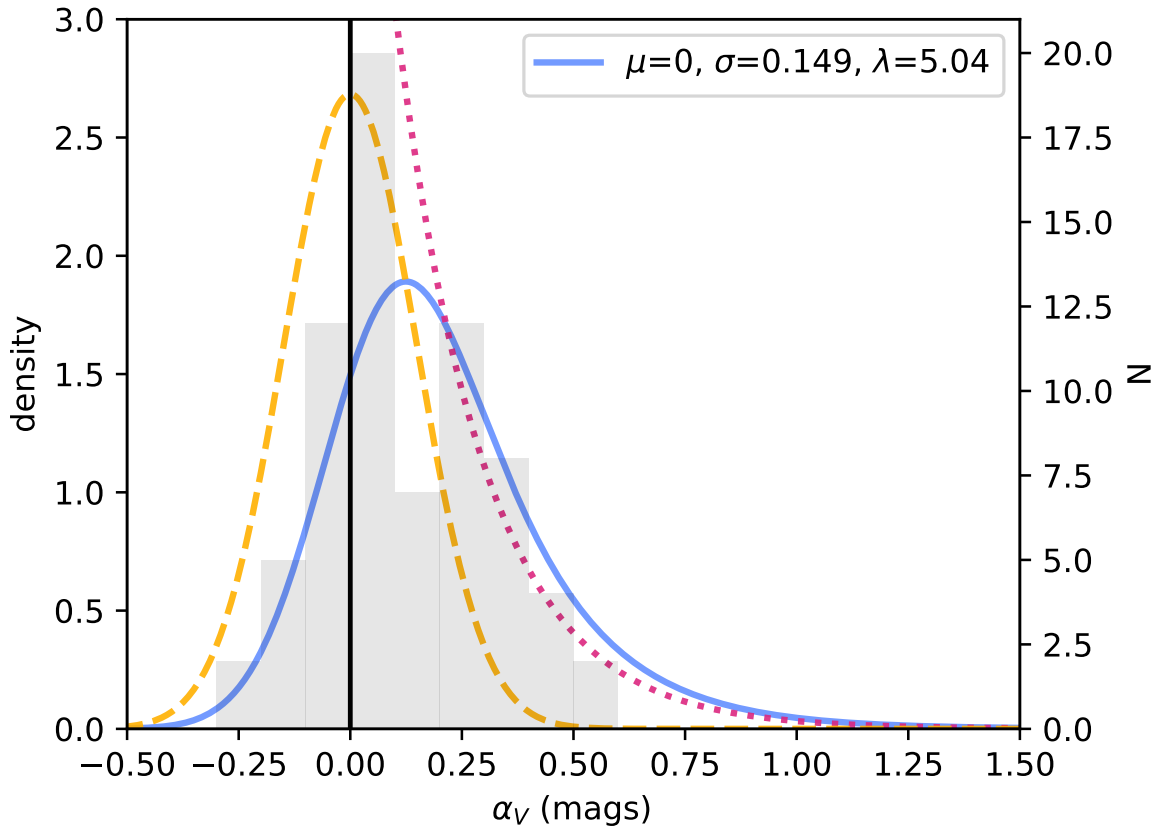

Figure 33: An exponentially modified (ExMod) Gaussian distribution with its three parameters (solid blue) is the convolution of an exponential distribution (dotted magenta) and a Gaussian distribution (dashed orange). The solid gray histogram is the best-fit α_V distribution. Posterior means for free parameters of the α_V population's model ExMod distribution are given in the legend.

lccr

Table 5: Priors/hyperpriors for the TSE model parameters/hyperparameters. Parameter bounds are provided, as global parameter posterior mean and standard deviation (Per-SN parameter posterior values are provided in Table 12).

Param.	Prior	Bounds	Best Fit
α_V	ExMod$(0, 1/K\lambda, \lambda)$	$(-\infty, \infty)$	Table 12
ρ_V	Cauchy$(0, 30)$	$(-\infty, \infty)$	Table 12
λ	N$(5, 0.1)$	$[0, \infty)$	5.04 ± 0.1
σ	N$(0, 0.5)$	$[0, \infty)$	0.15 ± 0.02
$\bar{\alpha}_V$	U$(-\infty, \infty)$	$[0, -\infty)$	0.28 ± 0.03
$\bar{\beta}_V$	U$(-\infty, \infty)$	$[0, -\infty)$	0.10 ± 0.007

constrained sample. The corresponding 68^{th} percentiles are $[2.35, 2.75]$, $[1.98, 2.52]$, and $[2.27, 2.69]$, respectively.

The bifurcation of ρ_V is not a physical effect, but instead an artifact of TSE model's dependence on ρ_V^{-1}. The pole at $\rho = 0$ leads to an asymmetric bias, driving down ρ_V values for $\alpha_V < 0$ and driving up ρ_V values for $\alpha_V > 0$. This model-induced bias has been confirmed with simulation. Note that if this model effect were ignored, one would erroneously measure an average ρ_V bias of $\Delta\rho_V \sim 0.2$ between intrinsic and extrinsic subsamples. Given that such a small effect is well within error for all per-SN ρ_V estimates, and because of the the aforementioned model bifurcation bias, we do not conclude intrinsic or extrinsic α_V subsamples have different ρ_V distributions. Similarly, we do not conclude R_V is systematically lower for intrinsic-dominated SNe Ia relative to extrinsic-dominated SNe Ia.

ρ_V values approach an asymptotic limit equal to the intersection $R_V^{\text{int}=2.4}$ as $|\alpha_V| \to \text{inf}$, the result of a the strong correlation between c_a and c_1' parameter sets. At face value, this asymptotic ρ_V behavior is qualitatively consistent with more reddened SNe Ia preferring lower R_V values [80, 28], but the aforementioned $2\sigma_c$ sample cut (Section 3.2) excludes very highly-reddened SN Ia such as SN 2012cu, for which Huang et al. 2017 estimates $R_V = 2.97$

with an $A_V \approx 3$ [75]; the highest $\alpha_V = A_V$ obtained by the TSE model is only $A_V \approx 0.5$. More importantly, this apparent increase in ρ_V for less dusty (but still 'dust-dominated) SNe Ia far more likely an artifact of the TSE model's bias due to its ρ_V^{-1} dependence than it is evidence of interesting physics.

The aforementioned limitations of the TSE model's implementation and data set compel us to refrain from further interpretation or from making additional conclusions about underlying per-SN dust-like parameters and their distributions. Importantly, these results highlight how a potentially incorrect interpretation can arise from unaccounted model bias or incomplete data.

3.6 Conclusion

In this article, we introduce a new empirical SN Ia linear model that expands beyond similar analyses by introducing a second phase-independent chromatic flux variation template into its architecture. We obtain three model variation components at high signal-to-noise: one phase-dependent chromatic flux variation template $\mathbf{M}_1$ and two phase-independent chromatic flux variation templates $\mathbf{L}_1$ and $\mathbf{L}_2$, which are represented together by the bivector $\mathcal{L}$. The phase-dependent model component recovers stretch and NIR bump variation; it along with the phase-independent templates are consistent with SALT2's two model components.

The model's extended phase-independent architecture captures a nuanced combination of variability. Analysis of the two-dimensional, phase-independent chromatic flux variation plane spanned by $\mathcal{L}$ is done two bases: one that maximizes variation ratios (MVR) between c_1 and c_2 parameter sets, and another that is defined with respect to the CCM89 dust plane. The MVR approach recovers nominally dust-like variation for its dominant component ${\mathbf{L}_1}^{\mathrm{mvr}}$, with a fit $R_V^{\mathrm{MVR}} = 2.18$, while ${\mathbf{L}_2}^{\mathrm{mvr}}$ trace potentially low-resolution intrinsic features. The CCM89 basis yields similar, albeit somewhat more physically-interpretable, results. Specifically, this basis naturally decomposes $\mathcal{L}$ into one template capturing continuum-like wavelength variation (${\mathbf{L}_1}'$) and another capturing rapidly changing chromatic flux variation w.r.t. wavelength (${\mathbf{L}_2}'$). Component ${\mathbf{L}_1}'$ is defined as the intersection of our model's phase-

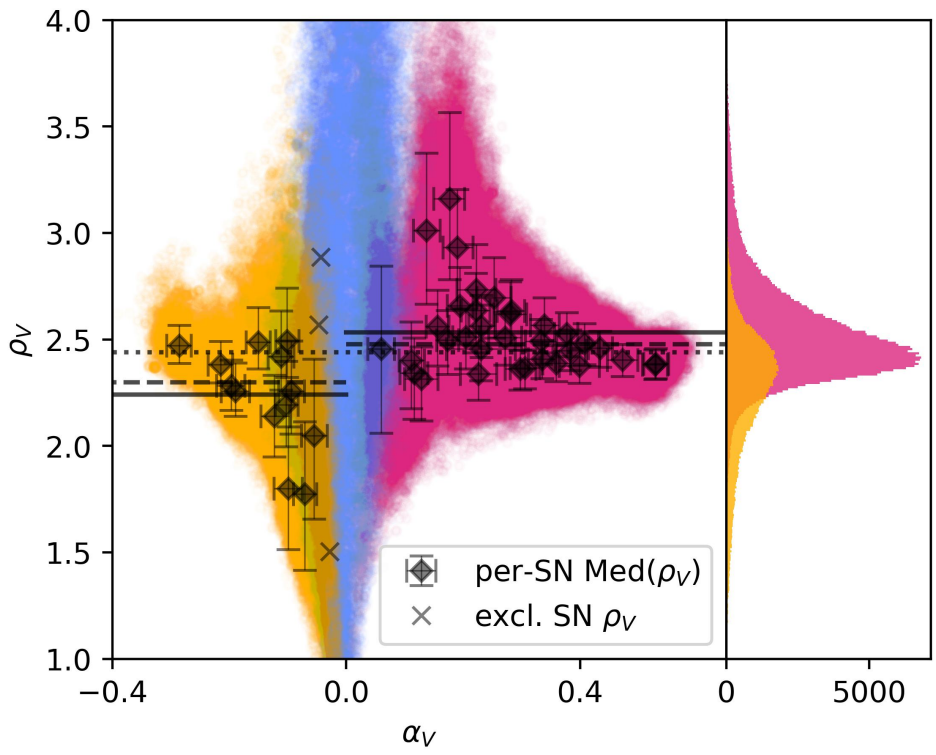

Figure 34: A comparison of fit ρ_V versus α_V from the TSE model. The obtained SN Ia sample is split into unconstrained (gray 'X' points) and constrained (solid black diamonds) ρ_V subsamples, where constrained ρ_V values have $\sigma_{\rho_V} < 3$. The blue shaded region is unconstrained subsample samplings. The constrained subsample is further split into extrinsic ($\alpha_V > 0$, magenta region) and intrinsic ($\alpha_V \leq 0$, yellow region) subsamples. The horizontal solid lines and dashed lines are mean and median ρ_V values, respectively, for both of the extrinsic and intrinsic subsamples. The horizontal dotted line across the entire plot corresponds to $R_V^{\rm int} = 2.4$, being there for reference only. Finally, a right-hand subplot presents extrinsic (magenta) and intrinsic (yellow) ρ_V samplings from the posterior. Note that the bifurcation is an artifact of the TSE model's dependence on ρ_V^{-1}, not due to underlying physics.

independent chromatic flux variation plane with CCM89 dust-like behavior. $\mathbf{L}_2{}'$ is orthogonal to $\mathbf{L}_1{}'$ and can contain phase-averaged intrinsic spectral variation not related to the $\mathbf{M}_1$ template; by construction, it can also contain residual CCM89-like variation.

Despite very different construction methods, $\mathbf{L}_2{}'$ and $\mathbf{L}_2{}^{\mathrm{mvr}}$ are remarkably similar. As derived from the CCM89 basis, the fractional variance of intrinsic spectral variation for the two-dimensional phase-independent chromatic flux variation plane (with 68^{th} percentiles) is $0.13^{-0.4}_{+0.05}$ — dust-like variation dominates $\mathbf{L}_1{}'$ and $\mathbf{L}_2{}'$ in combination, but residual spectroscopic-feature-like variation is not negligible. Despite this model's coarse $n_\lambda = 10$ wavelength bin count, we find that the features in $\mathbf{L}_2{}'$ and $\mathbf{L}_2{}^{\mathrm{mvr}}$ both align with known SN Ia spectral features. Because of intrinsic variation 'leaking' into these two phase-independent components, we make no strong conclusion about the recovered dust attenuation curve from either $\mathbf{L}_1{}'$ or $\mathbf{L}_1{}^{\mathrm{mvr}}$.

Per-SN dust-like properties proxies $A_V \to \alpha_V$ and $R_V \to \rho_V$ are estimated via additional forward modeling after assuming an underlying α_V model, here assumed to be assume an α_V exponentially modified Gaussian population distribution. Prior removal of heavily reddened SNe Ia from the training set limits the data's capacity to constrain the the α_V distribution's exponential tail during forward modeling. Meanwhile, the resulting bifurcation in the ρ_V sample is an artifact of the forward modeling, not evidence for intrinsic-dominated SNe Ia having systematically higher R_V values. Because of limits in data and the uncovered model bias, we draw no conclusions from forward modeling results, instead presenting it to avoid potential pitfalls in future research.

Future work will increase synthetic photometry spectral resolution to enable better identification of spectral features. We plan to directly integrated a two-component dust attenuation model into this future model's architecture to remove the additional forward modeling step. This dust recipe, which will be implemented to avoid a pole at $R_V = 0$, will be complemented by a single phase-independent template that will capture residual spectrum-like, phase-independent variation. These improvements will provide a framework to better study recovered dust-like properties and potentially separate true dust effects from intrinsic variation.

3.7 Acknowledgements

The authors thank Prof. Michael Wood-Vasey for his continuous feedback about model implementation and interpretation of results. This material is based upon work supported by the U.S. Department of Energy, Office of Science, Office of Workforce Development for Teachers and Scientists, Office of Science Graduate Student Research (SCGSR) 2018 S2 program. The SCGSR program is administered by the Oak Ridge Institute for Science and Education for the DOE under contract number DE-SC0014664. This work is also supported in part by the US Department of Energy Office of Science under DE-SC0007914. This research is supported in part by the University of Pittsburgh Center for Research Computing through the resources provided. This work was supported in part by the Director, Office of Science, Office of High Energy Physics of the US Department of Energy under contract No. DE-AC02-05CH11231. Support in France was provided by CNRS/IN2P3, CNRS/INSU, and PNC and French state funds managed by the National Research Agency within the Investissements d'Avenir program under grant reference numbers ANR-10-LABX-0066, ANR-11-IDEX-0004-02 and ANR-11-IDEX-0007. Additional support comes from the European Research Council (ERC) under the European Union's Horizon 2020 research and innovation program (grant agreement No. 759194–USNAC). Support in Germany was provided by DFG through TRR33 "The Dark Universe" and by DLR through grants FKZ 50OR1503 and FKZ 50OR1602. In China support was provided by Tsinghua University 985 grant and NSFC grant No. 11173017. Some results were obtained using resources and support from the National Energy Research Scientific Computing Center, supported by the Director, Office of Science, Office of Advanced Scientific Computing Research of the US Department of Energy under contract No. DE-AC02-05CH11231. We also thank the Gordon & Betty Moore Foundation for their support.

M.R. has received funding from the European Research Council (ERC) under the European Union's Horizon 2020 research and innovation program (grant agreement No. 759194—USNAC).

4.0 Thesis Concluding Remarks

Errors in current precision cosmological parameters measurements for H_0, Ω_m, and Ω_Λ are dominated by systematic errors [152]. Considering the dramatic increase in SN Ia statistics expected from next generation surveys such as LSST, the resulting decrease in random error will significantly help exploring systematics [79]. Naturally, concerted efforts have sought to explore the source and and quantify the effects of all known systematic errors in SN Ia cosmology over the past two decades. This dissertation presents projects exploring two such sources: the host galaxy bias and unaccounted SN Ia intrinsic variability.

The project presented in Chapter 2 asks a straightforward question: do the methods used to observe SN Ia host galaxies, or the techniques used to fit observations for physical host properties, influence the resulting host bias estimate? Although the host sample used in the Chapter 2 analysis is biased towards high-mass galaxies ($\log_{10} > M_\odot$), the resulting host bias measurements with respect to mass and sSFR are consistent regardless of observation method or fitting technique. Step sizes statistically consistent with zero are recovered across all analyses host property estimate samples. These findings are also consistent with past analyses finding a stronger host bias signal for sSFR compared to stellar mass [137] — although sSFR and mass steps are statistically consistent with a zero step, the recovered sSFR steps are 25% larger than the mass steps, despite reduced statistics. Overall, we demonstrate that host bias estimates are largely independent of the aforementioned methodology or techniques.

Chapter 3 introduced a new empirical SN Ia model that extends beyond the *de facto* standard SALT2 with an additional phase-independent chromatic flux variation template. This project's goal was to study SN Ia population variability beyond SALT2 to explore intrinsic variability and to better constrain variation from dust extinction. The new model's two phase-independent flux templates capture multi-modal dust-like behavior, but simultaneously capture phase-independent intrinsic variability as well. This complicates a quantitative interpretation, but the qualitative implications are clear. First, intrinsic SN Ia population variation can be readily captured by empirical models with phase-independent

templates. Whether this additional variability correlates with peak brightness is beyond the project's scope — we do not consider absolute magnitudes. That said, this new model clearly demonstrates that there is sufficient signal-to-noise to extract additional variation templates beyond those in SALT2. Note that our results are not in isolation — there is a growing list of new models similarly extracting additional variational modes beyond SALT2, with many further recovering unaccounted for covariance with peak brightness [108, 147, 101, 20, 157]. Where our model stands out is its unequivocal capture of intrinsic variability within its phase-independent chromatic flux variation templates.

This simultaneous extraction of intrinsic and dust-like variation in our model's phase-independent templates demonstrates the harsh reality of separating intrinsic variation from extrinsic variation using empirical models: it is incredibly difficult to do without having truly dust-free SN Ia observations *a priori*. Regardless, this new model's two phase-independent flux templates enable additional forward modeling beyond that afforded by SALT2 to constrain per-SN dust-like properties. In doing so, we find an interesting bifurcation in the R_V analog distribution with intrinsic-dominated SN Ia having systematically lower R_V analog values. Further investigation determined this is an artifact of the forward modeling itself, erroneously biasing R_V values high for positive A_V values. The bifurcation is not a physical effect. This, and limitations of the training data, lead us to refrain from making conclusions. As such, past concerns regarding low effective SN Ia population R_V relative to the Milky Way average $R_V = 3.1$ remain unchallenged by our analysis.

4.1 Future Directions

The project presented in Chapter 2 should be repeated using a less biased host galaxy sample (specifically, with stellar mass $8 < \log_{10}(M/M_\odot) < 10$) available now or in the near future. The ever-growing PISCO sample [58] is reducing said bias by targeting more lower-mass SN Ia hosts (Galbany private comm.). Alternatively, the AMUSING project, a similar program based in the southern hemisphere (as opposed to PISCO's northern hemisphere coverage) would provides a complementary SN Ia host sample with high resolution IFS with

which to repeat the original project [58, 104]. AMUSING IFS became available after the publication Hand et al. 2022.

Overall, the work summarized in Chapter 3 demonstrates that current observation data sets have sufficient signal-to-noise to extract at least two phase-independent variation templates. This achievement means it may be possible to separate dust extinction effects from intrinsic variation, and eventually improve our understanding of the underlying SN Ia population's intrinsic diversity. Such work will likely require NIR observations, a wavelength regime where dust extinction is negligible and where SNe Ia are standard candles independent of standardization [172, 10, 128].

We stopped short of performing any SN Ia standardization or cosmology with the new empirical SN Ia model presented in Chapter 3. This was partly because redshifts and the photometric zero-point for SNfactory observations remain private, complicating publications of cosmology analyses using said data. Nonetheless, a natural extension of our initial work would be to compare standardization performance with different model versions to quantify improvements from additional templates. For example, it would be interesting to define a simplified model version with architecture akin to a SALT2-like design (one phase-dependent template, one phase-independent template as opposed to one phase-dependent template, two phase-independent templates in the current model). From there, identical training samples could be standardized with these two models and intrinsic dispersion compared. After SNfactory's public release of all prerequisite data, such an analysis should be undertaken.

More care should be afforded when selecting the training sample for empirical SN Ia models. We made no effort to ensure the underlying training set is representative of known SN Ia host galaxy property demographics. A training sample that includes an appropriate collection of SNe Ia from low and high mass galaxies is an important consideration for all empirical models, ours included. Other host properties, such as star formation rate and metallicity, should be considered as well.

Overall, the future utility of SNe Ia in cosmology remains bright. Next-generation empirical SN Ia models and standardization procedures will further decrease standardized intrinsic dispersion, while homogeneous photometric calibration and massive statistics provided by LSST will dramatically reduce related systematics and random error. Such statistics will

also enable SNe Ia to be used not only as standard candles, but also as tracers of peculiar motion from large-scale structure in the local universe, providing yet another cosmological probe. LSST presents its own challenges due to unprecedented data volumes that must be addressed. For example, spectroscopic followup of allSNe Ia discovered by LSST will not be feasible, meaning photometric classification will be necessary to make full use of $\sim 10^5$ high-quality SN Ia light curves [106]. How to classify transients and account for false positives with LSST remains an open area of research and debate, although this is of less concern for high-fidelity SNe Ia light curve observations. With time and a growing data set, LSST's capacity to transform precision cosmology and extend the field's understanding is both widespread and palpable, setting the stage for future surveys and collaborations to succeed as SN Ia cosmology transitions into the realm of big data. Understanding the underlying SN Ia population, as the projects presented in this dissertation focused on, is ever more important during this transition, maximizing the transformative constraining power of LSST type Ia supernova observations in applications to astrophysics and cosmology.

Appendix A Issues with 1 kpc Photometry with GALEX

We initially planned to perform 1 kpc circular aperture photometry around our SNe Ia to compare local UV and Hα SFR estimates, but the large GALEX PSF proved cumbersome to work with. For pulse height bin values above 10 the PSF FWHM averaged at 5.3" or the NUV band and 4.2" for the FUV band [115]. The PSF for GALEX NUV and FUV images was notably asymmetric for many observations. Thus, we excluded local 1 kpc aperture photometry from this project as these apertures' angular sizes were almost always less than average PSF as shown in Figure 35.

To get an idea of flux loss, we assumed a Gaussian profile for the PSF of a centralized point source and calculated the fractional flux loss as 1 kpc apertures decreased in size with increasing redshift. T he left and right teal curves in Figure 35 correspond to point source NUV and FUV flux loss fraction with redshift, respectively. Such calculations were crude approximations of extended structure, but the rapid blurring of UV flux with increasing redshift was dramatically evident — only targets with $z < 0.025$ did not simultaneously suffer from $\sim 50\%$ point source flux loss and $\sim 50\%$ flux contribution from outside the 1 kpc aperture. By $z = 0.05$, you are effectively capturing none of the true flux originating from the 1 kpc aperture, instead almost entirely capturing photons originating from outside your aperture. This approximation for a point source at the center of the aperture ignored the far more complex flux blurring for a resolved host.

Motivating our use of 1 kpc aperture photometry was to better approximate local properties such as SFR and stellar mass. This was partly in response to GALEX's use in past SN Ia host galaxy studies using apertures with radii as large as 4 kpc [136, 84, 140]. To treat UV flux measured from such an aperture as a proxy for local UV SFR is not physical. Indeed, even a 1 kpc radius aperture is nearly four times the radius of the largest molecular clouds. With these issues, it was obvious that GALEX could not be used to reasonably estimate SFR rates smaller than the entire host galaxy for all but the closest targets with $z < 0.01$.

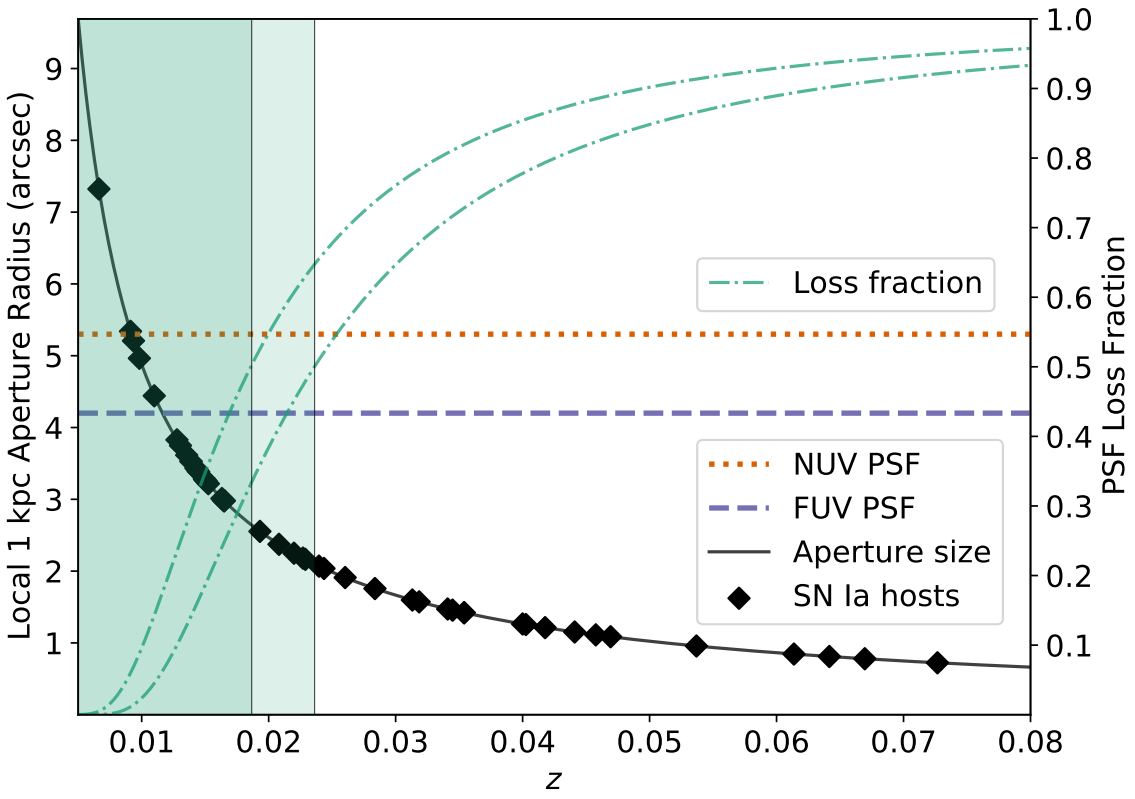

Figure 35: The solid monotonically-decreasing curve is the angular size of 1 kpc circular apertures in arc-seconds as a function of redshift z. Black diamonds correspond to the PISCO SNe Ia with 'usable' 1 kpc GALEX photometry. The horizontal orange dotted line is GALEX NUV average PSF size of 5.3", while the horizontal purple dashed line is GALEX FUV average PSF of 4.2". The monotonically-ascending teal dot-dashed curves approximates a central point source's NUV or FUV flux loss fraction as the 1 kpc aperture size decreases with redshift. Teal shaded regions cover apertures with less than 50% NUV (light+dark) and FUV (dark-only) point source flux loss.

Appendix B Tanh Model

`Stan`'s HMC sampler calculates a numerical Jacobian matrix of model parameters. A true step function such as a Heaviside function has an undefined derivative at the specified step location which prevented model convergence for nearly all data sets we used. Some works form the literature instead used a logistics function with a rapidly transitioning curve [152, 26, 129]. We chose to use a hyperbolic tangent function in place of a logistics function since $\tanh(0) = 0$ and its antisymmetry, although such properties were lost when adding the y-axis offset parameter $\Delta\mu_0$. You can derive a a shifted tanh from a logistics function:

$$\frac{1}{1+e^{-2x}} = \frac{1}{2} + \frac{1}{2}\tanh x. \tag{41}$$

A relatively loose prior was placed on $\Delta\mu$ to prevent the sampler from getting lost at extreme $\Delta\mu$ values:

$$\Delta\mu \sim \mathcal{N}(0, 0.5). \tag{42}$$

The measured host bias step size in the literature is on the order of 0.1 mag or less. Physically-motivated bounds were set to limit the sign of the step based on the host galaxy property being used: $\Delta\mu \in (-\infty, 0]$ and $\Delta\mu \in [0, \infty)$ for mass and sSFR, respectively. The direction of the host bias post-standardization is established, hence bounding the step direction.

For both The mass and sSFR step size parameters $x_s(M_\odot) \doteq M_s$ and $x_s(sSFR) \doteq sSFR_s$ both had a modest prior to deter the sampler from becoming stuck at parameter boundaries:

$$x_s \sim \mathcal{N}(c, 1) \tag{43}$$

where $c = 10$ for M_s and $c = -11$ for $sSFR_s$. Values for c were the midpoints for the boundaries $M_s \in [9, 11]$ and $sSFR_s \in [-12.5, -9.5]$. These bounds were placed to keep the fit step location within the actual mass or sSFR distribution for our subsamples used.

$\Delta\mu_0$ partly captured the systematic offset from zero for Hubble residual systematic offsets. As such, we used the informative prior:

$$\Delta\mu_0 \sim \mathcal{N}\big(\langle\mu - \mu(z)\rangle, \mathrm{SE}[\mu - \mu(z)]\big) \tag{44}$$

where SE$[\mu - \mu(z)]$ is the standard error of the subsample Hubble residual mean $\langle \mu - \mu(z) \rangle$. For our 76 host SN Ia mass subsample $\langle \mu - \mu(z) u \rangle = 0.010$ mag with SE$[\mu - \mu(z)] = 0.003$ mag and for our 66 host mass subsample $\langle \mu - \mu(z) \rangle = 0.012$ mag with SE$[\mu - \mu(z)] = 0.003$ mag. For our 51 host sSFR subsample $\langle \mu - \mu(z) \rangle = 0.042$ mag with SE$[\mu - \mu(z)] = 0.004$ mag and for our 73 host sSFR subsample $\langle \mu - \mu(z) \rangle = 0.031$ mag with SE$[\mu - \mu(z)] = 0.003$ mag.

Fixing the scaling term α and fitting our model with values increasing from $\alpha = 0.01$ up to $\alpha = 0.5$ had no appreciable effect on the sampled posterior. If instead promoted to a free parameter and provided a uniform prior, α trended to large values, resulting in a pseudo-linear regression. Providing an informative exponential prior with $\lambda = 0.3$ to keep α from trending past $\alpha = 1$ resulted in a near-identical posterior to those resulting from simpler models with fixed α. Promoting λ to a free hyperparameter with a inverse-gamma hyperprior again resulted in similar results, with the data only marginally influencing the λ marginal posterior. We opted to leave the scaling term fixed to $\alpha = 0.01$ to provide a smooth step function approximation.

Appendix C Centered Vectors for SN Ia Parameters

A centered vector is a vector $\mathbf{v}$ with the mean of its components being zero. There are numerous ways to structural enforce centered vectors in Stan[1]. For performance reasons we opt for a shifted simplex method.

A simplex $\mathbf{\Delta}$ of dimension n is a vector with the constraint that its components at to one: $\sum_n^i \Delta_i = 1$. Dividing the sum of the simplex by its component count n gives that simplex's mean: $\langle \mathbf{\Delta} \rangle = 1/n$. Therefore, any simplex $\mathbf{\Delta}$ instantiated in `Stan` can be transformed via translation by a factor $-1/n$ into a centered simplex $\mathbf{\Delta}^{\langle \mathbf{0} \rangle}$ with a mean of zero:

$$\Delta_i^{\langle 0 \rangle} = \Delta_i - 1/n. \tag{45}$$

Finally, any centered vector $\mathbf{r}$ with component r_i can be defined as the product of a centered simplex $\mathbf{\Delta}^{\langle \mathbf{0} \rangle}$ and a scaling parameter r:

$$r_i = r\Delta_i^{\langle 0 \rangle} = r\big(\Delta_i - 1/n\big). \tag{46}$$

[1] `https://mc-stan.org/docs/2_18/stan-users-guide/parameterizing-centered-vectors.html`

Appendix D Achromatic Offset and Chromatic Parameter Degeneracy

As described in Leget et al. 2020, for all SNe Ia there is a degeneracy between an achromatic offset parameter (i.e. χ_0) and a phase-independent chromatic variation vector (i.e. $c_1\,\mathbf{L}_1 + c_2\,\mathbf{L}_2$) [101]. With an explicit length-n_λ vector of ones $\mathbf{1}$ to represent achromatic offset behavior in wavelength space, one can define a vector for each SN Ia:

$$\mathbf{v} \equiv \chi_0\mathbf{1} + c_1\,\mathbf{L}_1 + c_2\,\mathbf{L}_2\,. \tag{47}$$

For two arbitrary constants $\{\alpha_1, \alpha_2\}$, the vector $\mathbf{v}$ is invariant under the following transformations:

$$\begin{aligned}
\mathbf{v} &= \chi_0'\mathbf{1} + c_1\,\mathbf{L}_1{}' + c_1\,\mathbf{L}_2{}' \\
\mathbf{L}_1{}' &= \mathbf{L}_1 - \alpha_1\mathbf{1} \\
\mathbf{L}_2{}' &= \mathbf{L}_2 - \alpha_2\mathbf{1} \\
\chi_0' &= \chi_0 + \alpha_1 c_1 + \alpha_2 c_2.
\end{aligned}$$

At each iteration during sampling or in post-processing, this degeneracy can be removed by choosing a fixed $\{\alpha_1, \alpha_2\}$ and then recalculating the components of $\mathbf{v}$. Both c_1 and c_2 parameter sets should be uncorrelated with peak brightness dispersion, so α_1 or α_2 are calculated so that both c_1 and χ_0, and c_2 and χ_0, are uncorrelated. Representing parameter sets as length-$n_{\rm sn}$ vectors $\mathbf{c}_1$, $\mathbf{c}_2$ and $\boldsymbol{\chi}_0'$, and starting from the transformation definition for χ_0' above, we require:

$$\begin{bmatrix}\sigma_{\mathbf{c}_1\boldsymbol{\chi}_0'}\\ \sigma_{\mathbf{c}_2\boldsymbol{\chi}_0'}\end{bmatrix} = \begin{bmatrix}\sigma_{\mathbf{c}_1\boldsymbol{\chi}_0}\\ \sigma_{\mathbf{c}_2\boldsymbol{\chi}_0}\end{bmatrix} + \begin{bmatrix}\alpha_1\sigma_{\mathbf{c}_1\mathbf{c}_1} + \alpha_2\sigma_{\mathbf{c}_1\mathbf{c}_2}\\ \alpha_1\sigma_{\mathbf{c}_2\mathbf{c}_1} + \alpha_2\sigma_{\mathbf{c}_2\mathbf{c}_2}\end{bmatrix} = \begin{bmatrix}\sigma_{\mathbf{c}_1\boldsymbol{\chi}_0}\\ \sigma_{\mathbf{c}_2\boldsymbol{\chi}_0}\end{bmatrix} + \begin{bmatrix}\alpha_1\\ \alpha_2\end{bmatrix}\begin{bmatrix}\sigma_{\mathbf{c}_1\mathbf{c}_1} & \sigma_{\mathbf{c}_1\mathbf{c}_2}\\ \sigma_{\mathbf{c}_2\mathbf{c}_1} & \sigma_{\mathbf{c}_2\mathbf{c}_2}\end{bmatrix} = 0, \tag{48}$$

or after solving for the vector $[\alpha_1, \alpha_2]^T$:

$$\begin{bmatrix}\alpha_1\\ \alpha_2\end{bmatrix} = -\begin{bmatrix}\sigma_{\mathbf{c}_1\boldsymbol{\chi}_0}\\ \sigma_{\mathbf{c}_2\boldsymbol{\chi}_0}\end{bmatrix}\begin{bmatrix}\sigma_{\mathbf{c}_1\mathbf{c}_1} & \sigma_{\mathbf{c}_1\mathbf{c}_2}\\ \sigma_{\mathbf{c}_2\mathbf{c}_1} & \sigma_{\mathbf{c}_2\mathbf{c}_2}\end{bmatrix}^{-1}, \tag{49}$$

where the matrix on the right-hand side of this equation as the precision matrix for our c_1 and c_2 samples.

Both $\mathbf{L}_1{}'$ and $\mathbf{L}_2{}'$ are maintained as unit vectors. This is enforced after each transformation by normalizing $\mathbf{L}_1{}'$ and $\mathbf{L}_2{}'$ by factors $|\,\mathbf{L}_1 - \alpha_1\mathbf{1}|$ and $|\,\mathbf{L}_2 - \alpha_2\mathbf{1}|$. Each parameter set for c_1 and c_2 are multiplied by their respective factors to preserve the products $c_1\,\mathbf{L}_1{}'$ and $c_2\,\mathbf{L}_2{}'$, respectively.

Appendix E Transforming the CCM89 Basis for Forward Modeling

Each SN Ia has its own phase-independent chromatic flux variation vector $\mathbf{c} = c_1' \, \mathbf{L}_1{}' + c_2' \, \mathbf{L}_2{}'$. Because $\mathbf{L}_2{}'$ is a combination of extrinsic and intrinsic chromatic flux variation, this two-component vector $\mathbf{c}$ provides unprecedented information to explore per-SN dust properties. To further explore these properties, $\mathbf{c}$ is transformed from this $\mathbf{L}_1{}'$ and $\mathbf{L}_2{}'$ to a CCM89 basis ($a(\lambda) \rightarrow \mathbf{a}$ and $b(\lambda) \rightarrow \mathbf{b}$): $\mathbf{c} = c_a \mathbf{a} + c_b \mathbf{b} + \mathbf{e}$. Here $\mathbf{e}$ is a perpendicular remainder that satisfies $\mathbf{e} \cdot \mathbf{a} = \mathbf{e} \cdot \mathbf{b} = 0$. Note that $\mathbf{e}$ can be identified as $c_2 \, \mathbf{L}_2{}'(\perp)$. Each $\mathbf{c}$ vector is then projected onto the CCM89 plane spanned by $\mathcal{L}^{\rm ccm}$: $\mathbf{c}^{\rm ccm} = c_1' \, \mathbf{L}_1{}' + c_2' \, \mathbf{L}_2{}'(\parallel) = c_a \mathbf{a} + c_b \mathbf{b}$. The transformation from $\{\mathbf{L}_1{}', \mathbf{L}_2{}'(\parallel)\}$ basis to the $\{\mathbf{a}, \mathbf{b}\}$ $\mathbf{c}^{\rm ccm}$ basis is constructed from following two equations:

$$\mathbf{c}^{\rm ccm} \cdot \mathbf{a} = c_a a^2 + c_b \mathbf{b} \cdot \mathbf{a} \tag{50}$$

$$\mathbf{c}^{\rm ccm} \cdot \mathbf{b} = c_a \mathbf{a} \cdot \mathbf{b} + c_b b^2 \tag{51}$$

from which solutions for c_a and c_b can be found via matrix inversion:

$$\begin{bmatrix} c_a \\ c_b \end{bmatrix} = \frac{1}{a^2 b^2 - (\mathbf{a} \cdot \mathbf{b})^2} \begin{bmatrix} b^2 & -\mathbf{a} \cdot \mathbf{b} \\ -\mathbf{a} \cdot \mathbf{b} & a^2 \end{bmatrix} \begin{bmatrix} \mathbf{c}^{\rm ccm} \cdot \mathbf{a} \\ \mathbf{c}^{\rm ccm} \cdot \mathbf{b} \end{bmatrix}. \tag{52}$$

Although this linear transformation mathematically permits us to equate $c_a \mathbf{a} + c_b \mathbf{b} = A_V(\mathbf{a} + \mathbf{b}/R_V)$, c_a and c_b cannot physically be identified as A_V nor $B_V = A_V/R_V$, respectively. To associate c_a and c_b with dust parameters A_V and R_V requires knowing the c_a and c_b values of a dust-free SN Ia, information for which we are lacking. Indeed, it is enforcing c_1 and c_2 parameter sets to be mean-zero that defines a dust-free SN Ia in our full model (Section **??**). Note that because our c_1' and c_2' parameter sets have a mean of zero, so do the transformed c_a and c_b parameter sets.

Appendix F Brief Introduction to Geometric Algebra

Geometric algebra provides a robust, elegant, and easy to interpret framework to perform geometric operations. It extends linear algebra by introducing the geometric product, a combination of the inner product and outer product. Although we directly calculate intersections, rotations, and projections/rejections using geometric algebra, these operations can be performed using linear algebra instead.

We will assume through that our vector space finite-dimensional and that each vector's elements is real-valued (specifically, we assume our vector space's field are the real numbers $\mathbb{R}$). We will also utilize a canonical basis representation of our vector, such a Cartesian basis for $\mathbb{R}^n$, $\{\hat{\mathbf{e}}_1, \hat{\mathbf{e}}_2, \ldots, \hat{\mathbf{e}}_n\}$. All geometric algebra calculations are implemented with the clifford package [139]. For a more detailed introduction, see Hitzer 2013 [71].

Geometric algebra extends elementary vector algebra using the geometric product. The geometric product of two vectors $\{\mathbf{x}, \mathbf{y}\} \in \mathbb{R}^n$ combines a symmetric inner (or dot) product with an antisymmetric outer (or wedge) product.

$$\mathbf{xy} = \mathbf{x} \cdot \mathbf{y} + \mathbf{x} \wedge \mathbf{y} = \sum_{i=1}^{n} x_i y_i + \sum_{i=1}^{n} \sum_{j>i}^{n} (x_i y_j - y_i x_j)\, \hat{\mathbf{e}}_i \wedge \hat{\mathbf{e}}_j \tag{53}$$

$$= |\mathbf{x}||\mathbf{y}| \cos\theta_{xy} + |\mathbf{x}||\mathbf{y}| \sin\theta_{xy} \hat{\mathbf{x}} \wedge \hat{\mathbf{y}}. \tag{54}$$

In the last step we define the angle θ_{xy} as the angle between the two vectors $\mathbf{x}$ and $\mathbf{y}$. The inner product maps our vectors to our underlying field $\mathbb{R}$, yielding a scalar and is a symmetric operation: $\mathbf{x} \cdot \mathbf{y} = \mathbf{y} \cdot \mathbf{x}$. The wedge product of two vectors $\mathbf{x}$ and $\mathbf{y}$ is an antisymmetric operation: $\hat{\mathbf{e}}_i \wedge \hat{\mathbf{e}}_j = -\,\hat{\mathbf{e}}_j \wedge \hat{\mathbf{e}}_i = 0\,(\text{if } i = j)$. The object output by the wedge product of two vectors is called a bivector and is an oriented plane element.

It is common in geometric algebra to refer to a scalar as the 0-blade and a bivector as the 2-blade. Similarly, vectors such as $\mathbf{x}$ and $\mathbf{y}$ are referred to as 1-blades. In general, a k-blade is a k-dimensional object with can be generated by k-wedge (or k-geometric) products of k independent vectors. These k-vectors are themselves oriented k-dimensional subspace

elements. The produced object $\mathbf{xy}$ is a linear combination of two grades of k-blades (a 0-vector and a 2-vector, specifically) that we call a multivector. In general, a multivector is a linear combination k-blades. Also, each multivector $\mathbf{M}$ has an inverse such that via the goemtric product $\mathbf{M}\mathbf{M}^{-1} = 1$. Furthermore, any multivector defined as a product of vectors $\mathbf{M} = \mathbf{a}_1\mathbf{a}_2...\mathbf{a}_m$ has a corresponding multivector called its reverse: $\mathbf{M}^\dagger = \mathbf{a}_m\mathbf{a}_{m-1}...\mathbf{a}_1$.

We can derive a canonical basis of our geometric algebra using the geometric product on our starting vector space's canonical basis as a generating set. Because canonical basis is orthogonal, the geometric product of canonical basis components reduces to a wedge product for $i \neq j$: $\hat{\mathbf{e}}_i\,\hat{\mathbf{e}}_j = 0 + \hat{\mathbf{e}}_i \wedge \hat{\mathbf{e}}_j$, or to an inner product for $i = j$: $\hat{\mathbf{e}}_i\,\hat{\mathbf{e}}_i = \hat{\mathbf{e}}_i \cdot \hat{\mathbf{e}}_i + 0$. As an example, for a vector space of dimension $n = 3$, the generated geometric algebra canonical basis has 8 basis elements: $\{1; \hat{\mathbf{e}}_1, \hat{\mathbf{e}}_2, \hat{\mathbf{e}}_3; \hat{\mathbf{e}}_1\,\hat{\mathbf{e}}_2, \hat{\mathbf{e}}_1\,\hat{\mathbf{e}}_3, \hat{\mathbf{e}}_2\,\hat{\mathbf{e}}_3; \hat{\mathbf{e}}_1\,\hat{\mathbf{e}}_2\,\hat{\mathbf{e}}_3\}$. This set of basis elements naturally fall into grades of equal subspace dimension: one scalar element, three one-dimensional basis vectors (the starting vector space's canonical vector basis), three two-dimensional basis bivectors, and one three-dimensional basis trivector. The geometric algebra over $\mathbb{R}^3$ basis elements therefore prescribes corresponding sets of orthogonal bases for all possible subspaces that exist within $\mathbb{R}^3$. The generation of basis elements generalizes naturally for any finite dimension vector space $\mathbb{R}^n$, with the resulting geometric algebra $\mathbb{G}^n$ having 2^n generated basis components. The respective subspaces, or grades, of the geometric algebra (i.e. the bivector or grade-2 components) have dimensionality $\binom{n}{k}$, where k is the grade of interest. Note that the last element in this geometric algebra basis is called the pseudoscalar i, since $ii = -1$ for any dimension n in a way analogous with an imaginary number. Finally, we can decompose any multivector $\mathbf{M}$ using a grade projection operation:

$$\mathbf{M} = \sum_{k=1}^{n} \langle \mathbf{M} \rangle_k, \tag{55}$$

where the k-grade projection operator $\langle \mathbf{M} \rangle_k$ returns the k-blade component of $\mathbf{M}$.

F.1 Reflections and Rotations

Consider two vectors $\mathbf{r}, \mathbf{x} \in \mathbb{R}^n$. Say we reflect $\mathbf{r}$ along $\mathbf{x}$. This operation can be interpreted as negating the component of $\mathbf{r}$ perpendicular to $\mathbf{x}$. The geometric product can be used to decompose $\mathbf{r}$ into its parallel and perpendicular components relative to the unit vector $\hat{\mathbf{x}}$:

$$\mathbf{r}\hat{\mathbf{x}} = \mathbf{r} \cdot \hat{\mathbf{x}} + \mathbf{r} \wedge \hat{\mathbf{x}} \tag{56}$$

$$\mathbf{r} = (\mathbf{r} \cdot \hat{\mathbf{x}})\hat{\mathbf{x}}^{-1} + (\mathbf{r} \wedge \hat{\mathbf{x}})\hat{\mathbf{x}}^{-1}. \tag{57}$$

The component $(\mathbf{r} \cdot \hat{\mathbf{x}})\hat{\mathbf{x}}^{-1}$ is proportional to the projection of $\mathbf{r}$ onto $\mathbf{x}$, while the component $(\mathbf{r} \wedge \hat{\mathbf{x}})\hat{\mathbf{x}}^{-1}$ is the perpendicular (or rejected) remainder. From this decomposition we can define a reflection $\mathbf{r}'$ of $\mathbf{r}$ along $\mathbf{x}$:

$$\begin{aligned}
\mathbf{r}' &= -(\mathbf{r} \cdot \hat{\mathbf{x}})\hat{\mathbf{x}}^{-1} + (\mathbf{r} \wedge \hat{\mathbf{x}})\hat{\mathbf{x}}^{-1} \\
&= -(\hat{\mathbf{x}} \cdot \mathbf{r})\hat{\mathbf{x}}^{-1} - (\hat{\mathbf{x}} \wedge \mathbf{r})\hat{\mathbf{x}}^{-1} \\
&= -(\hat{\mathbf{x}} \cdot \mathbf{r} + \hat{\mathbf{x}} \wedge \mathbf{r})\hat{\mathbf{x}}^{-1} \\
&= -\hat{\mathbf{x}}\mathbf{r}\hat{\mathbf{x}}^{-1} \\
&= -\hat{\mathbf{x}}\mathbf{r}\hat{\mathbf{x}}.
\end{aligned}$$

Here we exploit a unit vector's geometric algebra inverse being itself ($\hat{\mathbf{x}}\hat{\mathbf{x}} = \hat{\mathbf{x}} \cdot \hat{\mathbf{x}} = 1$).

Any rotation can be decomposed into two reflections, with the rotational plane being spanned by two vectors we reflect against. Picking another vector $\mathbf{y} \in \mathbb{R}^n$, we write the rotation $\mathbf{r}'$ of $\mathbf{r}$ in the plane corresponding to grade-2 (or bivector component) of the multivector $\mathbf{R} = \hat{\mathbf{x}}\hat{\mathbf{y}}$ as:

$$\begin{aligned}
\mathbf{r}' &= \hat{\mathbf{y}}\hat{\mathbf{x}}\mathbf{r}\hat{\mathbf{x}}\hat{\mathbf{y}} \\
&= \mathbf{R}^\dagger \mathbf{r} \mathbf{R}.
\end{aligned}$$

This bilinear operation on $\mathbf{r}$ by the unit 2-vector $\mathbf{R}$ is indeed a rotation. To see this, let us insert a more illuminating form of $\mathbf{R}$:

$$\mathbf{r}' = \Big(\cos\frac{\theta_{xy}}{2} - \sin\frac{\theta_{xy}}{2}\hat{\mathbf{x}} \wedge \hat{\mathbf{y}}\Big)\mathbf{r}\Big(\cos\frac{\theta_{xy}}{2} + \sin\frac{\theta_{xy}}{2}\hat{\mathbf{x}} \wedge \hat{\mathbf{y}}\Big). \tag{58}$$

To interpret this result, consider first the geometric algebra of vector space $\mathbb{R}^2$ with its four generated basis elements $\{1; \hat{\mathbf{e}}_1, \hat{\mathbf{e}}_2; \hat{\mathbf{e}}_1\,\hat{\mathbf{e}}_2\}$. In two dimensions any bivector $\hat{\mathbf{x}} \wedge \hat{\mathbf{y}}$ is proportional our unit pseudoscalar $\hat{\mathbf{e}}_1\,\hat{\mathbf{e}}_2$, itself which behaves identically to the imaginary number (similarly denoted as i). Substituting i for $\hat{\mathbf{x}} \wedge \hat{\mathbf{y}} = \hat{\mathbf{e}}_1\,\hat{\mathbf{e}}_2$ into Equation 58, we recover the canonical form of a rotation by an angle θ in two dimensions:

$$\mathbf{r}' = e^{-i\theta/2}\mathbf{r}e^{i\theta/2}. \tag{59}$$

For higher dimensions we can similarly treat the bivector $\hat{\mathbf{x}} \wedge \hat{\mathbf{y}}$ as being the imaginary number of the two-dimensional subspace spanned by said bivector. Therefore, any rotation of a vector $\mathbf{r}$ by an angle θ within a plane spanned by the unit bivector$\hat{\mathcal{A}} = \hat{\mathbf{x}} \wedge \hat{\mathbf{y}}$ can be written:

$$\mathbf{r}' = e^{-\hat{\mathcal{A}}\theta/2}\mathbf{r}e^{\hat{\mathcal{A}}\theta/2} = \mathbf{R}^\dagger\mathbf{r}\mathbf{R}. \tag{60}$$

This unit bivector is interpreted as a generator of rotation within the plane spanned by $\hat{\mathcal{A}}$; the multivector $\mathbf{R}$ (which has scalar and bivector components) is called a rotor.

F.2 Projection and Rejection of Vectors onto a Bivector

Consider a vector $\mathbf{v}$ and a bivector $\mathcal{A}$. Similar to Subsection F.1, we can decompose a $\mathbf{v}$ into components parallel and perpendicular to the plane spanned by $\mathcal{A}$:

$$\mathbf{v}\mathcal{A} = \mathbf{v} \cdot \mathcal{A} + \mathbf{v} \wedge \mathcal{A} \tag{61}$$

$$\mathbf{v} = (\mathbf{v} \cdot \mathcal{A})\mathcal{A}^{-1} + (\mathbf{v} \wedge \mathcal{A})\mathcal{A}^{-1}. \tag{62}$$

If the wedge product of any vector with a $\mathcal{A}$ is zero, then said vector must exist within the plane spanned by that $\mathcal{A}$. Alternatively, any vector with no projection onto $\mathcal{A}$ requires said vector be perpendicular to $\mathcal{A}$. Just as in Subsection F.1, we therefore identify this decomposition into parallel (projected) and perpendicular (rejected) components relative to a plane spanned by $\mathcal{A}$:

$$\mathbf{v}^{\parallel} = (\mathbf{v} \cdot \mathcal{A})\mathcal{A}^{-1} \tag{63}$$

$$\mathbf{v}^{\perp} = (\mathbf{v} \wedge \mathcal{A})\mathcal{A}^{-1}. \tag{64}$$

F.3 Intersection of Planes

This section describes the formalism readily displayed in Figure 20. It is the most complicated of the operations we implement using geometric algebra and is included for completeness, despite its complexity. As with other operations, it is possible to calculate this intersection using conventional linear algebra techniques. Indeed, we confirmed this geometric algebra implementation with such a conventional approach.

Intuitively, a bivector is to a plane what a vector is to a line. Just as one can find the intersection of two lines using their representing vectors, one also can find the intersection of two planes using their representing bivectors.

Consider two bivectors $\mathcal{A}$ and $\mathcal{B}$, each of which represent two different planes. If these two planes intersect (which we will assume they do), then there are at most two linearly independent vectors $\mathbf{a}$ and $\mathbf{b}$ that exist each of the respective planes spanned by $\mathcal{A}$ and $\mathcal{B}$, but that do not reside along these two planes' intersection. Furthermore, the intersection of $\mathcal{A}$ and $\mathcal{B}$ is a well-defined, one-dimensional subspace necessarily spanned by some vector, a vector that we will call $\mathbf{c}$. This means that $\mathcal{A} = \mathbf{a} \wedge \mathbf{a}$ and $\mathcal{B} = \mathbf{c} \wedge \mathbf{b}$, and taken together, these two bivectors span a three-dimensional subspace (because they share the intersection subspace spanned by $\mathbf{c}$). This volume and its orientation can be represented using a trivector $\mathbf{a} \wedge \mathbf{b} \wedge \mathbf{c}$. Normalizing this then trivector gives us the intersection's unit volume element:

$$i = \frac{\mathbf{a} \wedge \mathcal{B}}{|\mathbf{a} \wedge \mathcal{B}|} = \frac{\mathbf{b} \wedge \mathcal{A}}{|\mathbf{b} \wedge \mathcal{A}|}. \tag{65}$$

We want a formal expression for $\mathbf{c}$ from the starting bivectors $\mathcal{A}$ and $\mathcal{B}$, though. To get this, we first find a bivector whose plane is simultaneously perpendicular to both $\mathcal{A}$ and $\mathbf{B}$, which can be done by taking the grade projection of the geometric product $\mathcal{A}\mathcal{B}$ to its bivector component: $\langle \mathcal{A}\mathbf{B} \rangle_2$. The vector perpendicular to this bivector $\langle \mathcal{A}\mathbf{B} \rangle_2$, but which still exists within the volume spanned by the intersection unit volume i, is the intersection vector $\mathbf{c}$ we are looking for. It turns out that taking the geometric product of i with $\langle \mathcal{A}\mathbf{B} \rangle_2$ performs exactly this operation:

$$\mathbf{c} = i \langle \mathcal{A}\mathcal{B} \rangle_2. \tag{66}$$

Once way to think about this is that the unit volume i rotates the bivector $\langle \mathcal{A}\mathbf{B} \rangle_2$ by $\pi/2$ and projects out the vector $\mathbf{c}$ perpendicular to the bivector $\langle \mathcal{A}\mathbf{B} \rangle_2$.

Table 6: Global mass in $\log_{10}(M/M_{\odot})$. FAST++, ZPEG masses limited to SDSS or SDSS+GALEX coverage (labeled 'GALEX Mass'). The first 25 entries are shown here. A full version of this table is available online.

Galaxy	STARLIGHT Mass	Fast++ Mass	ZPEG Mass	GALEX Mass
2MASSJ00164451	10.094	10.200	10.765	–
2MASSJ00235669	9.653	9.790	10.192	9.770
2MASSJ23243021	10.219	9.910	10.452	9.890
2MASXJ22532475	9.891	9.960	10.348	10.300
2MASXJ00234829	10.539	9.850	10.829	9.860
2MASXJ01144386	10.434	10.300	10.723	10.430
2MASXJ01403375	10.640	10.760	11.262	11.000
2MASXJ02305208	10.013	9.660	10.787	10.300
2MASXJ04424248	11.023	–	–	–
2MASXJ07192718	9.939	–	–	–
2MASXJ08374557	9.387	9.710	9.436	9.980
2MASXJ09591230	9.826	–	–	–
2MASXJ10525434	10.147	9.780	10.787	–
2MASXJ12095669	10.285	10.410	10.816	–
2MASXJ12385810	10.638	9.900	10.844	9.840
2MASXJ15024995	9.311	9.490	9.938	–
2MASXJ15393305	10.996	11.150	11.530	11.090
2MASXJ15570268	9.839	10.080	10.082	10.080
2MASXJ16065563	10.163	10.050	10.500	10.240
2MASXJ16152860	9.807	9.950	10.207	10.030
2MASXJ16301506	10.725	10.450	10.910	10.390
2MASXJ17100856	10.202	10.170	10.605	10.160
2MASXJ18242915	9.475	–	–	–
2MASXJ21352164	11.302	11.160	11.360	11.200
2MASXJ23024668	10.675	10.640	11.161	10.650

Table 7: Global SFR in $M_{\odot}\mathrm{yr}^{-1}$.

Galaxy	FAST++ SFR	Hα SFR	NUV SFR	FUV SFR	ZPEG SFR
2MASXJ22532475	0.692	0.395	1.253	0.577	0.000
2MASXJ00234829	141.254	3.910	20.854	10.341	124.738
2MASXJ01144386	3.388	1.692	2.822	1.638	13.274
2MASXJ08374557	10.715	1.649	3.722	1.596	16.866
2MASXJ15570268	0.741	0.010	0.367	0.211	10.864
2MASXJ16152860	0.724	0.108	0.981	0.538	0.551
2MASXJ16301506	27.542	1.632	3.108	2.095	19.861
2MASXJ17100856	0.020	0.034	0.268	0.245	1.782
2MASXJ23024668	0.000	0.263	0.105	0.075	4.634
ARP143	4.898	1.482	5.137	3.094	5.383
ARP70	26.303	1.215	4.171	2.908	7.194
CGCG004-035	3.890	0.542	2.596	1.455	5.012
CGCG008-023	1.318	2.253	6.753	3.583	1.315
CGCG047-117	64.565	3.356	5.592	3.931	14.454
CGCG107-031	0.380	0.029	0.415	0.352	0.000
CGCG207-042	3.467	1.071	3.151	2.100	40.832
CGCG308-009	0.209	0.023	0.185	0.144	0.000
CGCG476117	51.286	1.193	2.242	1.362	8.433
FGC175A	0.155	0.260	1.076	1.318	1.239
GALEXASCJ012052	1.202	0.176	1.806	1.020	1.622
GALEXASCJ234457	30.903	0.495	3.326	2.141	26.363
IC0208	2.291	0.245	1.071	0.623	6.180
IC0701	11.749	2.350	2.752	1.749	8.610
IC0758	4.677	0.044	0.160	0.116	6.353
IC1481	3.020	1.411	6.567	2.494	19.588

Table 8: In-house global photometry for SDSS and GALEX, part 1. Only GALEX photometry with SDSS coverage was measured. Given as AB magnitudes; -99 marks negative flux. The first 25 entries are shown here. A full version of this table is available online.

Galaxy	m_u	σ_{m_u}	m_g	σ_{m_g}	m_r	σ_{m_r}
2MASSJ00164451	19.522	0.258	17.730	0.020	16.919	0.014
2MASSJ00235669	17.894	0.054	16.737	0.005	16.492	0.007
2MASSJ23243021	19.010	0.118	17.363	0.009	16.539	0.006
2MASXJ00234829	16.298	0.046	15.597	0.006	15.074	0.007
2MASXJ01144386	16.983	0.071	15.902	0.008	15.286	0.007
2MASXJ01403375	17.235	0.092	15.842	0.008	15.147	0.007
2MASXJ02305208	17.268	0.066	16.119	0.007	15.248	0.004
2MASXJ08374557	17.472	0.077	16.399	0.011	15.936	0.011
2MASXJ10525434	17.080	0.053	16.179	0.007	15.638	0.007
2MASXJ11123493	17.033	0.052	16.064	0.007	15.447	0.006
2MASXJ11500404	17.178	0.039	15.635	0.005	14.875	0.003
2MASXJ12095669	17.249	0.048	15.797	0.005	14.970	0.004
2MASXJ12385810	17.352	0.079	16.419	0.011	15.782	0.010
2MASXJ15024995	17.948	0.092	16.413	0.012	15.845	0.009
2MASXJ15393305	16.579	0.054	15.286	0.005	14.449	0.004
2MASXJ15570268	17.752	0.083	16.374	0.008	15.580	0.006
2MASXJ16065563	16.311	0.056	15.230	0.008	14.891	0.008
2MASXJ16152860	18.085	0.134	16.823	0.012	16.104	0.010
2MASXJ16301506	16.960	0.064	15.789	0.008	15.144	0.006
2MASXJ17100856	17.798	0.076	16.191	0.006	15.471	0.005
2MASXJ21352164	17.328	0.130	15.943	0.009	15.062	0.006
2MASXJ22532475	17.066	0.077	15.499	0.005	14.814	0.005
2MASXJ23024668	17.992	0.104	16.219	0.006	15.345	0.004
ARP143	13.572	0.007	12.328	0.001	11.720	0.001
ARP70	15.566	0.047	14.259	0.004	13.531	0.003

Table 9: In-house global photometry for SDSS and GALEX, part 2. Only GALEX photometry with SDSS coverage was measured. Given as AB magnitudes; -99 marks negative flux. The first 25 entries are shown here. A full version of this table is available online.

Galaxy	m_i	σ_{m_i}	m_z	σ_{m_z}	m_{NUV}	$\sigma_{m_{NUV}}$	m_{FUV}	$\sigma_{m_{FUV}}$
2MASSJ00164451	16.485	0.015	16.128	0.050	-99.000	-99.000	-99.000	-99.000
2MASSJ00235669	16.280	0.009	16.109	0.028	18.676	0.048	19.239	0.106
2MASSJ23243021	16.119	0.007	15.930	0.028	22.980	0.398	23.196	0.514
2MASXJ00234829	14.675	0.008	14.783	0.030	17.661	0.034	18.158	0.064
2MASXJ01144386	14.940	0.008	14.734	0.034	18.174	0.056	18.523	0.092
2MASXJ01403375	14.735	0.007	14.384	0.018	18.693	0.090	18.925	0.135
2MASXJ02305208	14.721	0.004	14.591	0.012	19.920	0.489	-99.000	-99.000
2MASXJ08374557	15.509	0.011	15.342	0.033	18.813	0.097	19.552	0.212
2MASXJ10525434	15.341	0.008	15.151	0.034	-99.000	-99.000	-99.000	-99.000
2MASXJ11123493	15.068	0.007	14.688	0.025	18.422	0.050	19.284	0.163
2MASXJ11500404	14.513	0.004	14.262	0.009	20.588	0.222	-99.000	-99.000
2MASXJ12095669	14.565	0.004	14.281	0.012	-99.000	-99.000	-99.000	-99.000
2MASXJ12385810	15.459	0.011	15.080	0.028	19.298	0.116	19.734	0.248
2MASXJ15024995	15.433	0.010	15.326	0.030	-99.000	-99.000	-99.000	-99.000
2MASXJ15393305	14.054	0.004	13.822	0.011	18.930	0.101	22.090	1.304
2MASXJ15570268	15.280	0.007	14.869	0.025	20.112	0.295	20.519	0.546
2MASXJ16065563	14.522	0.008	14.502	0.036	17.177	0.037	17.599	0.107
2MASXJ16152860	15.700	0.012	15.442	0.032	20.148	0.189	21.911	1.727
2MASXJ16301506	14.761	0.006	14.468	0.022	18.730	0.105	19.668	0.294
2MASXJ17100856	15.108	0.005	14.809	0.019	21.724	0.668	20.789	0.429
2MASXJ21352164	14.499	0.005	14.250	0.015	-99.000	-99.000	20.613	1.575
2MASXJ22532475	14.483	0.005	14.212	0.020	18.084	0.059	19.099	0.163
2MASXJ23024668	14.902	0.004	14.561	0.010	21.219	0.097	22.513	0.326
ARP143	11.417	0.001	11.179	0.004	14.712	0.010	15.149	0.019
ARP70	13.068	0.003	12.797	0.010	17.264	0.033	18.020	0.075

Table 10: In-house global photometry 2MASS. Only 2MASS photometry with SDSS coverage was measured. Given as AB magnitudes. -99 marks negative flux. The first 25 entries are shown here. A full version of this table is available online.

Galaxy	m_H	σ_{m_H}	m_J	σ_{m_J}	m_K	σ_{m_K}
2MASSJ00164451	15.485	0.397	16.047	0.451	16.439	1.304
2MASSJ00235669	15.755	0.479	16.203	0.475	18.210	5.562
2MASSJ23243021	15.358	0.324	15.465	0.268	15.180	0.404
2MASXJ00234829	13.329	0.171	14.607	0.326	14.105	0.417
2MASXJ01144386	-99.000	-99.000	14.672	0.377	14.144	0.455
2MASXJ01403375	13.856	0.208	14.157	0.182	13.793	0.242
2MASXJ02305208	13.160	0.100	13.805	0.104	13.574	0.134
2MASXJ08374557	14.847	0.462	15.332	0.506	14.678	0.456
2MASXJ10525434	-99.000	-99.000	15.940	0.948	-99.000	-99.000
2MASXJ11123493	14.657	0.504	14.719	0.399	14.487	0.567
2MASXJ11500404	12.939	0.120	13.699	0.097	13.465	0.150
2MASXJ12095669	14.019	0.268	14.034	0.156	14.034	0.250
2MASXJ12385810	16.121	2.423	15.263	0.731	14.925	0.922
2MASXJ15024995	14.778	0.570	15.113	0.463	14.607	0.453
2MASXJ15393305	12.818	0.127	13.347	0.129	13.106	0.165
2MASXJ15570268	14.630	0.406	14.387	0.203	14.981	0.547
2MASXJ16065563	13.338	0.244	13.982	0.316	13.817	0.426
2MASXJ16152860	13.842	0.192	14.678	0.251	14.398	0.321
2MASXJ16301506	13.701	0.179	13.994	0.158	13.769	0.232
2MASXJ17100856	14.163	0.183	14.317	0.139	13.955	0.189
2MASXJ21352164	13.649	0.231	13.797	0.180	14.021	0.288
2MASXJ22532475	14.868	0.777	13.796	0.187	14.147	0.419
2MASXJ23024668	13.672	0.143	14.053	0.097	14.050	0.158
ARP143	11.349	0.082	10.893	0.035	11.070	0.066
ARP70	12.872	0.270	12.415	0.098	12.783	0.194

Table 11: Model per-SN parameter median values with 68^{th} percentile upper and lower values or standard deviation for our first 10 SNe Ia. SALT2 x_1 and c included for reference. Per-SN parameters $\chi_0 - \langle\chi_0\rangle$, s_1, c_1, and c_2 have been transformed to magnitudes. A full table of all training SNe Ia is available upon request.

SN	$\chi_0 - \langle\chi_0\rangle$	s_1	c_1	c_2	t_0
SNF20060512-001	-0.04 ± 0.03	-0.02 ± 0.01	-0.33 ± 0.09	0.12 ± 0.03	53882.5 ± 0.12
SNF20060526-003	-0.06 ± 0.03	-0.07 ± 0.01	-0.31 ± 0.09	-0.04 ± 0.02	53893.4 ± 0.21
SNF20061020-000	0.30 ± 0.03	0.21 ± 0.01	0.44 ± 0.11	0.08 ± 0.03	54037.9 ± 0.19
SNF20061021-003	-0.08 ± 0.03	-0.05 ± 0.01	0.38 ± 0.08	-0.04 ± 0.02	54039.7 ± 0.13
SNF20061022-005	-0.11 ± 0.03	-0.08 ± 0.02	-0.34 ± 0.10	0.15 ± 0.03	54040.8 ± 0.17
SNF20061111-002	0.08 ± 0.03	-0.01 ± 0.01	-0.30 ± 0.12	-0.05 ± 0.03	54060.8 ± 0.18
SNF20070424-003	0.08 ± 0.03	-0.05 ± 0.01	-0.26 ± 0.09	-0.07 ± 0.02	54225.8 ± 0.16
SNF20070506-006	-0.19 ± 0.03	-0.07 ± 0.01	-0.94 ± 0.08	0.09 ± 0.02	54245.9 ± 0.10
SNF20070630-006	-0.09 ± 0.02	-0.04 ± 0.01	-0.16 ± 0.08	-0.06 ± 0.02	54294.9 ± 0.11
SNF20070717-003	-0.12 ± 0.02	0.03 ± 0.01	0.90 ± 0.08	-0.12 ± 0.02	54310.3 ± 0.11

Table 12: Selective extinction model derived per-SN parameter median values with 68th percentile uncertainty or standard deviation for our first 10 SNe Ia. Note SN2011hr was dropped when calculated derived parameters to resolve covariance matrix rank deficiency (flagged N/A). A corresponding full table of all training SNe Ia is available upon request.

SN	c_a	c_b	α_V	ρ_V
SNF20060512-001	-0.08 ± 0.02	-0.04 ± 0.01	0.04 ± 0.02	25.91 ± 37.11
SNF20060526-003	-0.08 ± 0.02	-0.03 ± 0.01	0.01 ± 0.02	10.02 ± 22.95
SNF20061020-000	0.12 ± 0.03	0.04 ± 0.01	0.23 ± 0.03	2.80 ± 0.19
SNF20061021-003	0.09 ± 0.02	0.04 ± 0.01	0.21 ± 0.02	2.55 ± 0.13
SNF20061022-005	-0.08 ± 0.03	-0.04 ± 0.01	0.04 ± 0.02	33.26 ± 43.43
SNF20061111-002	-0.08 ± 0.03	-0.03 ± 0.01	0.01 ± 0.01	10.92 ± 42.15
SNF20070424-003	-0.07 ± 0.02	-0.02 ± 0.01	0.01 ± 0.03	4.67 ± 20.31
SNF20070506-006	-0.23 ± 0.02	-0.10 ± 0.01	-0.11 ± 0.03	2.04 ± 0.21
SNF20070630-006	-0.04 ± 0.02	-0.01 ± 0.01	0.07 ± 0.02	2.55 ± 0.37
SNF20070717-003	0.22 ± 0.02	0.10 ± 0.01	0.34 ± 0.02	2.42 ± 0.09

Bibliography

[1] T. M. C. Abbott, A. Alarcon, S. Allam, P. Andersen, F. Andrade-Oliveira, J. Annis, J. Asorey, S. Avila, D. Bacon, N. Banik, B. A. Bassett, E. Baxter, K. Bechtol, M. R. Becker, G. M. Bernstein, E. Bertin, J. Blazek, S. L. Bridle, D. Brooks, D. Brout, D. L. Burke, J. Calcino, H. Camacho, A. Campos, A. Carnero Rosell, D. Carollo, M. Carrasco Kind, J. Carretero, F. J. Castander, R. Cawthon, P. Challis, K. C. Chan, C. Chang, M. Childress, M. Crocce, C. E. Cunha, C. B. D'Andrea, L. N. da Costa, C. Davis, T. M. Davis, J. De Vicente, D. L. DePoy, J. DeRose, S. Desai, H. T. Diehl, J. P. Dietrich, S. Dodelson, P. Doel, A. Drlica-Wagner, T. F. Eifler, J. Elvin-Poole, J. Estrada, A. E. Evrard, E. Fernandez, B. Flaugher, R. J. Foley, P. Fosalba, J. Frieman, L. Galbany, J. García-Bellido, M. Gatti, E. Gaztanaga, D. W. Gerdes, T. Giannantonio, K. Glazebrook, D. A. Goldstein, D. Gruen, R. A. Gruendl, J. Gschwend, G. Gutierrez, W. G. Hartley, S. R. Hinton, D. L. Hollowood, K. Honscheid, J. K. Hoormann, B. Hoyle, D. Huterer, B. Jain, D. J. James, M. Jarvis, T. Jeltema, E. Kasai, S. Kent, R. Kessler, A. G. Kim, N. Kokron, E. Krause, R. Kron, K. Kuehn, N. Kuropatkin, O. Lahav, J. Lasker, P. Lemos, G. F. Lewis, T. S. Li, C. Lidman, M. Lima, H. Lin, E. Macaulay, N. MacCrann, M. A. G. Maia, M. March, J. Marriner, J. L. Marshall, P. Martini, R. G. McMahon, P. Melchior, F. Menanteau, R. Miquel, J. J. Mohr, E. Morganson, J. Muir, A. Möller, E. Neilsen, R. C. Nichol, B. Nord, R. L. C. Ogando, A. Palmese, Y. C. Pan, H. V. Peiris, W. J. Percival, A. A. Plazas, A. Porredon, J. Prat, A. K. Romer, A. Roodman, R. Rosenfeld, A. J. Ross, E. S. Rykoff, S. Samuroff, C. Sánchez, E. Sanchez, V. Scarpine, R. Schindler, M. Schubnell, D. Scolnic, L. F. Secco, S. Serrano, I. Sevilla-Noarbe, R. Sharp, E. Sheldon, M. Smith, M. Soares-Santos, F. Sobreira, N. E. Sommer, E. Swann, M. E. C. Swanson, G. Tarle, D. Thomas, R. C. Thomas, M. A. Troxel, B. E. Tucker, S. A. Uddin, P. Vielzeuf, A. R. Walker, M. Wang, N. Weaverdyck, R. H. Wechsler, J. Weller, B. Yanny, B. Zhang, Y. Zhang, J. Zuntz, and DES Collaboration. Cosmological Constraints from Multiple Probes in the Dark Energy Survey. Phys. Rev. Lett., 122(17):171301, May 2019.

[2] J. Aird, A. L. Coil, and A. Georgakakis. X-rays across the galaxy population - I. Tracing the main sequence of star formation. MNRAS, 465(3):3390–3415, March 2017.

[3] Shadab Alam, Franco D. Albareti, Carlos Allende Prieto, F. Anders, Scott F. Anderson, Timothy Anderton, Brett H. Andrews, Eric Armengaud, Éric Aubourg, Stephen Bailey, Sarbani Basu, Julian E. Bautista, Rachael L. Beaton, Timothy C. Beers, Chad F. Bender, Andreas A. Berlind, Florian Beutler, Vaishali Bhardwaj, Jonathan C. Bird, Dmitry Bizyaev, Cullen H. Blake, Michael R. Blanton, Michael Blomqvist, John J. Bochanski, Adam S. Bolton, Jo Bovy, A. Shelden Bradley, W. N. Brandt, D. E. Brauer, J. Brinkmann, Peter J. Brown, Joel R. Brownstein, Angela Burden, Etienne Burtin, Nicolás G. Busca, Zheng Cai, Diego Capozzi, Aurelio Carnero Rosell,

Michael A. Carr, Ricardo Carrera, K. C. Chambers, William James Chaplin, Yen-Chi Chen, Cristina Chiappini, S. Drew Chojnowski, Chia-Hsun Chuang, Nicolas Clerc, Johan Comparat, Kevin Covey, Rupert A. C. Croft, Antonio J. Cuesta, Katia Cunha, Luiz N. da Costa, Nicola Da Rio, James R. A. Davenport, Kyle S. Dawson, Nathan De Lee, Timothée Delubac, Rohit Deshpande, Saurav Dhital, Letícia Dutra-Ferreira, Tom Dwelly, Anne Ealet, Garrett L. Ebelke, Edward M. Edmondson, Daniel J. Eisenstein, Tristan Ellsworth, Yvonne Elsworth, Courtney R. Epstein, Michael Eracleous, Stephanie Escoffier, Massimiliano Esposito, Michael L. Evans, Xiaohui Fan, Emma Fernández-Alvar, Diane Feuillet, Nurten Filiz Ak, Hayley Finley, Alexis Finoguenov, Kevin Flaherty, Scott W. Fleming, Andreu Font-Ribera, Jonathan Foster, Peter M. Frinchaboy, J. G. Galbraith-Frew, Rafael A. García, D. A. García-Hernández, Ana E. García Pérez, Patrick Gaulme, Jian Ge, R. Génova-Santos, A. Georgakakis, Luan Ghezzi, Bruce A. Gillespie, Léo Girardi, Daniel Goddard, Satya Gontcho A. Gontcho, Jonay I. González Hernández, Eva K. Grebel, Paul J. Green, Jan Niklas Grieb, Nolan Grieves, James E. Gunn, Hong Guo, Paul Harding, Sten Hasselquist, Suzanne L. Hawley, Michael Hayden, Fred R. Hearty, Saskia Hekker, Shirley Ho, David W. Hogg, Kelly Holley-Bockelmann, Jon A. Holtzman, Klaus Honscheid, Daniel Huber, Joseph Huehnerhoff, Inese I. Ivans, Linhua Jiang, Jennifer A. Johnson, Karen Kinemuchi, David Kirkby, Francisco Kitaura, Mark A. Klaene, Gillian R. Knapp, Jean-Paul Kneib, Xavier P. Koenig, Charles R. Lam, Ting-Wen Lan, Dustin Lang, Pierre Laurent, Jean-Marc Le Goff, Alexie Leauthaud, Khee-Gan Lee, Young Sun Lee, Timothy C. Licquia, Jian Liu, Daniel C. Long, Martín López-Corredoira, Diego Lorenzo-Oliveira, Sara Lucatello, Britt Lundgren, Robert H. Lupton, III Mack, Claude E., Suvrath Mahadevan, Marcio A. G. Maia, Steven R. Majewski, Elena Malanushenko, Viktor Malanushenko, A. Manchado, Marc Manera, Qingqing Mao, Claudia Maraston, Robert C. Marchwinski, Daniel Margala, Sarah L. Martell, Marie Martig, Karen L. Masters, Savita Mathur, Cameron K. McBride, Peregrine M. McGehee, Ian D. McGreer, Richard G. McMahon, Brice Ménard, Marie-Luise Menzel, Andrea Merloni, Szabolcs Mészáros, Adam A. Miller, Jordi Miralda-Escudé, Hironao Miyatake, Antonio D. Montero-Dorta, Surhud More, Eric Morganson, Xan Morice-Atkinson, Heather L. Morrison, Benôit Mosser, Demitri Muna, Adam D. Myers, Kirpal Nand ra, Jeffrey A. Newman, Mark Neyrinck, Duy Cuong Nguyen, Robert C. Nichol, David L. Nidever, Pasquier Noterdaeme, Sebastián E. Nuza, Julia E. O'Connell, Robert W. O'Connell, Ross O'Connell, Ricardo L. C. Ogando, Matthew D. Olmstead, Audrey E. Oravetz, Daniel J. Oravetz, Keisuke Osumi, Russell Owen, Deborah L. Padgett, Nikhil Padmanabhan, Martin Paegert, Nathalie Palanque-Delabrouille, Kaike Pan, John K. Parejko, Isabelle Pâris, Changbom Park, Petchara Pattarakijwanich, M. Pellejero-Ibanez, Joshua Pepper, Will J. Percival, Ismael Pérez-Fournon, Ignasi Prez-Ra'fols, Patrick Petitjean, Matthew M. Pieri, Marc H. Pinsonneault, Gustavo F. Porto de Mello, Francisco Prada, Abhishek Prakash, Adrian M. Price-Whelan, Pavlos Protopapas, M. Jordan Raddick, Mubdi Rahman, Beth A. Reid, James Rich, Hans-Walter Rix, Annie C. Robin, Constance M. Rockosi, Thaíse S. Rodrigues, Sergio Rodríguez-Torres, Natalie A. Roe, Ashley J. Ross, Nicholas P. Ross, Graziano Rossi, John J. Ruan, J. A. Rubiño-Martín, Eli S. Rykoff, Salvador Salazar-Albornoz, Mara Salvato, Lado Samushia, Ariel G. Sánchez, Basílio Santiago, Conor Sayres, Ricardo P. Schi-

avon, David J. Schlegel, Sarah J. Schmidt, Donald P. Schneider, Mathias Schultheis, Axel D. Schwope, C. G. Scóccola, Caroline Scott, Kris Sellgren, Hee-Jong Seo, Aldo Serenelli, Neville Shane, Yue Shen, Matthew Shetrone, Yiping Shu, V. Silva Aguirre, Thirupathi Sivarani, M. F. Skrutskie, Anže Slosar, Verne V. Smith, Flávia Sobreira, Diogo Souto, Keivan G. Stassun, Matthias Steinmetz, Dennis Stello, Michael A. Strauss, Alina Streblyanska, Nao Suzuki, Molly E. C. Swanson, Jonathan C. Tan, Jamie Tayar, Ryan C. Terrien, Aniruddha R. Thakar, Daniel Thomas, Neil Thomas, Benjamin A. Thompson, Jeremy L. Tinker, Rita Tojeiro, Nicholas W. Troup, Mariana Vargas-Magaña, Jose A. Vazquez, Licia Verde, Matteo Viel, Nicole P. Vogt, David A. Wake, Ji Wang, Benjamin A. Weaver, David H. Weinberg, Benjamin J. Weiner, Martin White, John C. Wilson, John P. Wisniewski, W. M. Wood-Vasey, Christophe Ye'che, Donald G. York, Nadia L. Zakamska, O. Zamora, Gail Zasowski, Idit Zehavi, Gong-Bo Zhao, Zheng Zheng, Xu Zhou, Zhimin Zhou, Hu Zou, and Guangtun Zhu. The Eleventh and Twelfth Data Releases of the Sloan Digital Sky Survey: Final Data from SDSS-III. ApJS, 219(1):12, July 2015.

[4] G. Aldering, P. Antilogus, C. Aragon, S. Bailey, C. Baltay, S. Bongard, K. Boone, C. Buton, N. Chotard, Y. Copin, S. Dixon, H. K. Fakhouri, U. Feindt, D. Fouchez, E. Gangler, B. Hayden, W. Hillebrandt, A. G. Kim, M. Kowalski, D. Küsters, P. F. Léget, Q. Lin, S. Lombardo, F. Mondon, J. Nordin, R. Pain, E. Pecontal, R. Pereira, S. Perlmutter, K. Ponder, M. Pruzhinskaya, D. Rabinowitz, M. Rigault, D. Rubin, K. Runge, C. Saunders, L. P. Says, G. Smadja, N. Suzuki, C. Tao, S. Taubenberger, R. C. Thomas, M. Vincenzi, B. Weaver, and Nearby Supernova Factory Collaboration. The SNEMO and SUGAR Companion Data Sets. *Research Notes of the American Astronomical Society*, 4(5):63, May 2020.

[5] Greg Aldering, G. Adam, P. Antilogus, Pierre Astier, R. Bacon, S. Bongard, C. Bonnaud, Y. Copin, Delphine Hardin, Francois Henault, Dale A. Howell, Jean-Pierre Lemonnier, Jean-Michel Levy, Stewart C. Loken, Peter E. Nugent, Reynald Pain, A. Pecontal, E. Pecontal, Saul Perlmutter, Robert M. Quimby, K. Schahmaneche, G. Smadja, and W. Michael Wood-Vasey. Overview of the Nearby Supernova Factory. In J. Anthony Tyson and Sidney Wolff, editors, *Survey and Other Telescope Technologies and Discoveries*, volume 4836 of *Society of Photo-Optical Instrumentation Engineers (SPIE) Conference Series*, pages 61–72, December 2002.

[6] J. P. Anderson, P. A. James, F. Förster, S. González-Gaitán, S. M. Habergham, M. Hamuy, and J. D. Lyman. On the environments of Type Ia supernovae within host galaxies. MNRAS, 448(1):732–753, March 2015.

[7] W. D. Arnett. Type I supernovae. I - Analytic solutions for the early part of the light curve. ApJ, 253:785–797, February 1982.

[8] Astropy Collaboration, T. P. Robitaille, E. J. Tollerud, P. Greenfield, M. Droettboom, E. Bray, T. Aldcroft, M. Davis, A. Ginsburg, A. M. Price-Whelan, W. E. Kerzendorf, A. Conley, N. Crighton, K. Barbary, D. Muna, H. Ferguson, F. Grollier, M. M. Parikh, P. H. Nair, H. M. Unther, C. Deil, J. Woillez, S. Conseil, R. Kramer, J. E. H. Turner, L. Singer, R. Fox, B. A. Weaver, V. Zabalza, Z. I. Edwards, K. Azalee Bostroem, D. J. Burke, A. R. Casey, S. M. Crawford, N. Dencheva, J. Ely, T. Jenness, K. Labrie, P. L. Lim, F. Pierfederici, A. Pontzen, A. Ptak, B. Refsdal, M. Servillat, and O. Streicher. Astropy: A community Python package for astronomy. A&A, 558:A33, October 2013.

[9] Éric Aubourg, Stephen Bailey, Julian E. Bautista, Florian Beutler, Vaishali Bhardwaj, Dmitry Bizyaev, Michael Blanton, Michael Blomqvist, Adam S. Bolton, Jo Bovy, Howard Brewington, J. Brinkmann, Joel R. Brownstein, Angela Burden, Nicolás G. Busca, William Carithers, Chia-Hsun Chuang, Johan Comparat, Rupert A. C. Croft, Antonio J. Cuesta, Kyle S. Dawson, Timothée Delubac, Daniel J. Eisenstein, Andreu Font-Ribera, Jian Ge, J. M. Le Goff, Satya Gontcho A. Gontcho, J. Richard Gott, James E. Gunn, Hong Guo, Julien Guy, Jean-Christophe Hamilton, Shirley Ho, Klaus Honscheid, Cullan Howlett, David Kirkby, Francisco S. Kitaura, Jean-Paul Kneib, Khee-Gan Lee, Dan Long, Robert H. Lupton, Mariana Vargas Magaña, Viktor Malanushenko, Elena Malanushenko, Marc Manera, Claudia Maraston, Daniel Margala, Cameron K. McBride, Jordi Miralda-Escudé, Adam D. Myers, Robert C. Nichol, Pasquier Noterdaeme, Sebastián E. Nuza, Matthew D. Olmstead, Daniel Oravetz, Isabelle Pâris, Nikhil Padmanabhan, Nathalie Palanque-Delabrouille, Kaike Pan, Marcos Pellejero-Ibanez, Will J. Percival, Patrick Petitjean, Matthew M. Pieri, Francisco Prada, Beth Reid, James Rich, Natalie A. Roe, Ashley J. Ross, Nicholas P. Ross, Graziano Rossi, Jose Alberto Rubiño-Martín, Ariel G. Sánchez, Lado Samushia, Ricardo Tanausú Génova-Santos, Claudia G. Scóccola, David J. Schlegel, Donald P. Schneider, Hee-Jong Seo, Erin Sheldon, Audrey Simmons, Ramin A. Skibba, Anže Slosar, Michael A. Strauss, Daniel Thomas, Jeremy L. Tinker, Rita Tojeiro, Jose Alberto Vazquez, Matteo Viel, David A. Wake, Benjamin A. Weaver, David H. Weinberg, W. M. Wood-Vasey, Christophe Yèche, Idit Zehavi, Gong-Bo Zhao, and BOSS Collaboration. Cosmological implications of baryon acoustic oscillation measurements. Phys. Rev. D, 92(12):123516, December 2015.

[10] Arturo Avelino, Andrew S. Friedman, Kaisey S. Mandel, David O. Jones, Peter J. Challis, and Robert P. Kirshner. Type Ia Supernovae Are Excellent Standard Candles in the Near-infrared. ApJ, 887(1):106, December 2019.

[11] S. Bailey, G. Aldering, P. Antilogus, C. Aragon, C. Baltay, S. Bongard, C. Buton, M. Childress, N. Chotard, Y. Copin, E. Gangler, S. Loken, P. Nugent, R. Pain, E. Pecontal, R. Pereira, S. Perlmutter, D. Rabinowitz, G. Rigaudier, K. Runge, R. Scalzo, G. Smadja, H. Swift, C. Tao, R. C. Thomas, C. Wu, and Nearby Supernova Factory. Using spectral flux ratios to standardize SN Ia luminosities. A&A, 500(2):L17–L20, June 2009.

[12] Kyle Barbary, Tom Barclay, Rahul Biswas, Matt Craig, Ulrich Feindt, Brian Friesen, Danny Goldstein, Saurabh Jha, Steve Rodney, Caroline Sofiatti, Rollin C. Thomas, and Michael Wood-Vasey. SNCosmo: Python library for supernova cosmology, November 2016.

[13] J. G. Bartlett. Galaxy Clusters in Cosmology: Cluster abundance as a probe of structure formation. In D. Valls-Gabaud, M. A. Hendry, P. Molaro, and K. Chamcham, editors, *From Quantum Fluctuations to Cosmological Structures*, volume 126 of *Astronomical Society of the Pacific Conference Series*, page 365, September 1997.

[14] Eric F. Bell and Roelof S. de Jong. Stellar Mass-to-Light Ratios and the Tully-Fisher Relation. ApJ, 550(1):212–229, March 2001.

[15] E. Bertin and S. Arnouts. SExtractor: Software for source extraction. A&AS, 117:393–404, Jun 1996.

[16] M. Betoule, R. Kessler, J. Guy, J. Mosher, D. Hardin, R. Biswas, P. Astier, P. El-Hage, M. Konig, S. Kuhlmann, J. Marriner, R. Pain, N. Regnault, C. Balland, B. A. Bassett, P. J. Brown, H. Campbell, R. G. Carlberg, F. Cellier-Holzem, D. Cinabro, A. Conley, C. B. D'Andrea, D. L. DePoy, M. Doi, R. S. Ellis, S. Fabbro, A. V. Filippenko, R. J. Foley, J. A. Frieman, D. Fouchez, L. Galbany, A. Goobar, R. R. Gupta, G. J. Hill, R. Hlozek, C. J. Hogan, I. M. Hook, D. A. Howell, S. W. Jha, L. Le Guillou, G. Leloudas, C. Lidman, J. L. Marshall, A. Möller, A. M. Mourão, J. Neveu, R. Nichol, M. D. Olmstead, N. Palanque-Delabrouille, S. Perlmutter, J. L. Prieto, C. J. Pritchet, M. Richmond, A. G. Riess, V. Ruhlmann-Kleider, M. Sako, K. Schahmaneche, D. P. Schneider, M. Smith, J. Sollerman, M. Sullivan, N. A. Walton, and C. J. Wheeler. Improved cosmological constraints from a joint analysis of the SDSS-II and SNLS supernova samples. A&A, 568:A22, August 2014.

[17] S. Blondin, T. Matheson, R. P. Kirshner, K. S. Mandel, P. Berlind, M. Calkins, P. Challis, P. M. Garnavich, S. W. Jha, M. Modjaz, A. G. Riess, and B. P. Schmidt. The Spectroscopic Diversity of Type Ia Supernovae. AJ, 143:126, May 2012.

[18] R. C. Bohlin. Hubble Space Telescope CALSPEC Flux Standards: Sirius (and Vega). AJ, 147(6):127, June 2014.

[19] S. Bongard, F. Soulez, É. Thiébaut, and É. Pecontal. 3D deconvolution of hyperspectral astronomical data. MNRAS, 418(1):258–270, November 2011.

[20] K. Boone, G. Aldering, P. Antilogus, C. Aragon, S. Bailey, C. Baltay, S. Bongard, C. Buton, Y. Copin, S. Dixon, D. Fouchez, E. Gangler, R. Gupta, B. Hay-

den, W. Hillebrandt, A. G. Kim, M. Kowalski, D. Küsters, P. F. Léget, F. Mondon, J. Nordin, R. Pain, E. Pecontal, R. Pereira, S. Perlmutter, K. A. Ponder, D. Rabinowitz, M. Rigault, D. Rubin, K. Runge, C. Saunders, G. Smadja, N. Suzuki, C. Tao, S. Taubenberger, R. C. Thomas, and M. Vincenzi. The Twins Embedding of Type Ia Supernovae. I. The Diversity of Spectra at Maximum Light. ApJ, 912(1):70, May 2021.

[21] David Branch, Leeann Chau Dang, and E. Baron. Comparative Direct Analysis of Type Ia Supernova Spectra. V. Insights from a Larger Sample and Quantitative Subclassification. PASP, 121(877):238, March 2009.

[22] David Branch, Adam Fisher, and Peter Nugent. On the Relative Frequencies of Spectroscopically Normal and Peculiar Type IA Supernovae. AJ, 106:2383, December 1993.

[23] J. Brinchmann, S. Charlot, S. D. M. White, C. Tremonti, G. Kauffmann, T. Heckman, and J. Brinkmann. The physical properties of star-forming galaxies in the low-redshift Universe. MNRAS, 351(4):1151–1179, July 2004.

[24] D. Brout, D. Scolnic, R. Kessler, C. B. D'Andrea, T. M. Davis, R. R. Gupta, S. R. Hinton, A. G. Kim, J. Lasker, C. Lidman, E. Macaulay, A. Möller, R. C. Nichol, M. Sako, M. Smith, M. Sullivan, B. Zhang, P. Andersen, J. Asorey, A. Avelino, B. A. Bassett, P. Brown, J. Calcino, D. Carollo, P. Challis, M. Childress, A. Clocchiatti, A. V. Filippenko, R. J. Foley, L. Galbany, K. Glazebrook, J. K. Hoormann, E. Kasai, R. P. Kirshner, K. Kuehn, S. Kuhlmann, G. F. Lewis, K. S. Mandel, M. March, V. Miranda, E. Morganson, D. Muthukrishna, P. Nugent, A. Palmese, Y. C. Pan, R. Sharp, N. E. Sommer, E. Swann, R. C. Thomas, B. E. Tucker, S. A. Uddin, W. Wester, T. M. C. Abbott, S. Allam, J. Annis, S. Avila, K. Bechtol, G. M. Bernstein, E. Bertin, D. Brooks, D. L. Burke, A. Carnero Rosell, M. Carrasco Kind, J. Carretero, F. J. Castander, C. E. Cunha, L. N. da Costa, C. Davis, J. De Vicente, D. L. DePoy, S. Desai, H. T. Diehl, P. Doel, A. Drlica-Wagner, T. F. Eifler, J. Estrada, E. Fernandez, B. Flaugher, P. Fosalba, J. Frieman, J. García-Bellido, D. Gruen, R. A. Gruendl, G. Gutierrez, W. G. Hartley, D. L. Hollowood, K. Honscheid, B. Hoyle, D. J. James, M. Jarvis, T. Jeltema, E. Krause, O. Lahav, T. S. Li, M. Lima, M. A. G. Maia, J. Marriner, J. L. Marshall, P. Martini, F. Menanteau, C. J. Miller, R. Miquel, R. L. C. Ogand o, A. A. Plazas, A. K. Romer, A. Roodman, E. S. Rykoff, E. Sanchez, B. Santiago, V. Scarpine, M. Schubnell, S. Serrano, I. Sevilla-Noarbe, R. C. Smith, M. Soares-Santos, F. Sobreira, E. Suchyta, M. E. C. Swanson, G. Tarle, D. Thomas, M. A. Troxel, D. L. Tucker, V. Vikram, A. R. Walker, Y. Zhang, and DES Collaboration. First Cosmology Results Using SNe Ia from the Dark Energy Survey: Analysis, Systematic Uncertainties, and Validation. ApJ, 874(2):150, April 2019.

[25] Dillon Brout, Dan Scolnic, Brodie Popovic, Adam G. Riess, Anthony Carr, Joe Zuntz, Rick Kessler, Tamara M. Davis, Samuel Hinton, David Jones, W. D'Arcy Kenworthy, Erik R. Peterson, Khaled Said, Georgie Taylor, Noor Ali, Patrick Armstrong, Pranav Charvu, Arianna Dwomoh, Cole Meldorf, Antonella Palmese, Helen Qu, Benjamin M. Rose, Bruno Sanchez, Christopher W. Stubbs, Maria Vincenzi, Charlotte M. Wood, Peter J. Brown, Rebecca Chen, Ken Chambers, David A. Coulter, Mi Dai, Georgios Dimitriadis, Alexei V. Filippenko, Ryan J. Foley, Saurabh W. Jha, Lisa Kelsey, Robert P. Kirshner, Anais Möller, Jessie Muir, Seshadri Nadathur, Yen-Chen Pan, Armin Rest, Cesar Rojas-Bravo, Masao Sako, Matthew R. Siebert, Mat Smith, Benjamin E. Stahl, and Phil Wiseman. The Pantheon+ Analysis: Cosmological Constraints. ApJ, 938(2):110, October 2022.

[26] Dillon Brout and Daniel Scolnic. It's Dust: Solving the Mysteries of the Intrinsic Scatter and Host-Galaxy Dependence of Standardized Type Ia Supernova Brightnesses. *arXiv e-prints*, page arXiv:2004.10206, April 2020.

[27] G. Bruzual and S. Charlot. Stellar population synthesis at the resolution of 2003. MNRAS, 344(4):1000–1028, October 2003.

[28] Christopher R. Burns, Maximilian Stritzinger, M. M. Phillips, E. Y. Hsiao, Carlos Contreras, S. E. Persson, Gaston Folatelli, Luis Boldt, Abdo Campillay, Sergio Castellón, Wendy L. Freedman, Barry F. Madore, Nidia Morrell, Francisco Salgado, and Nicholas B. Suntzeff. The Carnegie Supernova Project: Intrinsic Colors of Type Ia Supernovae. ApJ, 789(1):32, July 2014.

[29] Christopher R. Burns, Maximilian Stritzinger, M. M. Phillips, ShiAnne Kattner, S. E. Persson, Barry F. Madore, Wendy L. Freedman, Luis Boldt, Abdo Campillay, Carlos Contreras, Gaston Folatelli, Sergio Gonzalez, Wojtek Krzeminski, Nidia Morrell, Francisco Salgado, and Nicholas B. Suntzeff. The Carnegie Supernova Project: Lightcurve Fitting with SNooPy. AJ, 141(1):19, January 2011.

[30] C. Buton, Y. Copin, G. Aldering, P. Antilogus, C. Aragon, S. Bailey, C. Baltay, S. Bongard, A. Canto, F. Cellier-Holzem, M. Childress, N. Chotard, H. K. Fakhouri, E. Gangler, J. Guy, E. Y. Hsiao, M. Kerschhaggl, M. Kowalski, S. Loken, P. Nugent, K. Paech, R. Pain, E. Pécontal, R. Pereira, S. Perlmutter, D. Rabinowitz, M. Rigault, K. Runge, R. Scalzo, G. Smadja, C. Tao, R. C. Thomas, B. A. Weaver, C. Wu, and Nearby SuperNova Factory. Atmospheric extinction properties above Mauna Kea from the Nearby SuperNova Factory spectro-photometric data set. A&A, 549:A8, January 2013.

[31] Daniela Calzetti. *Star Formation Rate Indicators*, page 419. Camgridge University Press, 2013.

[32] Daniela Calzetti, Lee Armus, Ralph C. Bohlin, Anne L. Kinney, Jan Koornneef, and Thaisa Storchi-Bergmann. The Dust Content and Opacity of Actively Star-forming Galaxies. ApJ, 533(2):682–695, April 2000.

[33] Jason A. Cardelli, Geoffrey C. Clayton, and John S. Mathis. The Relationship between Infrared, Optical, and Ultraviolet Extinction. ApJ, 345:245, October 1989.

[34] Bob Carpenter, Andrew Gelman, Matthew D Hoffman, Daniel Lee, Ben Goodrich, Michael Betancourt, Marcus Brubaker, Jiqiang Guo, Peter Li, and Allen Riddell. Stan: A probabilistic programming language. *Journal of statistical software*, 76(1), 2017.

[35] Gilles Chabrier. Galactic Stellar and Substellar Initial Mass Function. PASP, 115(809):763–795, July 2003.

[36] K. C. Chambers, E. A. Magnier, N. Metcalfe, H. A. Flewelling, M. E. Huber, C. Z. Waters, L. Denneau, P. W. Draper, D. Farrow, D. P. Finkbeiner, C. Holmberg, J. Koppenhoefer, P. A. Price, A. Rest, R. P. Saglia, E. F. Schlafly, S. J. Smartt, W. Sweeney, R. J. Wainscoat, W. S. Burgett, S. Chastel, T. Grav, J. N. Heasley, K. W. Hodapp, R. Jedicke, N. Kaiser, R. P. Kudritzki, G. A. Luppino, R. H. Lupton, D. G. Monet, J. S. Morgan, P. M. Onaka, B. Shiao, C. W. Stubbs, J. L. Tonry, R. White, E. Bañados, E. F. Bell, R. Bender, E. J. Bernard, M. Boegner, F. Boffi, M. T. Botticella, A. Calamida, S. Casertano, W. P. Chen, X. Chen, S. Cole, N. Deacon, C. Frenk, A. Fitzsimmons, S. Gezari, V. Gibbs, C. Goessl, T. Goggia, R. Gourgue, B. Goldman, P. Grant, E. K. Grebel, N. C. Hambly, G. Hasinger, A. F. Heavens, T. M. Heckman, R. Henderson, T. Henning, M. Holman, U. Hopp, W. H. Ip, S. Isani, M. Jackson, C. D. Keyes, A. M. Koekemoer, R. Kotak, D. Le, D. Liska, K. S. Long, J. R. Lucey, M. Liu, N. F. Martin, G. Masci, B. McLean, E. Mindel, P. Misra, E. Morganson, D. N. A. Murphy, A. Obaika, G. Narayan, M. A. Nieto-Santisteban, P. Norberg, J. A. Peacock, E. A. Pier, M. Postman, N. Primak, C. Rae, A. Rai, A. Riess, A. Riffeser, H. W. Rix, S. Röser, R. Russel, L. Rutz, E. Schilbach, A. S. B. Schultz, D. Scolnic, L. Strolger, A. Szalay, S. Seitz, E. Small, K. W. Smith, D. R. Soderblom, P. Taylor, R. Thomson, A. N. Taylor, A. R. Thakar, J. Thiel, D. Thilker, D. Unger, Y. Urata, J. Valenti, J. Wagner, T. Walder, F. Walter, S. P. Watters, S. Werner, W. M. Wood-Vasey, and R. Wyse. The Pan-STARRS1 Surveys. *arXiv e-prints*, page arXiv:1612.05560, December 2016.

[37] M. Childress, G. Aldering, P. Antilogus, C. Aragon, S. Bailey, C. Baltay, S. Bongard, C. Buton, A. Canto, F. Cellier-Holzem, N. Chotard, Y. Copin, H. K. Fakhouri, E. Gangler, J. Guy, E. Y. Hsiao, M. Kerschhaggl, A. G. Kim, M. Kowalski, S. Loken, P. Nugent, K. Paech, R. Pain, E. Pecontal, R. Pereira, S. Perlmutter, D. Rabinowitz, M. Rigault, K. Runge, R. Scalzo, G. Smadja, C. Tao, R. C. Thomas, B. A. Weaver,

and C. Wu. Host Galaxies of Type Ia Supernovae from the Nearby Supernova Factory. ApJ, 770(2):107, June 2013.

[38] N. Chotard, E. Gangler, G. Aldering, P. Antilogus, C. Aragon, S. Bailey, C. Baltay, S. Bongard, C. Buton, A. Canto, M. Childress, Y. Copin, H. K. Fakhouri, E. Y. Hsiao, M. Kerschhaggl, M. Kowalski, S. Loken, P. Nugent, K. Paech, R. Pain, E. Pecontal, R. Pereira, S. Perlmutter, D. Rabinowitz, K. Runge, R. Scalzo, G. Smadja, C. Tao, R. C. Thomas, B. A. Weaver, C. Wu, and Nearby Supernova Factory. The reddening law of type Ia supernovae: separating intrinsic variability from dust using equivalent widths. A&A, 529:L4, May 2011.

[39] Roberto Cid Fernandes, Abílio Mateus, Laerte Sodré, Grażyna Stasińska, and Jean M. Gomes. Semi-empirical analysis of Sloan Digital Sky Survey galaxies - I. Spectral synthesis method. MNRAS, 358(2):363–378, April 2005.

[40] A. Conley, J. Guy, M. Sullivan, N. Regnault, P. Astier, C. Balland, S. Basa, R. G. Carlberg, D. Fouchez, D. Hardin, I. M. Hook, D. A. Howell, R. Pain, N. Palanque-Delabrouille, K. M. Perrett, C. J. Pritchet, J. Rich, V. Ruhlmann-Kleider, D. Balam, S. Baumont, R. S. Ellis, S. Fabbro, H. K. Fakhouri, N. Fourmanoit, S. González-Gaitán, M. L. Graham, M. J. Hudson, E. Hsiao, T. Kronborg, C. Lidman, A. M. Mourao, J. D. Neill, S. Perlmutter, P. Ripoche, N. Suzuki, and E. S. Walker. Supernova Constraints and Systematic Uncertainties from the First Three Years of the Supernova Legacy Survey. ApJS, 192:1, January 2011.

[41] A. Conley, M. Sullivan, E. Y. Hsiao, J. Guy, P. Astier, D. Balam, C. Balland, S. Basa, R. G. Carlberg, D. Fouchez, D. Hardin, D. A. Howell, I. M. Hook, R. Pain, K. Perrett, C. J. Pritchet, and N. Regnault. SiFTO: An Empirical Method for Fitting SN Ia Light Curves. ApJ, 681(1):482–498, July 2008.

[42] Charlie Conroy. Modeling the Panchromatic Spectral Energy Distributions of Galaxies. ARA&A, 51(1):393–455, August 2013.

[43] Charlie Conroy, James E. Gunn, and Martin White. The Propagation of Uncertainties in Stellar Population Synthesis Modeling. I. The Relevance of Uncertain Aspects of Stellar Evolution and the Initial Mass Function to the Derived Physical Properties of Galaxies. ApJ, 699(1):486–506, July 2009.

[44] Stéphane Courteau, Michele Cappellari, Roelof S. de Jong, Aaron A. Dutton, Eric Emsellem, Henk Hoekstra, L. V. E. Koopmans, Gary A. Mamon, Claudia Maraston, Tommaso Treu, and Lawrence M. Widrow. Galaxy masses. *Reviews of Modern Physics*, 86(1):47–119, January 2014.

[45] Chris B. D'Andrea, Ravi R. Gupta, Masao Sako, Matt Morris, Robert C. Nichol, Peter J. Brown, Heather Campbell, Matthew D. Olmstead, Joshua A. Frieman, Peter Garnavich, Saurabh W. Jha, Richard Kessler, Hubert Lampeitl, John Marriner, Donald P. Schneider, and Mathew Smith. SPECTROSCOPIC PROPERTIES OF STAR-FORMING HOST GALAXIES AND TYPE ia SUPERNOVA HUBBLE RESIDUALS IN a NEARLY UNBIASED SAMPLE. *The Astrophysical Journal*, 743(2):172, December 2011.

[46] Tamara M. Davis, Lam Hui, Joshua A. Frieman, Troels Haugbølle, Richard Kessler, Benjamin Sinclair, Jesper Sollerman, Bruce Bassett, John Marriner, and Edvard Mörtsell. The Effect of Peculiar Velocities on Supernova Cosmology. ApJ, 741(1):67, November 2011.

[47] S. Dhawan, B. Leibundgut, J. Spyromilio, and K. Maguire. Near-infrared light curves of Type Ia supernovae: studying properties of the second maximum. MNRAS, 448(2):1345–1359, April 2015.

[48] Eleonora Di Valentino, Olga Mena, Supriya Pan, Luca Visinelli, Weiqiang Yang, Alessandro Melchiorri, David F. Mota, Adam G. Riess, and Joseph Silk. In the realm of the Hubble tension-a review of solutions. *Classical and Quantum Gravity*, 38(15):153001, July 2021.

[49] M. Doi, M. Tanaka, M. Fukugita, J. E. Gunn, N. Yasuda, Ž. Ivezić, J. Brinkmann, E. de Haars, S. J. Kleinman, J. Krzesinski, and R. French Leger. Photometric Response Functions of the Sloan Digital Sky Survey Imager. AJ, 139:1628–1648, April 2010.

[50] Albert Einstein. Die Feldgleichungen der Gravitation. *Sitzungsberichte der Königlich Preussischen Akademie der Wissenschaften*, pages 844–847, January 1915.

[51] J. H. Elias, K. Matthews, G. Neugebauer, and S. E. Persson. Type I supernovae in the infrared and their use as distance indicators. ApJ, 296:379–389, September 1985.

[52] Edward L. Fitzpatrick. Correcting for the Effects of Interstellar Extinction. PASP, 111(755):63–75, January 1999.

[53] Ryan J. Foley. On spectral line profiles in Type Ia supernova spectra. MNRAS, 435(1):273–288, October 2013.

[54] Ryan J. Foley and Robert P. Kirshner. Metallicity Differences in Type Ia Supernova Progenitors Inferred from Ultraviolet Spectra. *The Astrophysical Journal*, 769(1):L1, May 2013.

[55] Wendy L. Freedman. Measurements of the Hubble Constant: Tensions in Perspective. ApJ, 919(1):16, September 2021.

[56] Wendy L. Freedman, Barry F. Madore, Dylan Hatt, Taylor J. Hoyt, In Sung Jang, Rachael L. Beaton, Christopher R. Burns, Myung Gyoon Lee, Andrew J. Monson, Jillian R. Neeley, M. M. Phillips, Jeffrey A. Rich, and Mark Seibert. The Carnegie-Chicago Hubble Program. VIII. An Independent Determination of the Hubble Constant Based on the Tip of the Red Giant Branch. ApJ, 882(1):34, September 2019.

[57] A. Friedmann. Über die Krümmung des Raumes. *Zeitschrift fur Physik*, 10:377–386, January 1922.

[58] L. Galbany, J. P. Anderson, F. F. Rosales-Ortega, H. Kuncarayakti, T. Krühler, S. F. Sánchez, J. Falcón-Barroso, E. Pérez, J. C. Maureira, M. Hamuy, S. González-Gaitán, F. Förster, and V. Moral. Characterizing the environments of supernovae with MUSE. MNRAS, 455(4):4087–4099, February 2016.

[59] L. Galbany, J. P. Anderson, S. F. Sánchez, H. Kuncarayakti, S. Pedraz, S. González-Gaitán, V. Stanishev, I. Domínguez, M. E. Moreno-Raya, W. M. Wood-Vasey, A. M. Mourão, K. A. Ponder, C. Badenes, M. Mollá, A. R. López-Sánchez, F. F. Rosales-Ortega, J. M. Vílchez, R. García-Benito, and R. A. Marino. PISCO: The PMAS/PPak Integral-field Supernova Hosts Compilation. ApJ, 855(2):107, March 2018.

[60] L. Galbany, V. Stanishev, A. M. Mourão, M. Rodrigues, H. Flores, R. García-Benito, D. Mast, M. A. Mendoza, S. F. Sánchez, C. Badenes, J. Barrera-Ballesteros, J. Bland-Hawthorn, J. Falcón-Barroso, B. García-Lorenzo, J. M. Gomes, R. M. González Delgado, C. Kehrig, M. Lyubenova, A. R. López-Sánchez, A. de Lorenzo-Cáceres, R. A. Marino, S. Meidt, M. Mollá, P. Papaderos, M. A. Pérez-Torres, F. F. Rosales-Ortega, and G. van de Ven. Nearby supernova host galaxies from the CALIFA Survey. I. Sample, data analysis, and correlation to star-forming regions. A&A, 572:A38, December 2014.

[61] Anna Gallazzi, Stéphane Charlot, Jarle Brinchmann, Simon D. M. White, and Christy A. Tremonti. The ages and metallicities of galaxies in the local universe. MNRAS, 362(1):41–58, September 2005.

[62] S. Gonzalez-Gaitan, T. de Jaeger, L. Galbany, A. Mourao, A. Paulina-Afonso, and A. V. Filippenko. The effects of varying colour-luminosity relations on supernova science. *arXiv e-prints*, page arXiv:2009.13230, September 2020.

[63] J. E. Gunn, W. A. Siegmund, E. J. Mannery, R. E. Owen, C. L. Hull, R. F. Leger, L. N. Carey, G. R. Knapp, D. G. York, W. N. Boroski, S. M. Kent, R. H. Lupton, C. M. Rockosi, M. L. Evans, P. Waddell, J. E. Anderson, J. Annis, J. C. Barentine, L. M. Bartoszek, S. Bastian, S. B. Bracker, H. J. Brewington, C. I. Briegel, J. Brinkmann, Y. J. Brown, M. A. Carr, P. C. Czarapata, C. C. Drennan, T. Dombeck, G. R. Federwitz, B. A. Gillespie, C. Gonzales, S. U. Hansen, M. Harvanek, J. Hayes, W. Jordan, E. Kinney, M. Klaene, S. J. Kleinman, R. G. Kron, J. Kresinski, G. Lee, S. Limmongkol, C. W. Lindenmeyer, D. C. Long, C. L. Loomis, P. M. McGehee, P. M. Mantsch, E. H. Neilsen, Jr., R. M. Neswold, P. R. Newman, A. Nitta, J. Peoples, Jr., J. R. Pier, P. S. Prieto, A. Prosapio, C. Rivetta, D. P. Schneider, S. Snedden, and S.-i. Wang. The 2.5 m Telescope of the Sloan Digital Sky Survey. AJ, 131:2332–2359, April 2006.

[64] Ravi R. Gupta, Chris B. D'Andrea, Masao Sako, Charlie Conroy, Mathew Smith, Bruce Bassett, Joshua A. Frieman, Peter M. Garnavich, Saurabh W. Jha, Richard Kessler, Hubert Lampeitl, John Marriner, Robert C. Nichol, and Donald P. Schneider. IMPROVED CONSTRAINTS ON TYPE ia SUPERNOVA HOST GALAXY PROPERTIES USING MULTI-WAVELENGTH PHOTOMETRY AND THEIR CORRELATIONS WITH SUPERNOVA PROPERTIES. *The Astrophysical Journal*, 740(2):92, October 2011.

[65] J. Guy, P. Astier, S. Baumont, D. Hardin, R. Pain, N. Regnault, S. Basa, R. G. Carlberg, A. Conley, S. Fabbro, D. Fouchez, I. M. Hook, D. A. Howell, K. Perrett, C. J. Pritchet, J. Rich, M. Sullivan, P. Antilogus, E. Aubourg, G. Bazin, J. Bronder, M. Filiol, N. Palanque-Delabrouille, P. Ripoche, and V. Ruhlmann-Kleider. SALT2: using distant supernovae to improve the use of type Ia supernovae as distance indicators. A&A, 466(1):11–21, April 2007.

[66] Mario Hamuy, N. B. Suntzeff, S. R. Heathcote, A. R. Walker, P. Gigoux, and M. M. Phillips. Southern Spectrophotometric Standards. II. PASP, 106:566, June 1994.

[67] Mario Hamuy, A. R. Walker, N. B. Suntzeff, P. Gigoux, S. R. Heathcote, and M. M. Phillips. Southern Spectrophotometric Standards. I. PASP, 104:533, July 1992.

[68] Jared Hand, Shu Liu, Lluís Galbany, Daniel Perrefort, W. M. Wood-Vasey, and Chris Burns. The Dependence of the Type Ia Supernova Host Bias on Observation or Fitting Technique. ApJ, 925(2):115, February 2022.

[69] Charles R. Harris, K. Jarrod Millman, Stéfan J. van der Walt, Ralf Gommers, Pauli Virtanen, David Cournapeau, Eric Wieser, Julian Taylor, Sebastian Berg, Nathaniel J. Smith, Robert Kern, Matti Picus, Stephan Hoyer, Marten H. van Kerkwijk, Matthew Brett, Allan Haldane, Jaime Fernández del Río, Mark Wiebe, Pearu Peterson, Pierre Gérard-Marchant, Kevin Sheppard, Tyler Reddy, Warren Weckesser, Hameer Abbasi, Christoph Gohlke, and Travis E. Oliphant. Array programming with NumPy. *Nature*, 585(7825):357–362, September 2020.

[70] Brian T. Hayden, Ravi R. Gupta, Peter M. Garnavich, Filippo Mannucci, Robert C. Nichol, and Masao Sako. The Fundamental Metallicity Relation Reduces Type Ia SN Hubble Residuals More than Host Mass Alone. ApJ, 764(2):191, Feb 2013.

[71] Eckhard Hitzer. Introduction to Clifford's Geometric Algebra. *arXiv e-prints*, page arXiv:1306.1660, June 2013.

[72] David W. Hogg. Distance measures in cosmology. *arXiv e-prints*, pages astro–ph/9905116, May 1999.

[73] F. Hoyle and William A. Fowler. Nucleosynthesis in Supernovae. ApJ, 132:565, November 1960.

[74] Wayne Hu and Scott Dodelson. Cosmic Microwave Background Anisotropies. ARA&A, 40:171–216, January 2002.

[75] X. Huang, Z. Raha, G. Aldering, P. Antilogus, S. Bailey, C. Baltay, K. Barbary, D. Baugh, K. Boone, S. Bongard, C. Buton, J. Chen, N. Chotard, Y. Copin, P. Fagrelius, H. K. Fakhouri, U. Feindt, D. Fouchez, E. Gangler, B. Hayden, W. Hillebrandt, A. G. Kim, M. Kowalski, P. F. Leget, S. Lombardo, J. Nordin, R. Pain, E. Pecontal, R. Pereira, S. Perlmutter, D. Rabinowitz, M. Rigault, D. Rubin, K. Runge, C. Saunders, G. Smadja, C. Sofiatti, A. Stocker, N. Suzuki, S. Taubenberger, C. Tao, R. C. Thomas, and Nearby Supernova Factory. The Extinction Properties of and Distance to the Highly Reddened Type IA Supernova 2012CU. ApJ, 836(2):157, February 2017.

[76] Edwin Hubble. A Relation between Distance and Radial Velocity among Extra-Galactic Nebulae. *Proceedings of the National Academy of Science*, 15(3):168–173, March 1929.

[77] Dragan Huterer. Weak lensing and dark energy. Phys. Rev. D, 65(6):063001, March 2002.

[78] Jr. Iben, I. and A. V. Tutukov. Supernovae of type I as end products of the evolution of binaries with components of moderate initial mass. ApJS, 54:335–372, February 1984.

[79] Željko Ivezić, Steven M. Kahn, J. Anthony Tyson, Bob Abel, Emily Acosta, Robyn Allsman, David Alonso, Yusra AlSayyad, Scott F. Anderson, John Andrew, James Roger P. Angel, George Z. Angeli, Reza Ansari, Pierre Antilogus, Constanza Araujo, Robert Armstrong, Kirk T. Arndt, Pierre Astier, Éric Aubourg, Nicole Auza, Tim S. Axelrod, Deborah J. Bard, Jeff D. Barr, Aurelian Barrau, James G. Bartlett, Amanda E. Bauer, Brian J. Bauman, Sylvain Baumont, Ellen Bechtol, Keith Bechtol, Andrew C. Becker, Jacek Becla, Cristina Beldica, Steve Bellavia, Federica B. Bianco, Rahul Biswas, Guillaume Blanc, Jonathan Blazek, Roger D. Blandford, Josh S. Bloom, Joanne Bogart, Tim W. Bond, Michael T. Booth, Anders W. Borgland, Kirk Borne, James F. Bosch, Dominique Boutigny, Craig A. Brackett, Andrew Bradshaw, William Nielsen Brandt, Michael E. Brown, James S. Bullock, Patricia Burchat, David L. Burke, Gianpietro Cagnoli, Daniel Calabrese, Shawn Callahan, Alice L. Callen, Jeffrey L. Carlin, Erin L. Carlson, Srinivasan Chandrasekharan, Glenaver Charles-Emerson, Steve Chesley, Elliott C. Cheu, Hsin-Fang Chiang, James Chiang, Carol Chirino, Derek Chow, David R. Ciardi, Charles F. Claver, Johann Cohen-Tanugi, Joseph J. Cockrum, Rebecca Coles, Andrew J. Connolly, Kem H. Cook, Asantha Cooray, Kevin R. Covey, Chris Cribbs, Wei Cui, Roc Cutri, Philip N. Daly, Scott F. Daniel, Felipe Daruich, Guillaume Daubard, Greg Daues, William Dawson, Francisco Delgado, Alfred Dellapenna, Robert de Peyster, Miguel de Val-Borro, Seth W. Digel, Peter Doherty, Richard Dubois, Gregory P. Dubois-Felsmann, Josef Durech, Frossie Economou, Tim Eifler, Michael Eracleous, Benjamin L. Emmons, Angelo Fausti Neto, Henry Ferguson, Enrique Figueroa, Merlin Fisher-Levine, Warren Focke, Michael D. Foss, James Frank, Michael D. Freemon, Emmanuel Gangler, Eric Gawiser, John C. Geary, Perry Gee, Marla Geha, Charles J. B. Gessner, Robert R. Gibson, D. Kirk Gilmore, Thomas Glanzman, William Glick, Tatiana Goldina, Daniel A. Goldstein, Iain Goodenow, Melissa L. Graham, William J. Gressler, Philippe Gris, Leanne P. Guy, Augustin Guyonnet, Gunther Haller, Ron Harris, Patrick A. Hascall, Justine Haupt, Fabio Hernandez, Sven Herrmann, Edward Hileman, Joshua Hoblitt, John A. Hodgson, Craig Hogan, James D. Howard, Dajun Huang, Michael E. Huffer, Patrick Ingraham, Walter R. Innes, Suzanne H. Jacoby, Bhuvnesh Jain, Fabrice Jammes, M. James Jee, Tim Jenness, Garrett Jernigan, Darko Jevremović, Kenneth Johns, Anthony S. Johnson, Margaret W. G. Johnson, R. Lynne Jones, Claire Juramy-Gilles, Mario Jurić, Jason S. Kalirai, Nitya J. Kallivayalil, Bryce Kalmbach, Jeffrey P. Kantor, Pierre Karst, Mansi M. Kasliwal, Heather Kelly, Richard Kessler, Veronica Kinnison, David Kirkby, Lloyd Knox, Ivan V. Kotov, Victor L. Krabbendam, K. Simon Krughoff, Petr Kubánek, John Kuczewski, Shri Kulkarni, John Ku, Nadine R. Kurita, Craig S. Lage, Ron Lambert, Travis Lange, J. Brian Langton, Laurent Le Guillou, Deborah Levine, Ming Liang, Kian-Tat Lim, Chris J. Lintott, Kevin E. Long, Margaux Lopez, Paul J. Lotz, Robert H. Lupton, Nate B. Lust, Lauren A. MacArthur, Ashish Mahabal, Rachel Mandelbaum, Thomas W. Markiewicz,

Darren S. Marsh, Philip J. Marshall, Stuart Marshall, Morgan May, Robert McKercher, Michelle McQueen, Joshua Meyers, Myriam Migliore, Michelle Miller, David J. Mills, Connor Miraval, Joachim Moeyens, Fred E. Moolekamp, David G. Monet, Marc Moniez, Serge Monkewitz, Christopher Montgomery, Christopher B. Morrison, Fritz Mueller, Gary P. Muller, Freddy Muñoz Arancibia, Douglas R. Neill, Scott P. Newbry, Jean-Yves Nief, Andrei Nomerotski, Martin Nordby, Paul O'Connor, John Oliver, Scot S. Olivier, Knut Olsen, William O'Mullane, Sandra Ortiz, Shawn Osier, Russell E. Owen, Reynald Pain, Paul E. Palecek, John K. Parejko, James B. Parsons, Nathan M. Pease, J. Matt Peterson, John R. Peterson, Donald L. Petravick, M. E. Libby Petrick, Cathy E. Petry, Francesco Pierfederici, Stephen Pietrowicz, Rob Pike, Philip A. Pinto, Raymond Plante, Stephen Plate, Joel P. Plutchak, Paul A. Price, Michael Prouza, Veljko Radeka, Jayadev Rajagopal, Andrew P. Rasmussen, Nicolas Regnault, Kevin A. Reil, David J. Reiss, Michael A. Reuter, Stephen T. Ridgway, Vincent J. Riot, Steve Ritz, Sean Robinson, William Roby, Aaron Roodman, Wayne Rosing, Cecille Roucelle, Matthew R. Rumore, Stefano Russo, Abhijit Saha, Benoit Sassolas, Terry L. Schalk, Pim Schellart, Rafe H. Schindler, Samuel Schmidt, Donald P. Schneider, Michael D. Schneider, William Schoening, German Schumacher, Megan E. Schwamb, Jacques Sebag, Brian Selvy, Glenn H. Sembroski, Lynn G. Seppala, Andrew Serio, Eduardo Serrano, Richard A. Shaw, Ian Shipsey, Jonathan Sick, Nicole Silvestri, Colin T. Slater, J. Allyn Smith, R. Chris Smith, Shahram Sobhani, Christine Soldahl, Lisa Storrie-Lombardi, Edward Stover, Michael A. Strauss, Rachel A. Street, Christopher W. Stubbs, Ian S. Sullivan, Donald Sweeney, John D. Swinbank, Alexander Szalay, Peter Takacs, Stephen A. Tether, Jon J. Thaler, John Gregg Thayer, Sandrine Thomas, Adam J. Thornton, Vaikunth Thukral, Jeffrey Tice, David E. Trilling, Max Turri, Richard Van Berg, Daniel Vanden Berk, Kurt Vetter, Francoise Virieux, Tomislav Vucina, William Wahl, Lucianne Walkowicz, Brian Walsh, Christopher W. Walter, Daniel L. Wang, Shin-Yawn Wang, Michael Warner, Oliver Wiecha, Beth Willman, Scott E. Winters, David Wittman, Sidney C. Wolff, W. Michael Wood-Vasey, Xiuqin Wu, Bo Xin, Peter Yoachim, and Hu Zhan. LSST: From Science Drivers to Reference Design and Anticipated Data Products. ApJ, 873(2):111, March 2019.

[80] Saurabh Jha, Adam G. Riess, and Robert P. Kirshner. Improved Distances to Type Ia Supernovae with Multicolor Light-Curve Shapes: MLCS2k2. ApJ, 659(1):122–148, April 2007.

[81] Saurabh W. Jha, Kate Maguire, and Mark Sullivan. Observational properties of thermonuclear supernovae. *Nature Astronomy*, 3:706–716, August 2019.

[82] Jonas Johansson, Daniel Thomas, Janine Pforr, Claudia Maraston, Robert C. Nichol, Mathew Smith, Hubert Lampeitl, Alessandra Beifiori, Ravi R. Gupta, and Donald P. Schneider. SN Ia host galaxy properties from Sloan Digital Sky Survey-II spectroscopy. MNRAS, 435(2):1680–1700, October 2013.

[83] D. O. Jones, D. M. Scolnic, R. J. Foley, A. Rest, R. Kessler, P. M. Challis, K. C. Chambers, D. A. Coulter, K. G. Dettman, M. M. Foley, M. E. Huber, S. W. Jha, E. Johnson, C. D. Kilpatrick, R. P. Kirshner, J. Manuel, G. Narayan, Y. C. Pan, A. G. Riess, A. S. B. Schultz, M. R. Siebert, E. Berger, R. Chornock, H. Flewelling, E. A. Magnier, S. J. Smartt, K. W. Smith, R. J. Wainscoat, C. Waters, and M. Willman. The Foundation Supernova Survey: Measuring Cosmological Parameters with Supernovae from a Single Telescope. ApJ, 881(1):19, August 2019.

[84] David O. Jones, Adam G. Riess, and Daniel M. Scolnic. Reconsidering the Effects of Local Star Formation on Type Ia Supernova Cosmology. ApJ, 812(1):31, October 2015.

[85] Daniel Kasen and S. E. Woosley. On the Origin of the Type Ia Supernova Width-Luminosity Relation. ApJ, 656(2):661–665, February 2007.

[86] Guinevere Kauffmann, Timothy M. Heckman, Simon D. M. White, Stéphane Charlot, Christy Tremonti, Jarle Brinchmann, Gustavo Bruzual, Eric W. Peng, Mark Seibert, Mariangela Bernardi, Michael Blanton, Jon Brinkmann, Francisco Castander, Istvan Csábai, Masataka Fukugita, Zeljko Ivezic, Jeffrey A. Munn, Robert C. Nichol, Nikhil Padmanabhan, Aniruddha R. Thakar, David H. Weinberg, and Donald York. Stellar masses and star formation histories for 10$ˆ5$ galaxies from the Sloan Digital Sky Survey. MNRAS, 341(1):33–53, May 2003.

[87] Brandon C. Kelly. Some Aspects of Measurement Error in Linear Regression of Astronomical Data. ApJ, 665(2):1489–1506, August 2007.

[88] Patrick L. Kelly, Malcolm Hicken, David L. Burke, Kaisey S. Mandel, and Robert P. Kirshner. HUBBLE RESIDUALS OF NEARBY TYPE ia SUPERNOVAE ARE CORRELATED WITH HOST GALAXY MASSES. *The Astrophysical Journal*, 715(2):743–756, May 2010.

[89] L. Kelsey, M. Sullivan, M. Smith, P. Wiseman, D. Brout, T. M. Davis, C. Frohmaier, L. Galbany, M. Grayling, C. P. Gutiérrez, S. R. Hinton, R. Kessler, C. Lidman, A. Möller, M. Sako, D. Scolnic, S. A. Uddin, M. Vincenzi, T. M. C. Abbott, M. Aguena, S. Allam, J. Annis, S. Avila, D. Bacon, E. Bertin, D. Brooks, D. L. Burke, A. Carnero Rosell, M. Carrasco Kind, J. Carretero, F. J. Castander, M. Costanzi, L. N. da Costa, S. Desai, H. T. Diehl, P. Doel, S. Everett, I. Ferrero, A. Ferté, B. Flaugher, P. Fosalba, J. García-Bellido, D. W. Gerdes, D. Gruen, R. A. Gruendl, J. Gschwend, G. Gutierrez, D. L. Hollowood, K. Honscheid, D. J. James, A. G. Kim, K. Kuehn, N. Kuropatkin, O. Lahav, M. Lima, J. L. Marshall, P. Martini, F. Menanteau, R. Miquel, R. Morgan, R. L. C. Ogando, A. Palmese, F. Paz-Chinchón, A. A. Plazas, A. K. Romer, C. Sánchez, E. Sanchez, S. Serrano, I. Sevilla-Noarbe,

E. Suchyta, G. Tarle, D. Thomas, C. To, T. N. Varga, A. R. Walker, R. D. Wilkinson, and DES Collaboration. The effect of environment on Type Ia supernovae in the Dark Energy Survey three-year cosmological sample. MNRAS, 501(4):4861–4876, March 2021.

[90] Andreas Kelz, Marc A. W. Verheijen, Martin M. Roth, Svend M. Bauer, Thomas Becker, Jens Paschke, Emil Popow, Sebastian F. Sánchez, and Uwe Laux. PMAS: The Potsdam Multi-Aperture Spectrophotometer. II. The Wide Integral Field Unit PPak. PASP, 118(839):129–145, January 2006.

[91] Jr. Kennicutt, Robert C. Star Formation in Galaxies Along the Hubble Sequence. ARA&A, 36:189–232, January 1998.

[92] Robert C. Kennicutt and Neal J. Evans. Star Formation in the Milky Way and Nearby Galaxies. ARA&A, 50:531–608, September 2012.

[93] W. D. Kenworthy, D. O. Jones, M. Dai, R. Kessler, D. Scolnic, D. Brout, M. R. Siebert, J. D. R. Pierel, K. G. Dettman, G. Dimitriadis, R. J. Foley, S. W. Jha, Y. C. Pan, A. Riess, S. Rodney, and C. Rojas-Bravo. SALT3: An Improved Type Ia Supernova Model for Measuring Cosmic Distances. ApJ, 923(2):265, December 2021.

[94] R. Kessler, A. C. Becker, D. Cinabro, J. Vanderplas, J. A. Frieman, J. Marriner, T. M. Davis, B. Dilday, J. Holtzman, S. W. Jha, H. Lampeitl, M. Sako, M. Smith, C. Zheng, R. C. Nichol, B. Bassett, R. Bender, D. L. Depoy, M. Doi, E. Elson, A. V. Filippenko, R. J. Foley, P. M. Garnavich, U. Hopp, Y. Ihara, W. Ketzeback, W. Kollatschny, K. Konishi, J. L. Marshall, R. J. McMillan, G. Miknaitis, T. Morokuma, E. Mörtsell, K. Pan, J. L. Prieto, M. W. Richmond, A. G. Riess, R. Romani, D. P. Schneider, J. Sollerman, N. Takanashi, K. Tokita, K. van der Heyden, J. C. Wheeler, N. Yasuda, and D. York. First-Year Sloan Digital Sky Survey-II Supernova Results: Hubble Diagram and Cosmological Parameters. ApJS, 185:32–84, November 2009.

[95] Lisa J. Kewley and Sara L. Ellison. Metallicity Calibrations and the Mass-Metallicity Relation for Star-forming Galaxies. ApJ, 681(2):1183–1204, July 2008.

[96] A. G. Kim. Type Ia Supernova Intrinsic Magnitude Dispersion and the Fitting of Cosmological Parameters. PASP, 123(900):230, February 2011.

[97] Alex Kim, Ariel Goobar, and Saul Perlmutter. A Generalized K Correction for Type IA Supernovae: Comparing R-band Photometry beyond z=0.2 with B, V, and R-band Nearby Photometry. PASP, 108:190, February 1996.

[98] M. Kriek, P. G. van Dokkum, I. Labbé, M. Franx, G. D. Illingworth, D. Marchesini, and R. F. Quadri. An Ultra-Deep Near-Infrared Spectrum of a Compact Quiescent Galaxy at z = 2.2. ApJ, 700:221–231, July 2009.

[99] Hubert Lampeitl, Mathew Smith, Robert C. Nichol, Bruce Bassett, David Cinabro, Benjamin Dilday, Ryan J. Foley, Joshua A. Frieman, Peter M. Garnavich, Ariel Goobar, Myungshin Im, Saurabh W. Jha, John Marriner, Ramon Miquel, Jakob Nordin, Linda Östman, Adam G. Riess, Masao Sako, Donald P. Schneider, Jesper Sollerman, and Maximilian Stritzinger. THE EFFECT OF HOST GALAXIES ON TYPE ia SUPERNOVAE IN THE SDSS-II SUPERNOVA SURVEY. *The Astrophysical Journal*, 722(1):566–576, September 2010.

[100] Blandine Lantz, Greg Aldering, Pierre Antilogus, Christophe Bonnaud, Lionel Capoani, Alain Castera, Yannick Copin, Dominique Dubet, Emmanuel Gangler, Francois Henault, Jean-Pierre Lemonnier, Reynald Pain, Arlette Pecontal, Emmanuel Pecontal, and Gerard Smadja. SNIFS: a wideband integral field spectrograph with microlens arrays. In Laurent Mazuray, Philip J. Rogers, and Rolf Wartmann, editors, *Optical Design and Engineering*, volume 5249 of *Society of Photo-Optical Instrumentation Engineers (SPIE) Conference Series*, pages 146–155, February 2004.

[101] P. F. Léget, E. Gangler, F. Mondon, G. Aldering, P. Antilogus, C. Aragon, S. Bailey, C. Baltay, K. Barbary, S. Bongard, K. Boone, C. Buton, N. Chotard, Y. Copin, S. Dixon, P. Fagrelius, U. Feindt, D. Fouchez, B. Hayden, W. Hillebrandt, A. Kim, M. Kowalski, D. Kuesters, S. Lombardo, Q. Lin, J. Nordin, R. Pain, E. Pecontal, R. Pereira, S. Perlmutter, K. A. Ponder, M. V. Pruzhinskaya, D. Rabinowitz, M. Rigault, K. Runge, D. Rubin, C. Saunders, L. P. Says, G. Smadja, C. Sofiatti, N. Suzuki, S. Taubenberger, C. Tao, and R. C. Thomas. SUGAR: An improved empirical model of Type Ia supernovae based on spectral features. A&A, 636:A46, April 2020.

[102] Claus Leitherer, Daniel Schaerer, Jeffrey D. Goldader, Rosa M. González Delgado, Carmelle Robert, Denis Foo Kune, Duília F. de Mello, Daniel Devost, and Timothy M. Heckman. Starburst99: Synthesis Models for Galaxies with Active Star Formation. ApJS, 123(1):3–40, July 1999.

[103] G. Lemaître. A homogeneous universe of constant mass and increasing radius accounting for the radial velocity of extra-galactic nebulae. MNRAS, 91:483–490, March 1931.

[104] Carlos López-Cobá, Sebastián F. Sánchez, Joseph P. Anderson, Irene Cruz-González, Lluís Galbany, Tomás Ruiz-Lara, Jorge K. Barrera-Ballesteros, José L. Prieto, and Hanindyo Kuncarayakti. The AMUSING++ Nearby Galaxy Compilation. I. Full

Sample Characterization and Galactic-scale Outflow Selection. AJ, 159(4):167, April 2020.

[105] K. G. Malmquist. On some relations in stellar statistics. *Meddelanden fran Lunds Astronomiska Observatorium Serie I*, 100:1–52, March 1922.

[106] A. I. Malz, R. Hložek, Jr. Allam, T., A. Bahmanyar, R. Biswas, M. Dai, L. Galbany, E. E. O. Ishida, S. W. Jha, D. O. Jones, R. Kessler, M. Lochner, A. A. Mahabal, K. S. Mandel, J. R. Martínez-Galarza, J. D. McEwen, D. Muthukrishna, G. Narayan, H. Peiris, C. M. Peters, K. Ponder, C. N. Setzer, (the LSST Dark Energy Science Collaboration, the LSST Transients, and Variable Stars Science Collaboration. The Photometric LSST Astronomical Time-series Classification Challenge PLAsTiCC: Selection of a Performance Metric for Classification Probabilities Balancing Diverse Science Goals. AJ, 158(5):171, November 2019.

[107] Kaisey S. Mandel, Daniel M. Scolnic, Hikmatali Shariff, Ryan J. Foley, and Robert P. Kirshner. The Type Ia Supernova Color-Magnitude Relation and Host Galaxy Dust: A Simple Hierarchical Bayesian Model. ApJ, 842(2):93, June 2017.

[108] Kaisey S. Mandel, Stephen Thorp, Gautham Narayan, Andrew S. Friedman, and Arturo Avelino. A hierarchical Bayesian SED model for Type Ia supernovae in the optical to near-infrared. MNRAS, 510(3):3939–3966, March 2022.

[109] Rachel Mandelbaum. Weak Lensing for Precision Cosmology. ARA&A, 56:393–433, September 2018.

[110] F. Mannucci, G. Cresci, R. Maiolino, A. Marconi, and A. Gnerucci. A fundamental relation between mass, star formation rate and metallicity in local and high-redshift galaxies. MNRAS, 408(4):2115–2127, Nov 2010.

[111] Dan Maoz, Filippo Mannucci, and Gijs Nelemans. Observational Clues to the Progenitors of Type Ia Supernovae. ARA&A, 52:107–170, August 2014.

[112] J. Marriner, J. P. Bernstein, Richard Kessler, Hubert Lampeitl, Ramon Miquel, Jennifer Mosher, Robert C. Nichol, Masao Sako, Donald P. Schneider, and Mathew Smith. A More General Model for the Intrinsic Scatter in Type Ia Supernova Distance Moduli. ApJ, 740(2):72, October 2011.

[113] D. Christopher Martin, James Fanson, David Schiminovich, Patrick Morrissey, Peter G. Friedman, Tom A. Barlow, Tim Conrow, Robert Grange, Patrick N. Jelinsky,

Bruno Milliard, Oswald H. W. Siegmund, Luciana Bianchi, Yong-Ik Byun, Jose Donas, Karl Forster, Timothy M. Heckman, Young-Wook Lee, Barry F. Madore, Roger F. Malina, Susan G. Neff, R. Michael Rich, Todd Small, Frank Surber, Alex S. Szalay, Barry Welsh, and Ted K. Wyder. The Galaxy Evolution Explorer: A Space Ultraviolet Survey Mission. ApJ, 619(1):L1–L6, January 2005.

[114] R. Minkowski. Spectra of Supernovae. PASP, 53(314):224, August 1941.

[115] Patrick Morrissey, Tim Conrow, Tom A. Barlow, Todd Small, Mark Seibert, Ted K. Wyder, Tamás Budavári, Stephane Arnouts, Peter G. Friedman, and Karl Forster. The Calibration and Data Products of GALEX. ApJS, 173(2):682–697, December 2007.

[116] John Moustakas, Alison L. Coil, James Aird, Michael R. Blanton, Richard J. Cool, Daniel J. Eisenstein, Alexander J. Mendez, Kenneth C. Wong, Guangtun Zhu, and Stéphane Arnouts. PRIMUS: Constraints on Star Formation Quenching and Galaxy Merging, and the Evolution of the Stellar Mass Function from z = 0-1. ApJ, 767(1):50, April 2013.

[117] Peter Nugent, Alex Kim, and Saul Perlmutter. K-Corrections and Extinction Corrections for Type Ia Supernovae. PASP, 114(798):803–819, August 2002.

[118] Peter Nugent, Mark Phillips, E. Baron, David Branch, and Peter Hauschildt. Evidence for a Spectroscopic Sequence among Type 1a Supernovae. ApJ, 455:L147, December 1995.

[119] The pandas development team. pandas-dev/pandas: Pandas, February 2020.

[120] F. Pedregosa, G. Varoquaux, A. Gramfort, V. Michel, B. Thirion, O. Grisel, M. Blondel, P. Prettenhofer, R. Weiss, V. Dubourg, J. Vanderplas, A. Passos, D. Cournapeau, M. Brucher, M. Perrot, and E. Duchesnay. Scikit-learn: Machine learning in Python. *Journal of Machine Learning Research*, 12:2825–2830, 2011.

[121] P. J. E. Peebles. Large-scale background temperature and mass fluctuations due to scale-invariant primeval perturbations. ApJ, 263:L1–L5, December 1982.

[122] R. Pereira, R. C. Thomas, G. Aldering, P. Antilogus, C. Baltay, S. Benitez-Herrera, S. Bongard, C. Buton, A. Canto, F. Cellier-Holzem, J. Chen, M. Childress, N. Chotard, Y. Copin, H. K. Fakhouri, M. Fink, D. Fouchez, E. Gangler, J. Guy, W. Hillebrandt, E. Y. Hsiao, M. Kerschhaggl, M. Kowalski, M. Kromer, J. Nordin,

P. Nugent, K. Paech, R. Pain, E. Pécontal, S. Perlmutter, D. Rabinowitz, M. Rigault, K. Runge, C. Saunders, G. Smadja, C. Tao, S. Taubenberger, A. Tilquin, and C. Wu. Spectrophotometric time series of SN 2011fe from the Nearby Supernova Factory. A&A, 554:A27, June 2013.

[123] S. Perlmutter, G. Aldering, G. Goldhaber, R. A. Knop, P. Nugent, P. G. Castro, S. Deustua, S. Fabbro, A. Goobar, D. E. Groom, I. M. Hook, A. G. Kim, M. Y. Kim, J. C. Lee, N. J. Nunes, R. Pain, C. R. Pennypacker, R. Quimby, C. Lidman, R. S. Ellis, M. Irwin, R. G. McMahon, P. Ruiz-Lapuente, N. Walton, B. Schaefer, B. J. Boyle, A. V. Filippenko, T. Matheson, A. S. Fruchter, N. Panagia, H. J. M. Newberg, W. J. Couch, and The Supernova Cosmology Project. Measurements of Omega and Lambda from 42 High-Redshift Supernovae. ApJ, 517:565–586, June 1999.

[124] M. M. Phillips. The absolute magnitudes of Type IA supernovae. ApJ, 413:L105–L108, August 1993.

[125] M. M. Phillips, Joshua D. Simon, Nidia Morrell, Christopher R. Burns, Nick L. J. Cox, Ryan J. Foley, Amanda I. Karakas, F. Patat, A. Sternberg, R. E. Williams, A. Gal-Yam, E. Y. Hsiao, D. C. Leonard, Sven E. Persson, Maximilian Stritzinger, I. B. Thompson, Abdo Campillay, Carlos Contreras, Gastón Folatelli, Wendy L. Freedman, Mario Hamuy, Miguel Roth, Gregory A. Shields, Nicholas B. Suntzeff, Laura Chomiuk, Inese I. Ivans, Barry F. Madore, B. E. Penprase, Daniel Perley, G. Pignata, G. Preston, and Alicia M. Soderberg. On the Source of the Dust Extinction in Type Ia Supernovae and the Discovery of Anomalously Strong Na I Absorption. ApJ, 779(1):38, December 2013.

[126] J. D. R. Pierel, D. O. Jones, W. D. Kenworthy, M. Dai, R. Kessler, C. Ashall, A. Do, E. R. Peterson, B. J. Shappee, M. R. Siebert, T. Barna, T. G. Brink, J. Burke, A. Calamida, Y. Camacho-Neves, T. de Jaeger, A. V. Filippenko, R. J. Foley, L. Galbany, O. D. Fox, S. Gomez, D. Hiramatsu, R. Hounsell, D. A. Howell, S. W. Jha, L. A. Kwok, I. Pérez-Fournon, F. Poidevin, A. Rest, D. Rubin, D. M. Scolnic, R. Shirley, L. G. Strolger, S. Tinyanont, and Q. Wang. SALT3-NIR: Taking the Open-source Type Ia Supernova Model to Longer Wavelengths for Next-generation Cosmological Measurements. ApJ, 939(1):11, November 2022.

[127] Planck Collaboration, N. Aghanim, Y. Akrami, M. Ashdown, J. Aumont, C. Baccigalupi, M. Ballardini, A. J. Banday, R. B. Barreiro, N. Bartolo, S. Basak, R. Battye, K. Benabed, J. P. Bernard, M. Bersanelli, P. Bielewicz, J. J. Bock, J. R. Bond, J. Borrill, F. R. Bouchet, F. Boulanger, M. Bucher, C. Burigana, R. C. Butler, E. Calabrese, J. F. Cardoso, J. Carron, A. Challinor, H. C. Chiang, J. Chluba, L. P. L. Colombo, C. Combet, D. Contreras, B. P. Crill, F. Cuttaia, P. de Bernardis, G. de Zotti, J. Delabrouille, J. M. Delouis, E. Di Valentino, J. M. Diego, O. Doré, M. Douspis,

A. Ducout, X. Dupac, S. Dusini, G. Efstathiou, F. Elsner, T. A. Enßlin, H. K. Eriksen, Y. Fantaye, M. Farhang, J. Fergusson, R. Fernandez-Cobos, F. Finelli, F. Forastieri, M. Frailis, E. Franceschi, A. Frolov, S. Galeotta, S. Galli, K. Ganga, R. T. Génova-Santos, M. Gerbino, T. Ghosh, J. González-Nuevo, K. M. Górski, S. Gratton, A. Gruppuso, J. E. Gudmundsson, J. Hamann, W. Hand ley, D. Herranz, E. Hivon, Z. Huang, A. H. Jaffe, W. C. Jones, A. Karakci, E. Keihänen, R. Keskitalo, K. Kiiveri, J. Kim, T. S. Kisner, L. Knox, N. Krachmalnicoff, M. Kunz, H. Kurki-Suonio, G. Lagache, J. M. Lamarre, A. Lasenby, M. Lattanzi, C. R. Lawrence, M. Le Jeune, P. Lemos, J. Lesgourgues, F. Levrier, A. Lewis, M. Liguori, P. B. Lilje, M. Lilley, V. Lindholm, M. López-Caniego, P. M. Lubin, Y. Z. Ma, J. F. Macías-Pérez, G. Maggio, D. Maino, N. Mandolesi, A. Mangilli, A. Marcos-Caballero, M. Maris, P. G. Martin, M. Martinelli, E. Martínez-González, S. Matarrese, N. Mauri, J. D. McEwen, P. R. Meinhold, A. Melchiorri, A. Mennella, M. Migliaccio, M. Millea, S. Mitra, M. A. Miville-Deschênes, D. Molinari, L. Montier, G. Morgante, A. Moss, P. Natoli, H. U. Nørgaard-Nielsen, L. Pagano, D. Paoletti, B. Partridge, G. Patanchon, H. V. Peiris, F. Perrotta, V. Pettorino, F. Piacentini, L. Polastri, G. Polenta, J. L. Puget, J. P. Rachen, M. Reinecke, M. Remazeilles, A. Renzi, G. Rocha, C. Rosset, G. Roudier, J. A. Rubiño-Martín, B. Ruiz-Granados, L. Salvati, M. Sandri, M. Savelainen, D. Scott, E. P. S. Shellard, C. Sirignano, G. Sirri, L. D. Spencer, R. Sunyaev, A. S. Suur-Uski, J. A. Tauber, D. Tavagnacco, M. Tenti, L. Toffolatti, M. Tomasi, T. Trombetti, L. Valenziano, J. Valiviita, B. Van Tent, L. Vibert, P. Vielva, F. Villa, N. Vittorio, B. D. Wand elt, I. K. Wehus, M. White, S. D. M. White, A. Zacchei, and A. Zonca. Planck 2018 results. VI. Cosmological parameters. *arXiv e-prints*, page arXiv:1807.06209, July 2018.

[128] Kara A. Ponder, W. Michael Wood-Vasey, Anja Weyant, Nathan T. Barton, Lluis Galbany, Peter Garnavich, and Thomas Matheson. Are Type Ia Supernovae in Rest-frame H Brighter in More Massive Galaxies? *arXiv e-prints*, page arXiv:2006.13803, June 2020.

[129] Brodie Popovic, Dillon Brout, Richard Kessler, Dan Scolnic, and Lisa Lu. Improved Treatment of Host-Galaxy Correlations in Cosmological Analyses With Type Ia Supernovae. *arXiv e-prints*, page arXiv:2102.01776, February 2021.

[130] M. V. Pruzhinskaya, A. K. Novinskaya, N. Pauna, and P. Rosnet. The dependence of Type Ia Supernovae SALT2 light-curve parameters on host galaxy morphology. MNRAS, 499(4):5121–5135, December 2020.

[131] A. G. Riess, A. V. Filippenko, P. Challis, A. Clocchiatti, A. Diercks, P. M. Garnavich, R. L. Gilliland, C. J. Hogan, S. Jha, R. P. Kirshner, B. Leibundgut, M. M. Phillips, D. Reiss, B. P. Schmidt, R. A. Schommer, R. C. Smith, J. Spyromilio, C. Stubbs, N. B. Suntzeff, and J. Tonry. Observational Evidence from Supernovae for an Accelerating Universe and a Cosmological Constant. AJ, 116:1009–1038, September 1998.

[132] A. G. Riess, W. H. Press, and R. P. Kirshner. A Precise Distance Indicator: Type IA Supernova Multicolor Light-Curve Shapes. ApJ, 473:88, December 1996.

[133] Adam G. Riess, Stefano Casertano, Wenlong Yuan, Lucas M. Macri, and Dan Scolnic. Large Magellanic Cloud Cepheid Standards Provide a 1% Foundation for the Determination of the Hubble Constant and Stronger Evidence for Physics Beyond LambdaCDM. *arXiv e-prints*, page arXiv:1903.07603, March 2019.

[134] Adam G. Riess, Peter Nugent, Alexei V. Filippenko, Robert P. Kirshner, and Saul Perlmutter. Snapshot Distances to Type IA Supernovae: All in "One" Night's Work. ApJ, 504(2):935–944, September 1998.

[135] Adam G. Riess, William H. Press, and Robert P. Kirshner. A Precise Distance Indicator: Type IA Supernova Multicolor Light-Curve Shapes. ApJ, 473:88, December 1996.

[136] M. Rigault, G. Aldering, M. Kowalski, Y. Copin, P. Antilogus, C. Aragon, S. Bailey, C. Baltay, D. Baugh, S. Bongard, K. Boone, C. Buton, J. Chen, N. Chotard, H. K. Fakhouri, U. Feindt, P. Fagrelius, M. Fleury, D. Fouchez, E. Gangler, B. Hayden, A. G. Kim, P.-F. Leget, S. Lombardo, J. Nordin, R. Pain, E. Pecontal, R. Pereira, S. Perlmutter, D. Rabinowitz, K. Runge, D. Rubin, C. Saunders, G. Smadja, C. Sofiatti, N. Suzuki, C. Tao, and B. A. Weaver. CONFIRMATION OF a STAR FORMATION BIAS IN TYPE ia SUPERNOVA DISTANCES AND ITS EFFECT ON THE MEASUREMENT OF THE HUBBLE CONSTANT. *The Astrophysical Journal*, 802(1):20, March 2015.

[137] M. Rigault, V. Brinnel, G. Aldering, P. Antilogus, C. Aragon, S. Bailey, C. Baltay, K. Barbary, S. Bongard, K. Boone, C. Buton, M. Childress, N. Chotard, Y. Copin, S. Dixon, P. Fagrelius, U. Feindt, D. Fouchez, E. Gangler, B. Hayden, W. Hillebrandt, D. A. Howell, A. Kim, M. Kowalski, D. Kuesters, P. F. Leget, S. Lombardo, Q. Lin, J. Nordin, R. Pain, E. Pecontal, R. Pereira, S. Perlmutter, D. Rabinowitz, K. Runge, D. Rubin, C. Saunders, G. Smadja, C. Sofiatti, N. Suzuki, S. Taubenberger, C. Tao, and R. C. Thomas. Strong dependence of Type Ia supernova standardization on the local specific star formation rate. A&A, 644:A176, December 2020.

[138] M. Rigault, Y. Copin, G. Aldering, P. Antilogus, C. Aragon, S. Bailey, C. Baltay, S. Bongard, C. Buton, A. Canto, F. Cellier-Holzem, M. Childress, N. Chotard, H. K. Fakhouri, U. Feindt, M. Fleury, E. Gangler, P. Greskovic, J. Guy, A. G. Kim, M. Kowalski, S. Lombardo, J. Nordin, P. Nugent, R. Pain, E. Pécontal, R. Pereira, S. Perlmutter, D. Rabinowitz, Runge, K., C. Saunders, R. Scalzo, G. Smadja, C. Tao, R. C. Thomas, B. A. Weaver, and The Nearby Supernova Factory. Evidence of en-

vironmental dependencies of type ia supernovae from the nearby supernova factory indicated by local h. *A&A*, 560:A66, 2013.

[139] Robert Kern and the Clifford Team. clifford: Geometric algebra for python.

[140] M. Roman, D. Hardin, M. Betoule, P. Astier, C. Balland, R. S. Ellis, S. Fabbro, J. Guy, I. Hook, and D. A. Howell. Dependence of Type Ia supernova luminosities on their local environment. A&A, 615:A68, July 2018.

[141] B. M. Rose, P. M. Garnavich, and M. A. Berg. Think Global, Act Local: The Influence of Environment Age and Host Mass on Type Ia Supernova Light Curves. ApJ, 874(1):32, March 2019.

[142] B. M. Rose, D. Rubin, L. Strolger, and P. M. Garnavich. Host Galaxy Mass Combined with Local Stellar Age Improve Type Ia Supernovae Distances. *arXiv e-prints*, page arXiv:2012.01460, December 2020.

[143] Martin M. Roth, Andreas Kelz, Thomas Fechner, Thomas Hahn, Svend-Marian Bauer, Thomas Becker, Petra Böhm, Lise Christensen, Frank Dionies, Jens Paschke, Emil Popow, Dieter Wolter, Jürgen Schmoll, Uwe Laux, and Werner Altmann. PMAS: The Potsdam Multi-Aperture Spectrophotometer. I. Design, Manufacture, and Performance. PASP, 117(832):620–642, June 2005.

[144] D. Rubin, G. Aldering, K. Barbary, K. Boone, G. Chappell, M. Currie, S. Deustua, P. Fagrelius, A. Fruchter, B. Hayden, C. Lidman, J. Nordin, S. Perlmutter, C. Saunders, C. Sofiatti, and The Supernova Cosmology Project. UNITY: Confronting Supernova Cosmology's Statistical and Systematic Uncertainties in a Unified Bayesian Framework. ApJ, 813(2):137, November 2015.

[145] Masao Sako, Bruce Bassett, Andrew C. Becker, Peter J. Brown, Heather Campbell, Rachel Wolf, David Cinabro, Chris B. D'Andrea, Kyle S. Dawson, Fritz DeJongh, Darren L. Depoy, Ben Dilday, Mamoru Doi, Alexei V. Filippenko, John A. Fischer, Ryan J. Foley, Joshua A. Frieman, Lluis Galbany, Peter M. Garnavich, Ariel Goobar, Ravi R. Gupta, Gary J. Hill, Brian T. Hayden, Renée Hlozek, Jon A. Holtzman, Ulrich Hopp, Saurabh W. Jha, Richard Kessler, Wolfram Kollatschny, Giorgos Leloudas, John Marriner, Jennifer L. Marshall, Ramon Miquel, Tomoki Morokuma, Jennifer Mosher, Robert C. Nichol, Jakob Nordin, Matthew D. Olmstead, Linda Östman, Jose L. Prieto, Michael Richmond, Roger W. Romani, Jesper Sollerman, Max Stritzinger, Donald P. Schneider, Mathew Smith, J. Craig Wheeler, Naoki Yasuda, and Chen Zheng. The data release of the sloan digital sky survey-II supernova

survey. *Publications of the Astronomical Society of the Pacific*, 130(988):64002, May 2018.

[146] S. F. Sánchez, R. García-Benito, S. Zibetti, C. J. Walcher, B. Husemann, M. A. Mendoza, L. Galbany, J. Falcón-Barroso, D. Mast, J. Aceituno, J. A. L. Aguerri, J. Alves, A. L. Amorim, Y. Ascasibar, D. Barrado-Navascues, J. Barrera-Ballesteros, S. Bekeraitè, J. Bland -Hawthorn, M. Cano Díaz, R. Cid Fernandes, O. Cavichia, C. Cortijo, H. Dannerbauer, M. Demleitner, A. Díaz, R. J. Dettmar, A. de Lorenzo-Cáceres, A. del Olmo, A. Galazzi, B. García-Lorenzo, A. Gil de Paz, R. González Delgado, L. Holmes, J. Iglésias-Páramo, C. Kehrig, A. Kelz, R. C. Kennicutt, B. Kleemann, E. A. D. Lacerda, R. López Fernández, A. R. López Sánchez, M. Lyubenova, R. Marino, I. Márquez, J. Mendez-Abreu, M. Mollá, A. Monreal-Ibero, R. Ortega Minakata, J. P. Torres-Papaqui, E. Pérez, F. F. Rosales-Ortega, M. M. Roth, P. Sánchez-Blázquez, U. Schilling, K. Spekkens, N. Vale Asari, R. C. E. van den Bosch, G. van de Ven, J. M. Vilchez, V. Wild, L. Wisotzki, A. Yıldırım, and B. Ziegler. CALIFA, the Calar Alto Legacy Integral Field Area survey. IV. Third public data release. A&A, 594:A36, October 2016.

[147] C. Saunders, G. Aldering, P. Antilogus, S. Bailey, C. Baltay, K. Barbary, D. Baugh, K. Boone, S. Bongard, C. Buton, J. Chen, N. Chotard, Y. Copin, S. Dixon, P. Fagrelius, H. K. Fakhouri, U. Feindt, D. Fouchez, E. Gangler, B. Hayden, W. Hillebrandt, A. G. Kim, M. Kowalski, D. Küsters, P. F. Leget, S. Lombardo, J. Nordin, R. Pain, E. Pecontal, R. Pereira, S. Perlmutter, D. Rabinowitz, M. Rigault, D. Rubin, K. Runge, G. Smadja, C. Sofiatti, N. Suzuki, C. Tao, S. Taubenberger, R. C. Thomas, M. Vincenzi, and The Nearby Supernova Factory. SNEMO: Improved Empirical Models for Type Ia Supernovae. ApJ, 869(2):167, December 2018.

[148] R. A. Scalzo, A. J. Ruiter, and S. A. Sim. The ejected mass distribution of Type Ia supernovae: a significant rate of non-Chandrasekhar-mass progenitors. MNRAS, 445(3):2535–2544, December 2014.

[149] David J. Schlegel, Douglas P. Finkbeiner, and Marc Davis. Maps of Dust Infrared Emission for Use in Estimation of Reddening and Cosmic Microwave Background Radiation Foregrounds. ApJ, 500(2):525–553, June 1998.

[150] C Schreiber. Fast++. `https://github.com/cschreib/fastpp`, 2019.

[151] C. Schreiber, K. Glazebrook, T. Nanayakkara, G. G. Kacprzak, I. Labbé, P. Oesch, T. Yuan, K. V. Tran, C. Papovich, and L. Spitler. Near infrared spectroscopy and star-formation histories of $3 \leq z \leq 4$ quiescent galaxies. A&A, 618:A85, October 2018.

[152] D. M. Scolnic, D. O. Jones, A. Rest, Y. C. Pan, R. Chornock, R. J. Foley, M. E. Huber, R. Kessler, G. Narayan, A. G. Riess, S. Rodney, E. Berger, D. J. Brout, P. J. Challis, M. Drout, D. Finkbeiner, R. Lunnan, R. P. Kirshner, N. E. Sand ers, E. Schlafly, S. Smartt, C. W. Stubbs, J. Tonry, W. M. Wood-Vasey, M. Foley, J. Hand, E. Johnson, W. S. Burgett, K. C. Chambers, P. W. Draper, K. W. Hodapp, N. Kaiser, R. P. Kudritzki, E. A. Magnier, N. Metcalfe, F. Bresolin, E. Gall, R. Kotak, M. McCrum, and K. W. Smith. The Complete Light-curve Sample of Spectroscopically Confirmed SNe Ia from Pan-STARRS1 and Cosmological Constraints from the Combined Pantheon Sample. ApJ, 859(2):101, June 2018.

[153] Daniel M. Scolnic, Adam G. Riess, Ryan J. Foley, Armin Rest, Steven A. Rodney, Dillon J. Brout, and David O. Jones. Color Dispersion and Milky-Way-like Reddening among Type Ia Supernovae. ApJ, 780(1):37, January 2014.

[154] M. F. Skrutskie, R. M. Cutri, R. Stiening, M. D. Weinberg, S. Schneider, J. M. Carpenter, C. Beichman, R. Capps, T. Chester, J. Elias, J. Huchra, J. Liebert, C. Lonsdale, D. G. Monet, S. Price, P. Seitzer, T. Jarrett, J. D. Kirkpatrick, J. E. Gizis, E. Howard, T. Evans, J. Fowler, L. Fullmer, R. Hurt, R. Light, E. L. Kopan, K. A. Marsh, H. L. McCallon, R. Tam, S. Van Dyk, and S. Wheelock. The Two Micron All Sky Survey (2MASS). AJ, 131(2):1163–1183, February 2006.

[155] M. Smith, M. Sullivan, P. Wiseman, R. Kessler, D. Scolnic, D. Brout, C. B. D'Andrea, T. M. Davis, R. J. Foley, C. Frohmaier, L. Galbany, R. R. Gupta, C. P. Gutiérrez, S. R. Hinton, L. Kelsey, C. Lidman, E. Macaulay, A. Möller, R. C. Nichol, P. Nugent, A. Palmese, M. Pursiainen, M. Sako, E. Swann, R. C. Thomas, B. E. Tucker, M. Vincenzi, D. Carollo, G. F. Lewis, N. E. Sommer, T. M. C. Abbott, M. Aguena, S. Allam, S. Avila, E. Bertin, S. Bhargava, D. Brooks, E. Buckley-Geer, D. L. Burke, A. Carnero Rosell, M. Carrasco Kind, M. Costanzi, L. N. da Costa, J. De Vicente, S. Desai, H. T. Diehl, P. Doel, T. F. Eifler, S. Everett, B. Flaugher, P. Fosalba, J. Frieman, J. García-Bellido, E. Gaztanaga, K. Glazebrook, D. Gruen, R. A. Gruendl, J. Gschwend, G. Gutierrez, W. G. Hartley, D. L. Hollowood, K. Honscheid, D. J. James, E. Krause, K. Kuehn, N. Kuropatkin, M. Lima, N. MacCrann, M. A. G. Maia, J. L. Marshall, P. Martini, P. Melchior, F. Menanteau, R. Miquel, F. Paz-Chinchón, A. A. Plazas, A. K. Romer, A. Roodman, E. S. Rykoff, E. Sanchez, V. Scarpine, M. Schubnell, S. Serrano, I. Sevilla-Noarbe, E. Suchyta, M. E. C. Swanson, G. Tarle, D. Thomas, D. L. Tucker, T. N. Varga, A. R. Walker, and DES Collaboration. First cosmology results using type Ia supernovae from the Dark Energy Survey: the effect of host galaxy properties on supernova luminosity. MNRAS, 494(3):4426–4447, April 2020.

[156] Noam Soker. Supernovae Ia in 2019 (review): A rising demand for spherical explosions. New A Rev., 87:101535, December 2019.

[157] George Stein, Uros Seljak, Vanessa Bohm, G. Aldering, P. Antilogus, C. Aragon, S. Bailey, C. Baltay, S. Bongard, K. Boone, C. Buton, Y. Copin, S. Dixon, D. Fouchez, E. Gangler, R. Gupta, B. Hayden, W. Hillebrandt, M. Karmen, A. G. Kim, M. Kowalski, D. Kusters, P. F. Leget, F. Mondon, J. Nordin, R. Pain, E. Pecontal, R. Pereira, S. Perlmutter, K. A. Ponder, D. Rabinowitz, M. Rigault, D. Rubin, K. Runge, C. Saunders, G. Smadja, N. Suzuki, C. Tao, R. C. Thomas, and M. Vincenzi. A Probabilistic Autoencoder for Type Ia Supernovae Spectral Time Series. *arXiv e-prints*, page arXiv:2207.07645, July 2022.

[158] M. Sullivan, A. Conley, D. A. Howell, J. D. Neill, P. Astier, C. Balland, S. Basa, R. G. Carlberg, D. Fouchez, J. Guy, D. Hardin, I. M. Hook, R. Pain, N. Palanque-Delabrouille, K. M. Perrett, C. J. Pritchet, N. Regnault, J. Rich, V. Ruhlmann-Kleider, S. Baumont, E. Hsiao, T. Kronborg, C. Lidman, S. Perlmutter, and E. S. Walker. The dependence of Type Ia Supernovae luminosities on their host galaxies. *Monthly Notices of the Royal Astronomical Society*, 406(2):782–802, 7 2010.

[159] Stephen Thorp, Kaisey S. Mandel, David O. Jones, Sam M. Ward, and Gautham Narayan. Testing the consistency of dust laws in SN Ia host galaxies: a BAYESN examination of Foundation DR1. MNRAS, 508(3):4310–4331, December 2021.

[160] Christy A. Tremonti, Timothy M. Heckman, Guinevere Kauffmann, Jarle Brinchmann, Stéphane Charlot, Simon D. M. White, Mark Seibert, Eric W. Peng, David J. Schlegel, Alan Uomoto, Masataka Fukugita, and Jon Brinkmann. The Origin of the Mass-Metallicity Relation: Insights from 53,000 Star-forming Galaxies in the Sloan Digital Sky Survey. ApJ, 613(2):898–913, October 2004.

[161] Robert Tripp. A two-parameter luminosity correction for Type IA supernovae. A&A, 331:815–820, March 1998.

[162] Syed A. Uddin, Christopher R. Burns, M. M. Phillips, Nicholas B. Suntzeff, Carlos Contreras, Eric Y. Hsiao, Nidia Morrell, Lluís Galbany, Maximilian Stritzinger, Peter Hoeflich, Chris Ashall, Anthony L. Piro, Wendy L. Freedman, S. E. Persson, Kevin Krisciunas, and Peter Brown. The Carnegie Supernova Project-I: Correlation Between Type Ia Supernovae and Their Host Galaxies from Optical to Near-Infrared Bands. *arXiv e-prints*, page arXiv:2006.15164, June 2020.

[163] Aki Vehtari, Andrew Gelman, Daniel Simpson, Bob Carpenter, and Paul-Christian Bürkner. Rank-normalization, folding, and localization: An improved $\widehat{R}$ for assessing convergence of MCMC. *arXiv e-prints*, page arXiv:1903.08008, March 2019.

[164] Pauli Virtanen, Ralf Gommers, Travis E. Oliphant, Matt Haberland, Tyler Reddy, David Cournapeau, Evgeni Burovski, Pearu Peterson, Warren Weckesser, Jonathan Bright, Stéfan J. van der Walt, Matthew Brett, Joshua Wilson, K. Jarrod Millman, Nikolay Mayorov, Andrew R. J. Nelson, Eric Jones, Robert Kern, Eric Larson, C J Carey, İlhan Polat, Yu Feng, Eric W. Moore, Jake VanderPlas, Denis Laxalde, Josef Perktold, Robert Cimrman, Ian Henriksen, E. A. Quintero, Charles R. Harris, Anne M. Archibald, Antônio H. Ribeiro, Fabian Pedregosa, Paul van Mulbregt, and SciPy 1.0 Contributors. SciPy 1.0: Fundamental Algorithms for Scientific Computing in Python. *Nature Methods*, 17:261–272, 2020.

[165] Jakob Walcher, Brent Groves, Tamás Budavári, and Daniel Dale. Fitting the integrated spectral energy distributions of galaxies. Ap&SS, 331:1–52, January 2011.

[166] X. Wang, A. V. Filippenko, M. Ganeshalingam, W. Li, J. M. Silverman, L. Wang, R. Chornock, R. J. Foley, E. L. Gates, B. Macomber, F. J. D. Serduke, T. N. Steele, and D. S. Wong. Improved Distances to Type Ia Supernovae with Two Spectroscopic Subclasses. ApJ, 699(2):L139–L143, July 2009.

[167] David H. Weinberg, Michael J. Mortonson, Daniel J. Eisenstein, Christopher Hirata, Adam G. Riess, and Eduardo Rozo. Observational probes of cosmic acceleration. Phys. Rep., 530(2):87–255, September 2013.

[168] Joseph C. Weingartner and B. T. Draine. Dust Grain-Size Distributions and Extinction in the Milky Way, Large Magellanic Cloud, and Small Magellanic Cloud. ApJ, 548(1):296–309, February 2001.

[169] John Whelan and Jr. Iben, Icko. Binaries and Supernovae of Type I. ApJ, 186:1007–1014, December 1973.

[170] K. D. Wilk, D. J. Hillier, and L. Dessart. Ejecta mass diagnostics of Type Ia supernovae. MNRAS, 474:3187–3211, March 2018.

[171] Kenneth C. Wong, Sherry H. Suyu, Geoff C. F. Chen, Cristian E. Rusu, Martin Millon, Dominique Sluse, Vivien Bonvin, Christopher D. Fassnacht, Stefan Taubenberger, Matthew W. Auger, Simon Birrer, James H. H. Chan, Frederic Courbin, Stefan Hilbert, Olga Tihhonova, Tommaso Treu, Adriano Agnello, Xuheng Ding, Inh Jee, Eiichiro Komatsu, Anowar J. Shajib, Alessandro Sonnenfeld, Roger D. Blandford, Léon V. E. Koopmans, Philip J. Marshall, and Georges Meylan. H0LiCOW - XIII. A 2.4 per cent measurement of H_0 from lensed quasars: 5.3σ tension between early- and late-Universe probes. MNRAS, 498(1):1420–1439, October 2020.

[172] W. Michael Wood-Vasey, Andrew S. Friedman, Joshua S. Bloom, Malcolm Hicken, Maryam Modjaz, Robert P. Kirshner, Dan L. Starr, Cullen H. Blake, Emilio E. Falco, Andrew H. Szentgyorgyi, Peter Challis, Stéphane Blondin, Kaisey S. Mandel, and Armin Rest. Type Ia Supernovae Are Good Standard Candles in the Near Infrared: Evidence from PAIRITEL. ApJ, 689(1):377–390, December 2008.

[173] D. G. York, J. Adelman, J. E. Anderson, Jr., S. F. Anderson, J. Annis, N. A. Bahcall, J. A. Bakken, R. Barkhouser, S. Bastian, E. Berman, W. N. Boroski, S. Bracker, C. Briegel, J. W. Briggs, J. Brinkmann, R. Brunner, S. Burles, L. Carey, M. A. Carr, F. J. Castander, B. Chen, P. L. Colestock, A. J. Connolly, J. H. Crocker, I. Csabai, P. C. Czarapata, J. E. Davis, M. Doi, T. Dombeck, D. Eisenstein, N. Ellman, B. R. Elms, M. L. Evans, X. Fan, G. R. Federwitz, L. Fiscelli, S. Friedman, J. A. Frieman, M. Fukugita, B. Gillespie, J. E. Gunn, V. K. Gurbani, E. de Haas, M. Haldeman, F. H. Harris, J. Hayes, T. M. Heckman, G. S. Hennessy, R. B. Hindsley, S. Holm, D. J. Holmgren, C.-h. Huang, C. Hull, D. Husby, S.-I. Ichikawa, T. Ichikawa, Ž. Ivezić, S. Kent, R. S. J. Kim, E. Kinney, M. Klaene, A. N. Kleinman, S. Kleinman, G. R. Knapp, J. Korienek, R. G. Kron, P. Z. Kunszt, D. Q. Lamb, B. Lee, R. F. Leger, S. Limmongkol, C. Lindenmeyer, D. C. Long, C. Loomis, J. Loveday, R. Lucinio, R. H. Lupton, B. MacKinnon, E. J. Mannery, P. M. Mantsch, B. Margon, P. McGehee, T. A. McKay, A. Meiksin, A. Merelli, D. G. Monet, J. A. Munn, V. K. Narayanan, T. Nash, E. Neilsen, R. Neswold, H. J. Newberg, R. C. Nichol, T. Nicinski, M. Nonino, N. Okada, S. Okamura, J. P. Ostriker, R. Owen, A. G. Pauls, J. Peoples, R. L. Peterson, D. Petravick, J. R. Pier, A. Pope, R. Pordes, A. Prosapio, R. Rechenmacher, T. R. Quinn, G. T. Richards, M. W. Richmond, C. H. Rivetta, C. M. Rockosi, K. Ruthmansdorfer, D. Sandford, D. J. Schlegel, D. P. Schneider, M. Sekiguchi, G. Sergey, K. Shimasaku, W. A. Siegmund, S. Smee, J. A. Smith, S. Snedden, R. Stone, C. Stoughton, M. A. Strauss, C. Stubbs, M. SubbaRao, A. S. Szalay, I. Szapudi, G. P. Szokoly, A. R. Thakar, C. Tremonti, D. L. Tucker, A. Uomoto, D. Vanden Berk, M. S. Vogeley, P. Waddell, S.-i. Wang, M. Watanabe, D. H. Weinberg, B. Yanny, N. Yasuda, and SDSS Collaboration. The Sloan Digital Sky Survey: Technical Summary. AJ, 120:1579–1587, September 2000.